Stress resultant shell approaches for simulations of textile composite reinforcement forming

Bo Chen

N°d'ordre NNT : 2022LYSEI034

THESE de DOCTORAT DE L'UNIVERSITE DE LYON
opérée au sein de
L'Institut National des Sciences Appliquées de Lyon

Ecole Doctorale N° 162
Mécanique, Energétique, Génie civil, Acoustique

Spécialité/ discipline de doctorat :
Génie Mécanique

Soutenue publiquement le 21/04/2022, par :
Bo Chen

STRESS RESULTANT SHELL APPROACHES FOR SIMULATIONS OF TEXTILE COMPOSITE REINFORCEMENT FORMING

Devant le jury composé de :

BINETRUY Christophe	Professeur (Ecole Centrale de Nantes)	Examinateur
KÄRGER Luise	Tenured Senior Scientist (Karlsruhe Institute of Technology)	Rapporteur
WANG Peng	Professeur (University of Haute-Alsace)	Rapporteur
NAOUAR Naim	Chargé de Recherche – CNRS (INSA Lyon)	Co-encadrant
BOISSE Philippe	Professeur (INSA Lyon)	Directeur de thèse
COLMARS Julien	Maitre de Conférences (INSA Lyon)	Co-encadrant

Département FEDORA – INSA Lyon - Ecoles Doctorales

SIGLE	ECOLEDOCTORALE	NOM ET COORDONNEES DU RESPONSABLE
CHIMIE	**CHIMIE DE LYON** **https://www.edchimie-lyon.fr** Sec. : Renée EL MELHEM Bât. Blaise PASCAL, 3e étage secretariat@edchimie-lyon.fr	**M. Stéphane DANIELE** C2P2-CPE LYON-UMR 5265 Bâtiment F308, BP 2077 43 Boulevard du 11 novembre 1918 69616 Villeurbanne **directeur@edchimie-lyon.fr**
E.E.A.	**ÉLECTRONIQUE, ÉLECTROTECHNIQUE, AUTOMATIQUE** **https://edeea.universite-lyon.fr** Sec. : Stéphanie CAUVIN Bâtiment Direction INSA Lyon Tél : 04.72.43.71.70 secretariat.edeea@insa-lyon.fr	**M. Philippe DELACHARTRE** INSA LYON Laboratoire CREATIS Bâtiment Blaise Pascal, 7 avenue Jean Capelle 69621 Villeurbanne CEDEX Tél : 04.72.43.88.63 **philippe.delachartre@insa-lyon.fr**
E2M2	**ÉVOLUTION, ÉCOSYSTÈME, MICROBIOLOGIE, MODÉLISATION** **http://e2m2.universite-lyon.fr** Sec. : Sylvie ROBERJOT Bât. Atrium, UCB Lyon 1 Tél : 04.72.44.83.62 secretariat.e2m2@univ-lyon1.fr	**M. Philippe NORMAND** Université Claude Bernard Lyon 1 UMR 5557 Lab. d'Ecologie Microbienne Bâtiment Mendel 43, boulevard du 11 Novembre 1918 69 622 Villeurbanne CEDEX **philippe.normand@univ-lyon1.fr**
EDISS	**INTERDISCIPLINAIRE SCIENCES-SANTÉ** **http://ediss.universite-lyon.fr** Sec. : Sylvie ROBERJOT Bât. Atrium, UCB Lyon 1 Tél : 04.72.44.83.62 secretariat.ediss@univ-lyon1.fr	**Mme Sylvie RICARD-BLUM** Institut de Chimie et Biochimie Moléculaires et Supramoléculaires (ICBMS) - UMR 5246 CNRS - Université Lyon 1 Bâtiment Raulin - 2ème étage Nord 43 Boulevard du 11 novembre 1918 69622 Villeurbanne Cedex Tél : +33(0)4 72 44 82 32 **sylvie.ricard-blum@univ-lyon1.fr**
INFOMATHS	**INFORMATIQUE ET MATHÉMATIQUES** **http://edinfomaths.universite-lyon.fr** Sec. : Renée EL MELHEM Bât. Blaise PASCAL, 3e étage Tél : 04.72.43.80.46 infomaths@univ-lyon1.fr	**M. Hamamache KHEDDOUCI** Université Claude Bernard Lyon 1 Bât. Nautibus 43, Boulevard du 11 novembre 1918 69 622 Villeurbanne Cedex France Tél : 04.72.44.83.69 **hamamache.kheddouci@univ-lyon1.fr**
Matériaux	**MATÉRIAUX DE LYON** **http://ed34.universite-lyon.fr** Sec. : Yann DE ORDENANA Tél : 04.72.18.62.44 yann.de-ordenana@ec-lyon.fr	**M. Stéphane BENAYOUN** Ecole Centrale de Lyon Laboratoire LTDS 36 avenue Guy de Collongue 69134 Ecully CEDEX Tél : 04.72.18.64.37 **stephane.benayoun@ec-lyon.fr**
MEGA	**MÉCANIQUE, ÉNERGÉTIQUE, GÉNIE CIVIL, ACOUSTIQUE** **http://edmega.universite-lyon.fr** Sec. : Stéphanie CAUVIN Tél : 04.72.43.71.70 Bâtiment Direction INSA Lyon mega@insa-lyon.fr	**M. Jocelyn BONJOUR** INSA Lyon Laboratoire CETHIL Bâtiment Sadi-Carnot 9, rue de la Physique 69621 Villeurbanne CEDEX **jocelyn.bonjour@insa-lyon.fr**
ScSo	**ScSo*** **https://edsciencessociales.universite-lyon.fr** Sec. : Mélina FAVETON INSA : J.Y. TOUSSAINT Tél : 04.78.69.77.79 melina.faveton@univ-lyon2.fr	**M. Christian MONTES** Université Lumière Lyon 2 86 Rue Pasteur 69365 Lyon CEDEX 07 **christian.montes@univ-lyon2.fr**

*ScSo : Histoire, Géographie, Aménagement, Urbanisme, Archéologie, Science politique, Sociologie, Anthropologie

Acknowledgements

With the completion of the dissertation, my doctoral research in INSA Lyon will come to an end. Looking back on my past research life, I'd like to thank everyone I met during this happy and unforgettable research period in France.

I would first like to devote my sincere appreciation to my supervisor, Professor Philippe Boisse. The completion of the thesis is inseparable from his careful guidance. He is always there for helping me and answering my question at any time. Even though the covid epidemic for nearly two years has prevented us from working at INSA Lyon for some time, our discussions have never stopped. He is a patient, rigorous, optimistic, and responsible supervisor. Many thanks for his care in my life and help in the scientific research.

I would like to thank my co-supervisor Dr. Julien Colmars. He plays an important role in promoting and supervising the thesis research. He is a creative researcher and always full of good ideas. Thanks for his help when I meet problems with my research. I also want to express my thanks to Dr. Naim Naouar for the kind help in programming and the suggestion in every discussion.

I would like also thanks to my colleagues and friends, Renzi, Ruochen, Jin, Jie, Yvan, Quentin, Guzman, Tarek, Yuanhang, Baptiste and all the other people. Thanks for the help, sharing, and discussion about life and research. My thanks also go to Mr. Philippe Chaudet for his help in my experiment.

Thanks to Professor Anne Tanguy and Assistant Professor Kerem Ege for the guidance in the annual dissertation supervision.

I wish to acknowledge the Chinese Scholarship Council (CSC) for providing me with this chance to study here.

I would also like to take this opportunity to thanks my girlfriend Dr. Ziyin Xiang. Hearty thanks for her company, concern, and encouragement.

At last, I sincerely thank my parents and my sister for being my spiritual support.

Bo

Residence Barcelona 17/02/2022

Résumé

Titre : Approches de coques en efforts résultants pour la simulation de la mise en forme des renforts textiles de composites

La simulation numérique du renfort composite textile joue un rôle essentiel dans l'amélioration de la qualité de fabrication, la réduction du cycle de fabrication et du coût de fabrication. L'épaisseur du renfort composite textile est significativement plus petite que les deux autres dimensions, ce qui permet de faire la simulation en utilisant des éléments de coque. Cependant, le glissement possible entre les fibres donne au matériau un comportement très spécifique : le comportement en flexion est indépendant du comportement de la membrane. La théorie classique des coques ne peut pas être adoptée directement. Une approche de coque résultante des contraintes est proposée pour la simulation du renforcement composite textile. Cette approche introduit une rigidité de flexion indépendante pour découpler le comportement de flexion du comportement de la membrane. Les résultantes et les moments de contrainte sont liés aux déformations et aux courbures de la membrane par des équations constitutives de taux (lois hypoélastiques). Différents types d'expériences de formage sous différentes conditions limites sont réalisés pour comparer la simulation et l'expérience. La comparaison montre l'efficacité et l'exactitude de l'approche proposée pour prédire le formage des composites textiles. Cette approche est implémentée dans le logiciel commercial ABAQUS et peut être utilisée par tous les utilisateurs de ce logiciel.

Par rapport aux approches de simulation existantes qui ne peuvent se concentrer que sur la déformation du matériau dans le plan, une méthode de post-traitement est proposée pour prédire la rotation des directeurs normaux. Basée sur le mécanisme de déformation du matériau, cette méthode suppose que la fibre est quasi-inextensible et que l'épaisseur reste constante. La rotation des directeurs normaux peut alors être obtenue sur la base de la déformation dans le plan. Un programme Matlab est codé pour effectuer le calcul, et une expérience de flexion en porte-à-faux multicouche est réalisée pour valider son efficacité.

Le plissement est l'un des principaux défauts lors de la mise en forme des renforts textiles composites. Pour caractériser la drapabilité du matériau textile, qui est la capacité à se déformer sans plis, un rapport entre la rigidité en cisaillement et la rigidité en flexion du matériau est défini. Une série d'expériences de formage de boîtes carrées et de cylindres est réalisée en utilisant différents types de renforts textiles composites. Il est démontré que le rapport défini peut représenter la drapabilité du matériau. Et le matériau avec un plus petit rapport de drapabilité est plus facile à mettre en forme sans plis des formes complexes.

Mots-clés: Composite textile; Analyse par éléments finis; coques en efforts résultants; Rotation normale; Drapabilité.

Abstract

Title: Stress resultant shell approaches for simulations of textile composite reinforcement forming

Numerical simulation of the textile composite reinforcement plays a critical role in improving the manufacturing quality, reducing the manufacturing cycle, and manufacturing cost. The thickness of the textile composite reinforcement is significantly smaller than the other two dimensions, which make it possible to make the simulation using shell element. However, the possible slippage between the fibers gives the material a very specific behavior: the bending behavior is independent of the membrane behavior. The classical shell theory cannot be directly adopted. Specific to the woven fabric, a stress resultant shell approach is proposed for conducting the forming simulation. This approach introduces an independent bending stiffness to decouple bending behavior with membrane behavior. The stress resultants and stress moments are related to membrane strains and curvatures by rate constitutive equations (hypoelastic laws). Different types of forming experiments under different boundary conditions are conducted to make the comparison between simulation and experiment. The comparison shows the effectiveness and correctness of the proposed approach in predicting the textile composite forming. This approach is implemented in the commercial software ABAQUS and can be used by all users of this software.

Specific to the existed simulation approaches that can only focus on the material in-plane deformation, a post-processing method is proposed to predict the rotation of normal directors. Based on the material deformation mechanism, this method assumes that the fiber is quasi-inextensible, and the thickness will keep constant. Then the rotation of normal directors can be obtained based on the in-plane deformation. A Matlab program is coded to conduct the computation, and multi-layer cantilever bending experiment is conducted to validate its effectiveness.

Wrinkling is one of the main defects during the textile composite reinforcement forming. To characterize the textile material drapability which is the ability to deform without wrinkles, a ratio of material shear stiffness and bending stiffness is defined. A series of square box and cylinder forming experiments are conducted using different types of textile composite reinforcements. It is demonstrated that the defined ratio can represent material drapability. And the material with a smaller drapability ratio is easier to form complex shapes without wrinkles.

Keywords: Textile composite; Finite element analysis; Stress resultant shells; Normal rotation; Drapability.

Content

Acknowledgements I

Résumé II

Abstract III

Content IV

List of Figures VII

List of Tables XIII

Introduction générale 1

General introduction 3

Les Résumé de Thèse en Français 5

Chapter 1 Composite material: introduction and simulation approach 19

1.1 Introduction to the composite material 20

1.1.1 Composite materials and their applications 20

1.1.2 Types of composite materials 22

1.2 Composite materials of woven fabric reinforcement 23

1.2.1 Structure of woven fabric 24

1.2.2 Types of woven fabric reinforcement 24

1.2.3 Non Crimp Fabric 27

1.2.4 Molding processes of woven fabric reinforcement 28

1.3 Numerical simulation approach for textile composites 31

1.3.1 Kinematic approach 31

1.3.2 Mechanical approach 33

1.4 Research motives and objectives 42

1.5 Summary 43

Chapter 2 A hypoelastic stress resultant shell approach for simulations of textile composite reinforcement forming 45

2.1 The specificity deformation of textile composite 46

2.2 The hypoelastic stress resultant approach 49

2.2.1 The stress resultant shells 49
2.2.2 The hypoelastic laws for the textile composite 51
2.3 Elementary test 56
2.4 The characterization of the mechanical behavior of the textile composites 58
2.4.1 Tensile behavior 60
2.4.2 In-plane shear behavior 60
2.4.3 Bending behavior 65
2.5 Summary of Chapter 2 70
Chapter 3 Numerical and experimental forming analysis of the textile composite 71
3.1 The introduction of the experiment process 73
3.1.1 Forming experimental platform 73
3.1.2 Material preparation 74
3.2 Simulation settings 76
3.2.1 Simulation modeling 76
3.2.2 The tested material properties 79
3.3 Hemisphere forming 81
3.3.1 In-plane shear angle comparison 81
3.3.2 Fabric contour comparison 83
3.3.3 Punch force comparison 85
3.3.4 Wrinkles comparison in multi-layers forming 86
3.3.5 Wrinkles comparison during forming without blank-holder 87
3.4 Tetrahedron forming 92
3.4.1 In-plane shear angle comparison 93
3.4.2 Fabric contour comparison 95
3.5 The deformation in the thickness direction 96
3.5.1 The insufficient of Kirchhoff shell 96
3.5.2 The insufficient of Mindlin shell 97
3.5.3 The specific bending behavior of fibrous material 100

3.5.4 Comparison of different simulation approach 102
3.5.5 The post-processing method 106
3.5.6 Verification of the post processing 108
3.6 Summary of Chapter 3 110
Chapter 4 Experimental analysis of the textile composite drapability 111
4.1 Drapability analysis of the textile composite 112
4.2 Introduction to the prepared textile composite reinforcement 114
4.3 Experimental determination of shear and bending behavior 115
4.3.1 In-plane shear stiffness 116
4.3.2 Bending stiffness 121
4.4 The definition of drapability ratio 123
4.5 Forming experiment 125
4.5.1 Experiment setup 126
4.5.2 Square box forming 126
4.5.3 Cylinder forming 131
4.6 Summary of Chapter 4 134
Conclusion and prospective 136
Bibliography 138
Thesis publications 153

List of Figures

Figure 1.1 (a) Schéma de principe du drapomètre. (b) Calcul du coefficient de drapé. [Vangheluwe & Kiekens, 1993]. 15

Fig. 1.1 Composition of composite materials 20

Fig. 1.2. Application of composite materials in Boeing 787 [Boeing Company, 2013]. 20

Fig. 1.3. Automotive part made of composite material [Guzman-Maldonado et al., 2016]. 21

Fig. 1.4. Structure of woven fabric [Y. Huang et al., 2017]. (a) The commercial fabric. (b) The plain weave structure. (c) The yarn. (d) The fibers..... 24

Fig. 1.5. The 2D woven fabric fabrication process [Florimond, 2013]. 24

Fig. 1.6. Different types of 2D woven fabric (Generated by TexGen). (a) Plain weave. (b) Twill weave. (c) Satin weave 25

Fig. 1.7. Different types of 2.5 and 3D woven fabric [Gu & Zhili, 2002]..... 26

Fig. 1.8. Schematic diagram of the stitching process for 3D fabric [Dransfield et al., 1994]. 27

Fig. 1.9. A biaxial NCF fabric. (a) Top side (b) Bottom side..... 27

Fig. 1.10. Steps of RTM process [Buet Gautier, 1998] 28

Fig. 1.11. Types of prepregs (a) Prepregs tow (b) prepregs tap..... 29

Fig. 1.12. Schematic diagram of Automated Fiber Placement (AFP) process [Han et al., 2017] 30

Fig. 1.13. Steps of thermoforming process [Guzman-Maldonado et al., 2016] 30

Fig. 1.14 Assumption of the kinematic approach [Aono et al., 1994]. 32

Fig. 1.15. The principle of kinematic approach [Boisse, 2004]. 32

Fig. 1.16. The three simulation scales for textile composites [Hamila & Boisse, 2013b]..... 33

Fig. 1.17. Modeling at the microscopic scale of a reinforcement. (a)Model of Wang [Y. Wang & Sun, 2001] (b) Model of Durville [Durville, 2010]. 34

Fig. 1.18. Model generation of 3D reinforcement. (a) Model in WiseTex [Lomov et al., 2000]. (b) Model in TexGen [Sherburn, 2007]. 35

Fig. 1.19. Modeling of an interlock fabric by processing a tomography [Naouar et al., 2015](a) 3D tomography image of the fabric architecture. (b) The 3D simulation model. 36

Fig. 1.20. The discrete modelling approach. (a) The typical ‘O’ discrete model. (b) Stretch. (c) Torsion. (d) Shear. (e) Bending [Sze & Liu, 2005]. 37

Fig. 1.21. The semi-discrete approach using three node shell element [Hamila et al., 2009] 38

Fig. 1.22. Forming simulation using the semi-discrete approach (a) Tetrahedron forming [Allaoui et al., 2011] (b) Square box forming [P. Wang, Legrand, et al., 2015]. 38

Fig. 1.23. Different constitutive for the continuous simulation approach (a) Non-orthogonal constitutive model [Peng & Cao, 2005]. (b)Orthogonal constitutive model [M. A. Khan et al., 2010]. 40

Fig. 1.24. The deformed fabric given by the non-orthogonal method [Badel, Vidal-Sallé, & Boisse, 2008] 41

Fig. 1.25 The comparison between experiment and simulation conducted by the orthogonal method. (a) Experiment. (b)Simulation [M. A. Khan et al., 2010]..... 41

Fig. 1.26. A meso model embedded in a macro element [J. Wang et al., 2020, 2022]. 42

Fig. 2.1. In-plane shear deformation in different cases. (a) Bias extension test of glass fiber. (b) Hemisphere forming[Boisse et al., 2017]. 46

Fig. 2.2. Wrinkle in the compression deformation of textile composite with different bending stiffness[Boisse et al., 2018]. (a) 1 $N \cdot mm^{-1}$. (b) 10 $N \cdot mm^{-1}$. 47

Fig. 2.3. Bending deformation in different cases. (a) G1151 fabric bending under its gravity (b) Bending of curtain..... 47

Fig. 2.4. Simulation approach considering the bending behavior of the textile composite. (a) Laminate approach [Döbrich et al., 2013]. (b) Superposition of beam and membrane element [Jauffrès et al., 2010]. (c) Superposition of membrane and shell element [Dörr et al., 2018]..... 48

Fig. 2.5. Stress resultants and moments in the shell elements 50

Fig. 2.6. Green-Naghdi frame rotation in a simple shear test (Abaqus/Explicit result). 53

Fig. 2.7. Orthonormal frames in the fiber direction and the Green Naghdi frame. 54

Fig. 2.8. Schematic of boundary conditions applied to the three elementary tests. (a) 45° simple shear test after a traction ratio 2. (b) Rigid body rotation test after a traction ratio 2. (c) Pure bending test. 57

Fig. 2.9. Stress resultants and moment on a woven unit cell (a) Tensions (b) In-plane shear (c) Bending 59

Fig. 2.10. The interlock fabric G1151 (a) The warp and weft yarn (b) the X-ray Tomography [Badel, Vidal-Sallé, Maire, et al., 2008]..... 59

Fig. 2.11. Biaxial tensile test..... 60

Fig. 2.12. The picture frame test 61

Fig. 2.13. The bias extension test 63

Fig. 2.14. Bias extension test of G1151. (a) The experimental deformation. (b) The experiment result of load-displacement. 64

Fig. 2.15. In-plane shear behavior verification (a) Shear angle comparison (b) Machine load comparison 65

Fig. 2.16. Cantilever test under gravity 66

Fig. 2.17. Cantilever test of G1151 (a) Bending experiment along warp yarn (b) Bending simulation along warp yarn (c) Bending experiment along weft yarn (d) Bending simulation along weft yarn. 67

Fig. 2.18. The bending behavior of G1151. (a) Weft yarn direction. (b) Warp yarn direction. ... 68

Fig. 2.19. The section comparison between simulation and experiment 69

Fig. 3.1. Experimental set-up 73

Fig. 3.2. Schematic diagram of the forming experiment 74

Fig. 3.3. Yarn orientation configuration of the specimen. (a) 0°/90°. (b) ±45°. 74

Fig. 3.4. Deformed fabric under different yarn configurations. (a) Asymmetry. (b) Symmetry.. 75

Fig. 3.5. The transparent square ruler 75

Fig. 3.6. Marker points on the specimen for forming experiment 76

Fig. 3.7. Modelling the forming specimen 76

Fig. 3.8. Modeling of multi-layers forming 77

Fig. 3.9. Hemisphere modelling. (a)Blank holder (b) punch (c) Die (d) Assembly 78

Fig. 3.10. Tetrahedron modelling. (a)Blank holder (b) punch (c) Die (d) Assembly 78

Fig. 3.11. The plain weave [Guzman-Maldonado et al., 2019]. 79

Fig. 3.12. The shear behavior comparison between G1151 and plain weave. 80

Fig. 3.13. Geometry setting of hemisphere forming 81

Fig. 3.14. Shear angle comparison in the final deformed shape. (a) Single layer of 0°/90°. (b) Single layer of ±45°. (c) Four layers of quasi-isotropic layer-up. 83

Fig. 3.15. Fabric contour comparison in the final deformed shape of hemisphere forming. (a) Single layer of 0°/90°. (b) Single layer of ±45°. (c) Four layers of quasi-isotropic layer-up..... 84

Fig. 3.16. Punch force during the hemispherical forming of a four-layer quasi-isotropic layer-up. 85

Fig. 3.17. Four layers of quasi-isotropic plain weave. (a)Experiment[Guzman-Maldonado et al., 2019]. (b) Simulation done with the stress resultant shell approach. 86

Fig. 3.18. The 0°/90° single-layer hemisphere forming without blank-holder. (a)Top view. (b)Bottom view 87

Fig. 3.19. 3D laser scanner approach 88

Fig. 3.20. Digital image correlation (DIC) approach 88

Fig. 3.21. Wrinkle measurement results of 0°/90° single-layer G1151 fabric. (a) 3D laser scanner (b) Digital image correlation (DIC). 89

Fig. 3.22. Experiment and simulation comparison of G1151 fabric hemisphere forming without blank-holder (a) Experiment (b) Simulation 91

Fig. 3.23. The defined two path in the G1151 fabric hemisphere forming without blank-holder 91

Fig. 3.24. Wrinkle amplitude comparison between simulation and experiment of the G1151 fabric. (a) 0° path (b) 45° path. 92

Fig. 3.25. Geometry setting of tetrahedron forming 93

Fig. 3.26. Shear angle comparison of single layer. (a) Single layer of 0°/90°. (b) Single layer of ±45°. 94

Fig. 3.27. Shear angle comparison of four-layer quasi-isotropic layup. (a) Bottom view (b) Top view 95

Fig. 3.28. Fabric contour comparison between experiment and simulation. (a) Single layer of 0°/90°. (b) Single layer of ±45°. (c) Four-layer with quasi-isotropic layup. 96

Fig. 3.29. The three-point bending test (a) Continuous material. (b) Fibrous material [Orliac, 2012]. 97

Fig. 3.30. The four-point bending test (a) The experiment setting (b) The bending moment and corresponding shear force 98

Fig. 3.31. The four-point bending comparison between Mindlin shell and fibrous material (a) Simulation result of Mindlin shell (SE4:transverse shear strain) (b) Experiment result of G1151 fabric material 99

Fig. 3.32. Simulation result using different transverse shear stiffness of Mindlin shell (a) k_{13}=100 (b) k_{13}=10 (c) k_{13}=1 100

Fig. 3.33. Bending deformation of multi-layers G1151 interlock fabric 101

Fig. 3.34. 3D Fibrous shell approach [Bai et al., 2020] 102

Fig. 3.35. The cantilever test with a predefined displacement 104

Fig. 3.36. Cantilever simulation results using different approaches. (a) Laminated shell approach. (b) Superimposed element approach. (c) Stress resultant shell approach. (d) Fibrous shell approach. 105

Fig. 3.37. Contour comparison of different approaches 105

Fig. 3.38. Simulation results of hemisphere forming using different approaches. (a) Laminated shell approach (b) Superimposed element approach. (c) Stress result shell approach. (d) Fibrous shell approach 106

Fig. 3.39. Schematic diagram of the post-processing approach 108

Fig. 3.40. Cantilever bending test of 130 layers paper. (a) The geometry setting. (b) Experimental results [Liang et al., 2017] (c) Post-processing results. 109

Fig. 3.41. Comparison between experiment results and post-processing results (a) The Middle line comparison. (b) The normal rotation comparison. 109

Fig. 4.1 (a) Schematic diagram of the drape meter. (b) Calculation of the Drape coefficient. [Vangheluwe & Kiekens, 1993] 112

Fig. 4.2. The role of the material behavior on the wrinkles forming through simulation [Boisse et al., 2011] (a) geometry setting (b) Tensile stiffness only. (c) Tensile stiffness and in-plane shear stiffness. (d) Tensile stiffness, in-plane shear stiffness and bending stiffness. 113

Fig. 4.3. Square box forming of a single layer oriented at 0°/90°. (a) Glass plain weave. (b) Carbon plain weave [J. Huang et al., 2021]. 114

Fig. 4.4 The three material deformation modes of woven material at the macro scale. (a)Tensile (b) In-plane shear (c) Out-of-plane bending 115

Fig. 4.5 The linear fitting of in-plane shear properties 116

Fig. 4.6 G1151 experimental curve of the clamping force at different stretch distance 118

Fig. 4.7 The picture frame test of triaxle NCF (a) Experimental setting (b) Experimental curve of stretch force versus stretch distance. 119

Fig. 4.8 Experimental curve of force versus displacement of the isotropic material 121

Fig. 4.9 The Peirce cantilever test 122

Fig. 4.10. The sorted drapability ratio of the selected materials 125

Fig. 4.11. Forming experiment setting 126

Fig. 4.12. Square box forming geometry parameters 127

Fig. 4.13. Square box forming with wrinkles. (a) Isotropic material (b) NCF triaxle (c) Glass 3 (d) Carbon 4 (e) Twill 1 (f) Glass 1 (g) Glass 2 128

Fig. 4.14. Square box forming without wrinkles (a) Twill 3 (b) Satin (c) Twill 2 (d)NCF Carbon (e) G1151 (f) G1100 129

Fig. 4.15. The relationship between drapability ratio and the material deformation in square box forming 130

Fig. 4.16. Cylinder forming geometry parameters 131

Fig. 4.17. Cylinder forming with wrinkles. (a) Isotropic material (b) Twill 1 (c) Glass 1 132

Fig. 4.18. Cylinder forming without wrinkles (a) Glass 2 (b) Twill 3 (c) Twill 2 (d) NCF Carbon (e) G1151 (f) G1100 133

Fig. 4.19. The relationship between drapability ratio and the material deformation in cylinder forming (legends of green are material used on the cylinder forming) 134

List of Tables

Table 2.1. The objective rate used in Abaqus different modules [SIMULIA, 2019] 53

Table 2.2. Theoretical value of the elementary test 58

Table 2.3. Geometric characteristics of the G1151 interlock fabric 59

Table 3.1. Comparison of geometric characteristics of the G1151 fabric and the plain weave ... 79

Table 3.2. Principal mechanical properties of G1151 and Plain weave 80

Table 3.3 Transverse shear strain in different approach 99

Table 3.4. Material behaviors input for all approach 103

Table 3.5. External force output for the different approach 104

Table 3.6. The properties of a single-layer of papers 108

Table 4.1 The selected materials for forming experiments 114

Table 4.2 Experiment parameters of the bias extension test 117

Table 4.3 The in-plane shear stiffness kc of the selected textile materials 118

Table 4.4 Experiment parameters of the picture frame test 119

Table 4.5 Experiment parameters of the tensile test 120

Table 4.6 The areal density of the selected materials 122

Table 4.7 The out of plane bending stiffness Db of the selected materials 123

Table 4.8. The drapability ratio of the selected materials 125

Introduction générale

Les composites à fibres continues ont été largement utilisés dans différents domaines industriels pour obtenir des composants légers à haute performance. L'un des principaux avantages de l'utilisation des composites réside dans la possibilité de concevoir les propriétés mécaniques pour répondre aux exigences de conception de l'application spécifique. Cependant, cet avantage entraîne également des défis importants au niveau du processus de fabrication. Il existe plusieurs procédés de fabrication des composites fibreux continus, notamment le moulage par transfert de résine (RTM) et le thermoformage. Afin d'éviter les processus "d'essai et d'erreur", la simulation de la déformation du matériau pendant la phase de fabrication joue un rôle important. Pour le renfort des composites textiles, des milliers de fibres tissées ensemble constituent le matériau du renfort, ce qui donne un comportement très spécifique pour lequel l'outil de simulation général ne peut être adopté. Dans cette thèse, le travail de recherche se concentrera principalement sur le développement d'un modèle de simulation pour prédire avec précision la déformation du renfort composite textile.

Le chapitre 1 présente les connaissances de base sur les matériaux composites, en accordant une attention particulière à la structure du composite textile et aux processus de fabrication. Les approches numériques précédentes, qui peuvent être classées en approches cinématiques et approches mécaniques, sont présentées dans le chapitre suivant. Les différentes approches numériques ont leurs avantages et leurs inconvénients. En raison de l'efficacité du calcul, le matériau peut être considéré comme un milieu continu à l'échelle macroscopique, et l'approche macroscopique est adoptée pour développer le modèle de simulation pour le renfort du composite textile.

Le chapitre 2 présente l'approche numérique développée pour la simulation du renfort textile composite. L'épaisseur du renfort textile est relativement plus faible que les deux autres dimensions, et donc l'élément de coque peut être adopté. Cependant, le glissement possible entre les fibres donne à ce type de matériau des comportements très spécifiques, et les théories générales de coque (coque de Kirchhoff et de Mindlin) ne peuvent pas être directement utilisées. Dans ces éléments de coque généraux, la rigidité en flexion est déterminée par la rigidité et l'épaisseur de la membrane, ce qui n'est pas le cas pour les renforts textiles. L'élément de coque résultant de la contrainte est adopté pour découpler le comportement en flexion du comportement de la membrane. Trois comportements du matériau (traction, cisaillement dans le plan et flexion hors du plan) qui jouent un rôle principal dans la déformation du matériau sont considérés dans l'élément de coque résultant de la contrainte, et les comportements du matériau sont décrits par des équations constitutives hypoélastiques dans l'approche de simulation. On présentera aussi la méthode pour caractériser le comportement du matériau. Cette simulation est implémentée dans la sous-routine

VUGENS du logiciel commercial Abaqus, ce qui rend l'approche proposée disponible pour toutes les utilisations d'Abaqus. La vérification élémentaire initiale est effectuée par la suite. Et la comparaison montre que les résultats de la simulation sont les mêmes que les résultats théoriques.

Le chapitre 3 présente les différents types d'expériences de formage dans le but de les comparer aux résultats de simulation obtenus par l'approche de simulation présentée dans le chapitre 2. Des expériences avec différentes configurations de couches sont menées, y compris avec une couche unique pour différentes orientations et différentes configurations multicouches. Les plissement sont l'un des principaux défauts du processus de formage. Afin de vérifier la capacité de l'approche proposée à prédire les plissement, le formage de l'hémisphère sans serre-flan est réalisé pour obtenir des plissement significatives. Toutes les expériences avec différentes conditions limites sont comparées avec les résultats de la simulation, les variables de comparaison sont l'angle de cisaillement dans le plan dans les différentes zones, le contour du tissu après la déformation du matériau, la force du poinçon et la géométrie des plissement. Les résultats de la comparaison indiquent l'efficacité et l'exactitude de l'approche proposée pour prédire la déformation du matériau.

Pour l'instant, l'approche de coques en efforts résultants se concentre uniquement sur la déformation du matériau dans le plan, comme l'ont fait certaines des méthodes précédentes en considérant la rigidité en flexion indépendante. La déformation dans le sens de l'épaisseur est également importante lorsque l'épaisseur est plus grande, comme dans le cas de la formation de multicouches et de tissus 3D. Sur la base du mécanisme de déformation du matériau dans le sens de l'épaisseur, une méthode simple de post-traitement est proposée pour prédire les directeurs normaux. Cette méthode est validée par le cas de la flexion en porte-à-faux multicouche.

Enfin, dans le chapitre 4, la drapabilité du renfort composite textile est étudiée. Afin de caractériser la capacité à se déformer sans plis, on définit un rapport de drapabilité qui est le rapport entre la rigidité en flexion et la rigidité en cisaillement. Différents types de composites textiles avec différentes rigidités en flexion et en cisaillement sont préparés, et les expériences de formation de boîtes carrées et de cylindres utilisant les composites textiles préparés sont menées. Grâce à l'observation des plissement pendant le formage de différents types de matériaux, on constate que la rigidité en cisaillement augmente la tendance à la formation de plissement, tandis que la rigidité en flexion la diminue. Et les résultats de l'expérience démontrent pleinement que le matériau avec un plus petit rapport de drapabilité est plus facile à mettre en forme sans plissement dans des formes complexes.

General introduction

Continuous fibrous composites have been widely used in the different industry fields to obtain lightweight components with high performance. One of the main advantages of the use of composites lies in the designability of the mechanical properties to meet the design requirement of the specific application. However, this advantage also brings significant challenges to the manufacturing process. There are several manufacturing processes of the continuous fibrous composites including the resin transfer molding (RTM) and thermoforming process. To avoid 'trial and error' processes, the simulation of the material deformation during the manufacturing stage plays an important role. For the textile composite reinforcement, thousands of fibers are weaved together to the material which gives these types of material a very specific material behavior, the general simulation tool cannot be adopted. In the thesis, research work will mainly focus on the development of a simulation model to accurately predict the deformation of the textile composite reinforcement.

In chapter 1, background knowledge of the composite material is presented with special attention on the structure of textile composite and the manufacturing process. The previous numerical approaches which can be classified into the kinematic approaches and mechanical approaches are introduced in the next. Different numerical approaches have their advantage and disadvantage. Due to the computational efficiency, the material can be considered as a continuous medium at the macroscale scope, and the macroscale approach is adopted to develop the simulation model for the textile composite reinforcement.

Chapter 2 gives the introduction of the numerical approach developed for the simulation of the textile composite reinforcement. The thickness of the textile reinforcement is relatively smaller than the other two dimensions, and thus the shell element can be adopted. However, the possible slippage between fibers gives this type of material very specific behaviors, and the general shell theories (Kirchhoff and Mindlin shells) cannot be directly used. In these general shell elements, the bending stiffness is determined by the membrane stiffness and thickness, which is not the case for textile reinforcements. The stress resultant shell element is adopted to decouple the bending behavior with the membrane behavior. Three material behaviors (tensile, in-plane bending, and out-of-plane bending) which play a main role in the material deformation are considered within the stress resultant shell element, and the material behaviors are described by hypoelastic constitutive equations in the simulation approach. The method to characterize the material behavior is introduced. This simulation is implemented in the subroutine VUGENS of the commercial software Abaqus which makes the proposed approach available to any user of Abaqus. The initial elementary verification is conducted in the next. And the comparison shows that the simulation results are the same as the theoretical results.

Chapter 3 conducts the different types of forming experiments with the objective of making a comparison with the simulation results obtained by the simulation approach introduced in Chapter 2, the forming shapes include hemisphere and tetrahedron. The experiments with different layer configurations are conducted, including the single-layer with different orientations and multi-layer configurations. Wrinkles are one of the main defects during the forming process. In order to verify the ability of the proposed approach to predict the wrinkles, the hemisphere forming without blank-holder is conducted to obtain the significant wrinkles. All experiments with different boundary conditions are compared with the simulation results, the comparison variables have the in-plane shear angle in the different zones, fabric contour after the material deformed, punch force, and wrinkles geometry. The comparison results indicate the effectiveness and correctness of the proposed approach in predicting material deformation.

For now, the stress-resultant approach only focuses on the material in-plane deformation, as did some of the previous methods considering the independent bending stiffness. The deformation in the thickness direction is also important when the thickness goes larger like the multi-layers forming and 3D fabric forming. Based on the material deformation mechanism in the thickness direction, a simple post-processing method is proposed to predict the normal directors. This method is validated by the multi-layer cantilever bending case.

Finally, in chapter 4, the drapability of the textile composite reinforcement is researched. In order to characterize the ability to deform without wrinkles, a drapability ratio is defined which is the ratio of the shear stiffness and bending stiffness. Different types of textile composites with different bending stiffness and shear stiffness are prepared, and the square box and cylinder forming experiments using the prepared textile composites are conducted. Through the observation of the wrinkles during forming different types of material, it can be found that the shear stiffness increases the tendency of the wrinkle formation while the bending stiffness decreases it. And the experiment results fully demonstrate that the material with a smaller drapability ratio is easier to form complex shapes without wrinkles.

Les Résumé de Thèse en Français

Chapitre 1 Le matériau composite et l'approche de la simulation

1.1 Introduction au matériau composite

Les matériaux composites sont composés d'au moins deux matériaux non miscibles, et les matériaux constitutifs resteront indépendants à l'échelle micro tout en formant une partie entière à l'échelle macro. Selon les propriétés mécaniques des matériaux constitutifs, les parties constitutives des matériaux composites peuvent être divisées en renforcement et matrice. Les matériaux composites combinent les propriétés de différents matériaux pour présenter de nombreuses propriétés excellentes, et les matériaux composites ont été largement utilisés dans différents domaines.

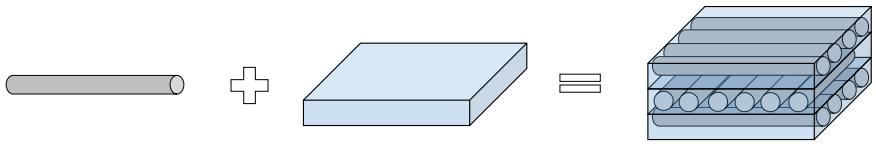

Figure 1.1 Composition of composite materials

1.2 Matériaux composites à base de tissu de renforcement

Les tissus tissés sont constitués de fibres continues de très petits diamètres (normalement compris entre 5 et 15 um). Les types de fibres sont la fibre de verre, la fibre de carbone et la fibre de Kevlar. Les fibres longues et continues s'assemblent pour former le fil, ce qui lui confère une très grande rigidité. Le fil peut être nommé par le nombre de fibres continues constitutives, comme le fil 7K qui représente que ce type de fil est composé de 7000 filaments de fibres. Les fils s'assemblent par tissage pour former le tissu destiné à la fabrication du composant composite.

Sur la base de l'arrangement des fils dans le tissu, le renforcement de tissu peut être divisé en renforcement de tissu 2D, 2.5D, et 3D. Le tissu unidirectionnel présente une résistance élevée dans la direction des fibres, mais la résistance est quasi nulle dans la direction transversale. Cela ne convient pas à une application réaliste. Pour surmonter cette difficulté, le tissu 2D est créé en entrelaçant les fils bidirectionnels dans le plan. Les tissus 2,5D et 3D sont conçus pour éviter la délamination dans le sens de l'épaisseur.

Il existe de nombreux procédés de fabrication pour le moulage des composites tissés. Dans ce chapitre, les deux procédés classiques de moulage : Le moulage par transfert de résine (RTM) et le thermoformage seront présentés car ces deux procédés sont adaptés à la production de masse.

Pour le RTM et le thermoformage, l'étape de formation est similaire. Le matériau est déformé dans la forme souhaitée sous l'action du moule. Plusieurs paramètres de fabrication vont influencer la déformation du matériau, comme la forme, la position et la pression du porte-banque. Afin d'éviter les processus d'essais et d'erreurs, il est nécessaire de procéder à la simulation de cette étape de formage, ce qui constitue le principal travail du manuscrit présenté au chapitre 2. La simulation de l'étape de formage a deux objectifs principaux :

- Déterminer si le procédé de formage est adapté à la formation de la pièce composite sans défaut, ou dans quelles conditions de fabrication cela est possible.
- Donnez les informations sur la déformation comme la direction du fil de la fibre et le profil.

1.3 Approche de la simulation numérique pour les composites textiles

Les approches de simulation numérique peuvent être classées en approches cinématiques et approches mécaniques [Lim & Ramakrishna, 2002 ; Boisse, 2015 ; Bussetta & Correia, 2018]. Les approches cinématiques, également appelées approches cartographiques ou approches fish-net, sont purement géométriques et peuvent donner l'orientation des fibres après la déformation du composite textile [Mack & Taylor, 1956 ; Pickett et al., 2005 ; Potluri et al., 2006 ; Hearle, 2015]. L'approche mécanique, aussi appelée approche finie, est basée sur le modèle constitutif du matériau pour prédire la déformation mécanique du matériau textile.

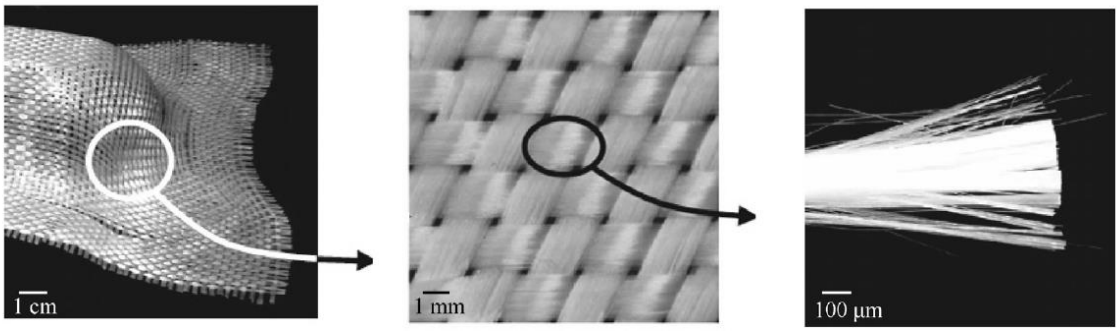

Macroscale Mesoscale Microscale

Figure 1.2 The three simulation scales for textile composites [Hamila & Boisse, 2013b]

Par rapport aux approches cinématiques, les approches mécaniques, qui sont basées sur le modèle constitutif du matériau, sont des approches plus complètes et ont reçu plus d'attention. Les approches mécaniques peuvent être classées en différentes échelles (voir la figure 1.2) : échelle microscopique, échelle du fil, échelle mésoscopique et échelle de la pièce (échelle macroscopique). L'approche de simulation à différentes échelles a ses avantages et ses inconvénients. Cependant, il n'existe pas actuellement de modèle de simulation largement accepté en raison du mécanisme de déformation spécifique des composites textiles.

1.4 Motifs et objectifs de la recherche

Le matériau composite textile est tissé à partir du fil et le fil est composé de milliers de fibres qui donnent à ce matériau un mécanisme de déformation spécifique. La thèse sera principalement consacrée au développement d'une approche de simulation à l'échelle macroscopique pour la mise en forme du composite textile. Trois comportements du matériau : la tension, le cisaillement dans le plan et la flexion hors du plan seront pris en considération. L'approche de simulation proposée sera implémentée dans Abaqus, ce qui la rendra accessible à tout utilisateur souhaitant effectuer l'analyse du drapage des composites textiles dans ce logiciel.

La couche unique du composite textile a une très faible épaisseur. Dans l'application du composite textile, il est nécessaire de combiner les multicouches ensemble dans la pièce composite finale. Ainsi, nous sommes également intéressés par la formation de multicouches, en particulier les multicouches avec différentes orientations de fibres. En outre, l'effort de recherche sera consacré au mécanisme de formation des plissement qui est l'un des principaux défauts dans la formation du renforcement des composites textiles à l'échelle macro.

1.5 Conclusion de Chapitre 1

Ce chapitre donne une brève introduction à l'état de l'art du renforcement textile depuis l'application du matériau composite jusqu'aux différentes approches de simulation à différentes échelles. On sait que le composite textile est tissé à partir de fils, et que le fil est composé de plusieurs milliers de fibres. Cette architecture particulière lui confère des propriétés mécaniques spécifiques. L'approche de simulation peut être menée à différentes échelles : micro-échelle, méso-échelle et macro-échelle. Parmi ces trois échelles, l'approche continue à la macro-échelle nécessite le coût de calcul le plus faible. Bien que la simulation à l'échelle macroscopique perde certaines informations à une échelle inférieure, elle reste acceptable dans le processus de formage qui concerne principalement l'orientation du fil et l'apparition des plissement.

Sur la base de ces connaissances, l'article précise que l'approche de simulation sera développée à l'échelle macroscopique et que trois comportements des matériaux seront pris en considération : la tension, le cisaillement dans le plan et la flexion hors du plan. La simulation de la formation de multicouches avec différentes orientations de fibres sera étudiée. En outre, le mécanisme de formation des plissement sera également étudié.

Chapitre 2 Une approche hypoélastique de coques en efforts résultants pour les simulations de la formation de renforts textiles composites

2.1 La déformation de la spécificité du composite textile

Le fil du tissu est composé de fibres continues de très petits diamètres. Ces fils sont maintenus ensemble par le processus de tissage, ce qui permet de considérer le tissu comme un milieu continu à l'échelle macroscopique. En même temps, le glissement possible entre les fils donne au matériau un comportement très spécifique : le comportement en flexion est indépendant du comportement de la membrane. Dans les éléments de coque classiques, la rigidité à la flexion est déterminée par la rigidité de la membrane et la rigidité de la coque, ce qui n'est pas le cas pour le composite textile.

Pour surmonter cette difficulté et réaliser la simulation de la formation de composites textiles, différentes approches ont été proposées. Une première approche efficace consiste à considérer la couche unique du composite de fibres comme un stratifié avec différentes épaisseurs de module d'Young. La rigidité de la membrane et la rigidité à la flexion requises peuvent être obtenues en ajustant l'épaisseur et le module de Young des différentes couches du stratifié. D'autres approches appliquent l'élément de superposition pour obtenir la rigidité en flexion indépendamment de la rigidité de la membrane. Le comportement en flexion et le comportement de la membrane sont obtenus dans des éléments différents. Puis ces éléments sont superposés ensemble. Ces approches sont validées comme efficaces pour prédire la déformation de la surface moyenne. Mais ces approches sont quelque peu artificielles, la physique du comportement de flexion du matériau est négligée. L'approche de la coque résultante de la contrainte est une approche disponible pour obtenir le comportement de la membrane découplé de la rigidité en flexion dans un élément de coque, et l'approche sera présentée ci-dessous.

2.2 L'approche de la résultante de contrainte hypoélastique

Dans les coques à résultante de contrainte, les états de contrainte sont décrits de manière simplifiée par les résultantes de contrainte et les moments de contrainte (ou couples de contrainte). Le travail virtuel interne δW_{int} qui est lié aux résultantes et aux moments de contrainte est le suivant :

$$\delta W_{\text{int}} = \int_A (\delta\varepsilon_{11} N^{11} + \delta\varepsilon_{22} N^{22} + \delta\varepsilon_{12} N^{12} + \delta\chi_{11} M^{11} + \delta\chi_{22} M^{22} + \delta\chi_{12} M^{12}) dA$$

A est l'aire de la surface médiane de la coquille. $\delta\varepsilon_{11}$, $\delta\varepsilon_{22}$ sont les déformations axiales virtuelles, $\delta\varepsilon_{12}$ est la déformation virtuelle en cisaillement dans le plan, $\delta\chi_{11}, \delta\chi_{22}, \delta\chi_{12}$ sont les courbures virtuelles. N^{11}, N^{22}, N^{12} sont les résultantes des contraintes et M^{11}, M^{22}, M^{12} sont les

moments (ou couples) de contrainte, et ils sont définis comme l'intégration de la contrainte dans la direction de l'épaisseur.

$$N^{\alpha\beta} = \int_{-\frac{h}{2}}^{\frac{h}{2}} \sigma^{\alpha\beta} dz \qquad M^{\alpha\beta} = \int_{-\frac{h}{2}}^{\frac{h}{2}} z\sigma^{\alpha\beta} dz$$

Ici, les indices grecs α, β appartiendront à l'ensemble (1, 2). $\sigma^{\alpha\beta}$ sont les composantes de la contrainte de Cauchy. Dans l'application classique, cette équation peut être utilisée pour calculer la réponse de la section de la coque, et adopter une seule équation constitutive pour obtenir la contrainte de Cauchy $\sigma^{\alpha\beta}$. De cette façon, le comportement en flexion sera couplé au comportement de la membrane. Ce n'est pas le cas pour le composite textile.

Afin de découpler le comportement de la flexion de celui de la membrane dans les éléments de coque à résultante de contrainte, le calcul des résultantes de contrainte $N^{\alpha\beta}$ et des moments de contrainte $M^{\alpha\beta}$ doit être totalement indépendant les uns des autres. Des lois hypoélastiques sont adoptées dans l'approche de simulation pour calculer la résultante de contrainte $N^{\alpha\beta}$ et les moments de contrainte $M^{\alpha\beta}$ séparément comme ci-dessous:

$$N^{\nabla} = \mathrm{C} : \dot{\varepsilon} \qquad M^{\nabla} = D : \dot{\chi}$$

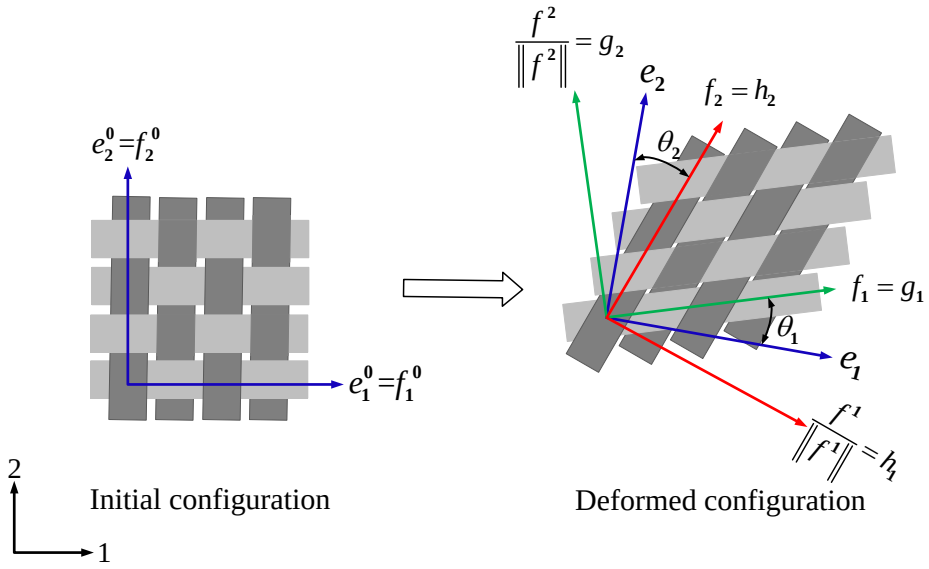

Figure 2.1 Cadres orthonormés dans la direction de la fibre et cadre de Naghdi vert.

Pour le composite textile, les comportements des matériaux dépendent fortement des directions des fils. Afin d'appliquer l'équation de constitution du matériau, deux cadres de fibres *g*, *h* sont construits pour suivre la direction du fil du matériau f_1, f_2. Des transformations de tenseur sont effectuées pour réaliser la transformation entre le cadre de Green-Naghdi et les deux cadres de fibres. L'équation de constitution du matériau est appliquée dans les deux cadres de fibres pour calculer l'incrément de la résultante de contrainte et du moment de contrainte:

$$[dN]_g = [C]_g [d\varepsilon]_g \qquad [dN]_h = [C]_h [d\varepsilon]_h$$
$$[dM]_g = [D]_g [d\chi]_g \qquad [dM]_h = [D]_h [d\chi]_h$$

Au cours du pas de temps de simulation [t_n , t_{n+1}], les résultantes de contraintes et le moment de contrainte seront cumulés selon le schéma de Hughes et Winget [Hughes & Winget, 1980; Badel, Vidal-Sallé, & Boisse, 2008]:

$$\left[N\right]_g^{n+1} = \left[N\right]_g^n + \left[dN\right]_g^{n+1/2} \qquad \left[N\right]_h^{n+1} = \left[N\right]_h^n + \left[dN\right]_h^{n+1/2}$$
$$\left[M\right]_g^{n+1} = \left[M\right]_g^n + \left[dM\right]_g^{n+1/2} \qquad \left[M\right]_h^{n+1} = \left[M\right]_h^n + \left[dM\right]_h^{n+1/2}$$

Trois comportements des matériaux sont pris en compte dans l'approche de la résultante des contraintes, à savoir le comportement en traction, en cisaillement dans le plan et en flexion. Le comportement en traction du matériau tissé peut être mesuré par l'essai de traction uniaxial ou biaxial. Le comportement en cisaillement dans le plan peut être testé par le test du cadre ou de l'extension du biais. Le comportement en flexion peut être mesuré par l'essai en porte-à-faux. En ce qui concerne le tissu interlock G1151, la caractérisation de ces trois comportements du matériau est effectuée pour une analyse de simulation ultérieure.

2.3 Conclusion du Chapitre 2

En raison du plissement possible entre les fibres dans un matériau tissé, la rigidité à la flexion est beaucoup plus faible que les valeurs calculées à partir de la rigidité à la traction et de l'épaisseur. La rigidité à la flexion joue un rôle important dans la déformation du matériau, donc l'approche de la coque pour modéliser le matériau tissé doit prendre en compte la rigidité à la flexion spéciale. Une approche hypoélastique de la résultante des contraintes est présentée dans ce chapitre. Une rigidité à la flexion indépendante de la rigidité de la membrane qui est liée au moment de contrainte avec la courbure de flexion est introduite dans l'approche. L'approche contrainte-résultat permet de considérer séparément le comportement de la membrane et de la flexion. L'approche est implémentée dans le logiciel Abaqus qui est disponible pour tout utilisateur de ce logiciel.

Trois comportements du matériau sont considérés dans l'approche, à savoir le comportement en traction, en cisaillement dans le plan et en flexion, le comportement du matériau étant sous forme hypoélastique. Les méthodes permettant de déterminer ces comportements des matériaux pour l'approche présentée sont présentées dans ce chapitre, et les différents comportements du matériau G1151 sont testés en conséquence. Dans ce processus, les simulations correspondantes utilisant l'approche présentée sont effectuées pour faire une comparaison avec l'expérience. Le résultat de la comparaison a vérifié au préalable l'exactitude et l'efficacité de l'approche présentée dans la prédiction de la membrane du matériau tissé et de la déformation par flexion.

Chapitre 3 Analyse numérique et expérimentale de la mise en forme du composite textile

3.1 L'introduction du processus d'expérimentation

Les expériences de formage sont réalisées dans le laboratoire du LaMCoS. Comme le montre la figure 3.1. Le dispositif expérimental est placé sur la machine d'essai universelle pour contrôler le mouvement du poinçon, notamment la vitesse de déplacement (30 mm·min^{-1} pour tous les types de processus de drapage) et la distance de déplacement. Le support d'ébauche et la matrice sont rendus transparents (en méthacrylate de méthyle (PMMA)) pour observer la déformation du matériau. Deux caméras ont été utilisées lors de l'expérience multicouches pour observer la déformation de la couche inférieure et de la couche supérieure.

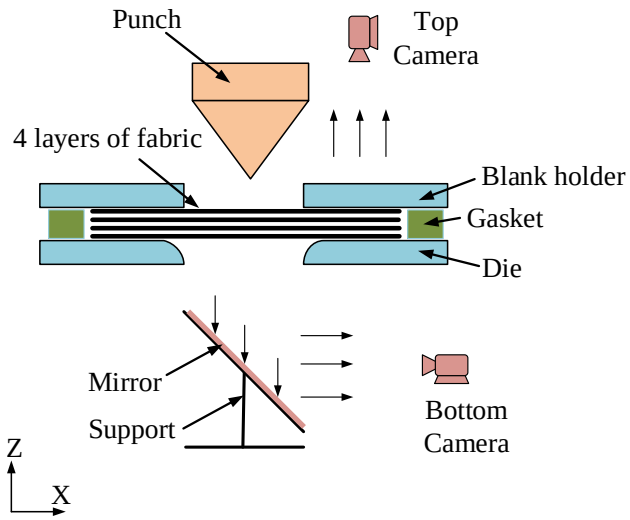

Figure 3.1 Schematic diagram of the forming experiment

3.2 Formation de l'hémisphère et du tétraèdre

Afin de vérifier l'efficacité et la justesse de l'approche de simulation proposée, une comparaison entre l'expérience et la simulation est effectuée dans ce chapitre. Le formage d'un hémisphère et d'un tétraèdre est effectué, ces deux formes sont toutes des formes de référence étudiées dans les expériences de formage [Allaoui et al., 2011, 2014 ; Komeili & Milani, 2016 ; Dörr et al., 2017 ; Thompson et al., 2020]. Les expériences de formage comprennent le formage monocouche et le formage multicouche. Pour le formage monocouche, les conditions de formage comprennent le formage avec des porte-flans et le formage sans porte-flan. Pour le formage multicouche, la pile de quatre couches quasi-isotropes est considérée dans les expériences. La variable de comparaison entre l'expérience et la simulation comprend l'angle de cisaillement dans le plan, le contour du tissu, la force du poinçon et les plis dans le cas d'un formage multicouche et d'un formage sans support de découpe.

Les simulations correspondant aux expériences sont réalisées dans la sous-routine VUGENS d'Abaqus/Explicit en utilisant l'approche présentée. Le serre-flan, la matrice et le poinçon sont considérés comme des corps rigides. La dimension initiale du matériau est de 300 mm ×300 mm et est maillée à l'aide de l'élément coquille triangulaire (S3 dans Abaqus/Explicit). Pour la simulation avec la configuration multicouche, la modélisation de l'éprouvette est l'assemblage de plusieurs plis en modélisation monocouche. La modélisation de la couche unique est indépendante l'une de l'autre, et la propriété de contact est appliquée entre les couches adjacentes, avec un coefficient de friction de coulomb constant.

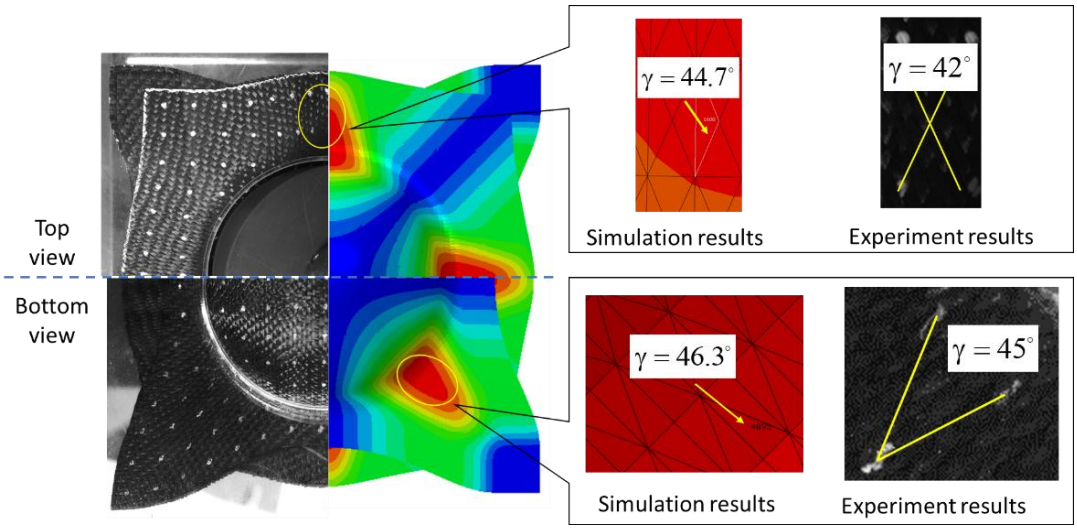

Figure 3.2 Multicouche d'hémisphère formant comparaison entre simulation et expérience.

La comparaison de quatre couches d'hémisphère quasi-isotrope est illustrée à la figure 3.2. Les points de repère sont tous peints le long de la direction des fils de chaîne et de trame pour calculer l'angle de cisaillement dans le plan après la déformation du matériau. On peut voir que le matériau G1151 à quatre couches est déformé en un hémisphère sans plis, ce qui est correctement prédit par la simulation.

Le froissement est l'un des principaux défauts de formage dans le formage du composite textile. Afin de réduire le coût de l'essai et le cycle de fabrication, il est essentiel que l'approche de simulation puisse prédire avec précision l'apparition des plissement. Pour obtenir les plissement évidentes pendant l'expérience de formage, le porte-flan est retiré. Le formage de l'hémisphère sans le serre-flan est illustré à la figure 3.3(a), et le résultat de la simulation correspondante est donné à la figure 3.3(b). La géométrie des plissement est obtenue par une approche de corrélation d'images numériques (DIC), et la comparaison entre l'expérience et la simulation indique que l'approche proposée est capable de prédire l'apparition de plissement.

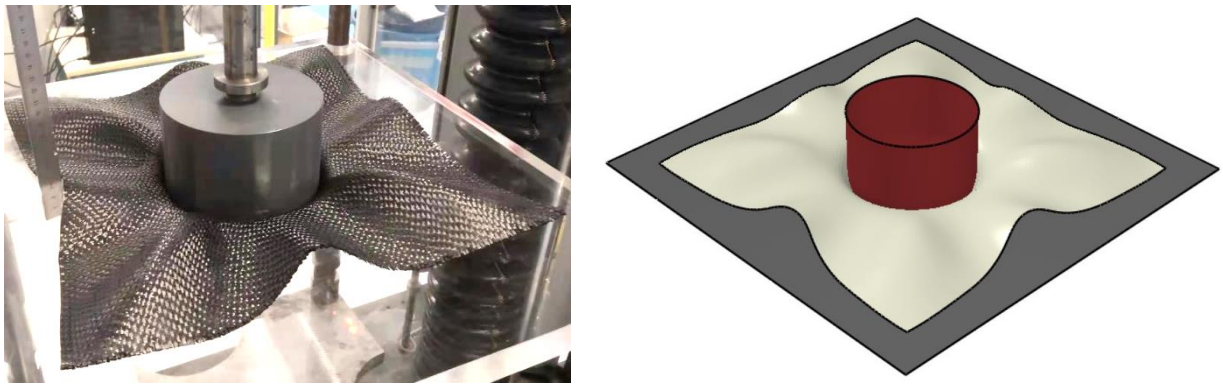

(a) (b)

Figure 3.3 Comparaison entre la simulation et l'expérience du formage d'un hémisphère monocouche sans support de flan. (a) Expérience. (b) Simulation par l'approche de la résultante de contrainte.

Le formage du tétraèdre est choisi comme autre cas pour la validation de l'approche de simulation introduite. La zone présentant le plus grand angle de cisaillement, qui est la plus importante dans le processus de fabrication, est comparée. La comparaison entre la simulation et l'expérience du formage de tétraèdres à une seule couche est présentée à la figure 3.4.

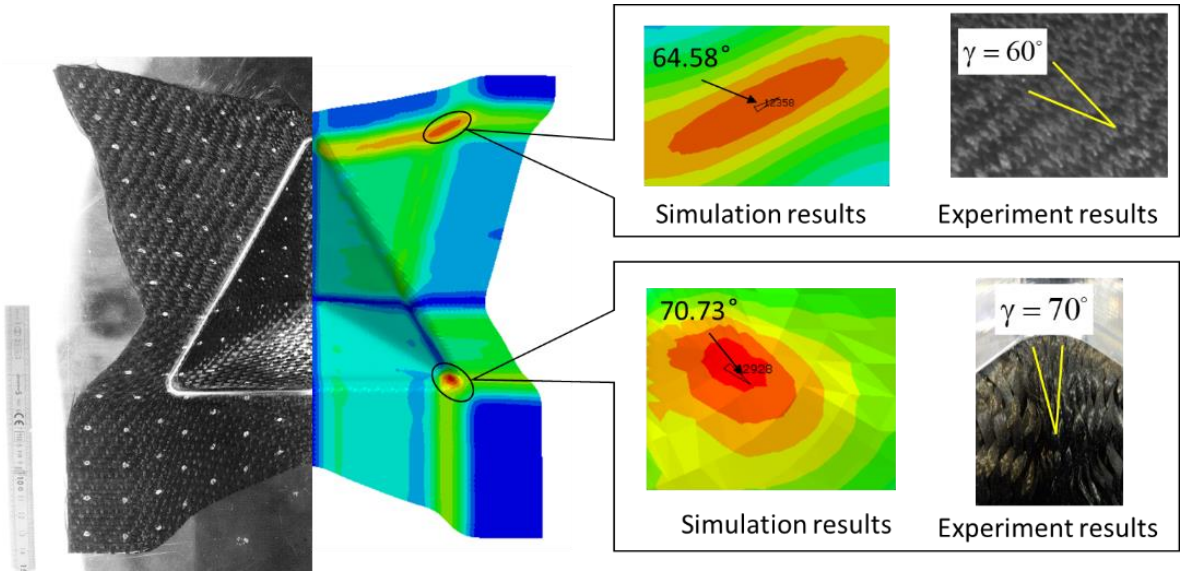

Figure 3.4 Comparaison entre la simulation et l'expérience de la formation d'un tétraèdre à une seule couche

3.3 Conclusion du Chapitre 3

En raison du glissement possible entre les fibres, le composite textile présente une spécificité de déformation en flexion différente de celle du matériau continu. Pour simuler le formage du composite textile à l'aide du modèle de coque, une approche hypoélastique de la résultante des contraintes est proposée dans le chapitre 2. A travers deux formes de référence : l'hémisphère et le tétraèdre, ce chapitre vise à valider l'efficacité de l'approche proposée.

Le dispositif expérimental permettant de réaliser l'expérience de formage et d'obtenir le résultat expérimental est tout d'abord présenté, et la procédure permettant de réaliser la simulation du formage des composites textiles dans Abaqus en utilisant l'approche présentée est également présentée. Ensuite, le formage de l'hémisphère et du tétraèdre avec une configuration à trois couches est effectué, la comparaison entre la simulation et l'expérience est faite à partir de différents aspects, y compris l'angle de cisaillement dans le plan, le contour du tissu, la force du poinçon et les plissement. Grâce à la comparaison, on peut conclure que l'approche présentée peut prédire correctement la déformation dans le plan du composite textile.

Chapitre 4 Analyse expérimentale de la drapabilité du composite textile

4.1 Analyse de la drapabilité du composite textile

Le comportement de drapage du renforcement composite textile peut être mesuré par le drapomètre [Chu et al., 1950 ; Cusick, 1968]. Comme illustré dans la Figure. 4.1(a), le drapomètre se compose de deux disques de support circulaires, et l'échantillon de tissu circulaire est pris en sandwich entre eux. Le tissu peut se draper sous l'effet de sa gravité. La zone de drapé sera projetée sur le Perspex avec la lumière placée sous l'échantillon. L'anneau de papier a été placé sur le plexiglas. Le rayon de l'anneau de papier est égal à l'échantillon de tissu initial. Au cours du processus de drapage, certains plis évidents seront générés. La drapabilité du matériau peut être directement décrite par le nombre de plis. Un coefficient de drapage est également défini pour quantifier la drapabilité du matériau. Comme le montre la figure 4.1(b), le coefficient de drapage est le rapport entre la surface projetée de l'échantillon de tissu drapé et sa surface non drapée [Chu et al., 1950].

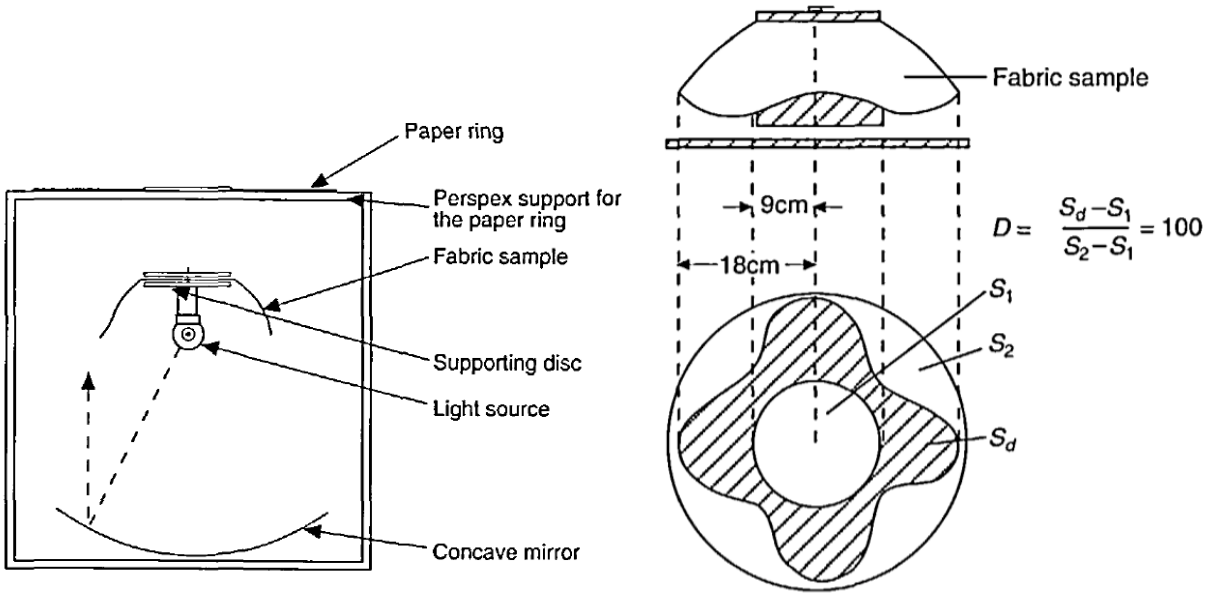

(a) (b)

Figure 1.1 (a) Schéma de principe du drapomètre. (b) Calcul du coefficient de drapé. [Vangheluwe & Kiekens, 1993].

Selon le principe du drapomètre, le nombre de plis testé ou le coefficient de drapé est uniquement lié au comportement de flexion du tissu. Cela n'est pas suffisant pour caractériser la capacité du matériau à résister au froissement. À l'échelle macroscopique, des recherches ont montré que les trois principaux comportements du matériau qui influencent sa déformation sont la

traction, le partage dans le plan et la rigidité à la flexion [Boisse et al., 2011, J. Huang et al., 2021]. Il est nécessaire de disposer de nouveaux paramètres pour caractériser la capacité du matériau à se draper sans plis.

4.2 La définition du ratio de drapabilité

En considérant les trois comportements du matériau (rigidité à la traction, rigidité au cisaillement dans le plan et rigidité à la flexion hors du plan) à l'échelle macro, le principe du travail virtuel du matériau textile peut s'écrire sous la forme suivante:

$$\delta W_{\text{int}} = \delta W_t + \delta W_s + \delta W_b$$

Lorsque le matériau est soumis à une déformation, il provoque les trois types de changements d'énergie ci-dessus. La minimisation de l'énergie interne totale W_{int} entraîne une compétition entre eux. Par rapport aux deux autres formes de comportement, la rigidité à la traction est relativement importante, et le matériau peut être considéré comme quasi-inextensible. Ainsi, afin de mieux décrire l'influence du comportement en cisaillement et en flexion sur la formation des plissement, un rapport de drapabilité *r* est défini comme suit :

$$r = \frac{k_c}{D_b}$$

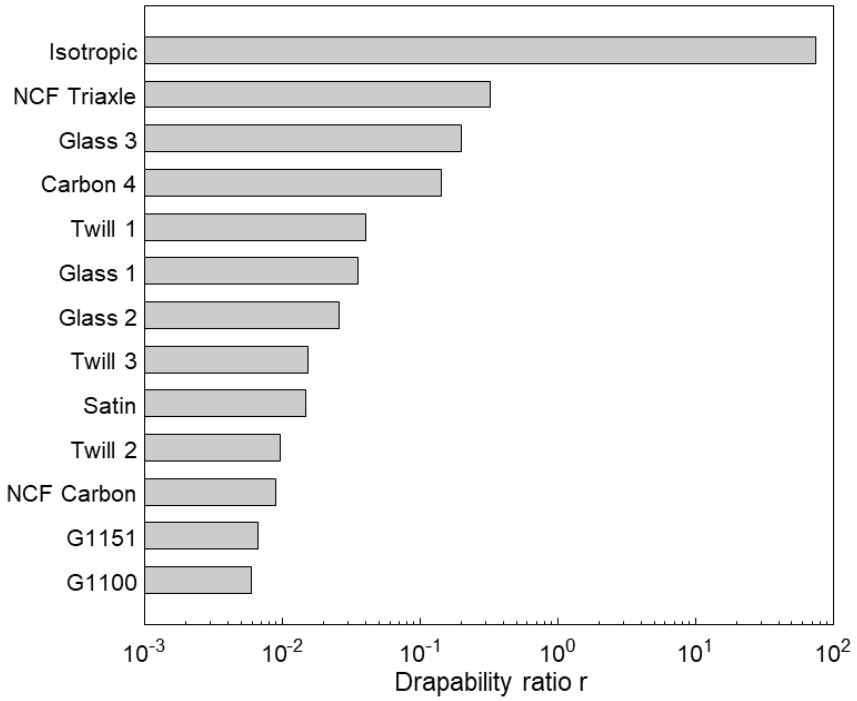

Figure 4.2 the drapability ratio of the selected materials

Ici, k_c est la rigidité au cisaillement dans le plan du matériau, et D_b est la rigidité à la flexion du matériau. Pour valider que le rapport de drapabilité défini r peut représenter la capacité du matériau à se draper sans plis, treize types de matériaux fibreux sont sélectionnés pour réaliser l'expérience de formage. Dans un premier temps, la rigidité au cisaillement et la rigidité à la flexion de ces matériaux sont testées à l'aide de la méthode présentée au chapitre 2. Le rapport de drapabilité r peut alors être déterminé, comme le montre la figure 4.2.

4.3 Expérience de formage de boîtes carrées

Lorsque le rapport entre la profondeur d'emboutissage et la longueur de la boîte carrée est important, le formage de la boîte carrée entraîne des plissement importantes [P. Wang et al., 2015]. L'expérience de formage de boîte carrée est donc menée dans le but de rechercher la relation entre le rapport de drapabilité du matériau défini et l'apparition de plissement. Dans le processus de formage, certains matériaux sont déformés avec des plissement tandis que d'autres matériaux sont déformés sans plissement. La figure 4.3 présente le formage d'une boîte carrée avec et sans plis avec différents matériaux. L'expérience de formage a permis de constater que les rapports de drapabilité de ces matériaux qui présentent des plissement sont tous plus grands que ceux des matériaux sans plissement. Ce phénomène s'applique également au formage des cylindres. On peut savoir que :

(1). La boîte carrée peut être formée sans plis en utilisant les matériaux composites textiles, même l'angle de cisaillement peut aller jusqu'à 70°.

(2). En fonction de leur capacité à draper la boîte carrée sans plis, le rapport de drapabilité défini peut diviser les matériaux en deux catégories. Le matériau ayant un rapport de drapabilité plus faible a de meilleures performances de formage.

(3). Il existe une valeur critique du rapport de drapabilité des matériaux pour une condition limite donnée. Lorsque le rapport de drapabilité du matériau est supérieur à la valeur critique, les plissement apparaissent, et dans le cas contraire, aucune ride n'apparaît.

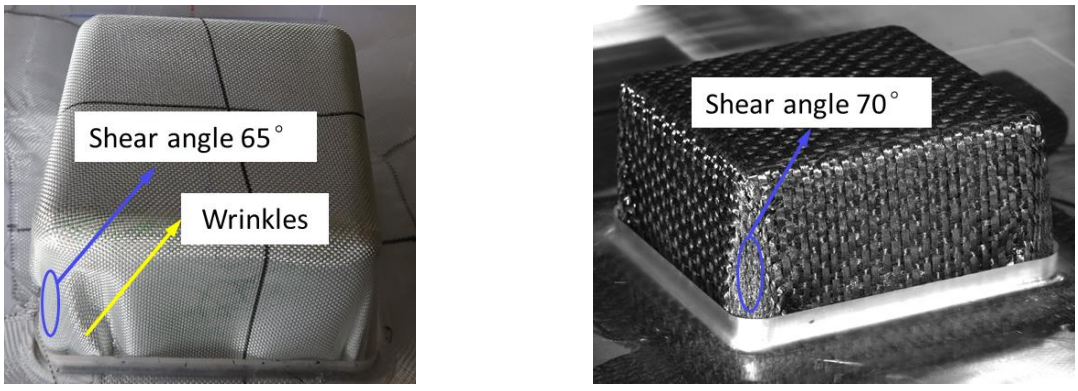

(a) (b)

Figure 4.3. Square box forming experiment using different material. (a) Glass 3. (b) G1151.

4.4 Conclusion du Chapitre 4

Ce chapitre fournit une analyse expérimentale complète de la drapabilité des composites textiles, qui est la capacité à se déformer sans plis. En considérant le comportement du matériau en cisaillement dans le plan et en flexion hors du plan, un rapport de drapabilité est défini pour quantifier la capacité de déformation du matériau. Les expériences de caractérisation du comportement du matériau sont d'abord menées pour déterminer la rigidité au cisaillement et la rigidité à la flexion du matériau, puis le rapport de drapabilité de tous les matériaux est calculé et trié du plus petit au plus grand. Enfin, des expériences de formation de boîtes carrées et de cylindres sont réalisées pour valider la relation entre le rapport de drapabilité défini et la capacité de déformation du matériau.

Dans les expériences de formage, on constate tout d'abord que l'angle de cisaillement du matériau peut être très grand sans plissement (pour la boîte carrée, l'angle de cisaillement est supérieur à 55° et pour le cylindre, la valeur est supérieure à 40°), on peut donc savoir que l'angle de blocage du cisaillement n'est pas complet pour prédire si des plissement vont apparaître pendant le processus de formage. Lorsque la forme de la pièce change, la valeur critique du rapport de drapabilité change également, car la formation et le développement des plissement sont également liés à la géométrie et aux conditions limites. Cependant, qu'il s'agisse d'une boîte carrée ou d'un cylindre, le rapport de drapabilité du matériau avec des plis est supérieur à celui du matériau sans plis.

En conclusion, la formation et le développement des plissement est un phénomène global qui dépend du comportement du matériau, de la géométrie de la formation et des conditions aux limites. Lorsque tous les autres éléments sont identiques, le rapport de drapabilité défini dans ce chapitre peut être un indicateur de la capacité de déformation du textile. Le matériau avec un rapport de drapabilité plus faible est plus facile à former des formes complexes sans plissement.

Chapter 1 Composite material: introduction and simulation approach

This chapter will focus on the background knowledge of the composite material with special attention on the structure of textile composite and the manufacturing process. Different simulation approaches will be reviewed. At last, the research objective will be presented.

Content of Chapter 1

Chapter 1 Composite material: introduction and simulation approach 19

1.1 Introduction to the composite material 20

1.1.1 Composite materials and their applications 20

1.1.2 Types of composite materials 22

1.2 Composite materials of woven fabric reinforcement 23

1.2.1 Structure of woven fabric 24

1.2.2 Types of woven fabric reinforcement 24

1.2.3 Non Crimp Fabric 27

1.2.4 Molding processes of woven fabric reinforcement 28

1.3 Numerical simulation approach for textile composites 31

1.3.1 Kinematic approach 31

1.3.2 Mechanical approach 33

1.4 Research motives and objectives 42

1.5 Summary 43

1.1 Introduction to the composite material

1.1.1 Composite materials and their applications

Composite materials are composed of at least two immiscible materials, and the constitutive materials will remain independent on the micro-scale while forming a whole part on the macro-scale. The constituent parts of composite materials can be divided into reinforcement and matrix (seen in Fig. 1.1), the reinforcement which controls the mechanical characteristics of the final product and the matrix which brings the cohesion of all the fibers. Composite materials combine the properties of different materials to exhibit many excellent properties, and thus these materials have been widely used in different fields.

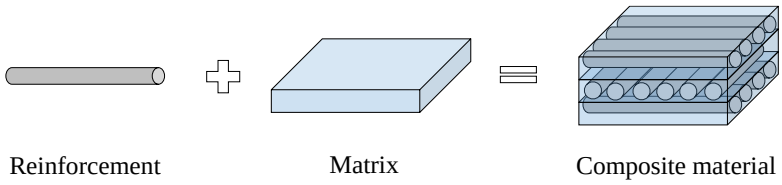

Fig. 1.1 Composition of composite materials

a) Aerospace

High strength, high rigidity, and lightweight are the basic requirements for structural materials in the aerospace field. Due to the excellent properties of advanced composite materials, different types of composite materials have been widely used in the aerospace field since the 1840s [Arif et al., 2017]. Compared with other materials, the use of advanced composite materials can make the aircraft lighter while providing the same structural strength, which can reduce the energy consumption in flight.

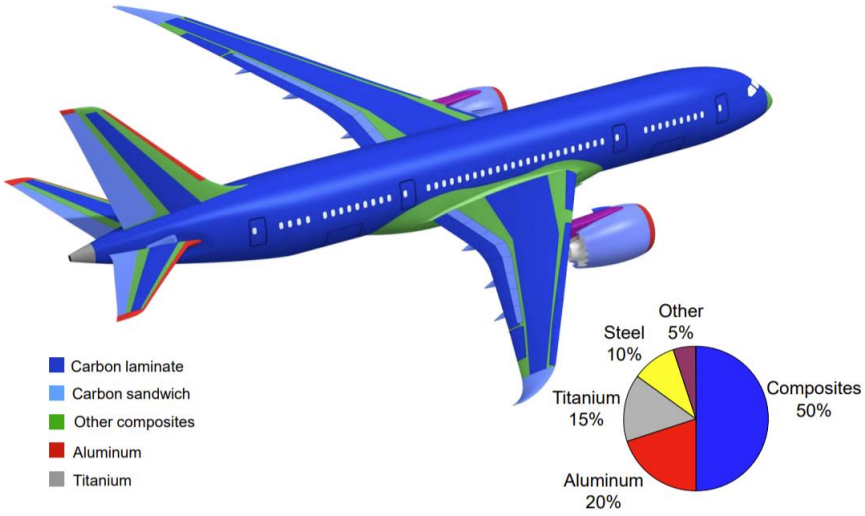

Fig. 1.2. Application of composite materials in Boeing 787 [Boeing Company, 2013].

Composite materials have become the fourth main aerospace structural material after steel, aluminum, and titanium. Due to the excellent properties of composite materials, the amount of composite materials has become one of the main indicators for evaluating advanced aircraft. Currently, the amount of composite materials has exceeded 25% in the structural weight of the advanced aircraft. For example, the US fourth-generation fighter F35 used about 35% of the composite material, the Swedish JAS39 fighter reached 39%, and the French Dassault Rafale fighter used 40% of the composite material. In the field of civil aircraft, composite materials are also widely used. The composite materials used in the Airbus A380 reached 25%, the Airbus A350-XWB reached 52% and composite materials for Boeing 787 account for 50% (As shown in Fig. 1.2).

Composite material is also widely used in the space industry. In addition to the high stiffness, high strength, and lightweight, the excellent dimensional stability of the composite structure makes it unique in space where the environment changes rapidly and plays an irreplaceable role in the manufacture of missiles, satellite vehicles, and launch vehicles.

b) Transportation

Composite materials have long been used in transportation. For example, car tires are composed of rubber and steel bars. The rubber makes the tire elastic and wear-resistant, so as to achieve shock absorption and resistance to road friction, and reinforcing bars make tires high strength. Composite materials can also be used as automobile bodies, bumpers, frames, and other parts. The lightweight of composite materials can highly reduce the overall weight, resulting in energy savings. Fig. 1.3 shows the composite automotive part made of fiber reinforcement. The composite part made of fiber reinforcement can absorb more energy than steel, which can highly improve the security in a collision.

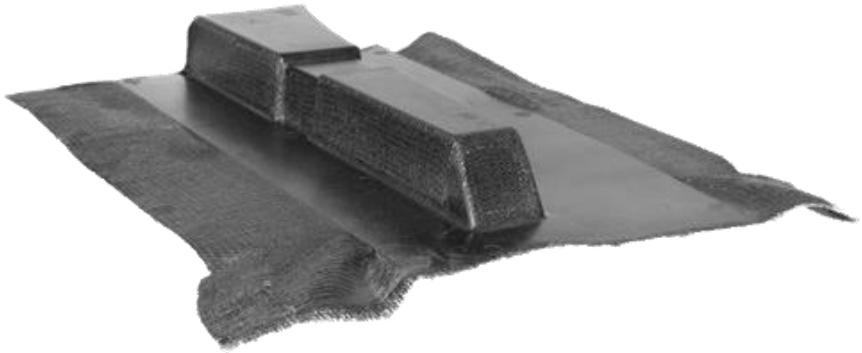

Fig. 1.3. Automotive part made of composite material [Guzman-Maldonado et al., 2016].

c) Other fields

With the development of composite material manufacturing technology, composite materials have been widely used in different fields. In the wind power industry, the blades made of composite materials can have complex shapes, lightweight, and high strength. In the weapons industry, tank armor, bulletproof vests, and helmets made of composite materials also have excellent performance and practicality. In addition, composite materials are also widely used in construction engineering, sports equipment, medical equipment, and so on, such as decorative panels and reinforcing beams in construction engineering, ski board, bicycles in sports equipment, medical artificial limbs in medical equipment.

1.1.2 Types of composite materials

Composite materials are composed of matrix and reinforcement. The matrix combines all the constitutive material into a whole and transfers the stress between reinforcement, the reinforcement provides the mechanical properties (strength and rigidity). The composite materials can be classified into different categories according to the types of matrix and reinforcement [Campbell, 2004].

a) Matrix

Based on the material matrix, composites are commonly classified into polymer matrix composites (PMCs), metal matrix composites (MMCs), and ceramics matrix composites (CMCs) [Kaw, 2005].

- Metal matrix composites take the metal or metal alloys as matrix, and add fibers, whiskers, nanoparticles or other reinforcements to the matrix. The metal matrix composites are different from metal alloys, which are substances with metallic properties formed by the melting of two or more materials, and the metal alloys don't have obvious interface distinction in the microscale. Compared with other types of composite materials, the molding process of metal matrix composite materials is relatively complex and the manufacturing cost is high, thus this types of composite material is mainly used in the military field.
- Ceramic matrix composites are composed of ceramic matrix and various fibers. The fibers with high strength and rigidity are added to the ceramic matrix. On the one hand, the composition overcomes the shortcoming of the brittle fracture properties of ceramic material and improves the fracture toughness of the composites. On the other hand, the high performance of ceramic is maintained, like the high temperature resistance, low expansion, good thermal stability, and so on. So that ceramic matrix composites can be used as structural materials in the high temperature and high pressure environment.

- Polymer matrix composites are made of polymer (thermosetting or thermoplastic) as matrix and fiber as reinforcement. The molding process of this type of composite material is relatively mature and the manufacturing cost is low, so the resin matrix is the dominant matrix in the application of composite materials.

b) Reinforcement

According to the geometry of the reinforcement, the reinforcement has three forms: particulate, short fiber, and continuous fiber. Correspondingly, composite materials can be divided into particular reinforcement composites, short fiber reinforcement composites, and continuous fiber composites.

- Particle reinforcement has the approximately same size in all directions, this type of reinforcement can hardly supply the excellent mechanical property in the composite part. Particle reinforcement usually is used in the design of functional composites. By embedding particle reinforcements in the matrix, the corresponding physical or chemical properties of the composites can be designed. Such as the ferromagnetic composites enable induced heat generation in external magnetic fields for medical applications [Xiang et al., 2020].
- Short fiber reinforcement has a significant length than the other directions, ranging millimeters to centimeters. The mechanical properties of the short fiber reinforcement composite are determined by the fiber length and orientation, are intermediate between the particle reinforcement composite and continuous reinforcement composite. The short fiber reinforcement composite can be manufactured with injection process [Fu et al., 2000], thermocompression processes [Le Corre et al., 2002] and three-dimensional (3D) printing [Christ et al., 2015]. The short fiber reinforcement composites can be used for complex part.
- Continuous fiber reinforcement are the most widely used in the application of composite materials. Due to the mechanical properties of composite materials mainly come from the reinforcement, the continuous fiber reinforcement composite has the best mechanical properties than the other two types of reinforcement, especially when loaded in the fiber direction.

The research work presented in the thesis manuscript will force on the deformation of continuous fiber reinforcement, mainly on woven fabric reinforcement which the warp and weft yarn are perpendicular in the initial configuration, and the matrix will be neglected. The composite materials of woven fabric reinforcement will be introduced in the next chapter.

1.2 Composite materials of woven fabric reinforcement

1.2.1 Structure of woven fabric

Woven fabric are made of continuous of fibers with very small diameter (normally ranging from 5 um to 15 um). The types of fiber have glass fiber, carbon fiber, and Kevlar fiber. The long and continuous fibers assemble together to the yarn which give the yarn very high stiffness and rigidity. The yarn can be named by the number of the constitutive continuous fibers, such as 7K yarn represent that this type of yarn is composed of 7000 fiber filaments. The yarns hold together by weaving to form the fabric for manufacturing the composite component. A woven fabric structure is shown in Fig. 1.4.

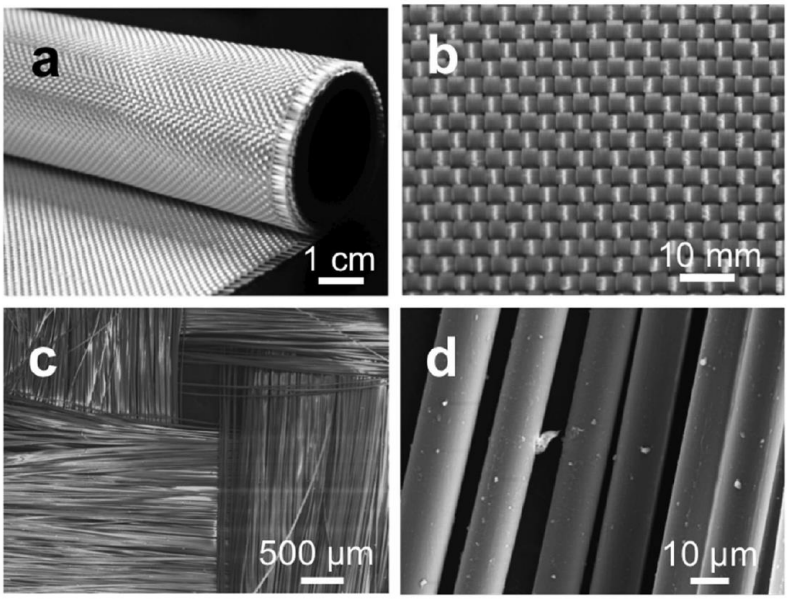

Fig. 1.4. Structure of woven fabric [Y. Huang et al., 2017]. (a) The commercial fabric. (b) The plain weave structure. (c) The yarn. (d) The fibers

1.2.2 Types of woven fabric reinforcement

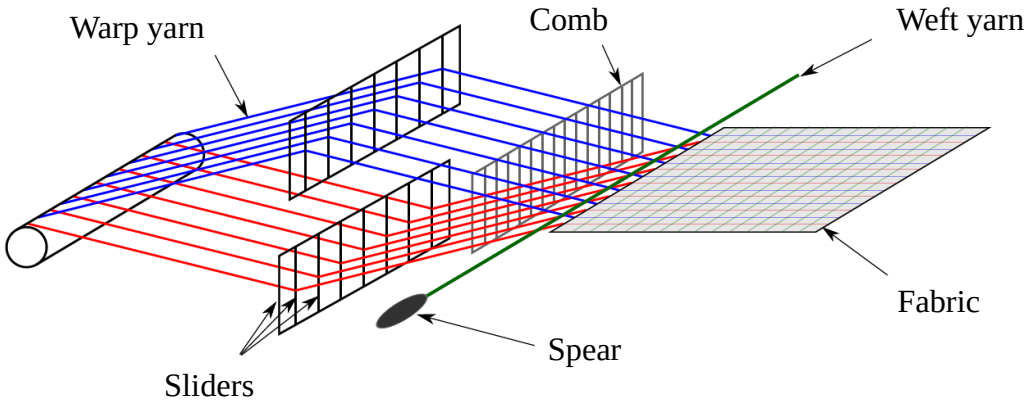

Fig. 1.5. The 2D woven fabric fabrication process [Florimond, 2013].

Based on the arrangement of the yarns in the fabric, the woven fabric reinforcement can be divided into 2D, 2.5D and 3D fabric reinforcement. Unidirectional fabric has high strength along the fiber direction, but the strength is quasi null in the transverse direction. In the realistic application, multilayers laminates of UD fabric with different orientations need to be combined. For a given load case, the layer configuration can be easily tailored.

The 2D woven fabric is created by interlacing the two-directional yarns in the plane at the manufacturing stage. The 2D woven fabric fabrication process is shown Fig. 1.5, a single layer of warp and weft yarn are perpendicular woven together into the fabric. The different weaving pattern can generate different weaving structures. Some research found that the woven architecture will influence the mechanical properties of the fabric [Adumitroaie & Barbero, 2011; Erol et al., 2017; Jahan, 2017]. There are three classical types: plain, twill, and satin, given in Fig. 1.6, and the warp and weft yarn in the figure are respectively drawn horizontally and vertically.

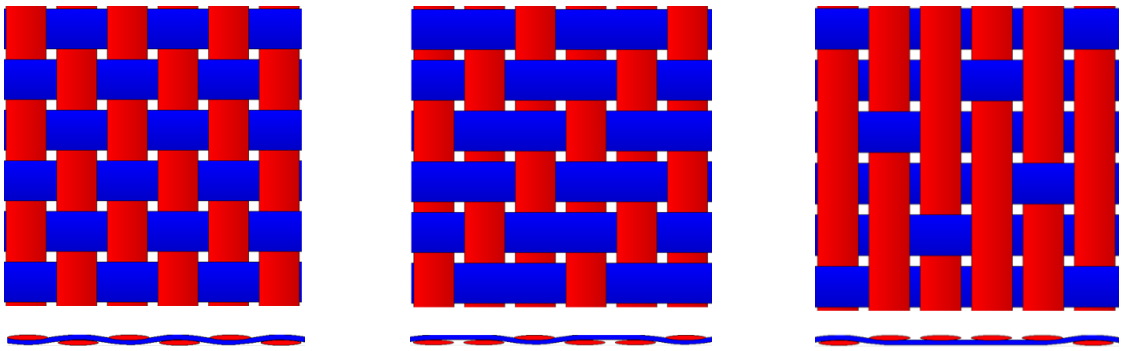

(a) (b) (c)

Fig. 1.6. Different types of 2D woven fabric (Generated by TexGen). (a) Plain weave. (b) Twill weave. (c) Satin weave

- Plain weave: the plain weave is the most classic weaving pattern and is most widely used in the woven fabric reinforcement application. In the plain weave, the warp and weft yarns are interlaced in a ‘one up – one down’ pattern. As shown in Fig. 1.6(a), the warp and weft yarn generates a chessboard pattern at both sides of the plain weave.
- Twill weave: the warp and weft yarns in the twill weave are interlaced in a ‘m up – n down’ pattern ($3\leq$ m, n ≥ 1 and at least one of m, n is larger than 1) to form the continuous rib diagonals on the faces of twill weave. And the twill weave is named as a fraction number which equal to m/n. Fig. 1.6(b) shows the 2/1 twill weave.
- Satin weave: the warp and weft yarns in the satin weave are interlaced in a ‘m up – one down’ pattern ($m\geq 3$), which means that the weft yarn passes m warp yarns and under one warp yarn. The satin is named as the m-harness (mH). Fig. 1.6 presents the 5H satin, the weft yarn passes over four warp yarns and then go under one warp yarn.

These three types of 2D woven fabric are called balanced fabric when the warp and weft yarn are identical, otherwise, they are unbalanced fabric. The out-of-plane bending behavior is linked with the yarn. When the unbalanced fabric is researched, the bending behavior along the warp and weft yarn direction will have some difference.

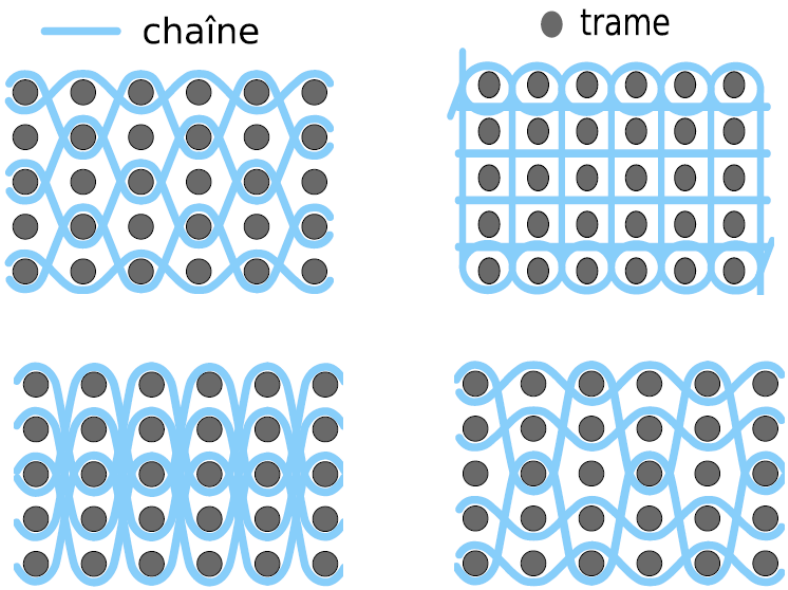

Fig. 1.7. Different types of 2.5 and 3D woven fabric [Gu & Zhili, 2002]

2D fabric is composed of a single layer of warp and weft yarn, the thickness is very small (several millimeters). To fabricate a certain composite component, it is need to stack several 2D woven fabric, NCF to form a laminate. In these case, the composite components are prone to delamination. The delamination can be avoid by 3D weaving to fabric the 2.5D and 3D fabric. The yarns are not only interlaced in the plane, but also in the thickness direction in 2.5D and 3D fabric [Mouritz et al., 1999; Gu & Zhili, 2002; Dufour et al., 2013]. Based on the woven architecture, the 2.5D and 3D fabric can be classified into orthogonal, angle interlock (2.5D), layer to layer [Boussu et al., 2015]. The different types of 2.5 and 3D woven fabric is given in Fig. 1.7.

As described before, the 2.5D and 3D woven fabrics are designed to avoid the delamination. Compared with the 2D woven fabric, the manufacturing process for the 2.5D and 3D woven fabrics is relatively complex and the cost is higher [Gnaba et al., 2018]. Expect the 3D weaving, the stitching process can also be used to fabricate the 3D fabrics. As shown in Fig. 1.8, the 3D fabrics are obtained by sewing high tensile strength yarn through a laminar which can be several layers of dry fabric or prepregs [Dransfield et al., 1994]. The main challenge of the stitching lay in improving the applicability of sewing machine to different occasions and fully understanding the stitching process on the influence of the 3D fabrics mechanical properties [Trabelsi et al., 2010]. Several researches have been devoted to the study of stitching parameters on the mechanical

behavior [Liu et al., 2017; Shen, Wang, Legrand, & Liu, 2019; Shen, Wang, Legrand, Liu, et al., 2019; Gnaba et al., 2021; Shen et al., 2021].

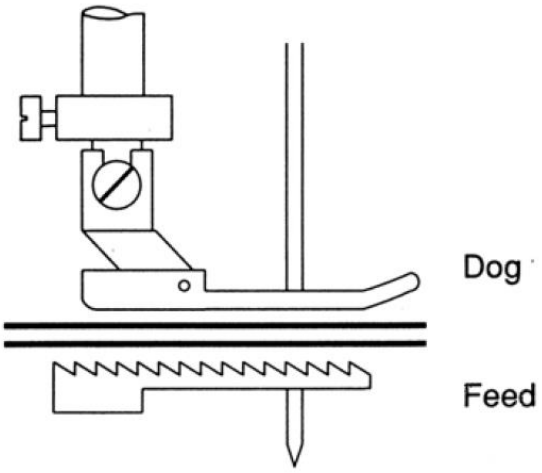

Fig. 1.8. Schematic diagram of the stitching process for 3D fabric [Dransfield et al., 1994].

1.2.3 Non Crimp Fabric

Non Crimp Fabric (NCF) is another way to add the cohesion between fibers. Compared with the woven fabric, NCF has no undulation in the fibers. The NCF is composed of a stack of unidirectional (UD) plies linked together by a stitching in the thickness direction, The NCF can be classified by the number of the UD plies, and there are three commonly used NCF: Uniaxial, biaxial and triaxial NCF. Fig. 1.9 present a biaxial NCF fabric. The fibers in the NCF are not undulated [W.-R. Yu et al., 2005; Lomov, 2011; Bel et al., 2012], and the mechanical behavior of NCF is different to the woven fabric. The stitching pattern (influenced by the stitching type, stitching density, stitching length, and yarn type) plays an important influence on its mechanical behavior [Lomov et al., 2002; Yudhanto et al., 2013; Vallons et al., 2014; Grieser & Mitschang, 2017].

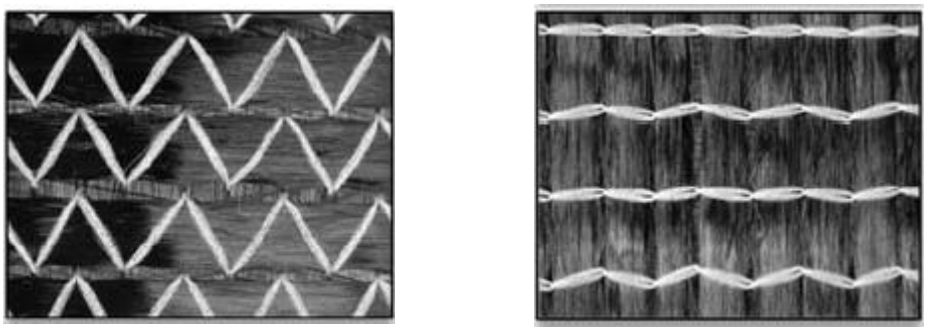

(a) (b)

Fig. 1.9. A biaxial NCF fabric. (a) Top side (b) Bottom side

1.2.4 Molding processes of woven fabric reinforcement

There are many manufacturing processes for the woven composite molding. The manufacturing processes focus on improving the forming efficiency, forming quality, and the ability to fabricate complex shapes of composite component, like the double curvature part. In this chapter, the two classical molding processes: Resin Transfer Molding (RTM) and Thermoforming will be introduced due to these two processes are suitable for the mass production.

a) Resin transfer molding (RTM)

Resin transfer molding and its improvement [C D Rudd, A C Long, K N Kendall, 1999; Halimi et al., 2012; Ageyeva et al., 2019; Seuffert et al., 2020], as type of Liquid Composite Molding (LCM) technologies, are the most widely used for the manufacturing composite part. Single-layer or multi-layers are formed by compression molding, the composite structure can be complex shape in medium and large series, and this process makes it possible for the mass production and dimensionally accurate composite parts. This RTM is mainly used for the dry composite forming. As shown in Fig. 1.10, the forming process can be divided into two main steps.

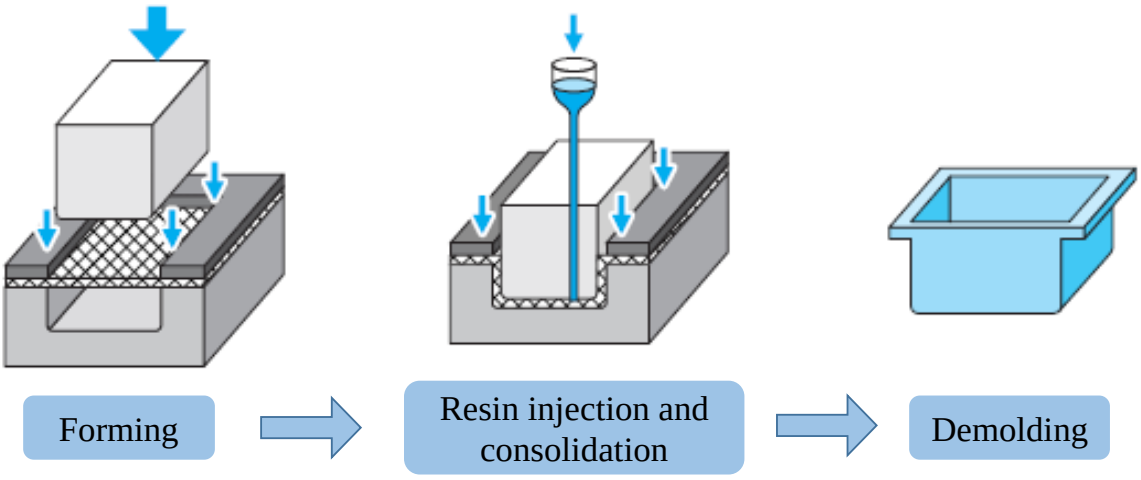

Fig. 1.10. Steps of RTM process [Buet Gautier, 1998]

Step 1: Forming. Under the pressure of the blank-holder, the dry reinforcement is firstly placed on the mold. The mold is composed of two separated parts called punch and die. These two rigid parts will generate a closed cavity by the displacement of the punch, aiming to form the dry reinforcement to the desired shape. Thus the dimension of the formed part can be accurately controlled under the pressure of the mold. The distance between die and punch can be adjusted to fabricate the composite part with different thicknesses.

Step 2: Resin injection and consolidation. The deformed dry reinforcement, called a preform, will be infused with a resin[Deléglise et al., 2011; Sozer et al., 2012]. The resin will fill the voids

between the fibers under external pressure. Next, the composite part will consolidate under pressure and temperature. At last the final composite part can be obtained by demolding.

In the RTM forming process, the different defects will appear depending on the forming parameters and the used material including the mechanical defect (like wrinkles, buckling, fiber gap or overlap), and the fluid defect (like resin void). These defects will highly influence the mechanical properties of the final composite. The mechanical defects will mainly occur in the forming stage when the dry reinforcement will subjected to the mechanical deformation, and the fluid defect occur in the resin injection and consolidation stage.

The research work presented in this manuscript is interested in the mechanical deformation of the dry composite at the forming stage. The deformation analysis at the forming stage will give the yarn direction at different locations which mainly decided the mechanical properties of the deformed fabric. Moreover, the fabric deformation at the forming stage will also affect its permeability [Bodaghi et al., 2019].

b) Thermoforming

The thermoforming process is used to fabricate thermoplastic composite parts from thermoplastic prepregs. The thermoplastic prepregs are the dry reinforcement that has been impregnated with a thermoplastic matrix. In the case of prepregs, the resin is present in the reinforcement during thermoforming [Verrey et al., 2006; Lukaszewicz & Potter, 2011; Henning et al., 2019], thus the manufacture of thermoplastic composites doesn't require the resin injection stage, avoiding the resin maldistribution and voids in the composite parts. As shown in Fig. 1.11, the thermoplastic prepregs can be classified into tow and tape according to their width.

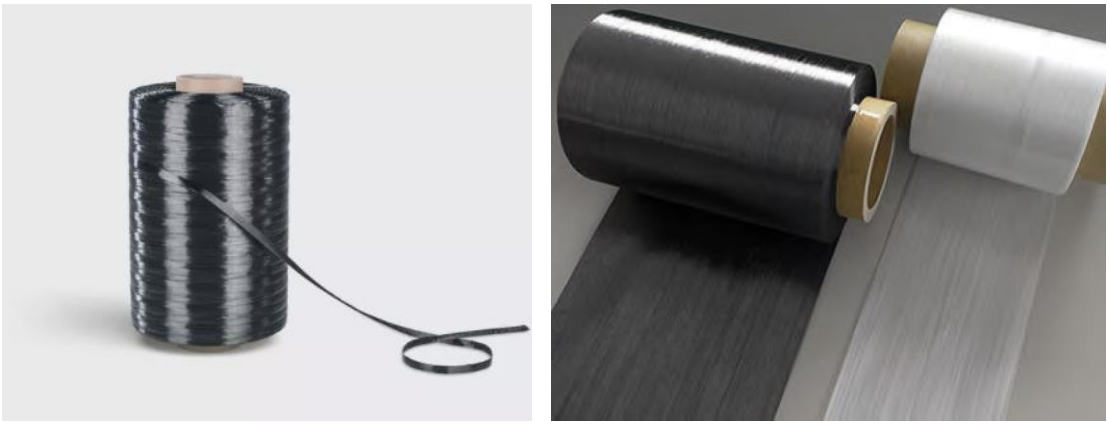

(a) https://www.sglcarbon.com/en/ (b) https://www.shindo.com/en/

Fig. 1.11. Types of prepregs (a) Prepregs tow (b) prepregs tap

Composite structural components with simple geometries can be manufactured by the Automated Fiber Placement (AFP) process. As shown in Fig. 1.12, the thermoplastic prepregs tow

or tape is added to the mold by the compression of the roller. This manufacturing process is highly automated and can be used for mass production. The application of the AFP process is limited by the dimension of the roller and the width of the prepregs. The smaller rollers and the narrower prepregs are needed to fabricate the complex curved surface, and this will reduce manufacturing efficiency.

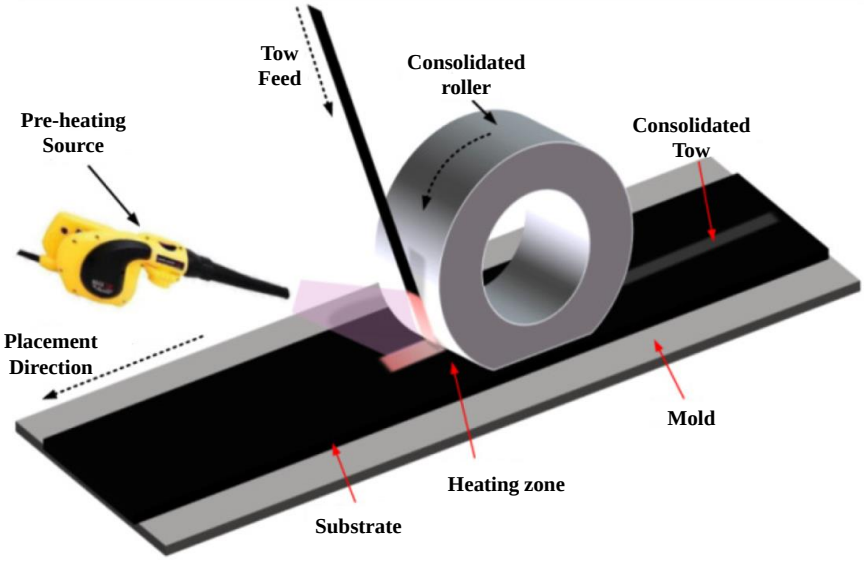

Fig. 1.12. Schematic diagram of Automated Fiber Placement (AFP) process [Han et al., 2017]

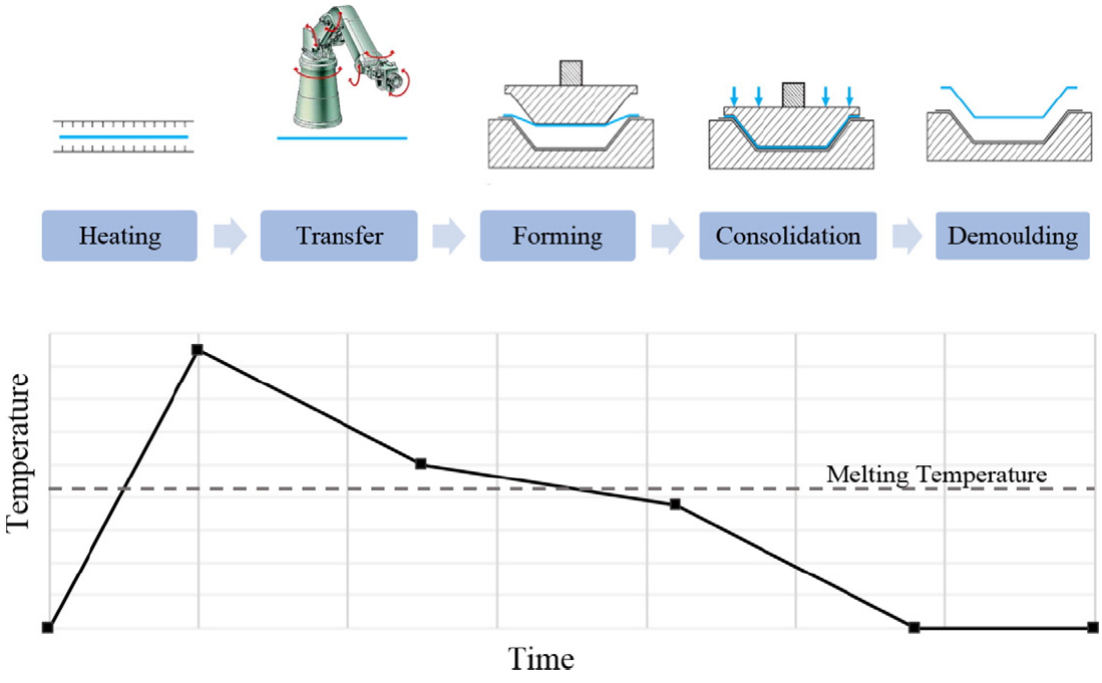

Fig. 1.13. Steps of thermoforming process [Guzman-Maldonado et al., 2016]

In order to manufacture structures with non-developable geometry (3D) in mass production, thermoforming is an ideal approach. As shown in Fig. 1.13, the thermoplastic prepregs are firstly heated in the oven over the resin melting temperature. The material behavior of the thermoplastic prepregs may change with the temperature [P. Wang et al., 2012; Liang et al., 2014; P. Wang, Hamila, et al., 2015]. And then the heated prepregs will be transferred onto the mold. The prepregs will be deformed into the desired shape in the closed mold under pressure. This forming stage is same with the RTM process. Next, the mold will remain closed under pressure and cool down to make the resin crystallize and solidify. The composite part can be obtained by removing the mold.

For the RTM and thermoforming, the forming stage is similar. The material is deformed into the desired shape under the action of the mold. There are several manufacturing parameters that will influence the material deformation like the bank holder shape, position, and pressure. To avoid 'trial and error' processes, it's needed to conduct the simulation of this forming stage which is the main work of the presented manuscript introduced in Chapter 2. There are two main aims to simulate the forming stage:

- Determine if the forming process is suitable for the formation of the composite part without defects, or under what are manufacturing conditions can make it possible.
- Give the deformation information like the fiber yarn direction, and profile.

Different numerical simulation approaches for the textile composites will be presented in the next section.

1.3 Numerical simulation approach for textile composites

A predictive numerical simulation of the textile composite is useful to reduce the 'trial and error' process during the forming stage. The numerical simulation approaches can be classified into the kinematic approaches and the mechanical approaches [Lim & Ramakrishna, 2002; Boisse, 2015; Bussetta & Correia, 2018]. The kinematic approaches, also called mapping approaches or fish-net approaches, is purely geometrics and can give the fiber orientation after the textile composite is deformed [Mack & Taylor, 1956; Pickett et al., 2005; Potluri et al., 2006; Hearle, 2015]. The mechanical approaches, also called finite element approaches, is based on the material constitutive model to predict the mechanical deformation of the textile material.

1.3.1 Kinematic approach

The kinematic approach is firstly proposed in the 1950s [Mack & Taylor, 1956] to give designers and manufacturers critical pre-production information. Different kinematic approaches have been proposed [Heisey & Haller, 1988; Van Der Weeën, 1991; West & Luby, 1997a, 1997b]. In the kinematic approach, the initial flat textile composite is transformed onto the three-dimension surface using the mapping algorithms based on the geometric assumptions.

As shown in the Fig. 1.14 Assumption of the kinematic approach, the initial flat woven fabric can be simplified as the 2D interwoven horizontal and vertical threads, the thickness of the woven fabric is neglected. The intersection between a weft and a warp defines a crossing called a 'crossing point'. The geometric assumptions are as follows [Mack & Taylor, 1956; Aono et al., 1994]:

- The fibers are assumed as incompressible and inextensible.
- The distance between neighboring crossover points are assumed as constant and unchanged.
- There are only relative rotation at the crossover point, while the slippage is neglected, and the relative rotation has no restriction.

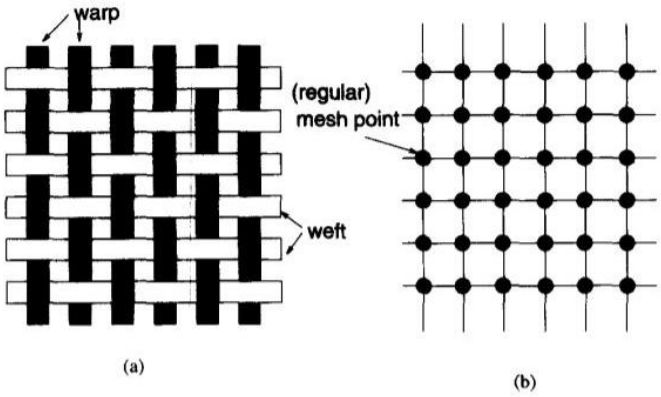

Fig. 1.14 Assumption of the kinematic approach [Aono et al., 1994].

In general, kinematic approaches need to define the initial position of an origin point and the direction of the warp and weft yarn. As shown in Fig. 1.15, the position of crossing point *C* can be determined by crossing points *A* and *B* based on the geometric assumptions. The length of the AC_2 and BC_1 should be equal. By considering all curves AC_2 and BC_1 on the surface, crossing point C can be obtained when crossing points C_1 and C_2 are coincident. All the crossing points can be obtained by repeating this process.

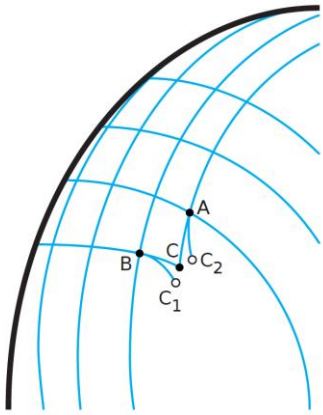

Fig. 1.15. The principle of kinematic approach [Boisse, 2004].

According to the calculation process of kinematic approach, it can be known that the kinematic approach can be very fast and need low computation cost, which is the main advantage of this approach. On the other hand, the limitation of these approach is clear and strong. Due to the material mechanical behavior isn't taken into consideration, the process parameters like the punch force, the force of the blank holder, and the interaction between adjacent layers cannot be simulated. Moreover, this approach can only be used for the single-layer forming and it cannot be used to simulation the wrinkles. So the kinematic approaches are mainly used in the occasion that only focus on the fiber direction.

Compared with kinematic approaches, the mechanical approaches which are based on the material constitutive model are more comprehensive approaches, and thus have received more attention. The mechanical approaches will be introduced in the next.

1.3.2 Mechanical approach

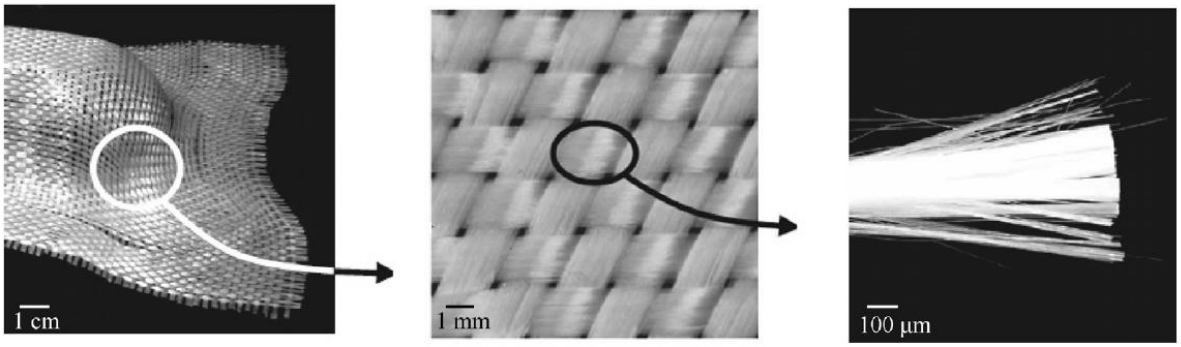

Fig. 1.16. The three simulation scales for textile composites [Hamila & Boisse, 2013b]

Due to the multi-scale of the textile composites (introduced in Section 1.2.1), the mechanical approaches are considered at different scales (Shown in Fig. 1.16): fiber scale (microscopic scale), yarn scale (mesoscopic scale), and part scale (macroscopic scale).

- The analysis at the microscopic scale is performed to simulate the motion and friction between fibers [Zhou et al., 2004; Durville, 2010; Latil et al., 2011]. The fibers can be modeled as a rod or beam. Due to there are several thousands of fibers in a yarn, and more in a part, the microscopic scale can hardly be used for the forming analysis.
- The simulation at mesoscopic scale can be used to conduct virtual tests on one or some representative unit cells (called RUC) [Cai & Gutowski, 1992; Chen & Chou, 2000; Xue et al., 2005; Badel et al., 2007; Lomov et al., 2007; Charmetant et al., 2011; Nguyen et al., 2013], and the whole fabric is obtained by in-plane translation. The deformation analysis of the RUC will determine the properties of the deformed element cell, like the permeability of the deformed reinforcement [Lekakou et al., 1996; Loix et al., 2008].

The yarns are independent in the mesoscopic scale analysis which allow this scale analysis simulate the defects at yarn scale [Matveev et al., 2019], like yarn buckling and gap.

- Considering the textile composites as a continuous medium, simulation conducted at the macroscopic scale is able to determine the optimal conditions of the forming process, the fiber direction, and the onset of defects [Pickett et al., 1995; Boisse et al., 1995; Hancock & Potter, 2005; Zouari et al., 2006; Jauffrès et al., 2010; Schirmaier et al., 2017].

The existed approaches to perform the simulation at these three scales will be introduced in the next.

a) Simulation at microscopic approach

For the microscale approach, the basic constituent is fiber. The behavior of fiber is linear orthotropic and its characteristic quantities are relatively well known. The objective of the microscale approach for the dry fiber reinforcement is to model the fiber behavior and the interactions between them.

Fig. 1.17 presents two methods to model the fiber behavior. Fig. 1.17 (a) [Zhou et al., 2004] model the fiber as a chain of rod elements, and the elements are connected by pins. The bending stiffness is neglected and a simple contact algorithm to simulate the weaving process and the fiber damage under perforation [Miao et al., 2008]. This modelling approach is relatively simple and can be adopted in different cases. Fig. 1.17(b) model the fiber as beam element, and more complex contact algorithm is adopted. This approach is more difficult to implement than the approach in Fig. 1.17(a). But this approach take into account the bending stiffness of the fibers, and thus it can better model the fiber behavior.

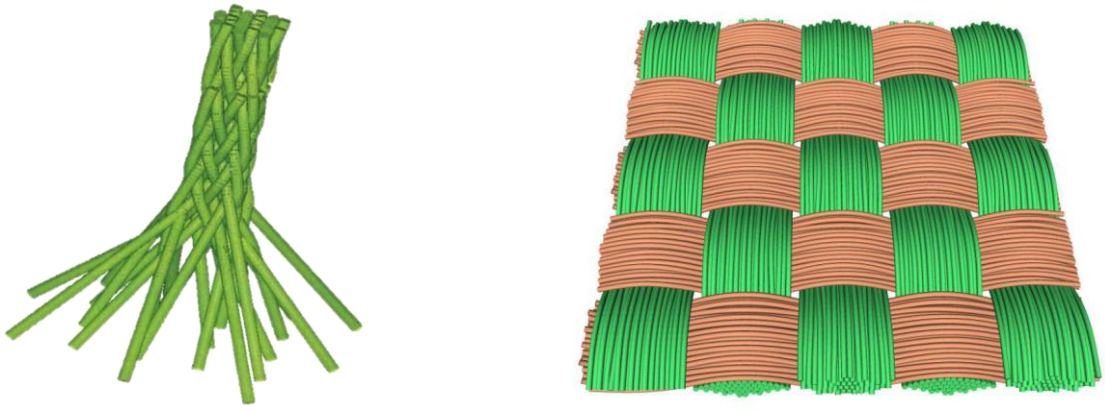

(a) (b)

Fig. 1.17. Modeling at the microscopic scale of a reinforcement. (a)Model of Wang [Y. Wang & Sun, 2001] (b) Model of Durville [Durville, 2010].

A single yarn is composed of several thousands of fibers. The main difficulty of the microscopic approach is the management of these many fibers constituting the model, in particular, the management of the contact between them. The microscopic approach is very time-consuming, and it is currently limited to a model with a moderate size.

b) Simulation at mesoscopic approach

For the mesoscopic approach, the basic constituent is yarn, which the yarn is considered as a continuous medium. The simulation conducted at the mesoscale is interested in the behavior of a unit cell of the reinforcement. The objective of these analysis is to obtain the fabric behaviors at the yarn scales while the experimental determination might be difficulty or expensive. These behaviors includes:

- The macroscopic mechanical behavior of the reinforcement by transferring the mesoscale model to the macroscale model.
- The macroscopic thermal properties of the fabric (with or without matrix) for the simulation of heat exchanges, like the macroscopic thermal conductivity [Dasgupta & Agarwal, 1992; Dasgupta et al., 1996; Hsiao & Kikuchi, 1999; David et al., 2001].
- The local permeability of the reinforcement. Through the mesoscale analysis, it can build a function between the local permeability and the deformation of the unit cell [Loix et al., 2008], which will be an input for the simulation of the resin flow in the LCM process.

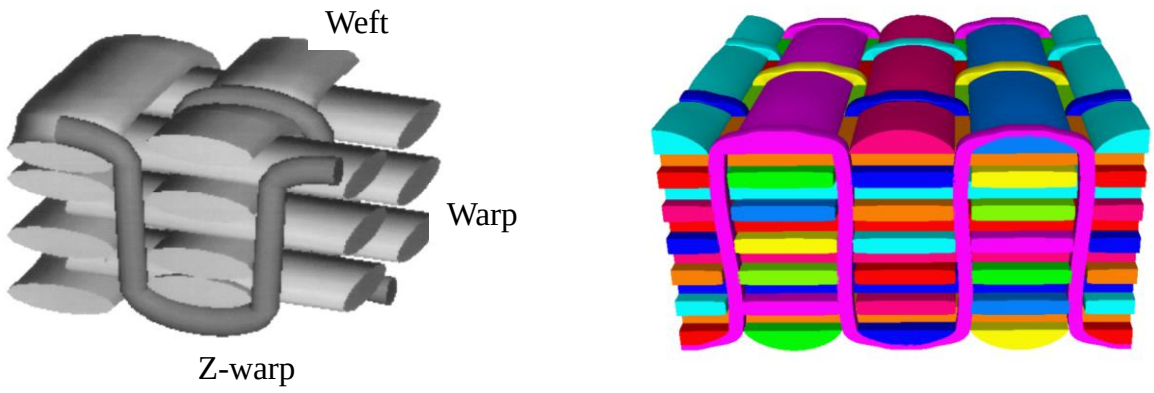

(a) (b)

Fig. 1.18. Model generation of 3D reinforcement. (a) Model in WiseTex [Lomov et al., 2000]. (b) Model in TexGen [Sherburn, 2007].

The properties of the unit cell are influenced by the yarn size, shape, and architecture. It is needed to accurately model the material geometry for the mesoscopic analysis. Several approaches have been developed to obtain the geometry of the textile fabric. Here, we will first introduce two software that can automatically generate the material geometry by inputting the corresponding parameters: The WiseTex software developed at Katholieke Universiteit Leuven [Lomov et al.,

2000; Lomov & Verpoest, 2006] and the TexGen software developed at the University of Nottingham [Sherburn, 2007]. In the case of WiseTex, this software takes different deformation modes into consideration (tension, shear, bending, torsion, compression of the yarns). The geometry of the material is obtained by minimizing the deformation energy of the yarns within the material. The experimental identification data is needed in this approach which are not easy to obtain. The TexGen software, unlike the WiseTex software, is easier to obtain the material geometry, and the mechanical deformation information is not needed. The model in TexGen software is generated by assigning different cross-sectional geometries to the mean line of the yarn. For these two approaches, the problem of interpenetration between yarns, although it has been reduced in the WiseTex software [Verpoest & Lomov, 2005], always exists.

To accurately model the reinforcement, X tomography is an effective experimental approach [Hsieh, 2003; Desplentere et al., 2005; A. H. Khan & Chaudhuri, 2014]. To obtain the 3D geometry, the X tomography technique first scans a reprehensive sample of the reinforcement and processes the resulting image to obtain the constituent element (yarn). At last, the 3D geometry can be built by cutting the yarn apart and meshing them with each other. The X tomography technique has huge advantages to model the material geometry. The interpenetration can be avoid through the proper numerical processing [Naouar et al., 2014, 2015]. An example of the modelling of an interlock fabric using the X tomography is presented in Fig. 1.19. Fig. 1.19 (a) is the 3D image obtained in the X tomography, and the built 3D simulation model in given in Fig. 1.19(b).

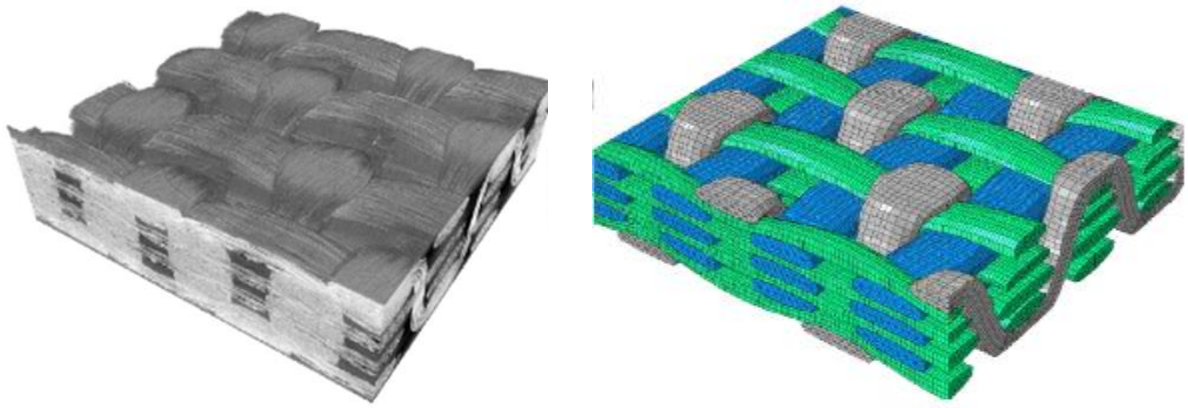

(a) (b)

Fig. 1.19. Modeling of an interlock fabric by processing a tomography [Naouar et al., 2015](a) 3D tomography image of the fabric architecture. (b) The 3D simulation model.

Once the geometry has been defined and discretized by finite elements, a constitutive law must be associated with the models to conduct the simulation. In most cases, the yarn is considered as a continuous medium. The fibrous nature of the yarn give is very specific behavior, most studies used hypoelastic [Gasser et al., 2000] or hyperelastic models [Charmetant et al., 2011] to describe this behavior. The mesoscopic model can be used for the preforming analysis of the textile

reinforcement. But it still need a lot of CPU times. The simulation at macroscopic approach which consider the material at part scale are therefore preferable for the simulating the draping process, even for the multi-layer reinforcement forming.

c) Simulation at macroscopic approach

The simulation at the macroscopic approach considers the textile composite at the part scale. Compared with the other lower scales, these approaches can save much more CPU time to conduct the simulation. Thus lots of research have devoted to the macroscopic approach. The macroscopic approach can be classified into three types: discrete approach, semi-discrete approach, and continuous approach.

Discrete approach: The discrete approaches considered the textile reinforcement as a combination of a series of deformable elements. The mechanical properties of the material is applies on the deformable elements and the connection between elements to model the material response in elongation, shear, torsion and bending. Among the existed of discrete approach, the work of Sze and Liu [Sze & Liu, 2005] (as shown in Fig. 1.20) is notable, the reinforcement is modeled using nodes connected to each other by bars and springs. The 2D reinforcement is modeled using bars and springs connected to each other at nodes. Different deformation mode is achieved through the different connection mode. Compared with semi-discrete approach and continuous approach, these discrete approaches are little used in the forming analysis of textile reinforcement due to the lack of precision and the difficulty in obtaining the stress state within the material.

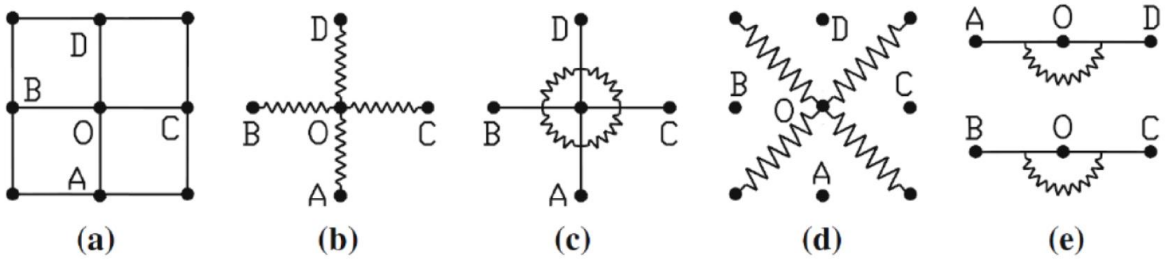

Fig. 1.20. The discrete modelling approach. (a) The typical ‘O’ discrete model. (b) Stretch. (c) Torsion. (d) Shear. (e) Bending [Sze & Liu, 2005].

Semi-discrete approach: The Semi-discrete approach falls between the discrete and continuous approaches. With this approach, only a type of specific finite element is used to mesh the textile reinforcement. The specific element is built according to the behavior of a representative unit cell (RUC) at mesoscale. Same with the discrete approach, the material mechanical behavior is split between the specific element and the connection of the element.

A remarkable semi-discrete approach is proposed by Hamila and Boisse [Hamila et al., 2009]. In this approach, the textile reinforcement is meshed using the three node shell element.

The warp and weft yarns are arbitrary with regard to the element sides to avoid the tension locking phenomena [Hamila & Boisse, 2013a]. Three type of material behavior are considered in the semi-discrete approach including tension, in-plane shear, and out-of-plane bending. The tension and in-plane shear behavior is described within the three node shell element, and the bending behavior is described by the two adjacent shell element.

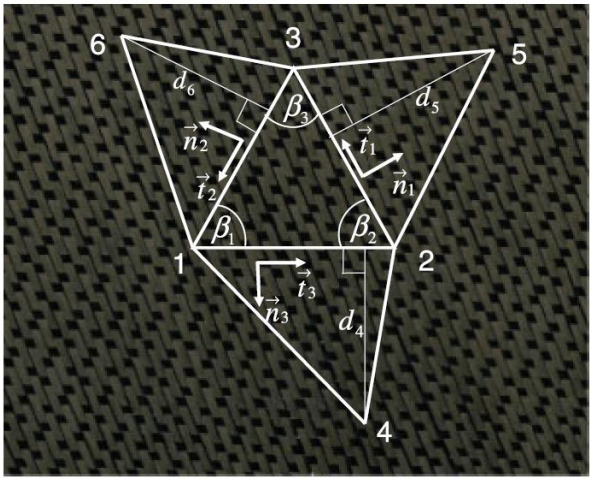

Fig. 1.21. The semi-discrete approach using three node shell element [Hamila et al., 2009]

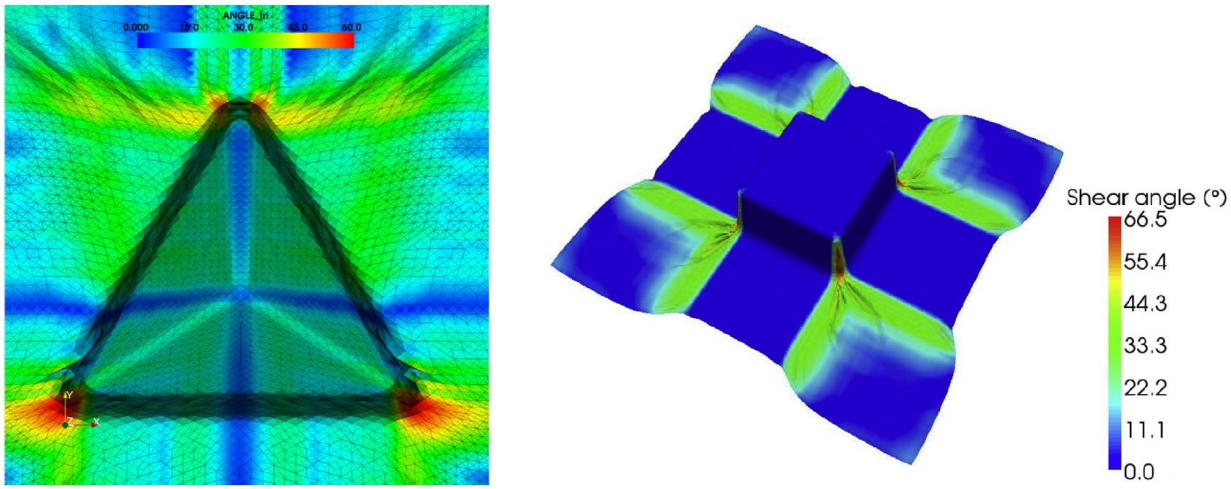

(a) (b)

Fig. 1.22. Forming simulation using the semi-discrete approach (a) Tetrahedron forming [Allaoui et al., 2011] (b) Square box forming [P. Wang, Legrand, et al., 2015].

This approach is implemented in a in-house F.E. code called Plasfib, and has been widely used for the textile draping research. The role of the three main behavior (tension, in-plane shear, and out-of-plane bending) on the influence of the occurrence of wrinkles are simulated by this approach [Boisse et al., 2011]. The research in the work of Boisse[Boisse et al., 2011] indicate that there is no direct link between shear angle with the onset of the wrinkles, the shear locking angle

is not sufficient for the prediction of wrinkle occurrence. And wrinkling is a global phenomenon related with all strains and stiffness and also the boundary condition. The semi-discrete approach was used in [Allaoui et al., 2011] to predict the textile draping in the tetrahedron forming. The numerical simulation result are in good agreement with the experimental result. It's also experimental found that the shear angle can go up to 60° without the occurrence of wrinkles. Wang and Huang [P. Wang, Legrand, et al., 2015; J. Huang et al., 2021] used this approach to predict the wrinkles in the square box under different conditions. In the research work [P. Wang et al., 2013], the semi-discrete approach was adopted to conduct the thermoforming simulation of multilayer composites with continuous fibers, friction model is developed and implemented between the layers and for ply/tool friction. Based on this approach, Liang and bai [Liang et al., 2017; Bai et al., 2020] developed a new fibrous shell element considering the deformation in the thickness.

Continuous approach: The continuous approach meshes the textile reinforcement using one type of finite element, and all considered material behavior is described within the used finite element. This approach has the most computationally efficient, and is a research hotspot. The simulation approach proposed in Chapter 2 also used the continuous approach.

The yarn of the textile composite is composed of thousands of fibers with a very small diameter. These yarns are woven together to the woven fabric reinforcement which gives the material very specific behavior, including the high anisotropy, and the ability to exhibit large shear and bending deformations. At the same time, the woven architecture makes it possible to consider the material as a continuous medium at the macroscopic scale. The material is not continuous at the macroscopic scale, but it can be seen as continuous on average.

During the draping process, the woven fabric can exhibit large shear and bending deformation. To describe the material mechanical behaviors, the hypoelastic laws is an alternative approach for the large strain, and the non-linearity of material behavior can also be achieved. The hypoelastic laws use a rotated frame to remove the body rotation and calculate the objective summation of the stress increments (detailed description in section 2.2). The rotated frame includes the Green Naghdi frame [Dienes, 1979] and corotational frame [Dafalias, 1983]. For the fibrous material, the material behavior is directly related with the orientation of the fiber. And the fiber orientation doesn't follow the orientation of the two frames (Green Naghdi frame and corotational frame). Two approaches has been developed to consider this particular aspect: Non-orthogonal method [W. R. Yu et al., 2002; Peng & Cao, 2005], and orthogonal method [Badel, Vidal-Sallé, & Boisse, 2008; M. A. Khan et al., 2010].

As illustrated in Fig. 1.23(a), non-orthogonal method constructs a non-orthogonal frame in which each axis of the frame is parallel to one direction of yarn respectively. It is achievable to track the fiber direction during the deformation using the deformation gradient tensor and initial fiber direction. The material constitutive laws is expressed in the built non-orthogonal frame, and

the approach to test the corresponding parameters of material behavior is presented in [Xue et al., 2005]. This approach is convenient to conduct the forming simulation because the objective derivative and the associated tensor transformation is integrated in the commercial code, and several forming analysis have been conducted in [Lin et al., 2007][Zhang et al., 2017]. However, the research in Badel [Badel, Vidal-Sallé, & Boisse, 2008] show that the non-orthogonal method could give the undesired result (given in Fig. 1.24) at mesoscale.

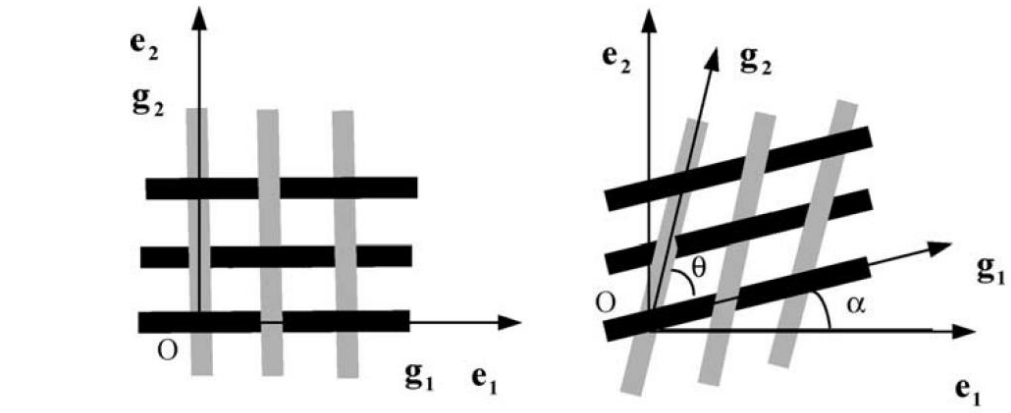

Before deformation After deformation

(a)

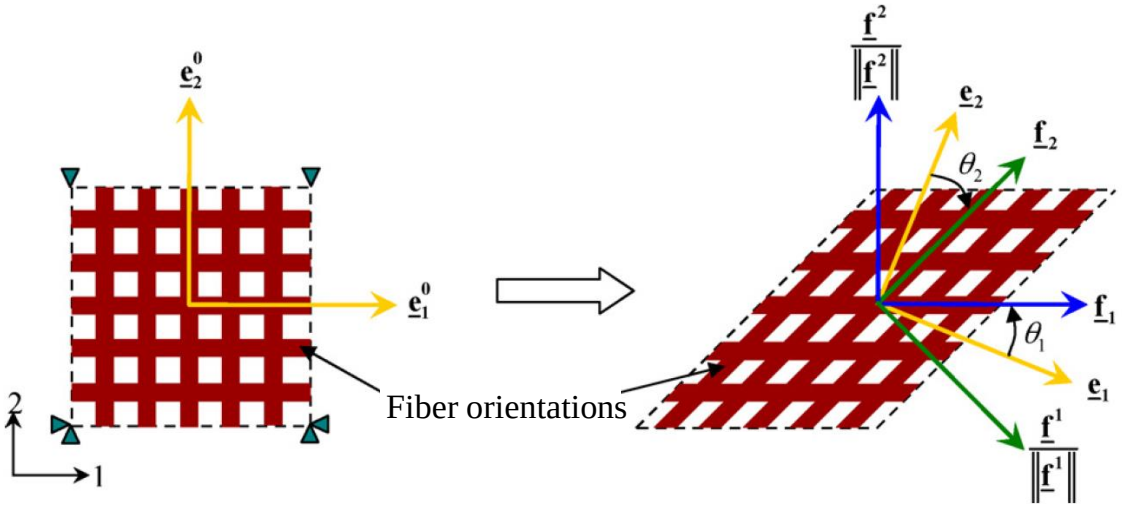

Before deformation After deformation

(b)

Fig. 1.23. Different constitutive for the continuous simulation approach (a) Non-orthogonal constitutive model [Peng & Cao, 2005]. (b)Orthogonal constitutive model [M. A. Khan et al., 2010].

As shown in Fig. 1.23(b), the orthogonal method construct the two orthogonal frames (called fiber base) while one axis of each frames is parallel to one of the yarn orientation. The stresses are integrated in the fiber base, and then transformed to the Green-Naghdi frame. Different tests have

been conducted to validate its effectiveness, and the double dome forming comparisons between the simulation and experiment is given in Fig. 1.25, they are in good agreement in the shape. Different simulation research have been conducted based on this orthogonal method. The thermoset prepregs is simulated using this method by coupling with a finite element modelling the resin [M. A. Khan, Reynolds, et al., 2015]. The influence of the process parameters, like the force on the blank holder, and the friction coefficient are analyzed using this method in the double dome and hemisphere forming [M. A. Khan, Saleem, et al., 2015]. The simulation approach proposed in Chapter 2 can be seen as an extension of this method. The proposed simulation approach in the manuscript take into three material behaviors: tension, in-plane shear, and out-of-plane bending behavior while the bending behavior is neglected in the orthogonal method [M. A. Khan et al., 2010]. The stress resultant shell is adopted to consider the independent bending behavior and also makes the simulation fast.

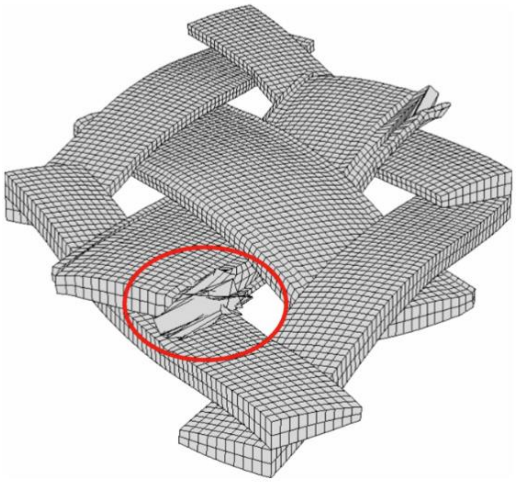

Fig. 1.24. The deformed fabric given by the non-orthogonal method [Badel, Vidal-Sallé, & Boisse, 2008]

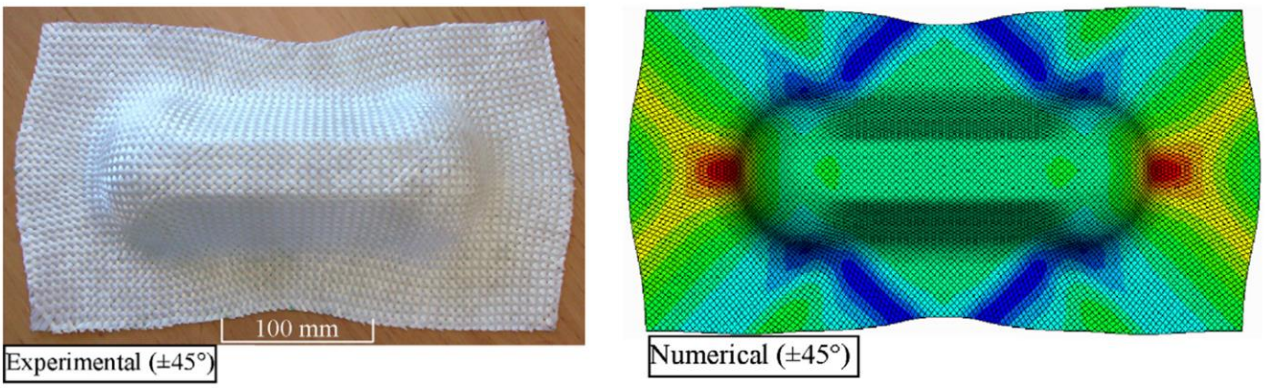

(a) (b)

Fig. 1.25 The comparison between experiment and simulation conducted by the orthogonal method. (a) Experiment. (b)Simulation [M. A. Khan et al., 2010]

d) Multi-scale approach

The simulation approach at different scales has its advantage and disadvantage. For example, to conduct the forming analysis, the most effective approach is the simulation approach at the macroscopic scale. However, this approach will neglect the information concerning the yarn deformation and the relative displacement between them. Therefore, multi-scale approaches are proposed in order to balance the CPU time and the deformation information at different scales. A meso-macro approach is shown in Fig. 1.26, the yarn mesoscopic geometry is embedded in the macro element which can obtain the fabric deformation information at the macroscale and also get the yarn deformation information at the mesoscale in a draping analysis.

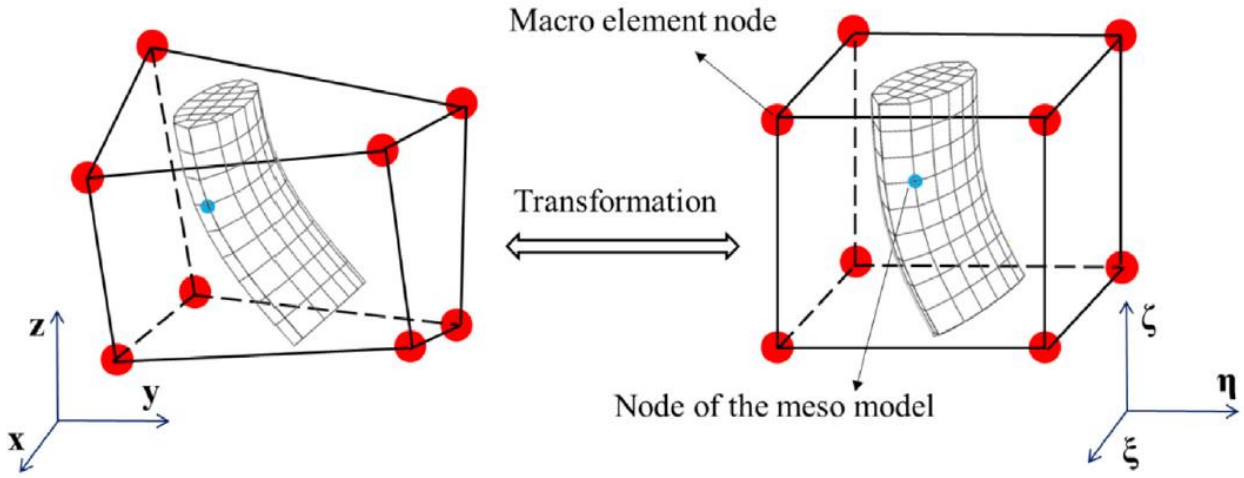

Fig. 1.26. A meso model embedded in a macro element [J. Wang et al., 2020, 2022].

1.4 Research motives and objectives

Due to its excellent performance, textile composite is widely used in different areas. In order to improve the manufacturing quality, reduce the manufacturing cycle, and manufacturing costs, it is critically important to conduct the numerical analysis to meet the different needs in the material performing step. The textile composite material is woven from the yarn and the yarn is composed of thousands of fibers which gives this material a specific deformation mechanism. The simulation approach can be conducted at different scales, and there is currently not a widely accepted simulation model.

Focusing on the deformation of materials at the macroscopic scale, the first objective of the Ph.D. work will be devoted to developing a more comprehensive simulation approach. There are three material behaviors: tension, in-plane shear, and out-of-plane bending which have been studied before that have a main influence on the material deformation. These three material behaviors will be taken into consideration in the proposed approach. In order to validate the effectiveness and correctness of the presented simulation approach, different tests from different

aspects will be conducted to make the comparison between the simulation results and the experimental or analytical results. The proposed approach will be implemented in Abaqus which make it available to any user who want to conduct the draping analysis of textile composites in Abaqus.

The single layer of textile composite has a very small thickness. In the application of the textiles composite, it is needed to combine the multi-layer together into the final composite part. Multilayer forming simulation can be achieved by stacking single layers and assigning suitable contact properties between adjacent layers. This is not very effective when there are many layers. Thus the second objective is to study the multi-layers analysis approach. Due to the specific material behavior, the material can be seen as quasi-inextensible in the yarn direction. This is a very important assumption. In multi-layer deformation, the rotation of the normal line is the main concern. Because if there is fiber in the thickness direction or for the 3D fabric, the normal rotation will determine the fiber direction in the thickness when the fabric is deformed. The Kirchhoff and Mindlin shell elements cannot be used to predict the normal rotation in the multi-layer forming. Based on the proposed simulation approach in the Ph.D. work, a simple post-processing method is introduced for the multi-layer forming with same orientation.

Wrinkle is one of the main defects in the forming of textile composite reinforcement at the macro scale. The onset of the wrinkles has relationships with the process parameters and the used material. The process parameters can be optimized through simulation analysis to determine the best process parameters. The used material which exhibits different material behavior will influence the onset of the wrinkles. The draping of material without wrinkles is called drapability. The third objective is to experimental research the influencing factors on the material drapability. The square box and cylinder forming using different materials with different mechanical behaviors are conducted to observe the relationship between the drapability and the onset of the wrinkles. A drapability ratio relating the in-plane shear stiffness and bending stiffness is defined for the description of the material drapability. The material with a lower drapability ratio is easier to be formed without wrinkles.

1.5 Summary

This chapter gives a brief introduction to the state of the art of textile reinforcement from the application of the composite material to the different simulation approaches at different scales. It can be known that the textile composite is woven from yarns, and the yarn is composed of several thousands of fibers. This special architecture gives its specific mechanical properties. The simulation approach can be conducted at different scales: microscale, mesoscale, and macroscale. Among these three scales, the continuous approach at the macroscale needs the lowest computation cost. Although simulation at macroscale will lose some information at a lower scale, it is still

acceptable in the forming process which mainly concerns the yarn orientation and the onset of wrinkle.

In the following chapters, the proposed approach will be introduced in Chapter 2, the validation of the simulation approach in the forming process will be given in Chapter 3. The post-processing approach for the deformation in the thickness will also be discussed in Chapter 3. Chapter 4 is about the drapability analysis through the different forming experiments.

Chapter 2 A hypoelastic stress resultant shell approach for simulations of textile composite reinforcement forming

Specific to the textile composite reinforcement material, a simulation approach at macroscale will be proposed and introduced in this chapter. Three material behaviors, the tensile, in-plane shear, and out of plane bending behavior will be considered in the simulation approach. These three material behaviors play a critical role in the material deformation, and the way to measure the corresponding material stiffnesses which need to be as an input in the simulation will also be presented in this chapter. At last, the elementary test will be conducted to verify the effectiveness of the simulation approach. This simulation approach proposed here is implemented in the commercial software Abaqus using the subroutine VUGENS which is available to any user.

Content of Chapter 2

Chapter 2 A hypoelastic stress resultant shell approach for simulations of textile composite reinforcement forming 45

2.1 The specificity deformation of textile composite 46

2.2 The hypoelastic stress resultant approach 49

2.2.1 The stress resultant shells 49

2.2.2 The hypoelastic laws for the textile composite 51

2.3 Elementary test 56

2.4 The characterization of the mechanical behavior of the textile composites 58

2.4.1 Tensile behavior 60

2.4.2 In-plane shear behavior 60

2.4.3 Bending behavior 65

2.5 Summary of Chapter 2 70

2.1 The specificity deformation of textile composite

The yarn of the woven fabric is composed of continuous fiber with very small diameters. These yarns are hold together by weaving process, which makes it possible to consider the woven fabric as a continuous medium at the macroscale. At the same time, this special architecture give the material with a very specific behavior. At the macroscale, there are three main material behaviors (tensile, in-plane shear, and out of bending) that dominate the material deformation. Compared with the other two material behaviors, the tensile stiffness is quite large, and the fiber can be seen as quasi-inextensible. In the fabric deformation, the material can exhibit large shear and bending deformation. Fig. 2.1shows the in-plane shear deformation at the bias extension test and the hemisphere forming. In the hemisphere forming (Fig. 2.1(b)), the yarn was painted black before the fabric deformed to observe the shear deformation, and it can be seen that the shear angle is very large. Research has indicated that the shear angle can go up to 60° without the onset of wrinkles in the textile composite draping. The large shear deformation is the main deformation mechanism for the material to deform from a flat into a complex shape, in particular the double-curvature surface. Due to the possible slippage between fibers, the textile composite has very small bending stiffness. The above phenomena led to simulating the textile composite deformation by membrane elements in some research before, and the bending stiffness is neglected.

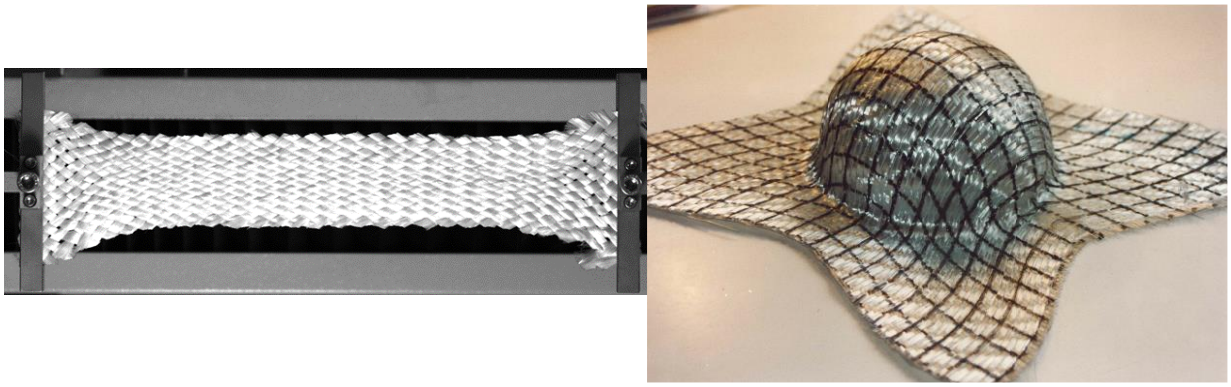

(a) (b)

Fig. 2.1. In-plane shear deformation in different cases. (a) Bias extension test of glass fiber. (b) Hemisphere forming[Boisse et al., 2017].

Wrinkles is one of the main defects during the preforming process of textile composite. In the simulation model, it's important that the onset of wrinkles can be accurately predicted. Recently studies [Boisse et al., 2011, 2018; Döbrich et al., 2013; Dangora et al., 2015; Thompson et al., 2020] have indicated that the bending stiffness play a critical role on the occurrence and development of wrinkles even the bending stiffness is very small. Fig. 2.2 shows the different shapes of wrinkles with different bending stiffness.

(a) (b)

Fig. 2.2. Wrinkle in the compression deformation of textile composite with different bending stiffness[Boisse et al., 2018]. (a) 1 N·mm^{-1}. (b) 10 N·mm^{-1}.

For the textile composite, the dimension in the thickness is several millimeters (2D textile composite) or several centimeters (3D textile composite). This thickness is relatively smaller compared with the dimension in the plane which the shell elements can be adopted to model the reinforcement. Compared with the solid elements, shell elements is more efficient and has lower computation cost. However, the classical shell element cannot be directly used for the simulation of textile composite, including the Kirchhoff and Mindlin shell elements. In these classical shell element, the bending stiffness is determined by the shell thickness and membrane stiffness, the function to calculate the classical shell bending stiffness $B_{classic}$ is given in Eq.(2.1) .

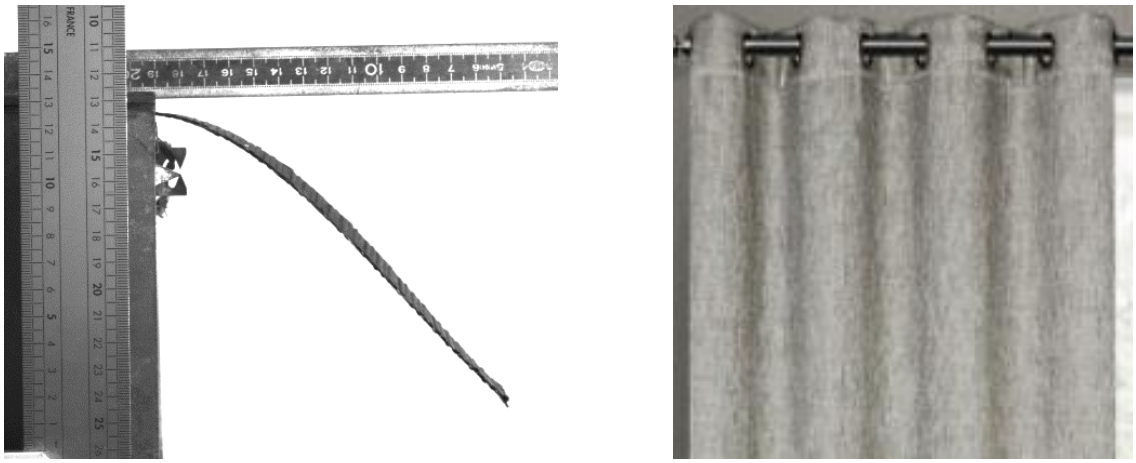

(a) (b)

Fig. 2.3. Bending deformation in different cases. (a) G1151 fabric bending under its gravity (b) Bending of curtain.

$$B_{classic} = \frac{Eh^3}{12(1-\nu^2)} \tag{2.1}$$

Here *E* is the Young's modulus of the fibers, *h* the shell thickness, and *v* is the Poison's ratio. The Kirchhoff and Mindlin shell elements cannot be directly used for the draping of textile reinforcement. The bending stiffness in the Kirchhoff and Mindlin shell elements (given in Eq.(2.1)) is greater than the bending stiffness of the textile composite material. Fig. 2.3 shows the material bending deformation in different cases. It can be known that the bending stiffness is very small while the tensile stiffness is very large. Thus in order to conduct a correct simulation of textile composite, it is need to decouple the bending stiffness with the membrane stiffness.

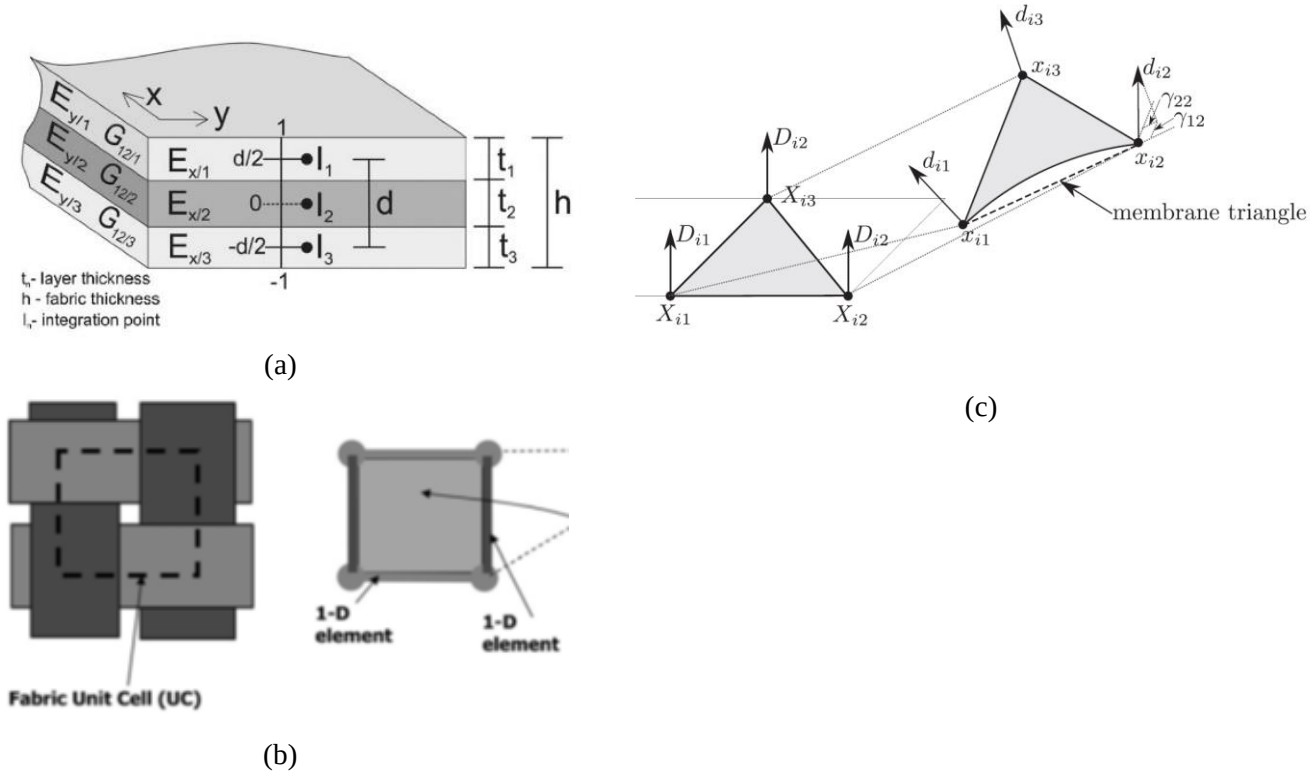

Fig. 2.4. Simulation approach considering the bending behavior of the textile composite. (a) Laminate approach [Döbrich et al., 2013]. (b) Superposition of beam and membrane element [Jauffrès et al., 2010]. (c) Superposition of membrane and shell element [Dörr et al., 2018].

In order to overcome the difficulty that the Kirchhoff and Mindlin is not suitable for the forming of textile reinforcement, and conduct the draping simulation considering the material independent bending stiffness. Different approaches have been proposed. As shown in Fig. 2.4(a), a first effective approach consider the single layer of fiber composite as a laminate with different Young's modulus stetting. The required membrane stiffness and bending stiffness can be achieved by adjusting the thickness and Young's modulus of different layers in the laminate. Another approach apply the superimposition element to achieve the bending stiffness independent of the membrane stiffness. Fig. 2.4(b) is the superimposition of beam elements and membrane elements [Jauffrès et al., 2010; Harrison et al., 2013; Mitchell et al., 2016; Giorgio et al., 2018]. In this approach the beam elements are used to model the small bending stiffness, and the membrane

elements are to model the membrane stiffness (tension and in-plane shear). Fig. 2.4(c) is the superimposition of shell elements (to model the bending behavior) and membrane elements (to model the membrane behavior) [Haanappel et al., 2014; Dörr et al., 2017, 2018; Thompson et al., 2020]. These approaches are validated effective in the predicting the deformation of the midsurface. But these approaches are somewhat artificial, the physics of the material bending behavior is neglected.

Stress resultant shell approach is an available approach to achieve the bending stiffness decoupled the membrane behavior within a shell element. The stress resultant shell is firstly adopted in a semi-discrete shell finite element approach for the simulation of textile composite, however, the approach is implemented in an in-house F.E. code. The stress resultant shell approach based on the hypoelastic constitutive laws will be introduced in the next, and this approach will be implemented in Abaqus subroutine VUGENS which is available for any user.

2.2 The hypoelastic stress resultant approach

The thickness of the textile composite is much smaller than the other two dimensions, which makes it possible to conduct the simulation of textile composite using shell elements. Considering the specificity of the textile composite deformation, a hypoelastic stress resultant approach is proposed in this chapter. The bending behavior and membrane behavior will be independently described within stress resultant shells.

2.2.1 The stress resultant shells

The finite element analysis using the shell element has been widely used due to its efficiency and low computation cost. The so-called continuum-based shell approach dominate the finite shell element analyses, the shell kinematic assumption is imposed in a three-dimensional finite element [Ahmad et al., 1970; Dvorkin & Bathe, 1984; Parisch, 1995]. Stress resultant shells constitute an alternative [Simo & Fox, 1989; Ibrahimbegović, 1994; Yang et al., 2000].

For any virtual displacement η, when η=0 on the imposed boundary with a prescribed displacement, the virtual work theory that relate with the internal work δW_{int}, external virtual work δW_{ext}, and the acceleration virtual work δW_{acc} can be expressed as:

$$\delta W_{\text{ext}} - \delta W_{\text{int}} = \delta W_{acc} \tag{2.2}$$

In the stress resultant shells, the stress state are simplified described by the stress resultants and the stress moments (or stress couples). The internal virtual work δW_{int} that links with the stress resultants and stress moments are as followed:

$$\delta W_{\text{int}} = \int_A (\delta\varepsilon_{11} N^{11} + \delta\varepsilon_{22} N^{22} + \delta\varepsilon_{12} N^{12} + \delta\chi_{11} M^{11} + \delta\chi_{22} M^{22} + \delta\chi_{12} M^{12}) dA \tag{2.3}$$

Here A is the area of the shell midsurface. $\delta\varepsilon_{11}$, $\delta\varepsilon_{22}$ are the virtual axial strains, $\delta\varepsilon_{12}$ is the virtual in-plane shear strain, $\delta\chi_{11}, \delta\chi_{22}, \delta\chi_{12}$ are the virtual curvatures. N^{11}, N^{22}, N^{12} are the stress resultants and M^{11}, M^{22}, M^{12} are the stress moments (or couples), and they are defined as the integration of the stress in the thickness direction (shown in Fig. 2.5):

$$N^{\alpha\beta} = \int_{-\frac{h}{2}}^{\frac{h}{2}} \sigma^{\alpha\beta} dz \qquad M^{\alpha\beta} = \int_{-\frac{h}{2}}^{\frac{h}{2}} z\sigma^{\alpha\beta} dz \tag{2.4}$$

In this manuscript, the Greek indices α, β will belong to the set (1, 2). $\sigma^{\alpha\beta}$ are the components of the Cauchy stress. In the conventional application, the Eq.(2.4) can be used to calculate the shell section response, and adopt a single constitutive equation to obtain the Cauchy stress $\sigma^{\alpha\beta}$. In this way, the bending behavior will be coupled with the membrane behavior. This is not the case for the textile composite. According to the description in section 2.1, it is basic requirement to decouple the bending behavior with the membrane behavior to conduct a correct simulation of textile composite.

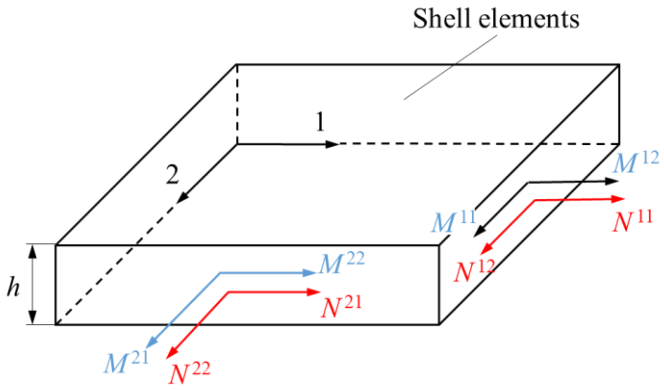

Fig. 2.5. Stress resultants and moments in the shell elements

In order to decouple the bending behavior with the membrane behavior within the stress resultant shell elements, the calculation of stress resultants $N^{\alpha\beta}$ and the stress moments $M^{\alpha\beta}$ need to be fully independent with each other. Hypoelastic laws are adopted in the simulation approach to calculate the stress resultant $N^{\alpha\beta}$ and the stress moments $M^{\alpha\beta}$ separately. Through the hypoelastic laws, the stress resultant $N^{\alpha\beta}$ is related with the membrane strains $\varepsilon_{\alpha\beta}$ through the membrane stiffness, and the stress moments $M^{\alpha\beta}$ is related with the curvatures $\chi_{\alpha\beta}$ through the bending stiffness. Thus the membrane behavior and bending behavior are naturally independent which meets the need of the woven material. The membrane stiffness and bending stiffness in the hypoelastic laws can be determined by the experiment that will be introduced in section 2.4.

The proposed hypoelastic stress resultant approach will be coded in the ABAQUS subroutine VUGENS. This subroutine supplies the membrane strain increment and curvature strain increment

to user at every simulation step. And the user need give ABAQUS solver the stress resultant $N^{\alpha\beta}$ and the stress moment $M^{\alpha\beta}$. Thus in the hypoelastic laws, the stress resultant rates will be determined by the membrane strain rates, and the stress moments will be determined by the curvature rates. For the woven fabric, the accumulation of the stress resultant and stress moment will be conducted in the fibrous medium. The implementation process of hypoelastic laws for the textile composite will be introduced in the next section.

2.2.2 The hypoelastic laws for the textile composite

Due to the specific deformation modes, large shear and bending deformation are the main characteristics of the textile composite draping. Experimental research has indicated that the behavior of the textile composite are non-linear, in particular, the in-plane shear behavior [Launay et al., 2008; Cao et al., 2008]. The constitutive equation adopted for modeling the behavior of textile composite must take these geometry and material non-linear into consideration. The hypoelastic laws can satisfy these requirements while also remains close to the physical deformation mechanism of the textile composite. The hypoelastic laws have been widely used in finite element codes and the subroutine in the commercial software [Hughes & Winget, 1980; Xiao et al., 1997; Belytschko et al., 2000]. The application of these hypoelastic laws also make it possible to extend the material behavior to the viscoelasticity and viscoplasticity while keeping an easy form.

In the stress resultant shells, the membrane strain increments and bending curvature increments are supplied at the simulation step time t_{n+1} from their values at t_n, the objective is to calculate the stress resultants and stress moments at the time t_{n+1} from the time t_n. The calculation of the stress resultants and stress moments need to be separate. The hypoelastic laws for the stress resultants and stress moments will be:

$$\mathbf{N}^{\nabla} = \mathbf{C} : \dot{\varepsilon} \qquad \mathbf{M}^{\nabla} = \mathbf{D} : \dot{\chi} \tag{2.5}$$

Here, $\dot{\varepsilon}$ and $\dot{\chi}$ are the time derivatives of the membrane strain and curvature tensors, $\mathbf{C}$ and $\mathbf{D}$ are the membrane and bending constitutive tensors, $\mathbf{N}^{\nabla}$ and $\mathbf{M}^{\nabla}$ are the objective derivatives of the stress resultant and stress moment. The principle of objectivity is to ensure that certain quantities are the same for all observers, regardless of the reference frame. For different types of quantities (scalar, vector, and tensor), the objectivity is as follows:

- The objectivity of a scalar:

For a scalar quantity, expressed as f in the configuration X, and f^* in the configuration x. The scalar can be seen as objectivity if they keep the following the relation:

$$f^* = f$$

The objectivity scalar quantities includes: mass, temperature, displacement.

- The objectivity of a vector

For a vector physical quantity, expressed as **u** in the configuration X, and **u*** in the configuration x, the vector can be seen as objectivity if they can be transformed as follow:

$$\mathbf{u}^{*} = \mathbf{Q} \cdot \mathbf{u}$$

Here **Q** is the transformation matrix.

- The objectivity of a second-order tensor

For a second-order tensor which is the considered in the hypoelastic laws, expressed as **C** in the configuration X, and **C*** in the configuration x, the tensor can be seen as objectivity if they can be transformed as follow:

$$\mathbf{C}^{*} = \mathbf{Q} \cdot \mathbf{C} \cdot \mathbf{Q}^{T}$$

The objective derivative is the time derivative for an observer fixed to the material which aims to remove the influence of the rigid body rotations in the deformation analysis. There are several approaches to achieve the objective derivative. Due to the simplicity, the rotational objective derivatives that the time derivative is made in a rotating frame are most used. In the commercial software Abaqus, there are only two types of objective rate: Jaumann (derivative in the co-rotational frame) [Dafalias, 1983] and Green Naghdi (derivative in the basis rotated by the polar rotation) [Dienes, 1979]. The objective rate used in Abaqus different modules is listed in Table 2.1.

The draping of the textile composite can be seen as a quasi-static process. To apply the highly nonlinear contact algorithm for the contact between plies in the multilayers forming to get the convergence results, the proposed simulation approach is implemented in Abaqus/Explicit modules, and the subroutine VUGENS is adopted to realize the hypoelastic constitutive equations. The explicit algorithm can also reduce the amount of calculation and improve the calculation speed at the same time. In Table 2.1, it can be know from that the Green-Naghdi frame is initial adopted to calculate the objective derivative. However, the Green-Naghdi frame cannot be directly used for the deformation of textile composite. A simple shear test is conducted in Abaqus/Explicit as shown in Fig. 2.6, the warp and weft yarns are assumed to be parallel to the element edge in the initial edge, and it will keep parallel to the edge when the element are under simple shear. On the one hand, it the can be known that the warp and weft yarn won't keep perpendicular to each other when the element is deformed, and the Green-Naghdi frame keeps as an orthogonal frames. On the other hand, the two axes of the Green-Naghdi frame are not parallel to any one of the yarns. The textile composite material behavior is highly dependent on the yarn direction, thus Green-

Naghdi rotation frame cannot be used for the calculation of objective derivate of the stress resultants and moment that the values are dependent on the yarn direction. Previous research has indicated that most appropriate rotation is the fiber for the objective derivative[Boisse et al., 2005; Badel, Vidal-Sallé, & Boisse, 2008]. The process to calculate the stress resultants and stress moments will be introduce in the following.

Table 2.1. The objective rate used in Abaqus different modules [SIMULIA, 2019]

Solver	Element type	Constitutive model	Objective rate
Abaqus/Standard	Solid (Continuum)	All built-in user-defined materials	Jaumann
	Structural (Shells, Membranes, Beam, Trusses)	All built-in user-defined materials	Green-Naghdi
Abaqus/Explicit	Solid (Continuum)	All except viscoelastic, brittle cracking, and VUMAT	Jaumann
	Solid (Continuum)	viscoelastic, brittle cracking, and VUMAT	Green-Naghdi
	Structural (Shells, Membranes, Beam, Trusses)	All built-in user-defined materials	Green-Naghdi

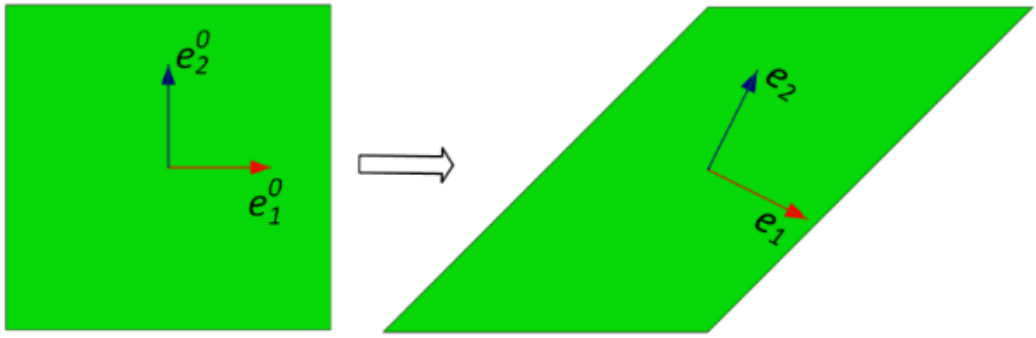

Fig. 2.6. Green-Naghdi frame rotation in a simple shear test (Abaqus/Explicit result).

In the used subroutine of ABAQUS/explicit code, the input and output quantities are expressed on the Green Naghdi basis e(e_1,e_2) which is obtained during deformation by the polar rotation R, defined by the polar decomposition of the defamation gradient F=RU.

$$\mathbf{e}_\alpha = \mathbf{R} \cdot \mathbf{e}_\alpha^0 \tag{2.6}$$

The initial orthogonal basis $(\mathbf{e}_1^0, \mathbf{e}_2^0)$ coincides with the initial directions of the warp and weft fibers $(\mathbf{f}_1^0, \mathbf{f}_2^0)$. Fiber directions are given by the deformation gradient during the deformation.

$$\mathbf{f}_\alpha = \frac{\mathbf{F}\cdot\mathbf{f}_\alpha^0}{\left\|\mathbf{F}\cdot\mathbf{f}_\alpha^0\right\|} = \frac{\mathbf{F}\cdot\mathbf{e}_\alpha^0}{\left\|\mathbf{F}\cdot\mathbf{e}_\alpha^0\right\|} \tag{2.7}$$

Two orthonormal bases are defined from the direction of the fibers: one basis directed by the warp fiber direction $\mathrm{g}(\mathbf{g}_1, \mathbf{g}_2)$ with $\mathbf{g}_1 = \mathbf{f}_1$ and the other directed by the weft fiber direction $\mathrm{h}(\mathbf{h}_1, \mathbf{h}_2)$ with $\mathbf{h}_2 = \mathbf{f}_2$ (Fig. 2.7).

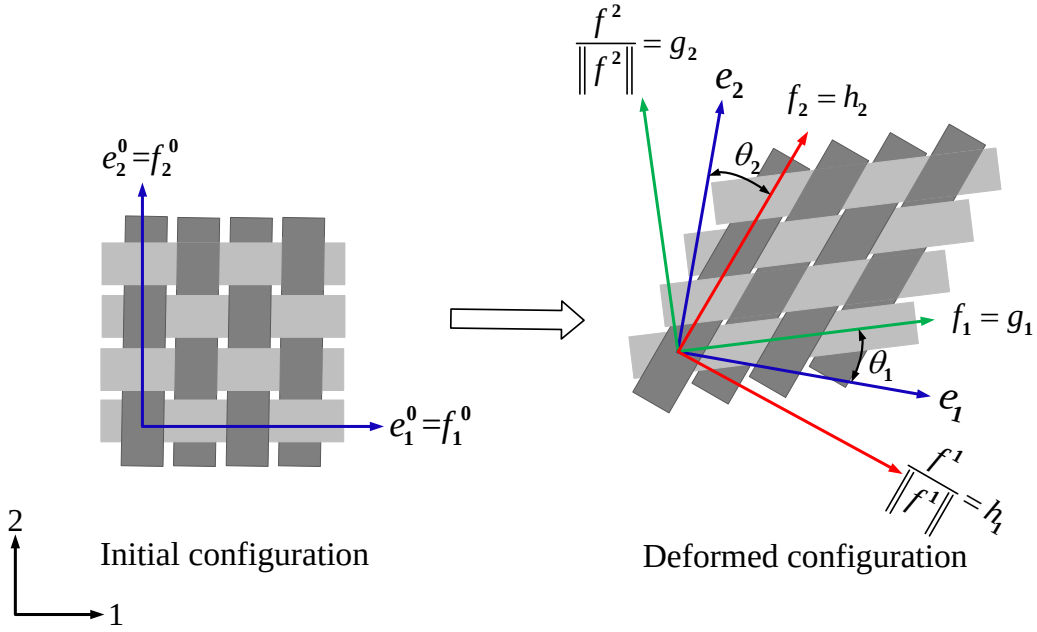

Fig. 2.7. Orthonormal frames in the fiber direction and the Green Naghdi frame.

Let θ_α be the angle between Green Naghdi axes and the two yarn axes, its values can be calculated when the Green Naghdi axes and the two yarns axes are determined using eqs (2.6)-(2.7):

$$\theta_\alpha = \arccos\left(\frac{\mathbf{e}_\alpha\cdot\mathbf{f}_\alpha}{\|\mathbf{e}_\alpha\|\cdot\|\mathbf{f}_\alpha\|}\right) \tag{2.8}$$

Then the transform matrix between Green Naghdi frame e and the two yarn frames g, h can be obtained:

$$[T_\alpha] = \begin{bmatrix} \cos\theta_\alpha & -\sin\theta_\alpha \\ \sin\theta_\alpha & \cos\theta_\alpha \end{bmatrix} \tag{2.9}$$

For the time increment $[t_n, t_{n+1}]$, the components of the membrane deformation increment and the curvature increment are given on the Green Naghdi basis:

$$\mathbf{d\varepsilon} = d\varepsilon_{\alpha\beta}^{GN}\mathbf{e}_\alpha \otimes \mathbf{e}_\beta \qquad \mathbf{d\chi} = d\chi_{\alpha\beta}^{GN}\mathbf{e}_\alpha \otimes \mathbf{e}_\beta \tag{2.10}$$

Through tensor transformation, the components of the membrane and curvature tensors on the bases of g and h can be deduced from:

$$\begin{aligned} \left[d\varepsilon\right]_g &= \left[T_1\right]^T \mathbf{d\varepsilon}\left[T_1\right] \quad \left[d\varepsilon\right]_h = \left[T_2\right]^T \mathbf{d\varepsilon}\left[T_2\right] \\ \left[d\chi\right]_g &= \left[T_1\right]^T \mathbf{d\chi}\left[T_1\right] \quad \left[d\chi\right]_h = \left[T_2\right]^T \mathbf{d\chi}\left[T_2\right] \end{aligned} \tag{2.11}$$

According to these obtained increments of membrane and curvatures tensors, the material constitutive equation will be used here to calculate the components of the stress resultant and stress moment on the bases of g and h.

$$\begin{aligned} \left[dN\right]_g &= \left[C\right]_g\left[d\varepsilon\right]_g \quad \left[dN\right]_h = \left[C\right]_h\left[d\varepsilon\right]_h \\ \left[dM\right]_g &= \left[D\right]_g\left[d\chi\right]_g \quad \left[dM\right]_h = \left[D\right]_h\left[d\chi\right]_h \end{aligned} \tag{2.12}$$

Three material behaviors at the macroscale (tensile stiffness, in-plane shear stiffness and out of plane bending stiffness) will be considered here, which play a main role in the material deformation. Then the Eq.(2.12) can be explicitly written as:

$$\begin{aligned} \begin{bmatrix} dN_{11} \\ dN_{22} \\ dN_{12} \end{bmatrix}_g &= \begin{bmatrix} C_{11} & 0 & 0 \\ 0 & 0 & 0 \\ 0 & 0 & C_{12} \end{bmatrix}_g \begin{bmatrix} d\varepsilon_{11} \\ d\varepsilon_{22} \\ d\varepsilon_{12} \end{bmatrix}_g \qquad \begin{bmatrix} dN_{11} \\ dN_{22} \\ dN_{12} \end{bmatrix}_h = \begin{bmatrix} 0 & 0 & 0 \\ 0 & C_{22} & 0 \\ 0 & 0 & C_{12} \end{bmatrix}_h \begin{bmatrix} d\varepsilon_{11} \\ d\varepsilon_{22} \\ d\varepsilon_{12} \end{bmatrix}_h \\ \begin{bmatrix} dM_{11} \\ dM_{22} \\ dM_{12} \end{bmatrix}_g &= \begin{bmatrix} D_{11} & 0 & 0 \\ 0 & 0 & 0 \\ 0 & 0 & D_{12} \end{bmatrix}_{g_1} \begin{bmatrix} d\chi_{11} \\ d\chi_{22} \\ d\chi_{12} \end{bmatrix}_{g_1} \qquad \begin{bmatrix} dM_{11} \\ dM_{22} \\ dM_{12} \end{bmatrix}_h = \begin{bmatrix} 0 & 0 & 0 \\ 0 & D_{22} & 0 \\ 0 & 0 & D_{12} \end{bmatrix}_h \begin{bmatrix} d\chi_{11} \\ d\chi_{22} \\ d\chi_{12} \end{bmatrix}_h \end{aligned} \tag{2.13}$$

Here, C_{11}, C_{22} are the tensile stiffness in the warp and weft directions respectively, C_{12} is the in-plane shear stiffness, D_{11}, D_{22} are the out of plane bending stiffness in the warp and weft directions and D_{12} is the cross term of bending stiffness (D_{12} is set as zero in the consitutive equations, which assumes that the bending stiffness of the woven reinforcement is given by that of the yarns in the waro direciton as well as the weft direciton. In the other aspects, this is aso because of the difficulty in the measuring the cross bending stiffness). These stiffnesses are not necessarily constant, they can be linear or non-linear, especially C_{12} depends on the in-plane shear which is experimental measured as non-linear for textile composites.

In the simulation step time [t_n , t_{n+1}], the stress resultants and stress moment are cumulated following the Hughes and Winget scheme [Hughes & Winget, 1980; Badel, Vidal-Sallé, & Boisse, 2008]:

$$\begin{aligned} \left[N\right]_g^{n+1} &= \left[N\right]_g^n + \left[dN\right]_g^{n+1/2} \qquad \left[N\right]_h^{n+1} = \left[N\right]_h^n + \left[dN\right]_h^{n+1/2} \\ \left[M\right]_g^{n+1} &= \left[M\right]_g^n + \left[dM\right]_g^{n+1/2} \qquad \left[M\right]_h^{n+1} = \left[M\right]_h^n + \left[dM\right]_h^{n+1/2} \end{aligned} \tag{2.14}$$

Then the stress resultants and stress moment on the Green Naghdi base *e* can be obtained by adding those in the basis g and h after transformation: (*n*+1 index is omitted, all the quantities are at t_{n+1})

$$\begin{aligned} \left[N\right]_e &= \left[T_1\right]\left[N\right]_g\left[T_1\right]^T + \left[T_2\right]\left[N\right]_h\left[T_2\right]^T \\ \left[M\right]_e &= \left[T_1\right]\left[M\right]_g\left[T_1\right]^T + \left[T_2\right]\left[M\right]_h\left[T_2\right]^T \end{aligned} \tag{2.15}$$

2.3 Elementary test

The elementary tests are simple, but very meaningful. Elementary tests can reflect if the calculation is right at the element level, and can be easily checked with the theoretical value. Thus elementary tests are conducted to validate the presented approach. A single four-node shell element was selected to conduct the analyses. As shown in Fig. 2.8, the initial element geometry was a square with an initial length l_0, the yarn directions were parallel to the element edges. Three types of elementary tests, listed below, were carried out and compared with the theoretical result.

(a). 45° simple shear test after the traction along the yarn direction f_1 (Fig. 2.8a)
(b). Rigid body rotation test after the traction along the yarn direction f_1 (Fig. 2.8b)
(c). Pure bending test (Fig. 2.8c)

In elementary tests (a) and (b), the tensile stiffness in the two yarn directions was $C_{12} = C_{22} = 1000$ N·mm^{-1}, and the other material stiffnesses were equal to zero. In the elementary test (c), the membrane stiffness was identical to that in the prior two element tests and the bending stiffness D_{11} along the yarn direction f_1 was 10 N·mm. The theoretical output values of the strain and the stress resultants for the three types of elementary tests are listed in Table 2.2.

The elementary tests (a) and (b) were two-step simulations. In the first step of these two elementary tests, they generated the strain and the resultant force only along the yarn direction f_1. In the second step of test (a), the element was subjected to a stretch deformation in the yarn direction f_2 while the deformation in the yarn direction f_1 remained unchanged. The objective of this step was to show that the deformation in one fiber direction did not affect the other. In the second step of test (b), the element was subjected to a rigid body rotation, and the strain and

resultant force were supposed to remain unchanged which would show the objectivity of the computation (the rigid body rotation should not lead to spurious stress resultants).

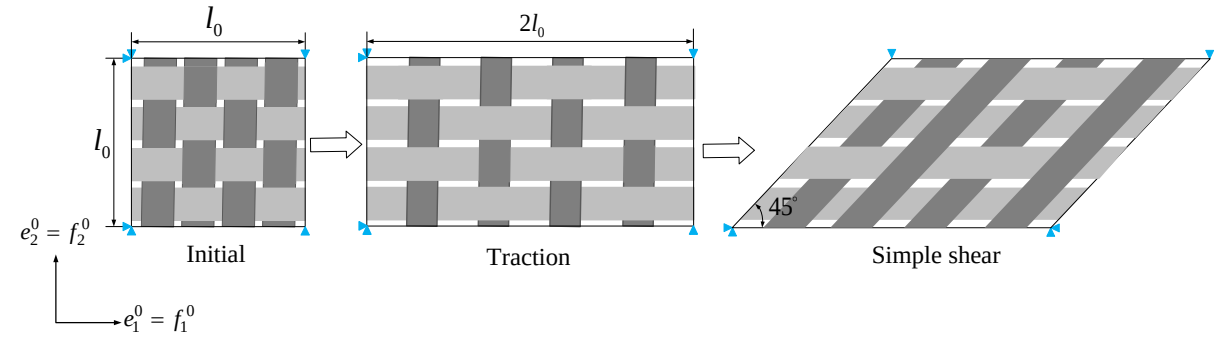

(a)

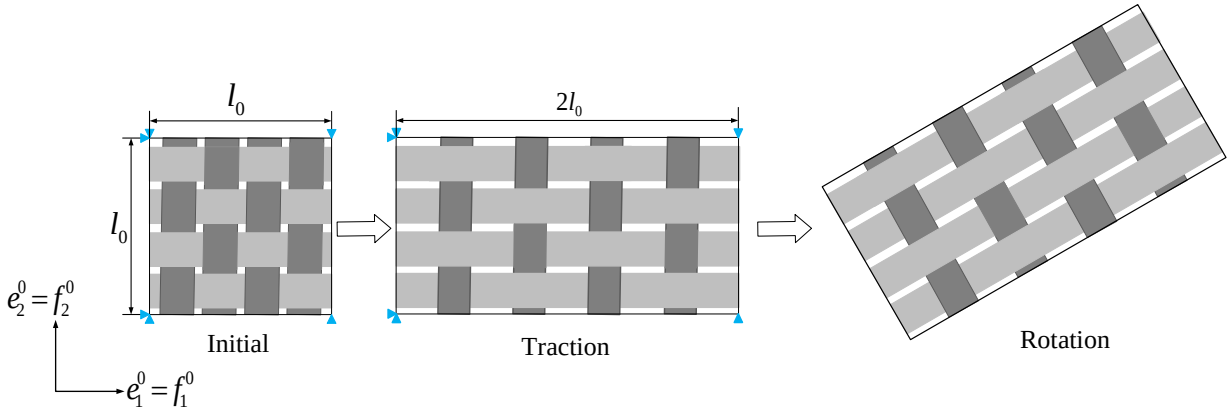

(b)

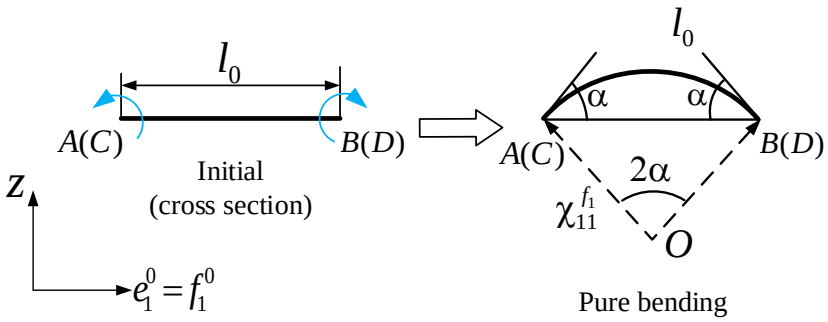

(c)

Fig. 2.8. Schematic of boundary conditions applied to the three elementary tests. (a) 45° simple shear test after a traction ratio 2. (b) Rigid body rotation test after a traction ratio 2. (c) Pure bending test.

The elementary test (c) was a single-step simulation. The two edges AC and BD of the element were subjected to a rotation, thus the element should have a uniform bending along the

yarn direction f_1, and the rotation angle was set as $\alpha = \frac{1}{2l_0}$. The objective of this test (c) was to show that the bending moment would be obtained according to the yarn curvature and the introduced hypoelastic laws, thus indicating that the element's bending behavior was well decoupled from that of the membrane.

These three elementary simulation tests were performed using the presented stress resultant shell approach, and the numerical simulations gave rise to the expected theoretical results in all cases.

Table 2.2. Theoretical value of the elementary test

		Strain output	Stress resultant output
Simple shear test after the traction	First step	$\boldsymbol{\varepsilon}^f = \begin{bmatrix} \varepsilon_{11} \\ \varepsilon_{22} \\ \varepsilon_{12} \end{bmatrix}^f = \begin{bmatrix} 0.693 \\ 0 \\ 0 \end{bmatrix}$	$\mathbf{N}^f = \begin{bmatrix} N_{11} \\ N_{22} \\ N_{12} \end{bmatrix}^f = \begin{bmatrix} 693 \\ 0 \\ 0 \end{bmatrix}$
	Second step	$\boldsymbol{\varepsilon}^f = \begin{bmatrix} \varepsilon_{11} \\ \varepsilon_{22} \\ \varepsilon_{12} \end{bmatrix}^f = \begin{bmatrix} 0.693 \\ 0.347 \\ 0.785 \end{bmatrix}$	$\mathbf{N}^f = \begin{bmatrix} N_{11} \\ N_{22} \\ N_{12} \end{bmatrix}^f = \begin{bmatrix} 693 \\ 347 \\ 0 \end{bmatrix}$
Rigid body rotation test after the traction	First step	$\boldsymbol{\varepsilon}^f = \begin{bmatrix} \varepsilon_{11} \\ \varepsilon_{22} \\ \varepsilon_{12} \end{bmatrix}^f = \begin{bmatrix} 0.693 \\ 0 \\ 0 \end{bmatrix}$	$\mathbf{N}^f = \begin{bmatrix} N_{11} \\ N_{22} \\ N_{12} \end{bmatrix}^f = \begin{bmatrix} 693 \\ 0 \\ 0 \end{bmatrix}$
	Second step	$\boldsymbol{\varepsilon}^f = \begin{bmatrix} \varepsilon_{11} \\ \varepsilon_{22} \\ \varepsilon_{12} \end{bmatrix}^f = \begin{bmatrix} 0.693 \\ 0 \\ 0 \end{bmatrix}$	$\mathbf{N}^f = \begin{bmatrix} N_{11} \\ N_{22} \\ N_{12} \end{bmatrix}^f = \begin{bmatrix} 693 \\ 0 \\ 0 \end{bmatrix}$
Pure bending		$\boldsymbol{\chi}^f = \begin{bmatrix} \chi_{11} \\ \chi_{22} \\ \chi_{12} \end{bmatrix}^f = \begin{bmatrix} 1 \\ 0 \\ 0 \end{bmatrix}$	$\mathbf{M}^f = \begin{bmatrix} M_{11} \\ M_{22} \\ M_{12} \end{bmatrix}^f = \begin{bmatrix} 10 \\ 0 \\ 0 \end{bmatrix}$

2.4 The characterization of the mechanical behavior of the textile composites

In the presented hypoelastic approach, the deformation in the thickness is neglected, and the simulation only concern the deformation on the middle plane. The decoupled of bending behavior with the membrane behavior is achieved through introducing an independent bending stiffness.

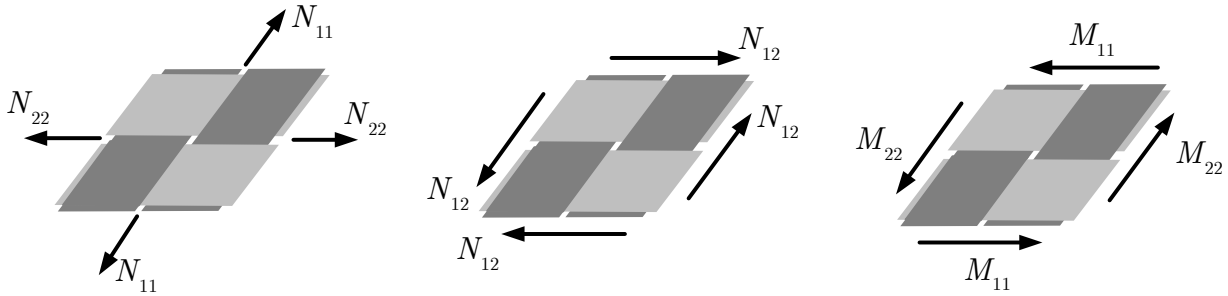

(a) (b) (c)

Fig. 2.9. Stress resultants and moment on a woven unit cell (a) Tensions (b) In-plane shear (c) Bending

According to the Eq.(2.13), to make the simulation of textile composites using the presented hypoelastic approach introduced in this chapter, it is needed to measure there material behavior which are tensile stiffness C_{11}, C_{22} in the warp and weft directions, in-plane shear stiffness C_{12} and the out of plane bending stiffness D_{11}, D_{22} in the warp and weft directions. Corresponding to these material stiffness, the stress resultants and moment on a woven unit cell are given in Fig. 2.9. The way to measure these material stiffness will be introduced in the below.

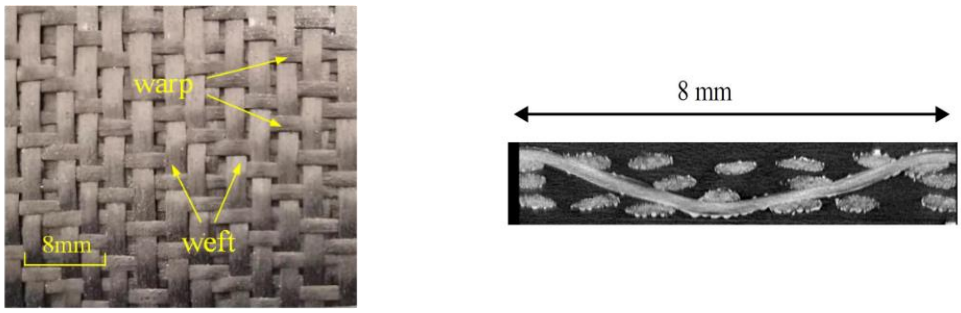

(a) (b)

Fig. 2.10. The interlock fabric G1151 (a) The warp and weft yarn (b) the X-ray Tomography [Badel, Vidal-Sallé, Maire, et al., 2008]

Table 2.3. Geometric characteristics of the G1151 interlock fabric

Areal density	Single layer thickness	Warp yarn width	Weft yarn width	Warp yarn density	Weft yarn density
630 g/m^2	1.3 mm	1.92 mm	2.21 mm	0.75 yarns/mm	0.74 yarns/mm

The interlock fabric G1151® is the main researched material in my research work. This G1151 material (shown in Fig. 2.10) is manufactured by Hexcel Company, the geometric

parameters of the textile reinforcements are listed in Table 2.3. The material behaviors of the interlock fabric will be measured accordingly.

2.4.1 Tensile behavior

The tensile behavior of woven material can be measured by the uniaxial or biaxial tensile test. The schematic diagram of biaxial tensile test is shown in

Fig. 2.11. The warp and weft yarns of the woven material are clamped by two bars respectively. Under the machine external load, the material will be subjected to a tensile deformation in the two yarns direction. The coupling of the tensile behavior between warp and weft yarn can be considered in the biaxial tensile test [Kawabata et al., 1973; Buet-Gautier & Boisse, 2001; Willems et al., 2008; Carvelli et al., 2008]. However, the coupling in tensile between warp and weft yarn does not play a major role in the material deformation in the macroscale.

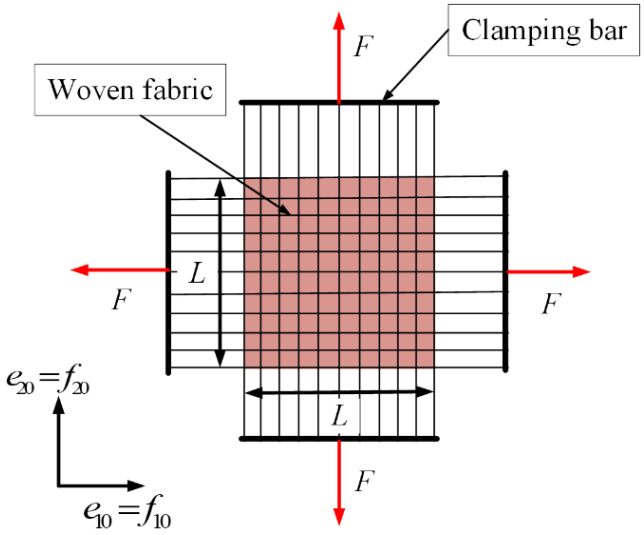

Fig. 2.11. Biaxial tensile test

Due to the specific material behavior of the woven material, the tensile stiffness in the warp and warp yarn direction C_{11}, C_{22} is much larger than the other two types of material stiffness. The material can be considered as quasi-insensible in the yarn direction. Actually the tensile strain in the yarn direction is also first variable to check whether the simulation of woven material is correct (the tensile strain should be small than 10^{-3}). In the presented research work, a very large and constant tensile stiffness is chosen as input for the woven material considered in the presented simulation approach.

2.4.2 In-plane shear behavior

The in-plane shear deformation of woven textile composite is the relative rotation between the warp and weft yarns. The warp and weft yarn is initial perpendicular, and the in-plane

deformation is measured by the shear angel γ which is the rotation angle between warp and weft yarns. The relationship between the shear angle γ and the shear strain ε_{12} is:

$$d\gamma = 2d\varepsilon_{12} \tag{2.16}$$

The characterization of in-plane shear behavior of fibrous composite can be conducted by the picture frame test and bias-extension test[Lebrun et al., 2003; Harrison et al., 2004; Launay et al., 2008; Cao et al., 2008; Schirmaier et al., 2016; Poppe et al., 2018].

a) Picture frame test

In the picture frame test, the specimen is clamped in a square frame as shown in Fig. 2.12, and the warp and weft yarn are parallel to the side of the square frame in the initial configuration. The uniform shear deformation will occur in the specimen when the square frame is deformed into a rhombus under the external force *F* loaded on the opposite node of the frame [Lebrun et al., 2003; Harrison et al., 2004; Lomov et al., 2006; Hosseini et al., 2018].

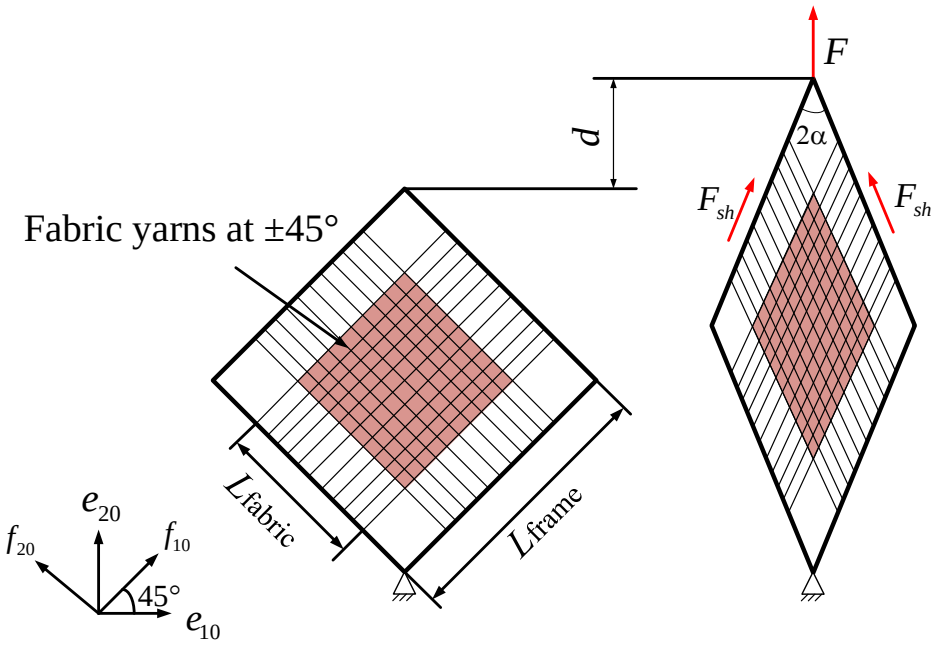

Fig. 2.12. The picture frame test

The shear angle γ can be theoretically calculated as:

$$\gamma = \frac{\pi}{2} - 2\alpha = \frac{\pi}{2} - 2\cos^{-1}\left(\frac{\sqrt{2}L_{\text{frame}} + d}{2L_{\text{frame}}}\right) \tag{2.17}$$

Here, L_{frame} is the side length of the frame, *d* is the relative displacement of the opposite node, and α is the half of the angle between the frame two adjacent sides.

The external machine force F is recorded by the load senor in the experiment, the stress resultant N_{12} (units: N/mm) on the specimen can be obtained by:

$$N_{12} = \frac{F_{sh}}{L_{\text{fabric}}} = \frac{F}{2L_{\text{fabric}}\cos\alpha} = \frac{F}{2L_{\text{fabric}}\cos(\frac{\pi}{4} - \frac{\gamma}{2})} \tag{2.18}$$

Here, F_{sh} is the shear force applied on the specimen, L_{fabric} is the side length of the specimen. Combining formulas(2.17)-(2.18), the in-plane shear stiffness C_{12} can be determined, and the expression of C_{12} can be approximated by a polynomial (shown in(2.19)).

$$dN_{12} = C_{12}d\gamma \qquad C_{12} = K_0 + K_1|\gamma| + K_2|\gamma|^2 + K_3|\gamma|^3 + K_4|\gamma|^4 \quad (\gamma = 2\varepsilon_{12}) \tag{2.19}$$

b) Bias extension test

For woven materials, the boundary condition need to be carefully controlled in the picture frame test. It is required that the warp and weft yarns are strictly parallel to the sides of the square frame. Otherwise, the additional tensile force along the yarn direction will be generated when the frame is deformed in the experiment which will cause the measured value of C_{12} is larger than the actual in-plane shear stiffness of the specimen [Launay et al., 2008].Compared with the picture frame, the additional tensile force can be avoided in the bias extension test.

In the bias extension test, the rectangular specimen is clamped at the two ends, and the warp and weft yarns are at ±45° of the stretched direction. Based on the following assumptions：

(1). The relative slippage between the warp and weft yarns is neglected.
(2). The yarns are considered as quasi-inextensibility.

The specimen can be divided into three different zones according to the shear deformation as shown in Fig. 2.13. In the zone C, the material will subjected to a uniform shear deformation. And there will has no stretch deformation due to the two ends of yarns are free. The shear angle in zone B will be half of the angle in zone C, and the shear angle will be zero in zone A. The bias extension test mainly concern the shear angle in zone C to measure the specimen in-plane behavior. When the specimen is stretched from the initial length L to the deformed length $L+d$, the theoretical shear angle γ in zone C can be calculated as:

$$\gamma = \frac{\pi}{2} - 2\cos^{-1}(\frac{D+d}{\sqrt{2}D}) \tag{2.20}$$

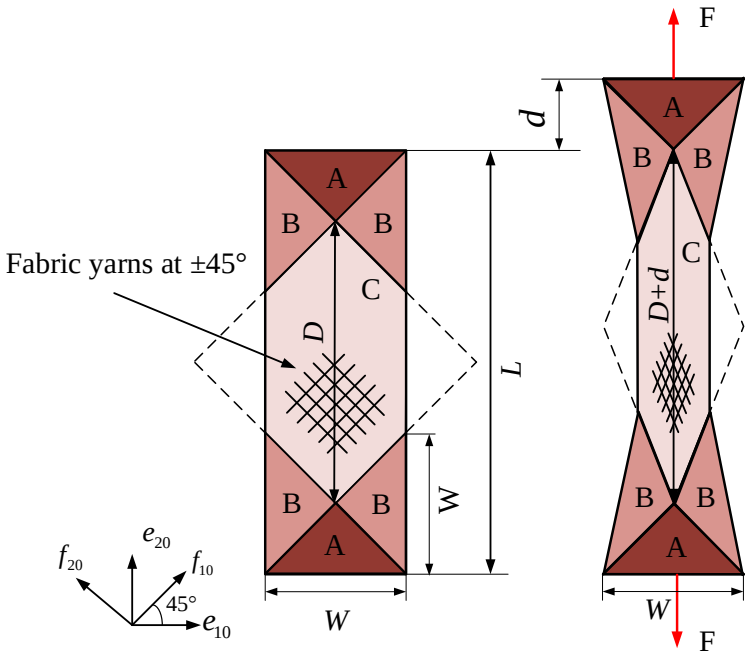

Fig. 2.13. The bias extension test

Based on the energy conservation, the machine external load F will transformed into the internal shear energy, and the expression resultant shear force N_{12} will be obtained as followed:

$$N_{12}(\gamma)=\frac{1}{(2L-3W)\cos\gamma}\left(\left(\frac{L}{W}-1\right)F\left(\cos\frac{\gamma}{2}-\sin\frac{\gamma}{2}\right)-W\,N_{12}\left(\frac{\gamma}{2}\right)\cos\frac{\gamma}{2}\right) \tag{2.21}$$

The Eq.(2.21) is an iterative relation, it cannot be used directly for the calculation of the resultant shear force N_{12}. A further iterative program is needed the obtain the polynomial curve of $N_{12}(\gamma)$. The expression of the in-plane shear C_{12} can be obtained by taking the derivative of the polynomial of $N_{12}(\gamma)$.

c) The in-plane shear behavior test of G1151

The bias extension test is preformed to measure the in-plane shear behavior test of G1151. In order to verify the membrane response of the presented stress-resultant approach, the bias extension simulation will be conducted using the tested shear behavior, and then make comparison with experimental and theoretical data.

The experimental figure is shown in Fig. 2.14(a). The length of the specimen L is 210 mm and the width W is 70 mm. The load-displacement curve recorded by the load sensor is presented in Fig. 2.14(b). According to Eq.(2.21), an iterative program is coded in Matlab software, and the in-plane shear behavior C_{12} (unit: N/mm) of G1151 can be obtained as a polynomial:

$$C_{12} = 0.09 - 0.83|\gamma| + 2.92|\gamma|^2 - 4.01|\gamma|^3 + 2.03|\gamma|^4 \quad (2.22)$$

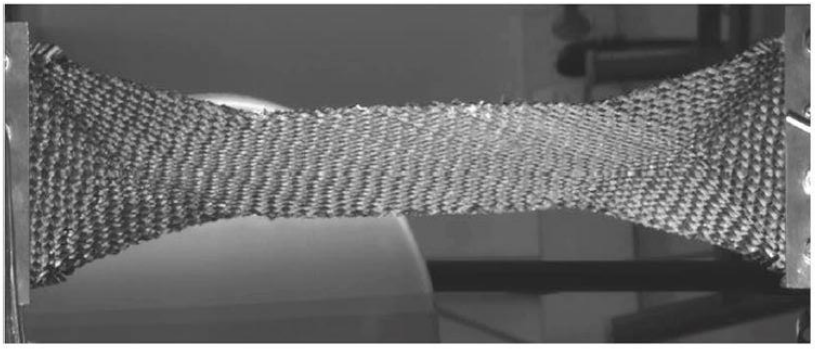

(a)

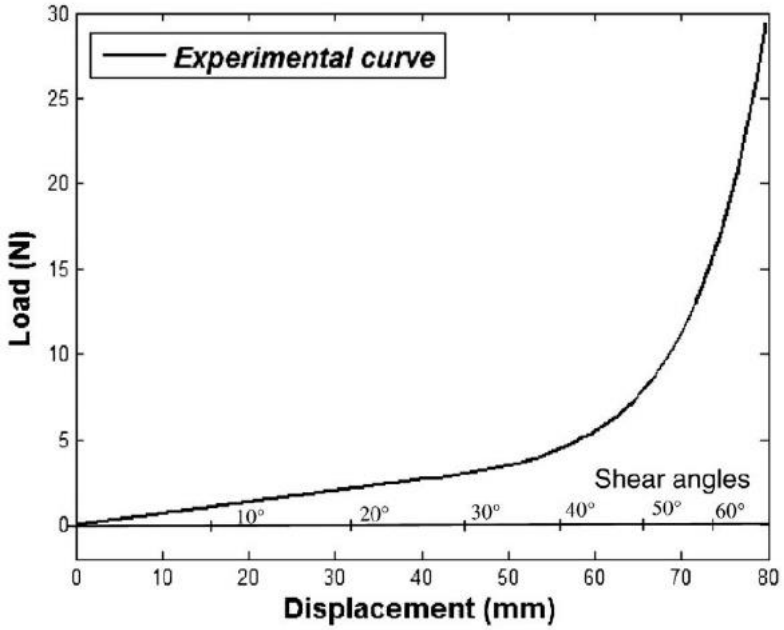

(b)

Fig. 2.14. Bias extension test of G1151. (a) The experimental deformation. (b) The experiment result of load-displacement.

Next the bias extension simulation is conducted, the geometry setting and boundary conditions is same with the experiment. A general-purpose 3D triangle shell element (S3) in Abaqus is selected to conduct the analyses. 4800 elements are chosen to mesh the specimen, the yarn tensile modulus is C_{11}=C_{22}=1000 N/mm, the shear behavior is Eq.(2.22), and the shell section transverse shear properties which are needed as input in Vugens subroutine are set as K_{11}=300 N/mm, K_{12}=0 N/mm, K_{22}=300 N/mm.

The shear angle at zone C and the machine load are selected as comparison variables between simulation and experiment. Fig. 2.15 lists the comparison result, it can be seen that the simulation

results have good agreement with the theoretical value and the experiment results which indicated that the presented approach can well predict the membrane behavior.

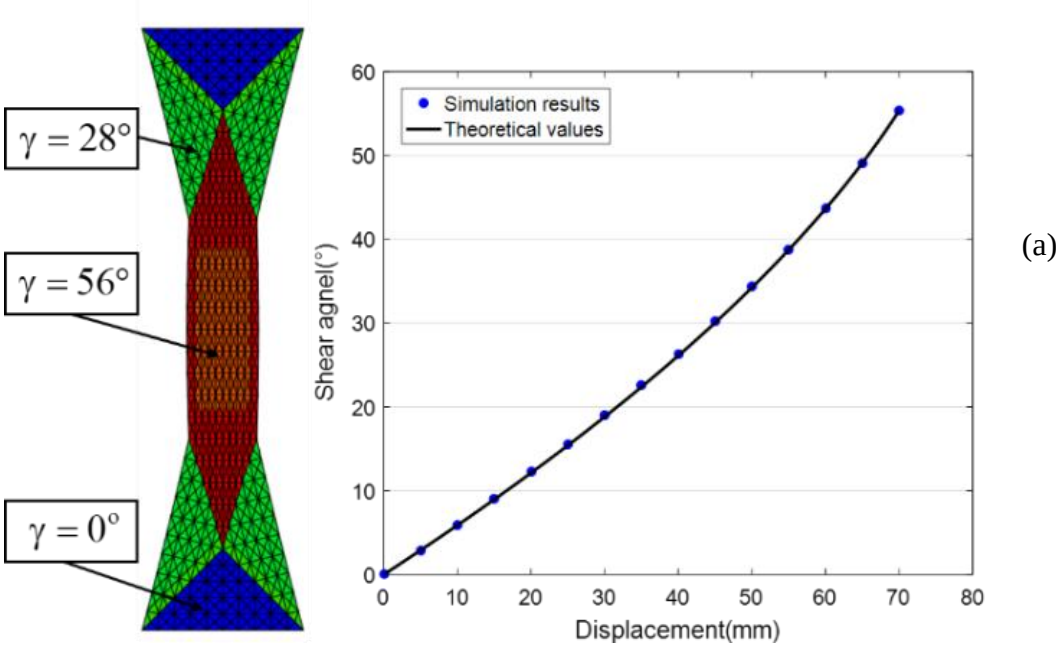

(a)

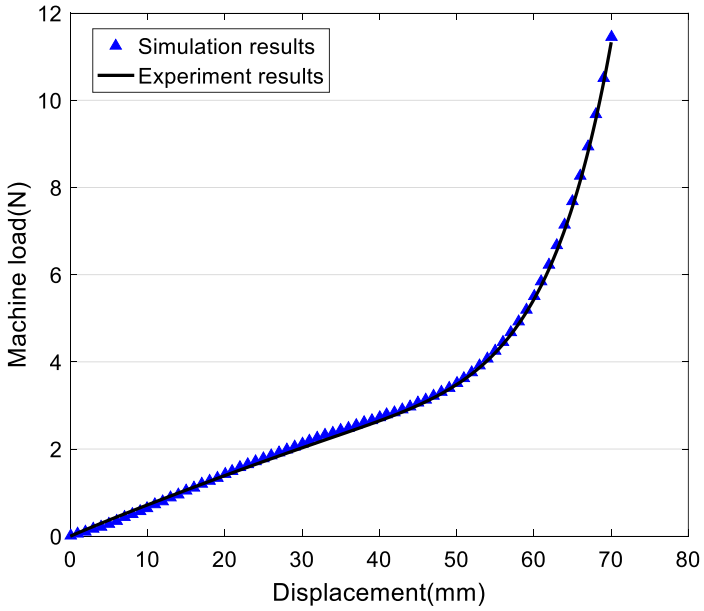

(b)

Fig. 2.15. In-plane shear behavior verification (a) Shear angle comparison (b) Machine load comparison

2.4.3 Bending behavior

For the woven material, the bending behavior is independent of the membrane behavior. The bending behavior can be measured by the cantilever test[ASTM, 2002; de Bilbao et al., 2010;

Syerko et al., 2012; Lammens et al., 2014; Alshahrani & Hojjati, 2017; Sachs & Akkerman, 2017; Boisse et al., 2018].

a) Cantilever test

A rectangular specimen will be used for the cantilever test. The warp and weft yarn will be parallel to the specimen sides. As shown in Fig. 2.16, one end of the specimen is fixed and the other end is free, thus the specimen will be subjected to the bending deformation along warp or weft yarn direction under gravity.

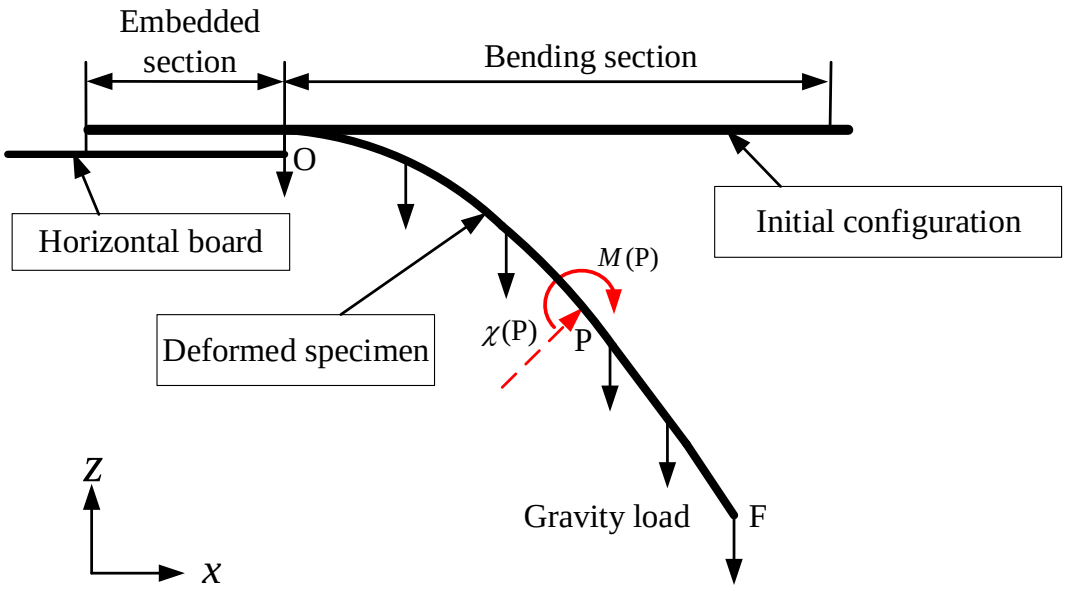

Fig. 2.16. Cantilever test under gravity

The bending deformation of the specimen will be recorded by camera. The bending section formula can be obtained through the image processing, and it can be expressed as polynomial. Set the section curve formula as $f(x)$, the curvature $\chi(x)$ (units: mm^{-1}) at different location will be:

$$\chi(x) = \frac{f'(x)}{\left[1+\left[f'(x)\right]^2\right]^{3/2}} \tag{2.23}$$

Here, x is the abscissa of any point P on the section curve.

The stress moment M (units: N) at point P is determined by the point location and the material density as follows:

$$M(s) = \int_s^L q(u-s)\cos(\phi(u))du \tag{2.24}$$

Here, *s* is the curvilinear coordinate of the point *P*, *q* is the areal weight of the specimen ($N \cdot mm^{-2}$) , *L* is the total bending section length, μ and ϕ are the Frenet's coordinates of the point from point *P* to the end point *F* .

By combing Eq.(2.23)-(2.24), the bending behavior $M_{\alpha\alpha}(\chi_{\alpha\alpha})$ will be determined, the cantilever test will be conducted in both warp and weft yarn directions (α=1, 2). The bending stiffness D_{11} and D_{22} will be obtained by taking derivative of the expression of $M_{\alpha\alpha}(\chi_{\alpha\alpha})$ as followed:

$$dM_{11} = D_{11} d\chi_{11} \qquad dM_{22} = D_{22} d\chi_{22} \tag{2.25}$$

b) The bending behavior test of G1151

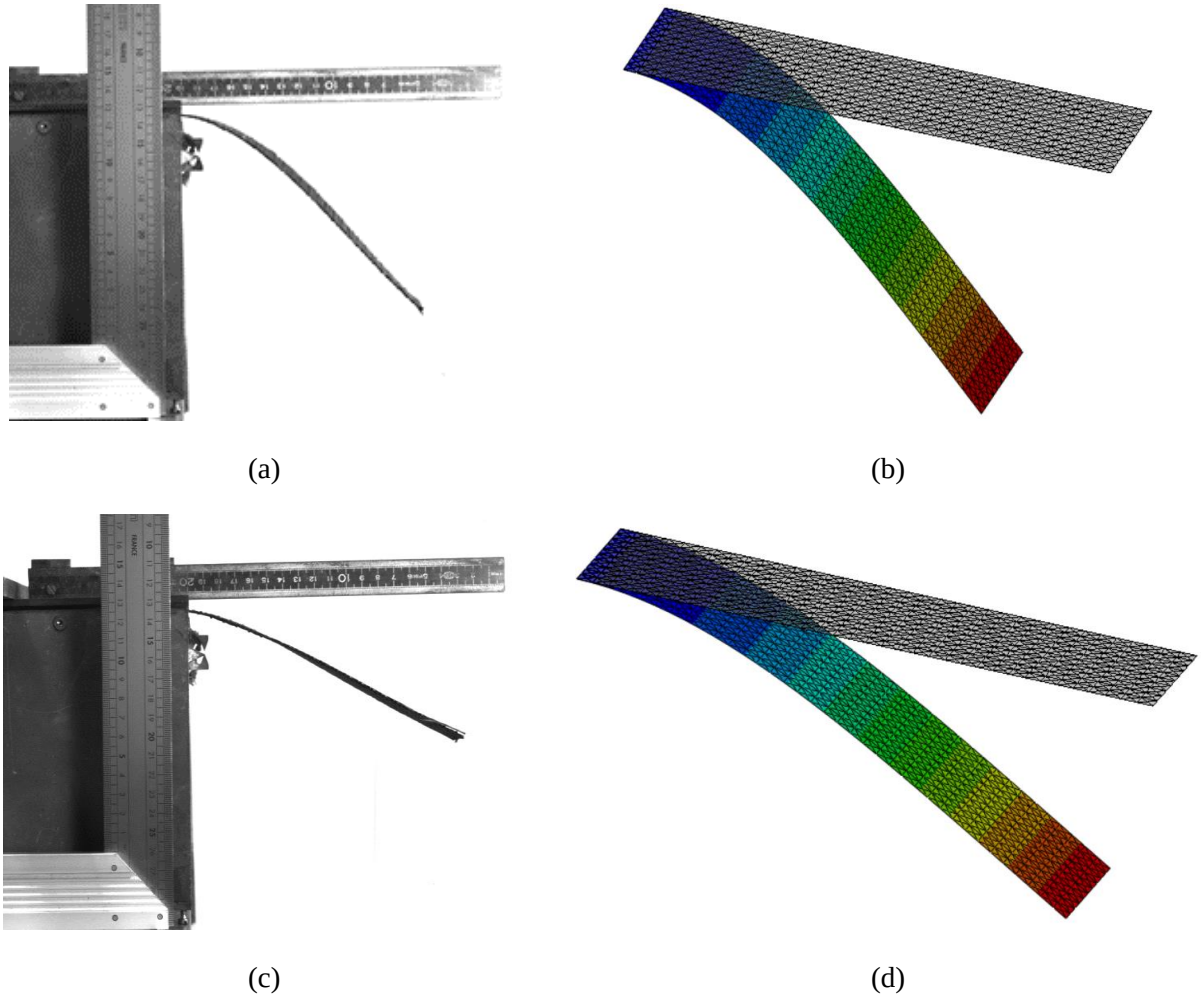

(a) (b)

(c) (d)

Fig. 2.17. Cantilever test of G1151 (a) Bending experiment along warp yarn (b) Bending simulation along warp yarn (c) Bending experiment along weft yarn (d) Bending simulation along weft yarn.

The cantilever bending experiments were conducted to obtain the bending behavior of G1151 material, and then the bending simulations using the obtained bending behavior were performed to verify the bending response of the presented approach.

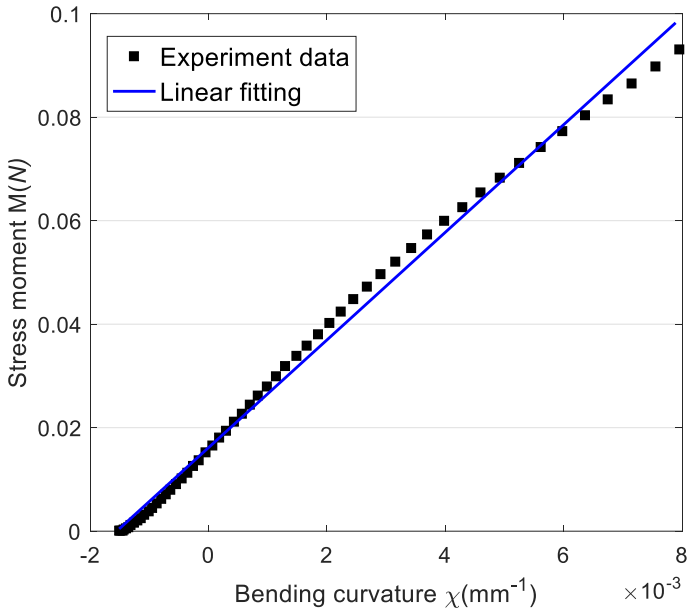

(a)

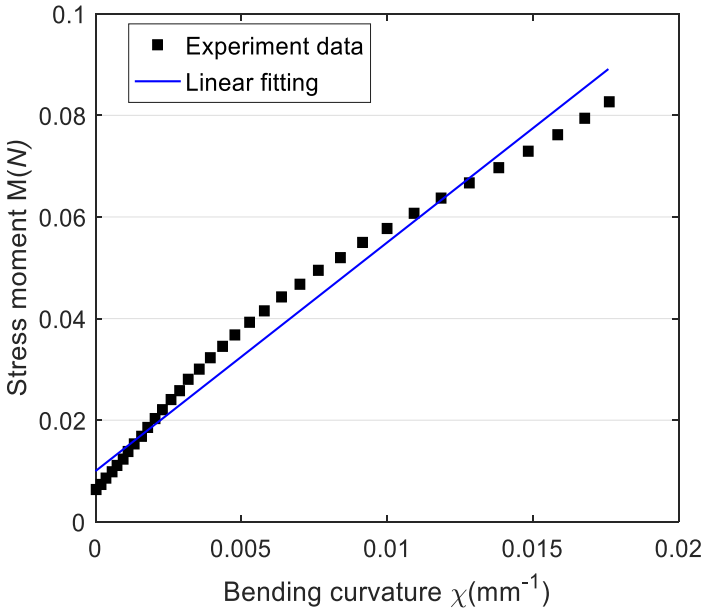

(b)

Fig. 2.18. The bending behavior of G1151. (a) Weft yarn direction. (b) Warp yarn direction.

In the cantilever experiment, the bending length is 180 mm and the width of the specimen is 50 mm. The specimen is bent under gravity in the length direction, and both the cantilever tests

along warp and weft yarn direction were conducted. The experimental bending section of the warp and weft are given in Fig. 2.17(a) and (c). The two rulers are used in the experiment to build the orthogonal coordinate system for the image processing.

Through the date processing according to Eqs.(2.23)-(2.24), the bending behavior $M_{\alpha\alpha}(\chi_{\alpha\alpha})$ is obtained in Fig. 2.18. It can be observed that the bending behavior which is related the stress moment *M* and bending curvature χ is almost linear. For simplify, the linear fitting is used to obtain the expression of the bending behavior, and the bending stiffness along weft and warp direction are given in (2.26) respectively. (Remarks: For simplicity to conduct the simulation, this difference is neglected and average bending stiffness is adopted in the numerical analysis.)

Note: the experimental data of the relationship between stress moment *M* and bending curvature χ didn't pass through the origin point (0, 0). This may be due to the initial curvature of the material when it is cut from the barrel.

$$D_{11} = 10.5\ \mathrm{N}\cdot\mathrm{mm} \qquad D_{22} = 4.3\ \mathrm{N}\cdot\mathrm{mm} \tag{2.26}$$

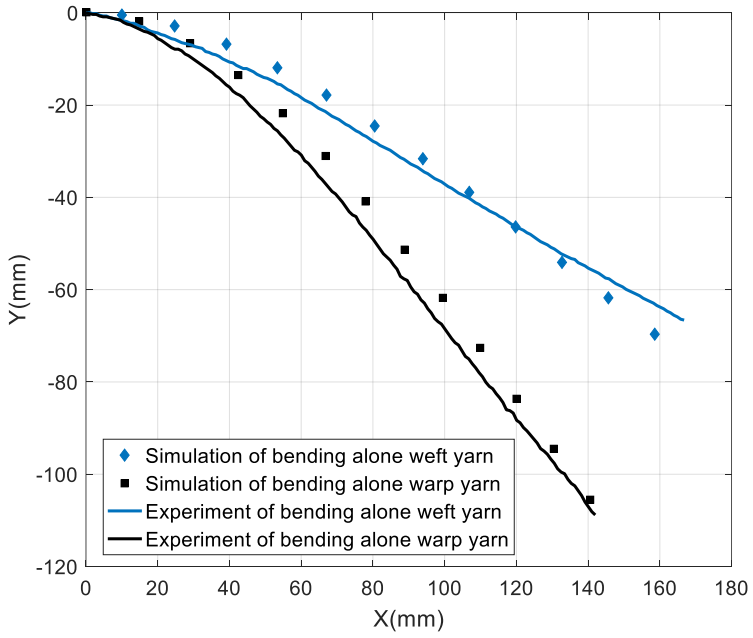

Fig. 2.19. The section comparison between simulation and experiment

Then the bending stiffness in (2.26) was used as input for the stress-resultant approach to perform the corresponding cantilever simulation test. The membrane behavior and mesh setting are same with bias extension test in section 2.4.2c). The cantilever section in the warp and weft yarn direction of the simulation results are given in Fig. 2.17(b) and (d) respectively. The section comparison between the experiment and simulation are shown in Fig. 2.19. The simulation result has a good agreement with the experiment. The bending response is correctly predicted by the

simulation which indicated that the presented approach well achieved the decoupling of bending behavior with membrane behavior.

2.5 Summary of Chapter 2

Due to the possible slippage between the fibers in woven material, the bending stiffness is much smaller than the values calculated from tensile stiffness and thickness. The bending stiffness plays an important role in the material deformation, thus the shell approach for modeling the woven material must take the special bending stiffness into consideration. A hypoelastic stress-resultant approach is presented in this chapter. A bending stiffness independent of membrane stiffness which is related to the stress moment with bending curvature is introduced in the approach. The stress-resultant approach makes it possible to consider the membrane and bending behavior separately. The approach is implemented in the Abaqus/VUGNES which is available for any user of this software.

Three material behaviors are considered in the approach which are the tensile, in-plane shear, and bending behavior, the material behavior is in hypoelastic form. The methods to determine these material behaviors for the presented approach are introduced in this chapter, and the different behavior of material G1151 is tested accordingly. In this process, the corresponding simulations using the presented approach are conducted to make a comparison with the experiment. The comparison result preliminary verified the correctness and effectiveness of the presented approach in the prediction of the woven material membrane and bending deformation.

Chapter 3 Numerical and experimental forming analysis of the textile composite

Numerical simulation plays a critical role in the textile composites forming, such as in the reducing the manufacturing cycle, manufacturing cost, and improving the manufacturing quality. Specific to the deformation mechanism, the hypoelastic stress resultant approach for the simulation of textile composite forming has been presented in Chapter 2. The approach considers the deformation of textile composite at macroscopic scale. Three material property (tensile, in-plane shear and out-of-plane bending) which plays a main role on the textile composite forming are considered in the proposed approach. The characterization of the material mechanical property was also introduced in Chapter 2. The approach are implemented in Abaqus subroutine VUGENS. The validation of the simulation approach has been preliminary conducted in the aspect of elementary test, in-plane shear response, and bending response respectively. The validation of simulation in forming process will be presented in this chapter. In the forming experiment, the three material property will influence the material deformation at same time. The comparison of experiment and simulation will verify the simulation approach more comprehensively.

Both hemisphere and tetrahedron forming are conducted, these two shapes are all benchmark shapes researched in the forming experiment [Allaoui et al., 2011, 2014; Komeili & Milani, 2016; Dörr et al., 2017; Thompson et al., 2020]. The forming experiments in this chapter include single layer with different yarn orientation, and multi layers with quasi-isotropic layer-up. Wrinkle is one of the main defect in the draping process of textile composites. In order to verify the ability of the approach in predicting wrinkle, hemisphere forming without blank holder is also conducted in this chapter. The corresponding simulation are performed using Abaqus with the presented approach in Chapter 2. The output variables in-plane shear angle, fabric deformed contour and material draw-in in different orientations are chosen to make comparison with experiment.

Chapter 3 Numerical and experimental forming analysis of the textile composite 71

3.1 The introduction of the experiment process 73

3.1.1 Forming experimental platform 73

3.1.2 Material preparation 74

3.2 Simulation settings 76

3.2.1 Simulation modeling 76

3.2.2 The tested material properties 79

3.3 Hemisphere forming 81
3.3.1 In-plane shear angle comparison 81
3.3.2 Fabric contour comparison 83
3.3.3 Punch force comparison 85
3.3.4 Wrinkles comparison in multi-layers forming 86
3.3.5 Wrinkles comparison during forming without blank-holder 87
3.4 Tetrahedron forming 92
3.4.1 In-plane shear angle comparison 93
3.4.2 Fabric contour comparison 95
3.5 The deformation in the thickness direction 96
3.5.1 The insufficient of Kirchhoff shell 96
3.5.2 The insufficient of Mindlin shell 97
3.5.3 The specific bending behavior of fibrous material 100
3.5.4 Comparison of different simulation approach 102
3.5.5 The post-processing method 106
3.5.6 Verification of the post processing 108
3.6 Summary of Chapter 3 110

3.1 The introduction of the experiment process

3.1.1 Forming experimental platform

The forming experiments are completed in LaMCoS laboratory. As shown in Fig. 3.1, the experimental platform mainly consist of the motion control system, camera, mirror, punch, blank holder, and die.

The motion control system included the universal testing machine (ZwichRoell 100KN), and TestXpertII software. The experimental set-up is placed on the universal testing machine, the motion part of the universal testing machine is controlled by the TestXpertII software, including motion speed (30 $mm \cdot min^{-1}$ for all types of draping process) and motion distance. In the experimental process, blank holder and die are connected with the base of the universal machine and will keep still. The punch will be connected with the moving part, and thus the material deforms under the motion of the punch. The blank holder and die are made transparent (made of methyl methacrylate (PMMA)) to observe the material deformation during the draping process. Two camera were used when in the multi-layers experiment (shown in Fig. 3.2). One is at top side which is directly perpendicular to the material in order to observe the deformation of top layer. And the other one camera is at bottom side to observe to the deformation of bottom layer. Since the space limitation, the bottom camera captures the photo through the reflection of the mirror, and the mirror plane is at 45° with the base. The camera is connected with Acquisition software (developed by LaMCoS). Through the software, the camera will capture the photo by setting frequency.

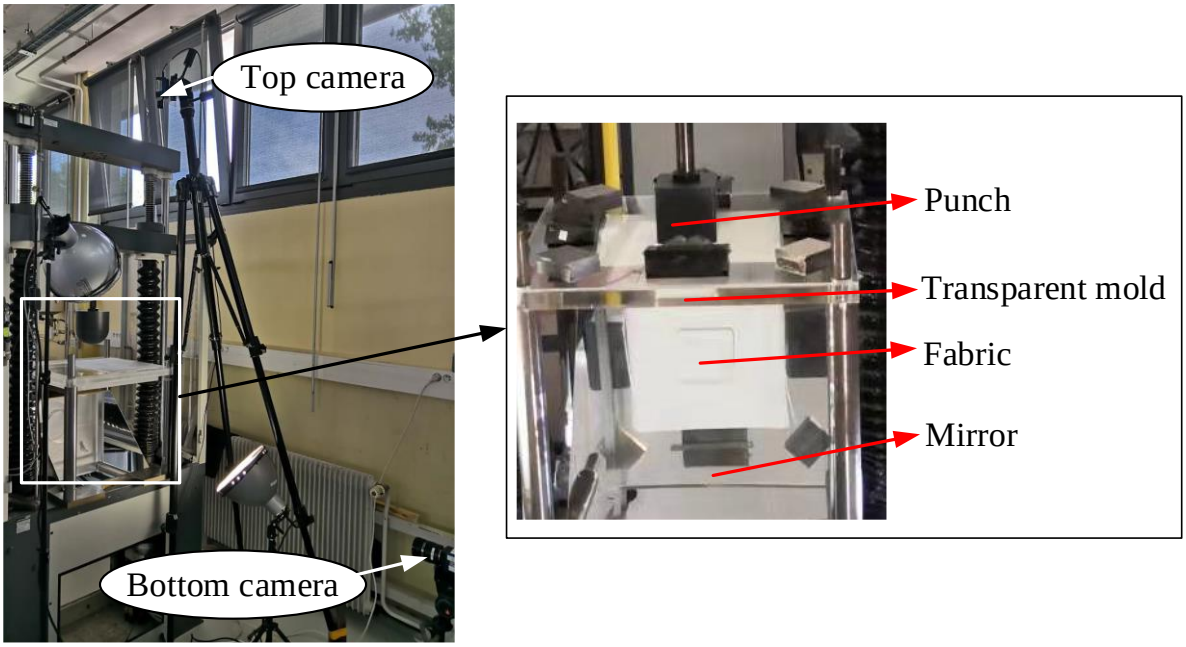

Fig. 3.1. Experimental set-up

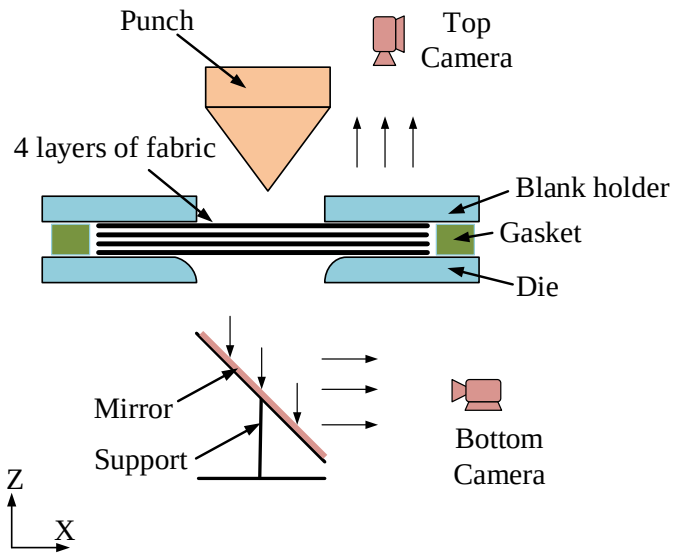

Fig. 3.2. Schematic diagram of the forming experiment

3.1.2 Material preparation

The specimens used for the forming experiment are cut as squares from the material roller. The cutting can be done by machine or manually. To study the influence of yarn orientation on material deformation, two types of specimens for single-layer were used in the forming experiment. As shown in Fig. 3.3, we used 0°/90° layers and ±45° layers (the angle is with respect to the edges of the rectangular specimen).

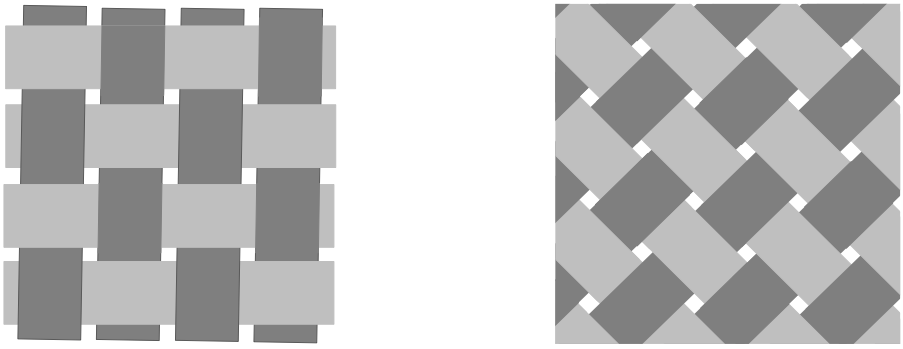

(a) (b)

Fig. 3.3. Yarn orientation configuration of the specimen. (a) 0°/90°. (b) ±45°.

As the material behavior of textile composite highly depends on yarn direction, it is need accurately ensure that the yarn direction is the same between experiment and simulation in the initial configuration. For the 0°/90° layer, the yarn direction can be easily guaranteed by cutting the material along the yarn direction because the warp and weft yarn are perpendicular to each other in the initial state without deformation. For the ±45° layer, it is not easy to directly obtain the desired angle configuration due to the lack of a reference. As shown in Fig. 3.4(a), the final

deformed fabric is axial asymmetry in the tetrahedron forming when the specimen yarn configuration is not at ±45° (actually +41°/-49°).

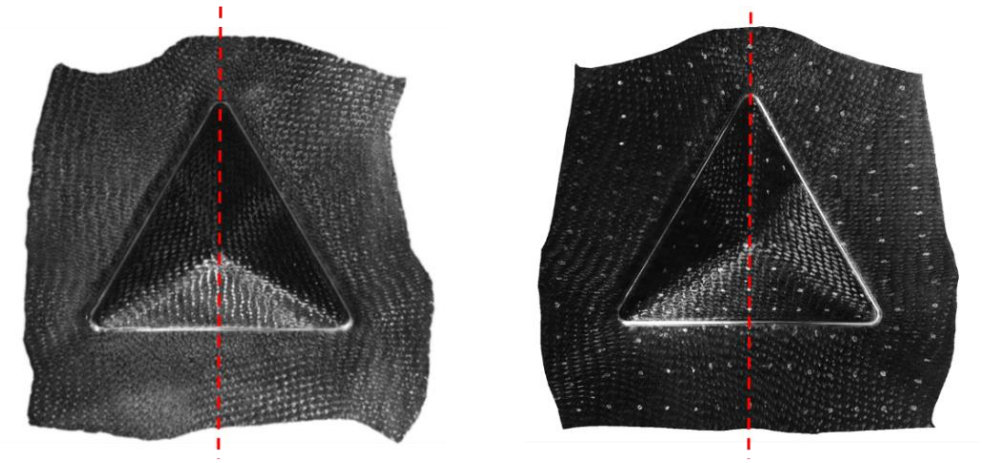

(a) (b)

Fig. 3.4. Deformed fabric under different yarn configurations. (a) Asymmetry. (b) Symmetry.

In order to overcome this difficulty when manually cutting the material, a transparent square ruler is adopted in the process of preparing specimens. The diagonal lines are marked on the square ruler, which can be made as a reference for cutting the ±45° layer. When the yarn configuration is at ±45°, the final deformed shape of single-layer fabric is presented in Fig. 3.4(b), and the deformed shape is axial symmetry.

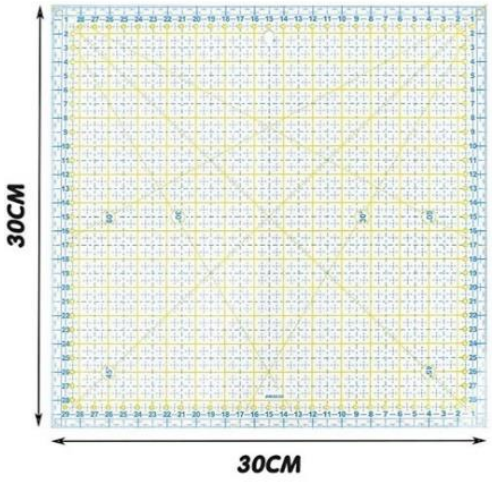

Fig. 3.5. The transparent square ruler

After cutting the material from the roller, the material will be painted by marker points. As shown in Fig. 3.6. The marker points are in equal interval at 20 mm, and they are 10 mm away from the specimen boundary. The marker points are painted along the warp and warp yarn direction. The specimen boundary are also painted as white in order to obtain the deformed profile. The experimental results recorded by the camera used in the experiment will be processed in Matlab

software, and the marker-based tracking approach is used to get the material deformation in different positions. The shear angle when the material is deformed is also calculated according to these adjacent marker-points.

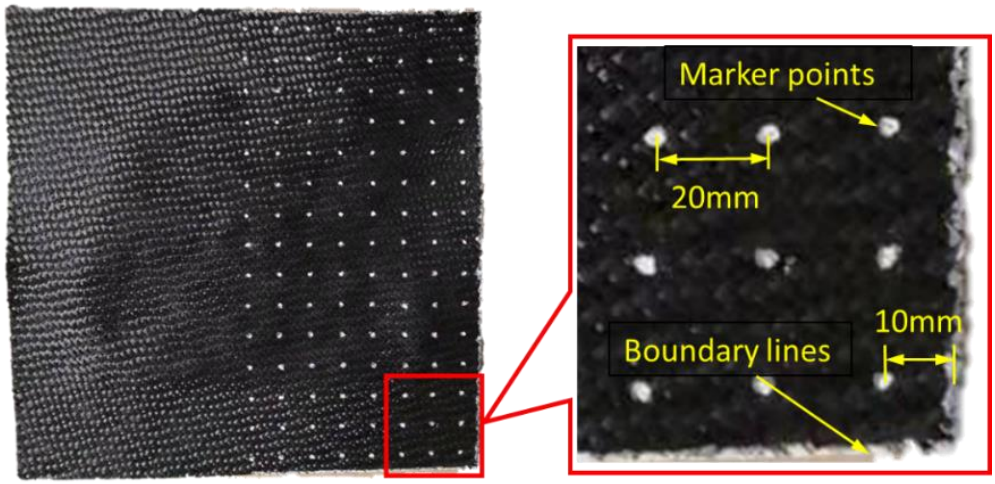

Fig. 3.6. Marker points on the specimen for forming experiment

3.2 Simulation settings

3.2.1 Simulation modeling

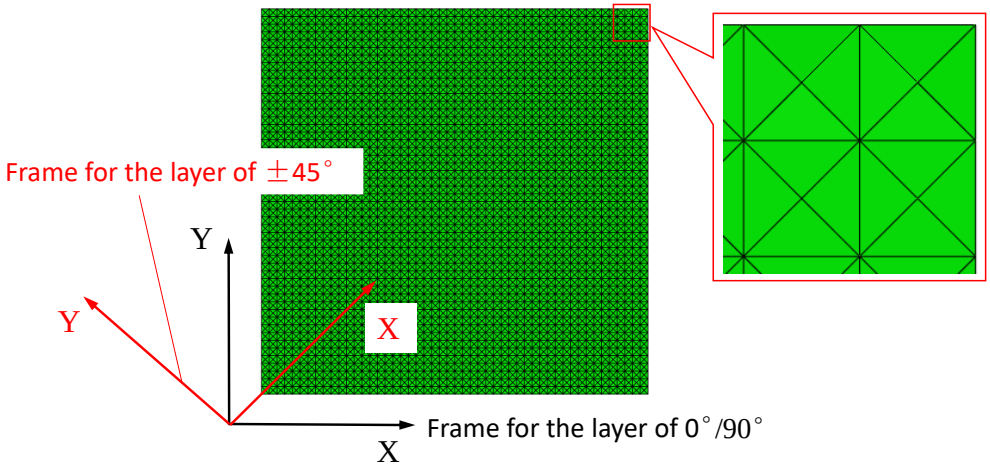

Fig. 3.7. Modelling the forming specimen

The simulations corresponding to the experiments are performed in Abaqus/Explicit using the presented approach implemented in the Abaqus subroutine VUGENS. The finite element modeling of the forming setup includes the forming specimen, blank holder, die, and punch. The forming specimen will be deformed under the action of the blank holder, die, and punch. The modeling of a single-layer forming specimen is presented in Fig. 3.7. The specimen model is meshed using triangular shell element (S3 in Abaqus/Explicit), and the length of the right-angle

side of the triangular element is 3.5 mm. The size of the specimen is different in the different forming experiments and will be introduced in the following section. For the two types of yarn orientations (0°/90°, ±45°), it's achieved by different coordinate system settings. The material constitutive equation is realized in the corresponding coordinate system. As shown in Fig. 3.7, the coordinate system marked as black is for the yarn orientations in 0°/90°, and the coordinate system marked as red is for the yarn orientations in ±45°.

For the simulation with the multi-layers configuration, the specimen modeling is the assembly of several plies single-layer modeling. The modeling of single-layer is independent of each other, and the contact property is applied between adjacent layers, with a Coulomb friction coefficient.

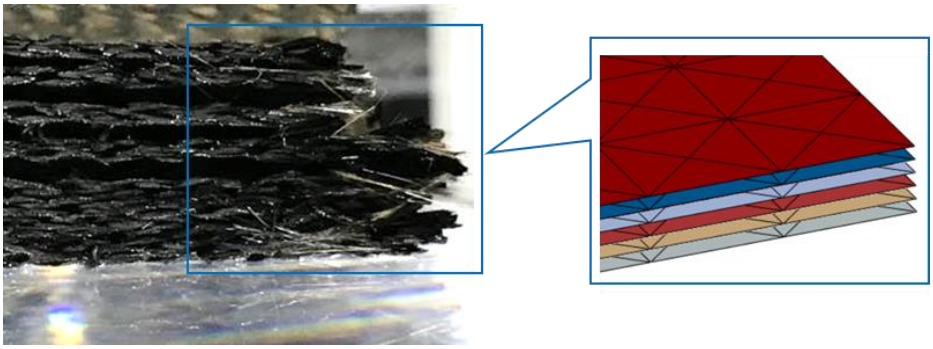

Fig. 3.8. Modeling of multi-layers forming

As the forming tools, the deformation of the blank holder, die, and punch is much smaller than the specimen, thus these forming tools are considered as rigid bodies in Abaqus/Explicit which will have no deformation in the simulation process. Each part will be meshed by the quadrilateral rigid body element (R3D4 in Abaqus Abaqus/Explicit) and the mesh size changes with the curvature, the geometry parameter setting of the part will be presented in the following section.

(a) (b)

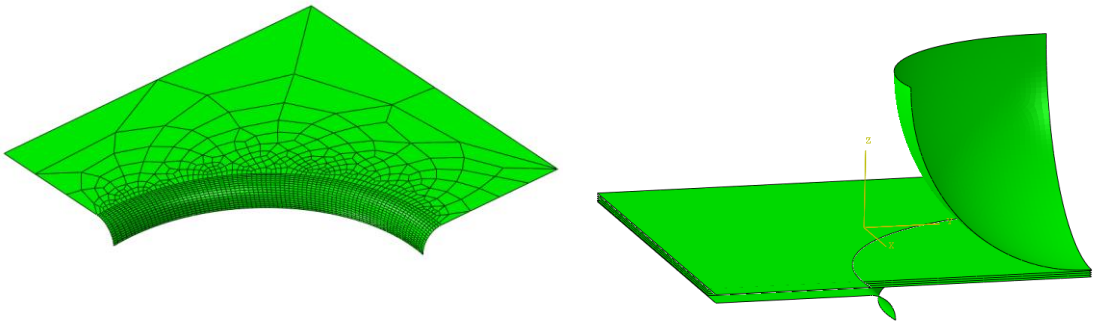

(c) (d)

Fig. 3.9. Hemisphere modelling. (a)Blank holder (b) punch (c) Die (d) Assembly

The forming experiments presented in this chapter include two types of forming: hemisphere and tetrahedron. For the hemisphere modeling, the hemisphere shape is centrally symmetric. In order to save the simulation time, only a quarter of the model is created in the simulation (shown in Fig. 3.9).

For the tetrahedron modeling, the tetrahedron shape is axisymmetric and only half of the model is created in the simulation (shown in Fig. 3.10).

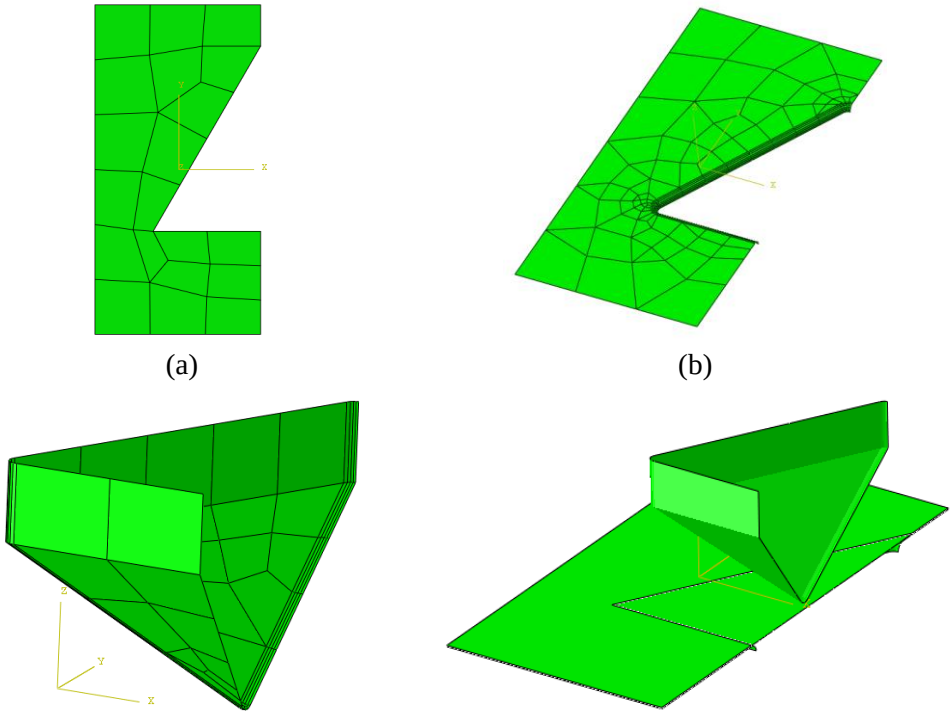

(a) (b)

(c) (d)

Fig. 3.10. Tetrahedron modelling. (a)Blank holder (b) punch (c) Die (d) Assembly

3.2.2 The tested material properties

Two types of textile composite are considered in the forming experiments, they are G1151 and plain weave. The G1151 is used for most of the experiment presented in this chapter, and its woven geometry is presented in Fig. 2.10 in Chapter 2. The plain weave (Fig. 3.11) is only used in the multi-layer forming experiment (seen in section 3.3.4), and it will be found that the wrinkles will appear for the used plain weave, but not for the G1151 fabric. The comparison of geometric characteristics of the G1151 and the plain weave is listed in Table 3.1.

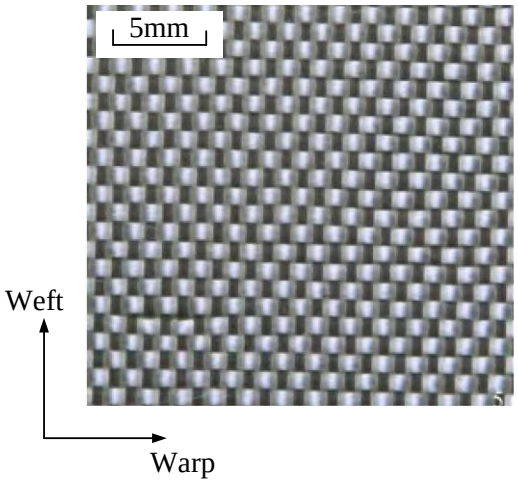

Fig. 3.11. The plain weave [Guzman-Maldonado et al., 2019].

Table 3.1. Comparison of geometric characteristics of the G1151 fabric and the plain weave

Material	G1151 fabric	Plain weave
Manufacturer	Hexcel	Hexcel
Fibers	Carbon 6K	Glass EC9 68
Areal density	630 g/m^2	160 g/m^2
Single layer thickness	1.3 mm	0.14 mm
Yarn density	Warp: 7.5 yarns/cm	Warp: 11.8 yarns/cm
	Weft: 7.4 yarns/cm	Weft: 10.7 yarns/cm

The mechanical properties of G1151 and plain weave are given in Table 3.2, including three material properties for the stress-resultant approach, coulomb friction coefficient between adjacent layers for the multi-layers forming and the coulomb friction coefficient between specimens and forming tool. The coulomb friction coefficient is set as constant. For the three material properties of G1151 and the plain weave, the methods to measure the material mechanical behavior has been introduced, and the material property of G1151 has also been tested and given in Chapter 2. The

material property of the plain weave is referred in [Guzman-Maldonado et al., 2019]. Due to the fiber can be seen as quasi-inextensible in the draping process, thus the tensile stiffness of the fabric material will be set as a quite large value for the draping simulation. The tensile stiffness of G1151 fabric and plain weave are listed in Table 3.2, and the value are calculating from the Young's modulus of yarns.

Table 3.2. Principal mechanical properties of G1151 and Plain weave

Mechanical properties	G1151 fabric	Plain weave
In plane shear ($\gamma=2\varepsilon_{12}$) $dN_{12}= C_{12}\, d\gamma$ $C_{12} = K_0 + K_1\lvert\gamma\rvert + K_2\lvert\gamma\rvert^2 + K_3\lvert\gamma\rvert^3 + K_4\lvert\gamma\rvert^4$	K_0 = 0.09 N/mm K_1 = −0.83 N/mm K_2 = 2.92 N/mm K_3 = −4.01 N/mm K_4 = 2.03 N/mm	K_0 = 0.41 N/mm K_1 = −1.11 N/mm K_2 = 5.57 N/mm K_3 = −18.71 N/mm K_4 = 19.50 N/mm
Out of plane bending		
$dM_{11}= D_{11}\, d\chi_{11}$	D_{11}= 7.45 N·mm	D_{11}= 0.5 N·mm
$dM_{22}= D_{22}\, d\chi_{22}$	D_{22}= 7.45 N·mm	D_{22}= 0.5 N·mm
Tensile stiffness		
$dN_{11}= C_{11}\, d\varepsilon_{11}$	C_{11}= 21500 N/mm	C_{11}= 1150 N/mm
$dN_{22}= C_{22}\, d\varepsilon_{22}$	C_{22}= 21500 N/mm	C_{22}= 1150 N/mm
Coulomb friction coefficient		
Ply to ply	0.21	
Ply to mold	0.23	

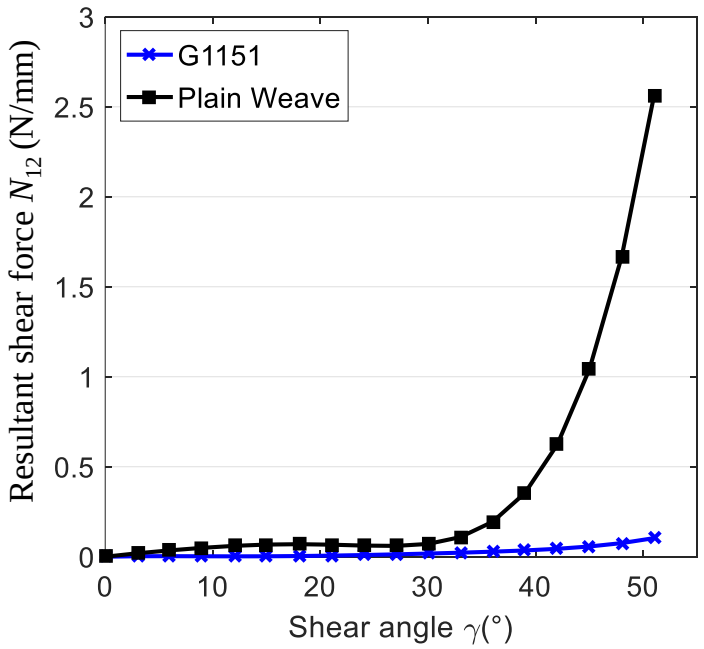

Fig. 3.12. The shear behavior comparison between G1151 and plain weave.

Both materials, G1151 and plain weave, are considered as quasi-inextensibility, thus the tensile stiffness of these two material are set as constant and large compared with the other two material stiffness. The shear behavior of both material is no linear, and it can be found that the shear stiffness of the plain weave is larger than the case of G1151 material. The comparison of shear behavior between G1151 and plain weave is presented in Fig. 3.12. For the bending behavior, it is set as linear according to the cantilever test in Chapter 2. The bending stiffness along warp and weft yarn is considered to be the same, and the average value of the bending stiffness in warp and weft direction is adopted in the simulation in this chapter. It can be observed that the bending stiffness of the G1151 material is much larger than that of the plain weave.

3.3 Hemisphere forming

The geometry setting of the hemisphere forming is given in Fig. 3.13. The diameter of the punch is 150 mm, and the punch final displacement for the forming experiment is 75 mm. The diameter of the hole in the blank holder and die is 160 mm. The initial dimension of the specimen is 300 mm× 300 mm. The forming experiment includes single-layer forming and multi-layers forming. For the single-layer forming, the forming condition includes the forming with blank holders and forming without blank holders. For the multi-layer forming, as shown in Fig. 3.13, the stack of four layers with quasi-isotropic are considered in the experiments.

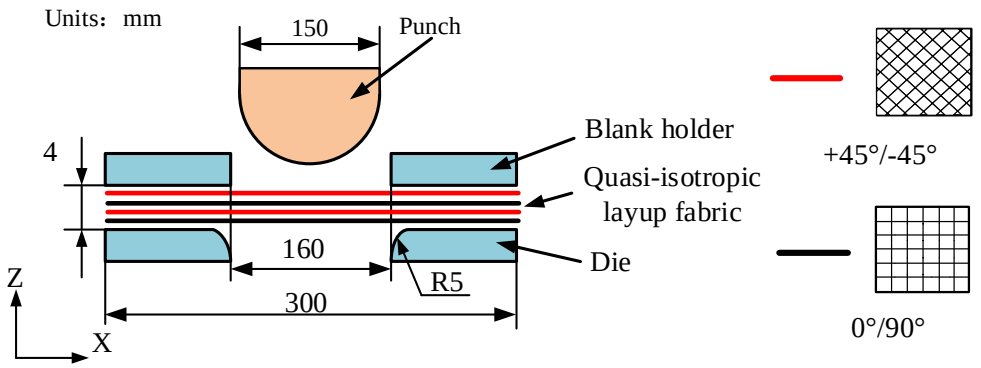

Fig. 3.13. Geometry setting of hemisphere forming

The simulations were conducted using the parameters set in Section 3.2. The quantitative comparison between simulation results and experimental results will be presented below. Now we discuss the results using output variables such as in-plane shear angle, specimen contour, punch force, and the wrinkles that appeared during draping.

3.3.1 In-plane shear angle comparison

After the RTM process, the mechanical properties of the final cured component is mainly determined by the yarn direction. It is the basic requirement that the simulation approach can correctly trace the yarn direction. The warp and weft yarn are perpendicular to each other in the

initial conditions. The angle change between warp and weft yarns in the forming is called in-plane shear angle, it will determine the yarn direction at different positions. Thus, in-plane shear angle is usually considered as a critical variable for woven fabric composite forming; the in-plane shear angle comparison is made first.

For the in-plane shear angel output in the experiments, the marker points are all painted along the warp and weft yarn direction no matter for the specimen with 0°/90° or ±45°. Thus, the shear angle between warp and weft yarn can be calculated with the help of the marker points (shown in Fig. 3.14).

For the in-plane shear angel output in the simulations, the fiber yarn direction $f_\alpha(\alpha = 1,2)$ is traced by the deformation gradient tensor *F* as presented in the Eq.(2.7) . In-plane shear angle γ can be calculated as below.

$$\gamma = \frac{\pi}{2} - \cos^{-1}\left(\frac{\mathbf{f}_1 \cdot \mathbf{f}_2}{\|\mathbf{f}_1\|\|\mathbf{f}_2\|}\right) \tag{3.1}$$

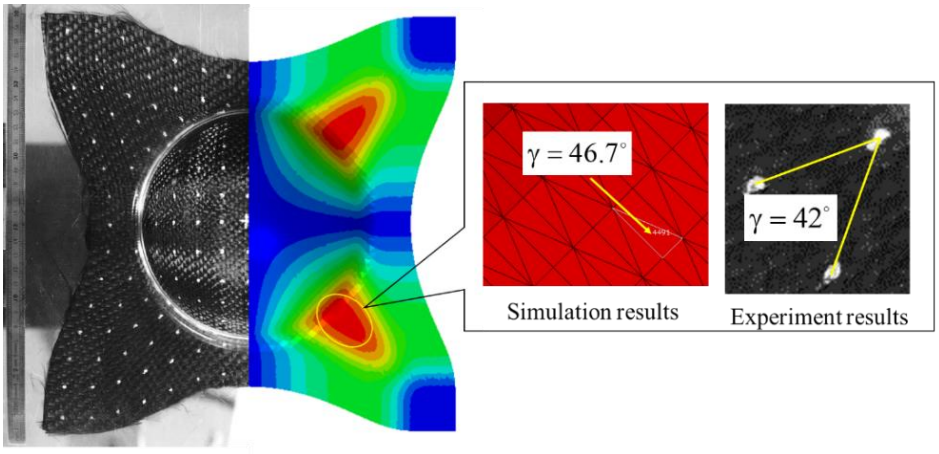

(a)

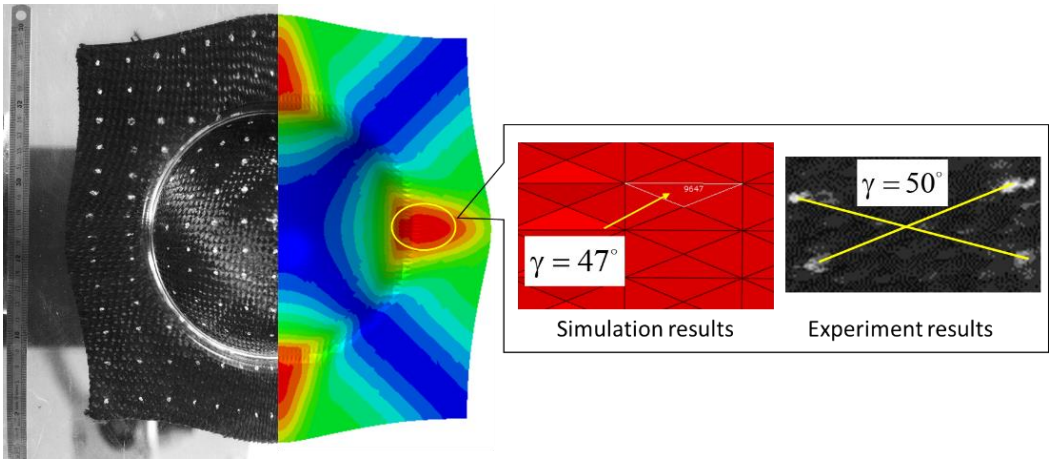

(b)

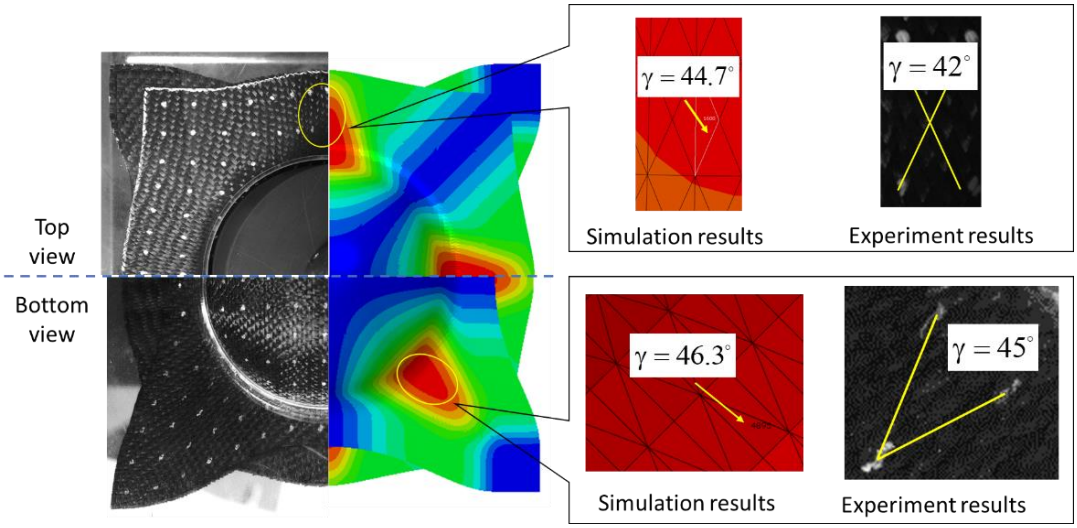

(c)

Fig. 3.14. Shear angle comparison in the final deformed shape. (a) Single layer of 0°/90°. (b) Single layer of ±45°. (c) Four layers of quasi-isotropic layer-up.

The final deformed fabric of experiment and simulation when the punch displacement is 75 mm is shown on the left of Fig. 3.14, and the in-plane shear angle comparison is presented on the right of Fig. 3.14. The comparison result of single-layer 0°/90° and ±45° is listed in Fig. 3.14(a) and (b) respectively. The comparison result of four-layer quasi-isotropic layer-up is given in Fig. 3.14(c). The comparison is performed at the top and the bottom layer because only the experiment result can be obtained at the top and the bottom with the two cameras used in the experiment. According to the comparison shown in Fig. 3.14, the in-plane shear angles measured in the experiments and calculated by simulations are close.

3.3.2 Fabric contour comparison

The fabric contour shows the final shape of the material deformation, it can intuitively reflect the degree of material deformation. The fabric contour is the sum of the material draw-in at different locations, and it can be considered as a global characteristic for the material draping. The initial dimension setting of the specimen in experiment and simulation are the same, the deformed fabric contour comparison can be validated the correctness of the simulation model for the textile composite forming. The final deformed shape can be divided into the effective zone and non-effective zone, the effective zone is the desired forming shape, and the non-effective zone needs to be cut off in the subsequent process. To ensure that the forming effective zone is filled with material, the area of the prepared specimen is larger than the desired shape. In the factory manufacturing process, the fabric contour prediction of the simulation model can also be used to design the size and shape of the prepared specimen, which can reduce material waste and production costs.

In the experiment, the ruler is placed next to the specimen (as shown on the left Fig. 3.14(a)), a calibration system was constructed to make a transformation between the pixel coordinates and the real coordinate system which represent the real dimension of an object in the picture. The transformation equation in the image process is as followed：

$$I_r = \frac{L}{N_p} \tag{3.2}$$

Here, I_r is the transformation ratio for the image processing, L is the ruler length, and N_P is the pixel number corresponding to the ruler length. The fabric deformed contour of the simulation result can be directly output by calculating the displacement of the mesh points on the contour.

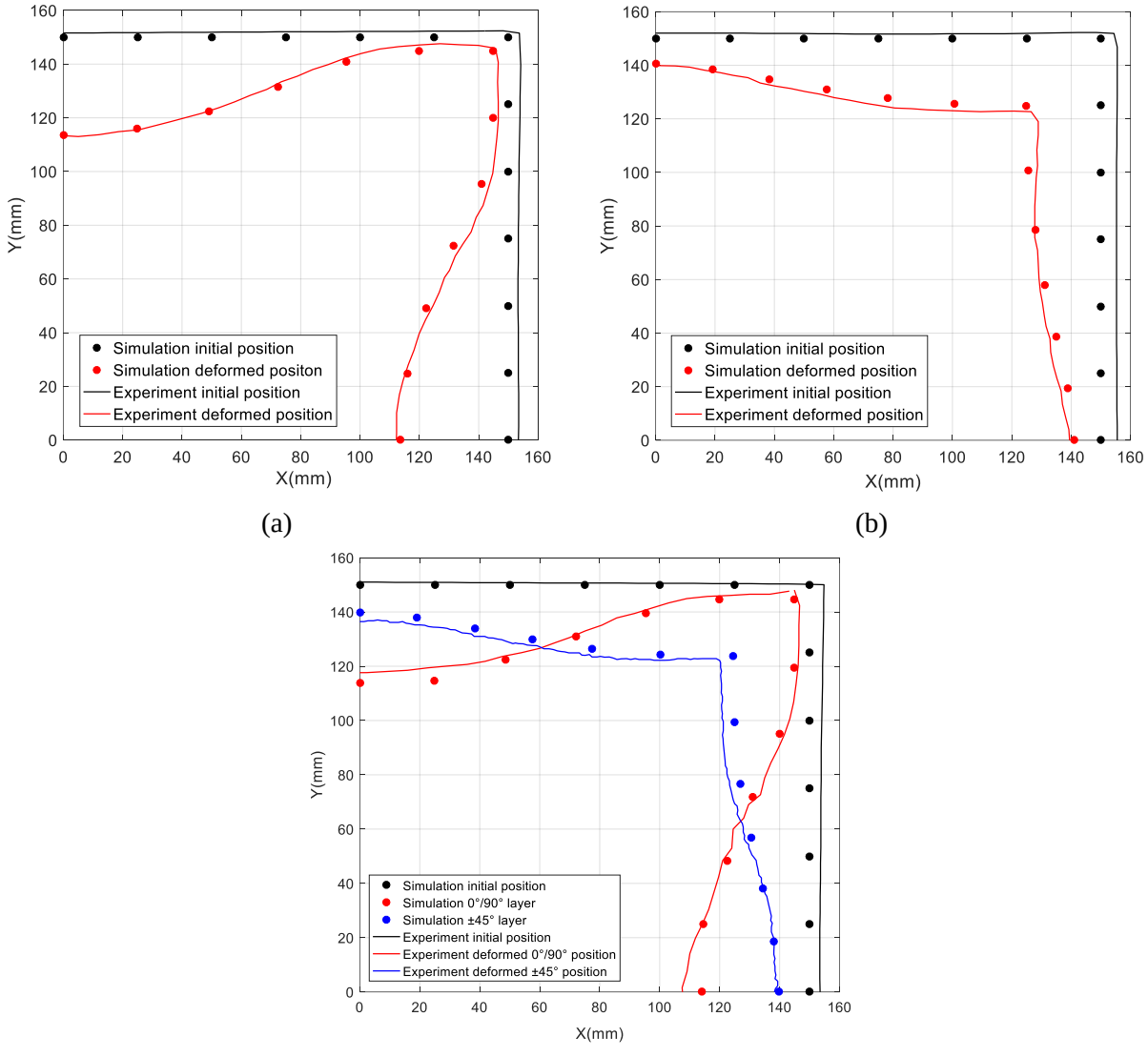

Fig. 3.15. Fabric contour comparison in the final deformed shape of hemisphere forming. (a) Single layer of 0°/90°. (b) Single layer of ±45°. (c) Four layers of quasi-isotropic layer-up

The fabric contour comparisons of hemispherical forming are listed in Fig. 3.15, including the forming of single-layer 0°/90°, ±45° and four-layer with quasi-isotropic layer-up. Only one-quarter of the contour is presented due to the hemisphere is central symmetry. The black line and dots respectively represent the initial position of the specimen in the experiment and simulation. And the red line and dots respectively represent the deformed position of the specimen in the experiment and simulation. Through these comparisons, the deformed specimen contour obtained by the simulation is in good agreement with that of the experiment.

3.3.3 Punch force comparison

The punch force is the external force used to deform the specimen, and it is determined by the mechanical properties of the material and the interaction between the specimen and the forming tools. Thus, the punch force can be considered as a parameter to validate the numerical simulation in the textile composite forming. The punch force of experiment at different displacement is recorded by a load sensor. Take the hemispherical forming of four-layer with quasi-isotropic layer-up as an example, the force-displacement curve comparison between experiment and simulation is given in the Fig. 3.16. It can be viewed that the load value of the experiment and simulation are in agreement when the punch displacement is large, and the experimental load is larger than the numerical load when the punch displacement is small. This may have a relation with some friction in the forming system during the forming experiment.

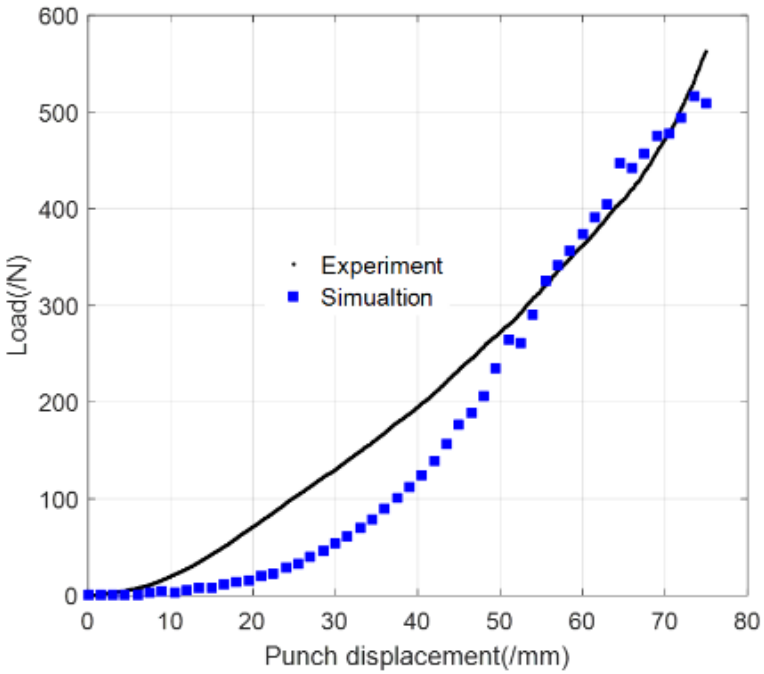

Fig. 3.16. Punch force during the hemispherical forming of a four-layer quasi-isotropic layer-up.

3.3.4 Wrinkles comparison in multi-layers forming

When draping the textile composite, wrinkling is one of the main forming defects that can occur at the macroscopic level. The occurrence of wrinkles in the effective zone will greatly reduce the mechanical properties of the final cured component. In the manufacturing process, the wrinkles appearing in the effective zone can be avoided by adjusting the forming condition [Breuer et al., 1996; Obermeyer & Majlessi, 1998; Lee et al., 2007; Lin et al., 2007; Kärger et al., 2015, 2018; Nosrat Nezami et al., 2017; Pfrommer et al., 2018; Shanwan & Allaoui, 2019; Zimmerling et al., 2022]. In order to reduce the trial cost and the manufacturing cycle, it is critical that the simulation approach can accurately predict the wrinkles.

The appearance of wrinkles will increase in the multilayers fabric with different orientation forming. The different deformation for the two adjacent layers with different yarn orientation will cause slippage between layers. If the slippage is restricted because of the interlayer friction, the compressive force will be generated in the yarn direction which will cause the occurrence of wrinkles.

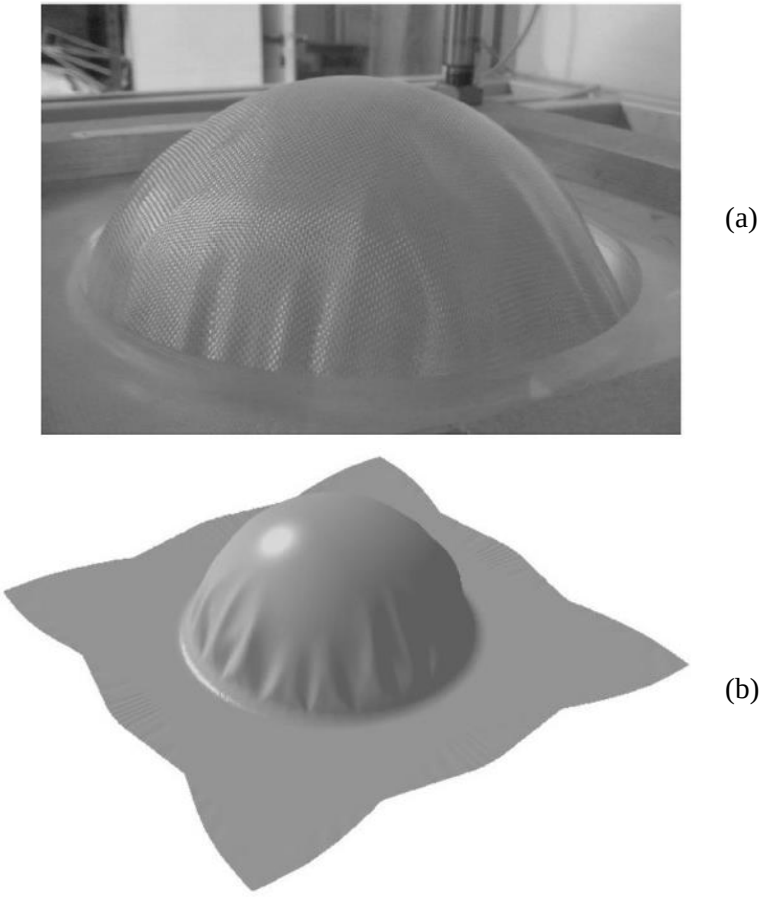

(a)

(b)

Fig. 3.17. Four layers of quasi-isotropic plain weave. (a)Experiment[Guzman-Maldonado et al., 2019]. (b) Simulation done with the stress resultant shell approach.

The wrinkles appeared in the effective zone of four layers with quasi-isotropic layer-up forming experiment have been observed in [Guzman-Maldonado et al., 2019], see Fig. 3.17(a), the material used in the experiment is plain wave fabric (introduced in Fig. 3.11), the material properties are listed in Table 3.1, and the experimental geometry parameters are the same as the previous hemisphere forming experiment in Section 3.3 (described in Fig. 3.13). The corresponding simulation is conducted using the presented simulation approach in Chapter 2, and the simulation result is given in Fig. 3.17(b). The wrinkles that appeared in the hemispherical zone in the experiment are well predicted by the simulation model.

Note: For the four layers with quasi-isotropic layer-up of G1151 fabric, no wrinkles were observed in the hemispherical zone (shown in Fig. 3.14(c)), and wrinkles appeared when the material change to the plain weave. These two experiments have the same boundary conditions. The appearance of wrinkle is due to the differential material properties, the relationship between the material properties and the wrinkle formation will be discussed in Chapter 4.

3.3.5 Wrinkles comparison during forming without blank-holder

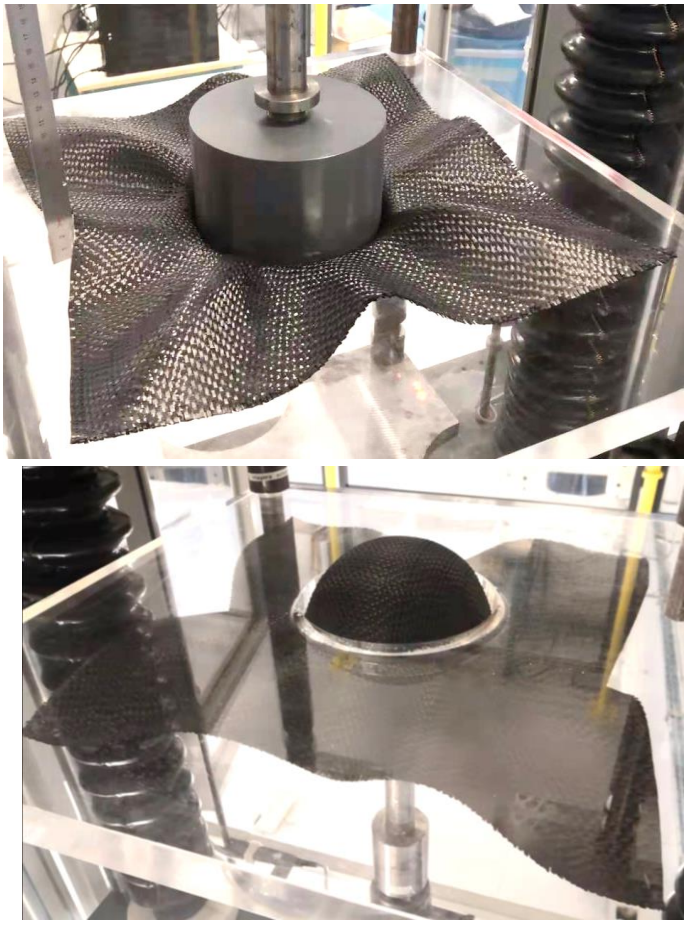

(a)

(b)

Fig. 3.18. The 0°/90° single-layer hemisphere forming without blank-holder. (a)Top view. (b)Bottom view

As shown in Fig. 3.14(c) and Fig. 3.17, wrinkles appear in the hemispherical zone in the forming of four-layers with quasi-isotropic using plain weave material while no wrinkle formation using the G1151material, and this phenomenon is accurately predicted by the simulation results using the stress-resultant approach. For quantitative analysis of wrinkles, the size and position of wrinkles form during the experiment and simulation will be compared in this chapter.

The blank-holder plays an important role in avoiding wrinkle formation. The application of the blank-holder will prevent the undesired bending deformation which will avoid wrinkles formation. Thus, in order to form wrinkles in the hemisphere forming experiment and make comparison with simulation results, the blank-holder is removed in the experiment. The single-layer hemisphere forming without the blank-holder using G1151 material is performed in this chapter. The dimension of the specimen is 430 mm × 430 mm, and the yarn orientation of the specimen is 0°/90°. The geometry of the forming is given in Fig. 3.13. The forming experimental result is shown in Fig. 3.18, and it can be seen that severe wrinkles appear on the non-effective zone. To quantitative analysis the wrinkles the simulation and experiment, the method to measure the dimension of the wrinkles will be introduced in the following.

a) Wrinkles measurement

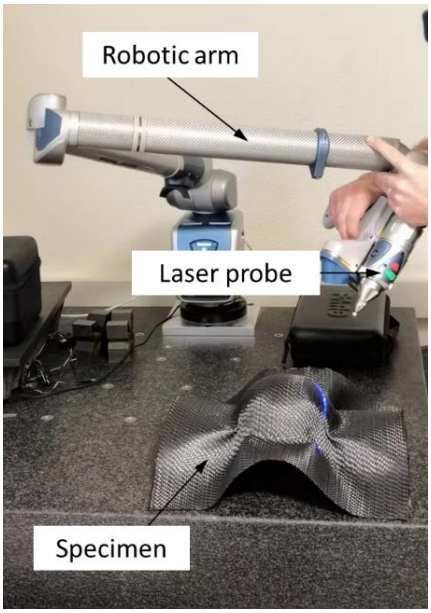

Fig. 3.19. 3D laser scanner approach

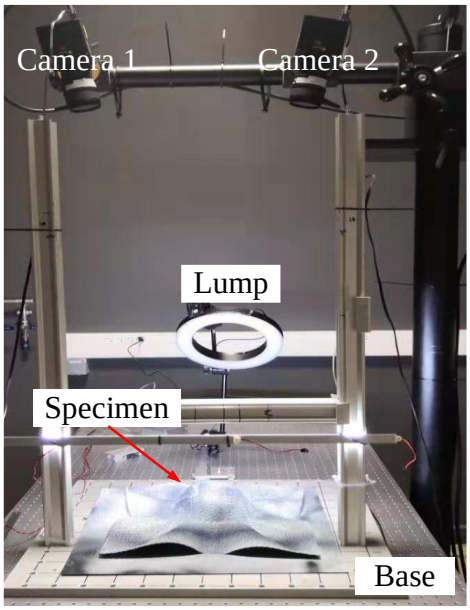

Fig. 3.20. Digital image correlation (DIC) approach

Wrinkles is one of the main defects that may occur in the forming, several approaches can be used to characterize wrinkles, including the laser scanner technology, and image processing. Georg et al [Bardl et al., 2016] apply the 3D scanner with a high-frequency eddy current sensor to obtain the final deformed shape and also the yarn direction at different positions. For the image processing, Arnold et al[Arnold et al., 2016] use the ‘Shape from focus’ technology from a stack

of photo to obtain the wrinkle amplitude in the forming of NCF materials. Based on the 'Structure from motion' technology, Shen et al[Shen, Wang, Legrand, & Liu, 2019] reconstruct the deformed shape through continuously recording the deformed specimen at different positions using a digital camera. Viisainen et al [Viisainen et al., 2021] use the 3D digital image correlation (DIC) to study the wrinkling behavior and the wrinkling mechanisms of a biaxial NCF, and the DIC method allow to track the full-field of a speckled surface from which both displacements and surface strains [Sutton et al., 2009].

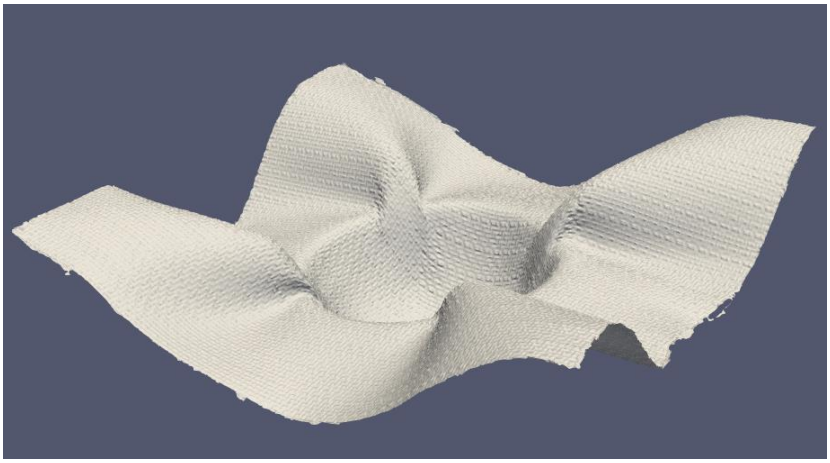

(a)

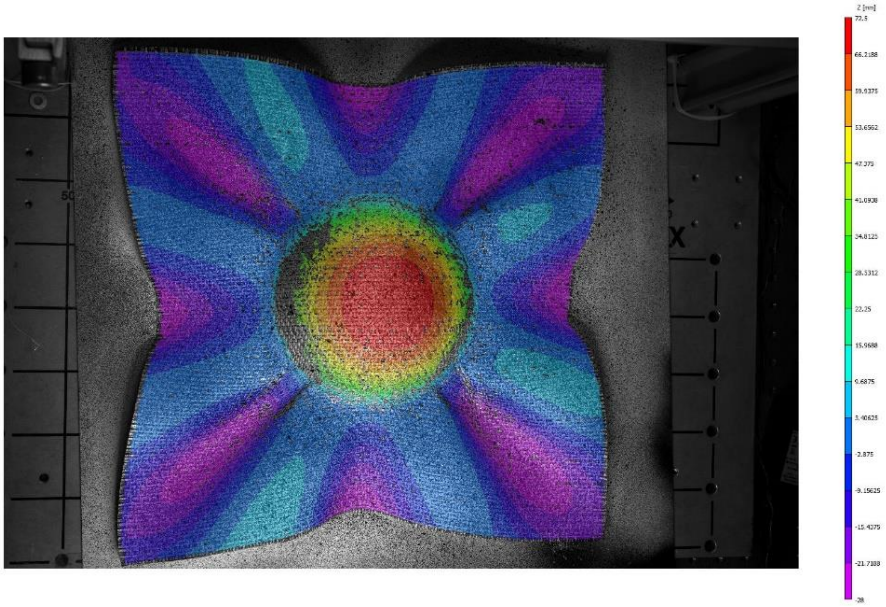

(b)

Fig. 3.21. Wrinkle measurement results of 0°/90° single-layer G1151 fabric. (a) 3D laser scanner (b) Digital image correlation (DIC).

In order to obtain the dimension of the wrinkles, the two measurement approaches are studied here: the 3D laser scanner method and the digital image correlation (DIC).

- The 3D laser scanner system is shown in Fig. 3.19. The laser probe is placed on a robotic arm, and it can detect the specimen through programing or manual control of the robotic arm. By acquiring the data of the laser probe and processing it in the corresponding software, the specimen can be reconstructed, and the reconstructed model can be output in 3D graphic file format (such as '.stp' file) or data point cloud ('.xyz' file).

The digital image correlation (shown in Fig. 3.20) is composed of two CCD cameras placed at different positions. The tested specimen geometry information can be directly obtained on the VIC-3D software.

Due to the limitations of the forming equipment in LaMCoS laboratory, the in-situ measurement of wrinkles cannot be performed. The deformed fabric will be pre-cured using hair spray to fix the sample in the deformed configuration, and then then sample is taken from the mold for individual measurement. The measurement results using 3D laser scanner and DIC are respectively presented in Fig. 3.21(a) and (b). According to the measurement processing, the 3D laser scanner can very accurately obtain the material deformation, and even the orientation of the fiber tow. But in order to get the wrinkle geometry, the output file needs to be post-processed. The digital image correlation measurement process is faster and simpler, and the geometric parameters of the wrinkle can be obtained directly in the commercial VIC-3D software. Therefore, the measurement results of Digital image correlation are used in the thesis to make comparison with the simulation.

b) Wrinkles comparison

The result obtained by 3D scanning requires secondary processing to obtain the wrinkle geometry while can be directly obtained through DIC method. Here the measurement result by DIC will be compared with the simulation result using the stress-resultant approach.

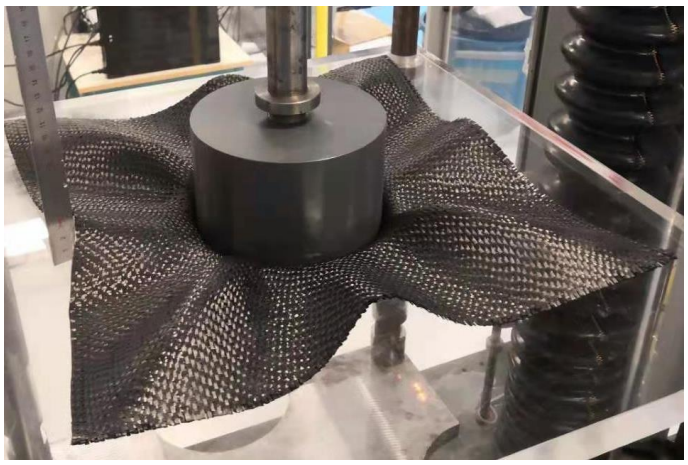

(a)

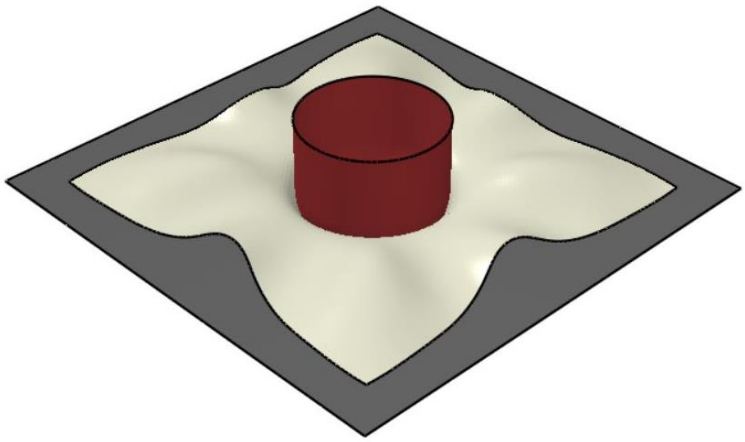

(b)

Fig. 3.22. Experiment and simulation comparison of G1151 fabric hemisphere forming without blank-holder (a) Experiment (b) Simulation

The experiment result of single-layer 0°/90° hemisphere forming without blank-holder is presented in Fig. 3.22(a). And the corresponding simulation result is given in Fig. 3.22(b). They are in same shape. In order to quantitatively analyze the wrinkles in the simulation and experiment, two paths which are marked as 0° path and 45° path are selected to make the comparison (shown in Fig. 3.23).

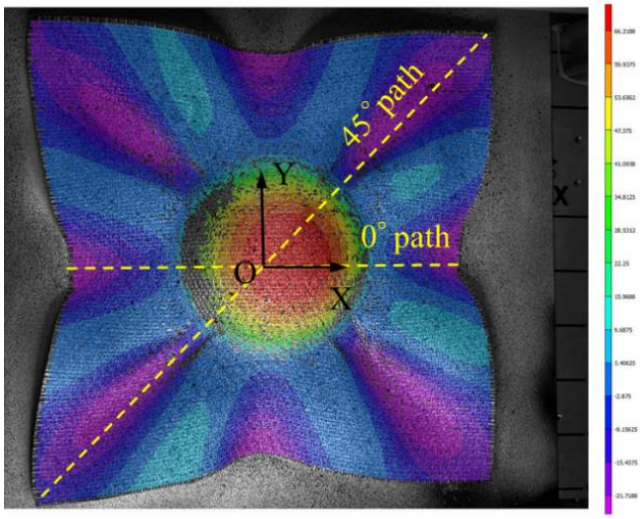

Fig. 3.23. The defined two path in the G1151 fabric hemisphere forming without blank-holder

The wrinkles amplitude in the two marked paths will be compared between simulation and experiment. The wrinkles of the experiment are from the DIC experiment, and the comparison result is given in Fig. 3.24. It can be observed that the simulation result fairly agrees with the experiment result.

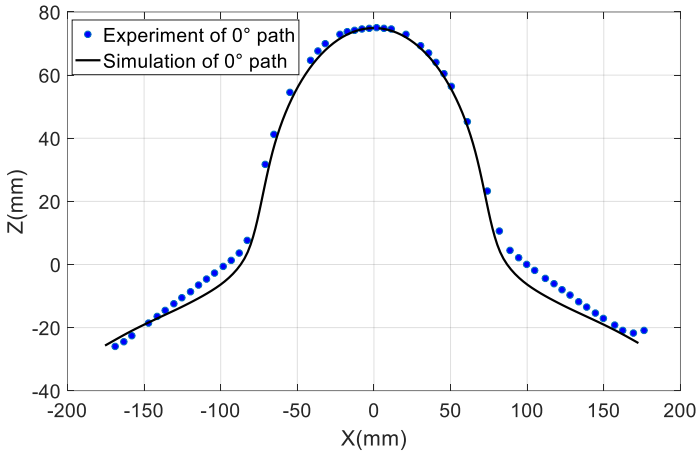

(a)

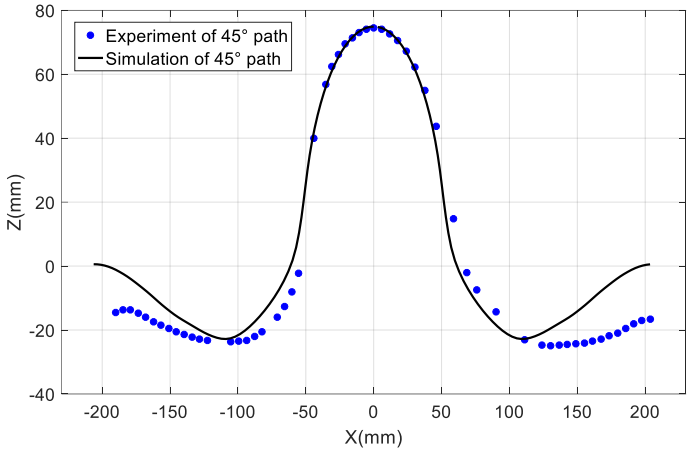

(b)

Fig. 3.24. Wrinkle amplitude comparison between simulation and experiment of the G1151 fabric. (a) 0° path (b) 45° path.

3.4 Tetrahedron forming

A lot of research work has devoted to the tetrahedron forming and it has become a benchmark shape for the textile composite forming [Allaoui et al., 2011, 2014; Thompson et al., 2020]. Thus, the tetrahedron forming is selected as another case for the validation of the introduced simulation approach. The geometry parameters of the tetrahedron forming is presented in Fig. 3.25. The G1151 material is used in the tetrahedron forming, and same as the hemisphere forming introduced before, three layup configurations of the specimen are considered in the forming experiment which are a single layer of 0°/90°, a single layer of ±45°, and four layers with a quasi-isotropic layup. The punch displacements are different in the different layers forming to avoid a collision. For the single-layer forming, the punch final displacement is set to 90 mm, and for the four-layer forming, due to the distance limitations between punch and die mold, the punch final displacement is set to 70 mm to form the tetrahedral part.

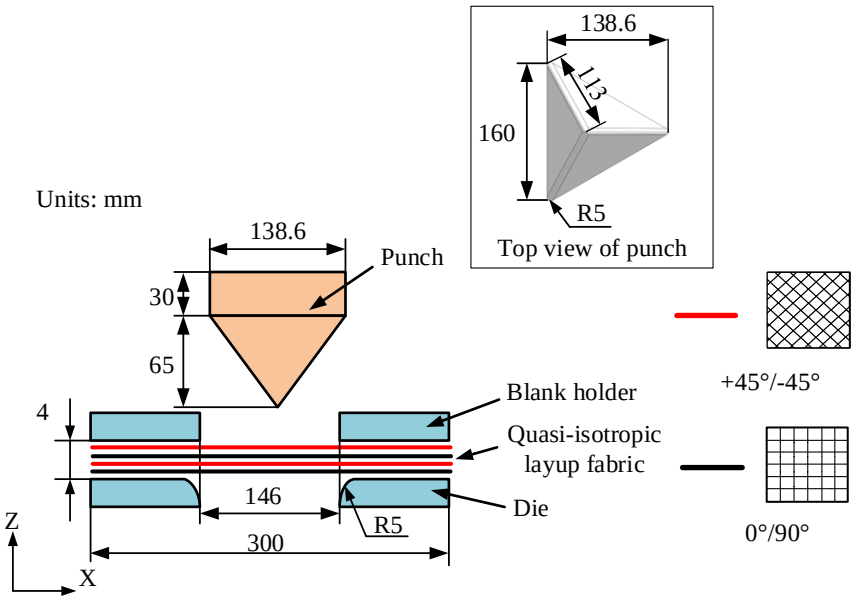

Fig. 3.25. Geometry setting of tetrahedron forming

The finial deformed fabric in the experiment are listed in the left side of Fig. 3.26 and Fig. 3.27, the single-layer 0°/90° and ±45° are respectively given in Fig. 3.26(a) and (b). For the four-layer forming, the deformed top layer and bottom layer are respectively given in the Fig. 3.27 (a) and (b) with the help of the two camera in the experiment. It can be observed that there are all no wrinkles in the three types of forming experiments.

3.4.1 In-plane shear angle comparison

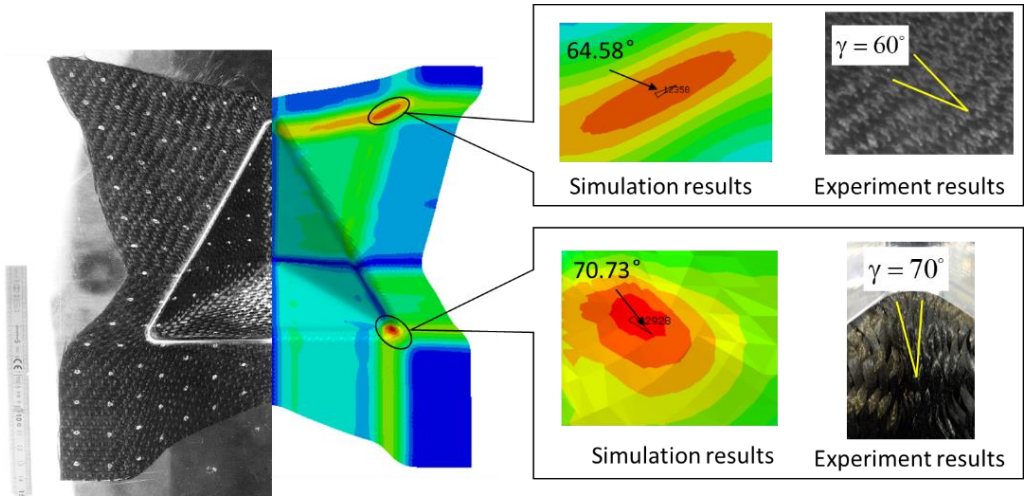

(a)

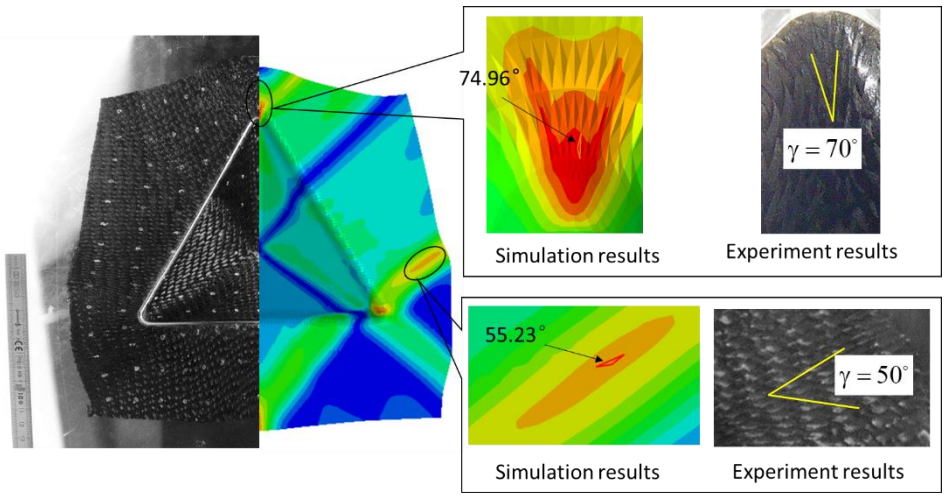

(b)

Fig. 3.26. Shear angle comparison of single layer. (a) Single layer of 0°/90°. (b) Single layer of ±45°.

The in-plane shear angle is firstly compared between experiment and simulation. The in-plane shear angle can be determined with the help of the white dots painted on the specimen. The zone with a larger shear angle is compared between experiment and simulation. The single-layer comparisons of 0°/90° and ±45° are respectively shown in the right of Fig. 3.26 (a) and (b), and the four-layer comparisons are given in the right of Fig. 3.27 (a) and (b), including the bottom layer and top layer respectively. Through the comparison given in Fig. 3.26 and Fig. 3.27, it can be concluded that the simulation approach can correctly predict the fabric in-plane shear angle at different zone.

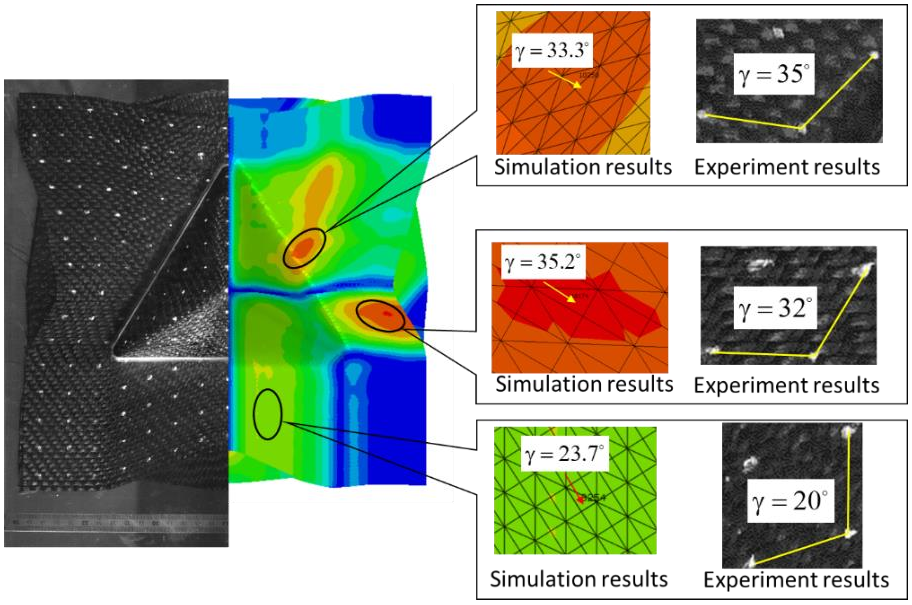

（a）

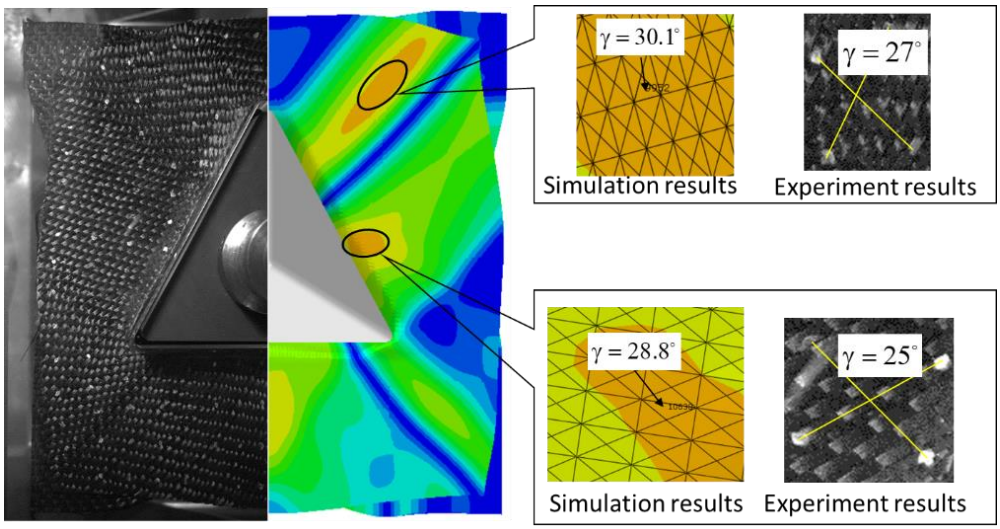

（b）

Fig. 3.27. Shear angle comparison of four-layer quasi-isotropic layup. (a) Bottom view (b) Top view

3.4.2 Fabric contour comparison

The deformed fabric contour is next compared with the simulation. As shown in Fig. 3.28, half of the contour is presented due to the tetrahedron shape is axis-symmetry. Fig. 3.28(a) is the comparison of single layer of 0°/90°, Fig. 3.28(b) is the comparison of single layer of ±45° and Fig. 3.28(c) is the comparison of four-layer with quasi-isotropic layup. The comparisons show that the deformed fabric profile between experiment and simulation are very similar.

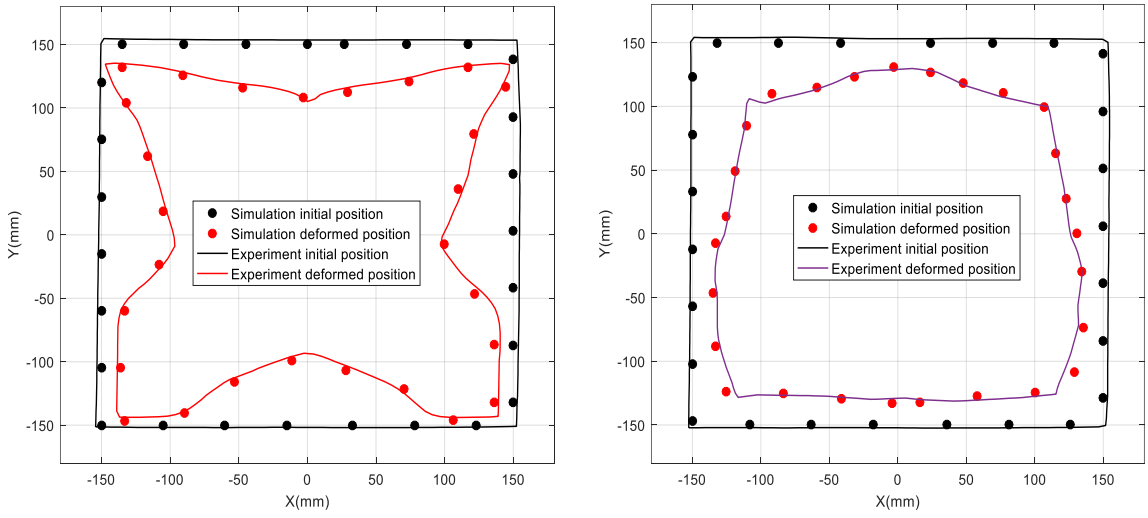

(a) (b)

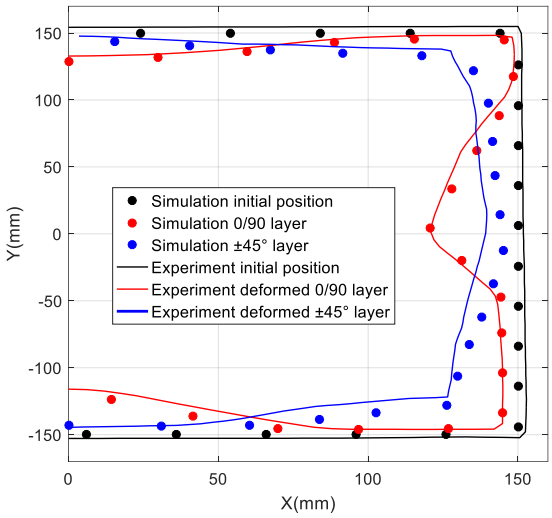

(c)

Fig. 3.28. Fabric contour comparison between experiment and simulation. (a) Single layer of 0°/90°. (b) Single layer of ±45°. (c) Four-layer with quasi-isotropic layup.

3.5 The deformation in the thickness direction

Due to the specific material behavior, the motion of material normal directors in the thickness direction will be different from the general shell kinematics when forming the thick woven composite material. In this section, the specific motion of the material normal director in the thickness will be researched. This specific deformation in the thickness direction will be firstly studied. And next a post-processing method to obtain the material director when the thick woven material is deformed will be presented and validated.

3.5.1 The insufficient of Kirchhoff shell

In the thickness direction, the material is stretched on one side and compressed on the other side. The material is without stretch deformation in the neutral surface. For the Kirchhoff shell, the material normal directors which are perpendicular to the mid-surface will keep a straight line and perpendicular to the mid-surface when the shell is under bending deformation. This is not the case for the woven material. For fibrous material, the material can be assumed as quasi-insensibility due to the material tensile stiffness is much greater than the other material deformation stiffness. And the possibility of the relative sliding between different layers will lead to the large rotation of the material normal directors. Thus the material normal directors of fibrous material won't keep perpendicular to the mid-surface when deformed.

Fig. 3.29 is the three-point bending test comparison between continuous material and fibrous material. Fig. 3.29(a) is the bending of continuous material and it is 15 mm thick silicone. It can be found that the motion of the normal directors obey the Kirchhoff kinematics. Fig. 3.29(b) is the bending of fibrous material and the material is 15 mm thick 3D interlock fabric. It can be observed

that the material directors didn't keep perpendicular to the mid-surface which is different with the motion in Fig. 3.29(a).

Through the above analysis and experimental comparison, it can be concluded that the shell based on the Kirchhoff kinematics cannot be used to predict the motion of the normal directors of woven materials.

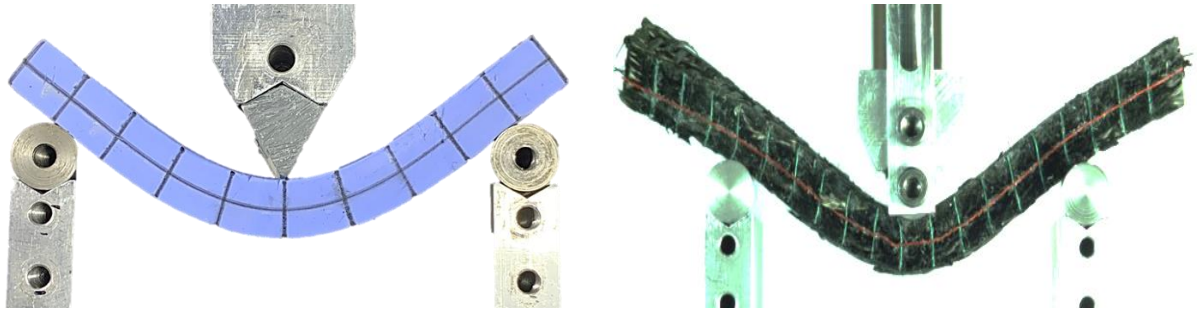

(a) (b)

Fig. 3.29. The three-point bending test (a) Continuous material. (b) Fibrous material [Orliac, 2012].

3.5.2 The insufficient of Mindlin shell

For the Mindlin shell, the material normal directors will also keep as a straight line after the material deformed. But they can non-perpendicular to the mid-plane which is not same with the Kirchhoff shell. The transverse shear behavior in the Mindlin shell is determined by the transverse shear stiffness which linked the shear strain and shear stress. This does not meet the deformation physics of the fibrous material which the rotation of the normal directors is due to the quasi-inextensibility of fiber. The insufficient of Mindlin shell for the deformation of fibrous material can be proved by the 4-point bending test.

As shown in Fig. 3.30(a), the specimen is bent under the press of the punch located above the specimen and the support below (four-point bending). Through the mechanical analysis of the four-point bending test neglecting the friction between the specimen and the experiment device, the specimen can be divided into three different zone. The material is free without constraint in the zone I, thus there will has no bending moment and transverse shear force. In the zone Ⅱ, the bending moment will change evenly, and there will has a constant transverse shear force. In the zone Ⅲ, the bending moment will keep constant and the transverse shear force will keep as zero (Thus this test is also called as pure bending test). The variation of the bending moment and transverse shear force is presented in Fig. 3.30(b).

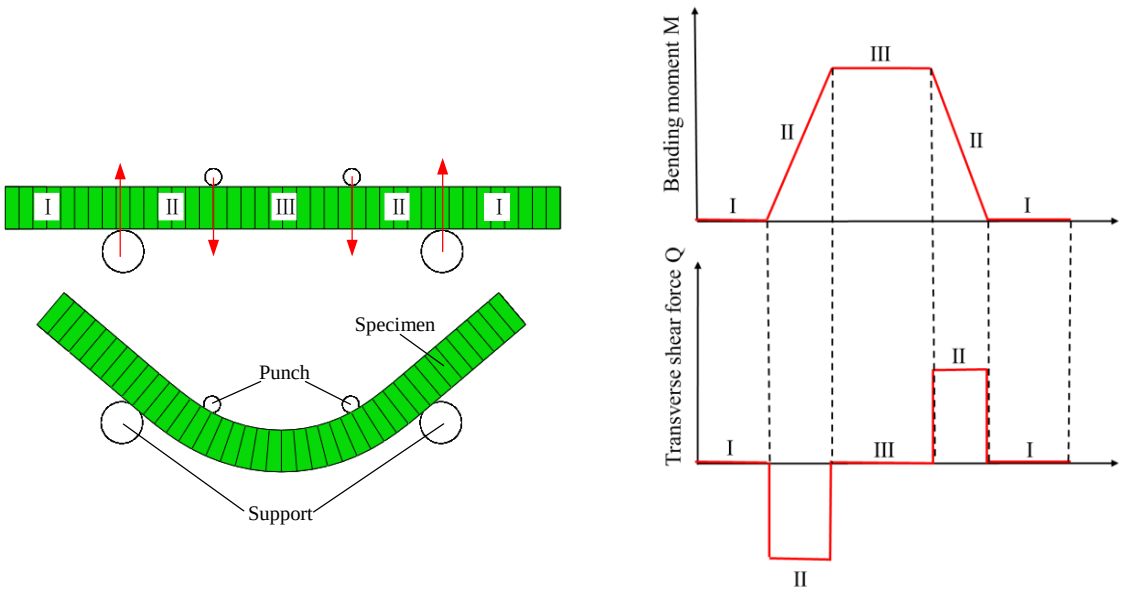

(a) (b)

Fig. 3.30. The four-point bending test (a) The experiment setting (b) The bending moment and corresponding shear force

For the Mindlin shell, the transverse shear strain is determined by:

$$\begin{Bmatrix} Q^1 \\ Q^2 \end{Bmatrix} = \mathbf{C}_s \begin{Bmatrix} \gamma_1 \\ \gamma_1 \end{Bmatrix} \tag{3.3}$$

Here Q^1, Q^2 are the transverse shear force in the two plane which are vertical to the mid-plane, γ_1, γ_2 are the transverse shear strain, and $\mathbf{C}_s$ are the corresponding transverse shear stiffness.

Thus for the four-point bending experiment, there is no transverse shear strain in the zone I and zone II within the Mindlin shell, and a constant transverse shear strain will exist in zone II. The simulation result using the Mindlin shell in Abaqus are listed in Fig. 3.31(a). In the simulation, the shell thickness is 15 mm, and the length is 300 mm. the general shell element S4R is adopted to conduct the simulation, and the element size is 5 mm × 5 mm. The material bending properties is corresponding to 10 layers of G1151 interlock fabric.

The four-point bending experiment of 10 layers of G1151 interlock fabric is shown in Fig. 3.31(b). Both the mid-line and the normal directors are painted as white. It can be found that the normal directors won't keep perpendicular to the mid-line in the zone I-III. Thus the transverse shear strain existed in the zone I-III. The transverse shear strain distributed in the different zone for different approach are given in the Table 3.3

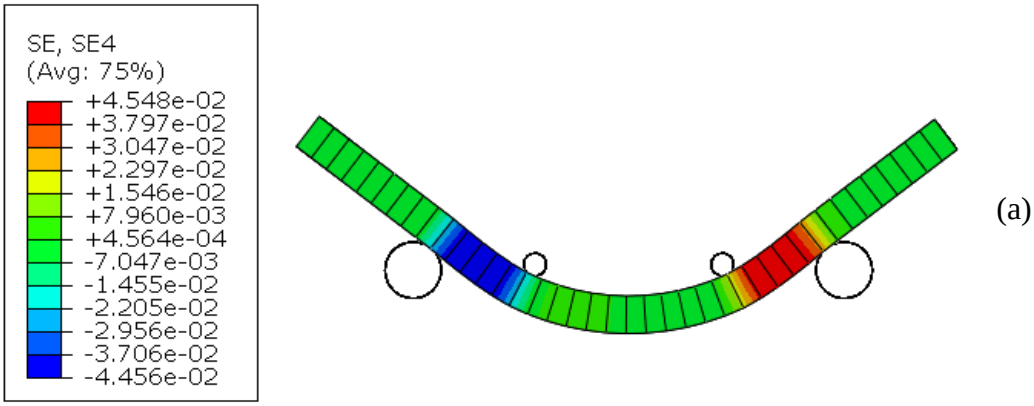

(a)

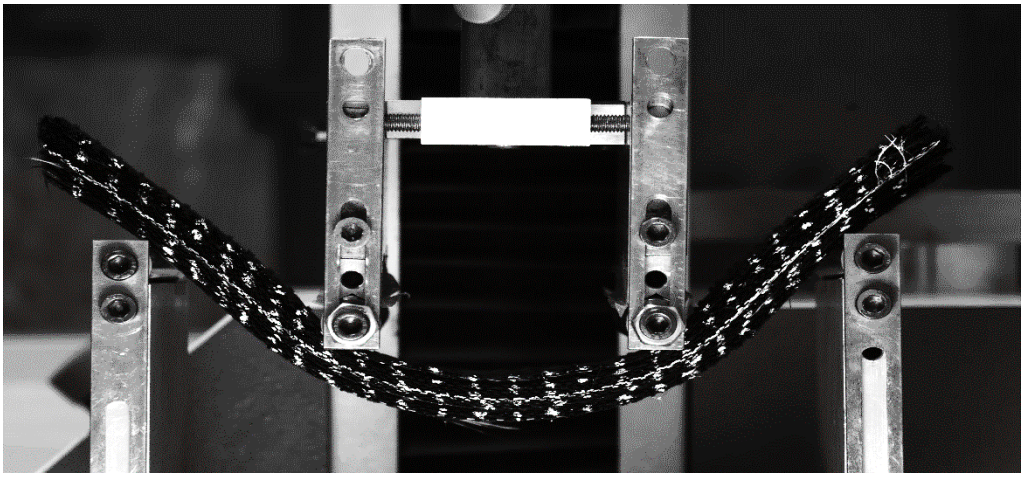

(b)

Fig. 3.31. The four-point bending comparison between Mindlin shell and fibrous material (a) Simulation result of Mindlin shell (SE4:transverse shear strain) (b) Experiment result of G1151 fabric material

Table 3.3 Transverse shear strain in different approach

Element type	Zone I	Zone II	Zone III
Kirchhoff shell	No	No	No
Mindlin shell	No	Yes	No
Fibrous material	Yes	Yes	Yes

The four-point bending tests using Mindlin shell with different transverse shear stiffness are conducted in Abaqus (Fig. 3.32(a)-(c)). The other material behavior and geometry setting are the same as the setting in Fig. 3.31(a). The transverse shear stiffness varied from 100 $N \cdot mm^{-1}$ to 1 $N \cdot mm^{-1}$ in Fig. 3.32(a)-(c). It can be found that the change between transverse shear stiffness and shear strain are inversely proportional.

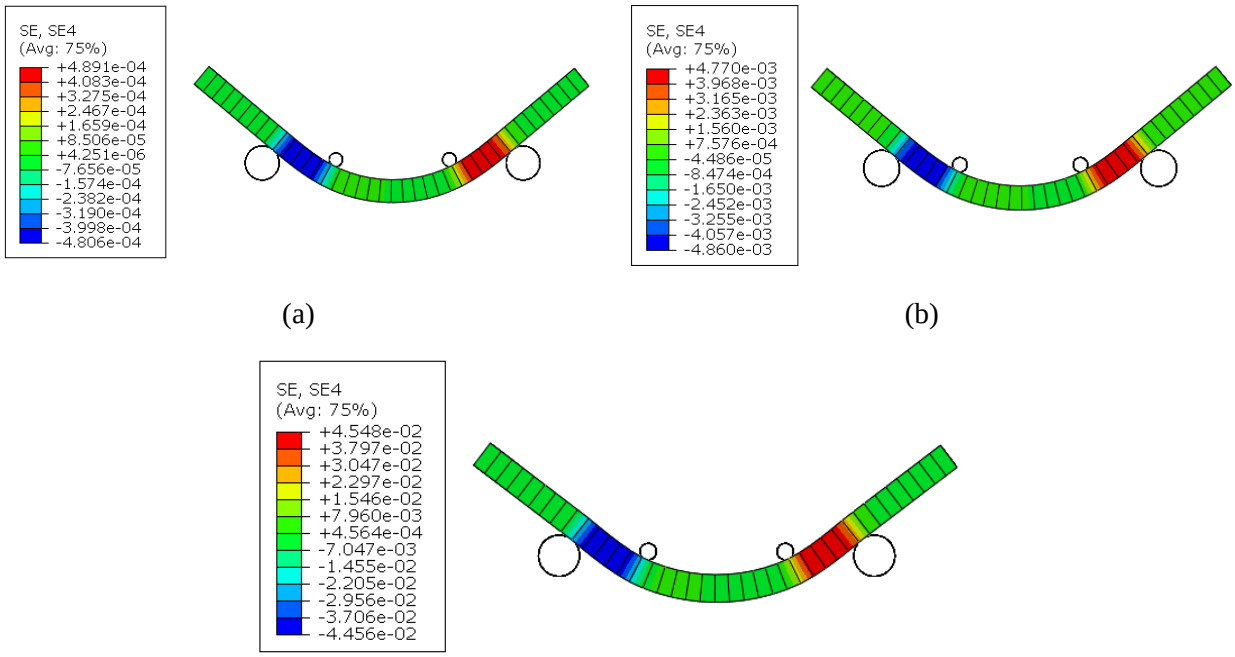

Fig. 3.32. Simulation result using different transverse shear stiffness of Mindlin shell (a) k_{13}=100 (b) k_{13}=10 (c) k_{13}=1

Through the above analysis and comparison, it can be concluded that the shell based on the Mindlin kinematics also cannot be used to predict the motion of the normal directors of woven materials.

3.5.3 The specific bending behavior of fibrous material

The special architecture of fabric in the textile composite and the special behavior considering the tensile, in-plane shear, and bending behavior give the fibrous material a very specific bending behavior, in particular, for the multi-layers forming. With the objective to modelling the multi-layer forming, the specific bending behavior of textile composite in the multi-layer forming will be analyzed here. The manuscript will force on the multi-layers with the same orientation, which will lay the groundwork for the further research on the multilayer with different orientations.

The bending characteristics of the multi-layer reinforcement are as follows:

(1). The bending stiffness is significantly smaller than the value given by the material tensile stiffness and the thickness.

The bending stiffness of a single layer reinforcement has been well discussed in section 2.1. For the multi-layer bending stiffness, Liang and Bai [Liang et al., 2017; Bai et al., 2020] has conducted the cantilever and three-point bending test to compare the bending stiffness between

single-layer and multi-layers, it is found that the bending stiffness of multi-layer is indeed larger than the summation of the bending stiffness of single-layer. And this phenomenon is because of the friction between the adjacent layers. Even though, it can be known that the bending stiffness of multi-layer reinforcement is still much smaller than the value given by the material tensile stiffness and the thickness.

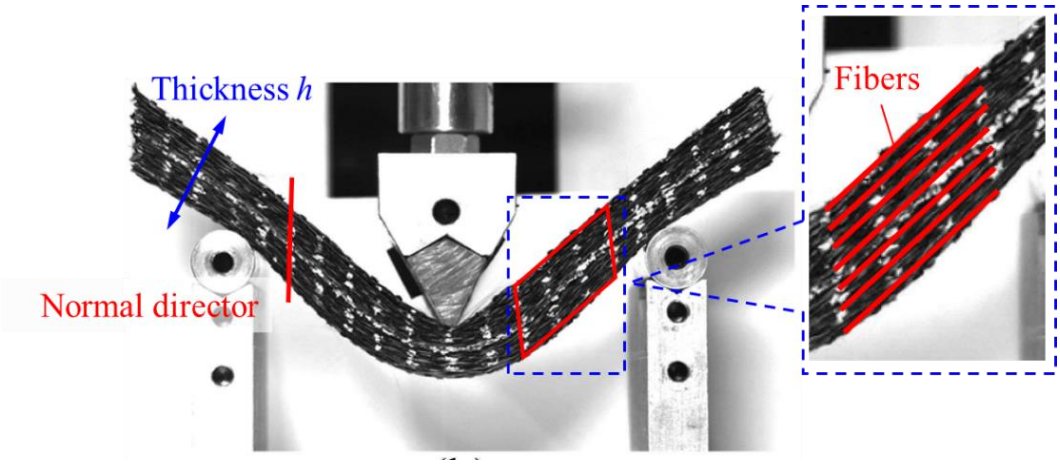

Fig. 3.33. Bending deformation of multi-layers G1151 interlock fabric

(2). The fibers at different position in the thickness direction keeps quasi-inextensibility, and the thickness will keep constant

The fibrous material tensile stiffness is much larger than the other two material stiffness: in plane shear stiffness and bending stiffness. The material will exhibit the large shear deformation and bending deformation during the draping process, and the tension deformation can be neglected as the fibers are supposed to be quasi-inextensibility. This is a very important point which lead to the material won't keep perpendicular to the middle surface, and the bending deformation in the thickness direction cannot be simulated by the classical shell elements including both the Kirchhoff and Mindlin shell elements. A three-point bending test of multi-layers G1151 interlock fabric is shown in Fig. 3.33. The thickness of the multilayer can be considered as constant when the wrinkles didn't appear in the forming process. The thickness will change due to the in-plane shear deformation, but the change is very small and can be seen as constant anyway. This is a reasonable assumption that will make the modelling of the multilayer deformation in the thickness be simple.

Several simulation approaches have been proposed considering specific bending behavior of the fibrous material (seen Fig. 2.4). These approaches will be conducted through different types of deformation to verify if these approach can predict the normal rotation in the thickness direction in the next section.

3.5.4 Comparison of different simulation approach

As introduced in Chapter 2, there are several approaches for the simulation analysis of the forming of the textile composite material taking into consideration of the bending behavior. These approaches have been validated that they can properly predict the in-plane deformation in the draping process of the textile composites. When the thickness of the material go relatively large for the multi-layers forming of 3D composite, it is critical important that the approach can predict the normal rotation in the thickness direction. In this section, the ability to predict the normal rotation of the proposed approach will be investigated. The considered simulation approaches here has:

- Laminated shell approach (seen in Fig. 2.4(a))
- Superimposition of shell element and membrane element (seen in Fig. 2.4(c))
- Stress result shell approach [Chen et al., 2021]
- Fibrous shell approach [Liang et al., 2017; Bai et al., 2020]

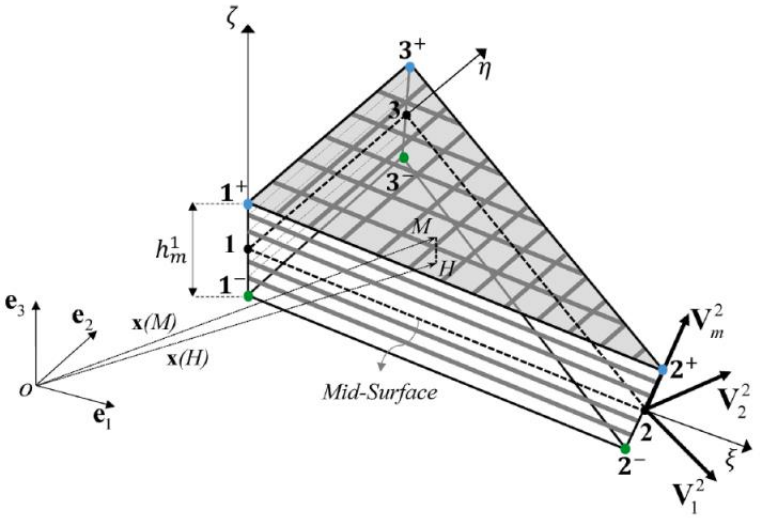

Fig. 3.34. 3D Fibrous shell approach [Bai et al., 2020]

For the laminated shell approach and the superimposition of shell element and membrane element, there are developed to decouple the bending behavior with the membrane behavior. The stress resultant approach have been introduced in Chapter 2 and been validated in Chapter 3. The proposed stress resultant approach has also been published in the [Chen et al., 2021]. The parameters input for the material behavior of these approaches have been described in the corresponding literature and listed in the Table 3.4. These approaches will be implemented in the commercial software Abaqus.

Besides these approaches, there is another simulation approach called the fibrous shell approach. With the objective to simulate the normal rotation, a fibrous shell dedicated to the multi-

layers reinforcement is developed in the work of Liang [Liang et al., 2017] for the 2D case like cantilever bending, and Bai[Bai et al., 2020] extend this approach to the 3D case bending deformation. The 3D fibrous shell element is presented in Fig. 3.34.

Table 3.4. Material behaviors input for all approach

Approach	Tensile	In plane shear	Bending
Laminated shell approach	Young's modulus	Geometry	Geometry
Superimposed approach	√ Membrane element	√	√ Shell element
Stress resultant	√	√	√
Fibrous shell	√	√	√

a) Cantilever test with a predefined displacement

In order to initial verify the ability to predict the normal rotation in the thickness direction of these approaches, a cantilever test with a predefined displacement at the endpoint is conducted at first. As shown in Fig. 3.35, the length of the specimen is 100 mm while the thickness is 10 mm. The boundary condition is a predefined displacement at the endpoint, and the displacement is 50 mm at the Y direction. The tensile stiffness are set as 10000 $N \cdot mm^{-1}$, and the bending stiffness is 74.1 N·mm. The input values of the tensile stiffness and bending stiffness for the different approaches are variant because the constitutive equations are different, but they are equivalent to describe to the same material behavior. This is a simple test but very meaningful, the normal directors should not be perpendicular to the middle surface due to the thickness is relatively large compared with the length of the specimen.

The output external force of the simulation results are listed in Table 3.5, it can be found that the external force at the nodes is all very small in different approaches. The tensile stiffness is very large and the bending deflection is also large. Thus the small external force proves that these approaches are well implemented in the Abaqus, and the decoupling of the bending behavior with the membrane behavior is achieved.

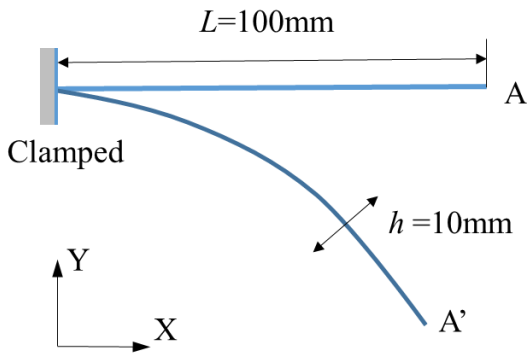

Fig. 3.35. The cantilever test with a predefined displacement

Table 3.5. External force output for the different approach

Simulation approach	Laminated shell	Superimposed elements	Stress resultant shell
Maximum external force (N)	0.077	0.076	0.076

The cantilever simulation results using different approach are listed in Fig. 3.36. For the simulation approaches: Laminated shell approach, Superimposition of shell element and membrane element, and stress resultant approach, the normal director keep perpendicular to the mid-surface.

Note: For the stress-resultant approach, the thickness didn't take into consideration, thus the deformation cannot be given in the Abaqus visualization. A Matlab code is programmed to view the normal rotation according to the results of mid-surface deformation and the normal rotation at the nodes.

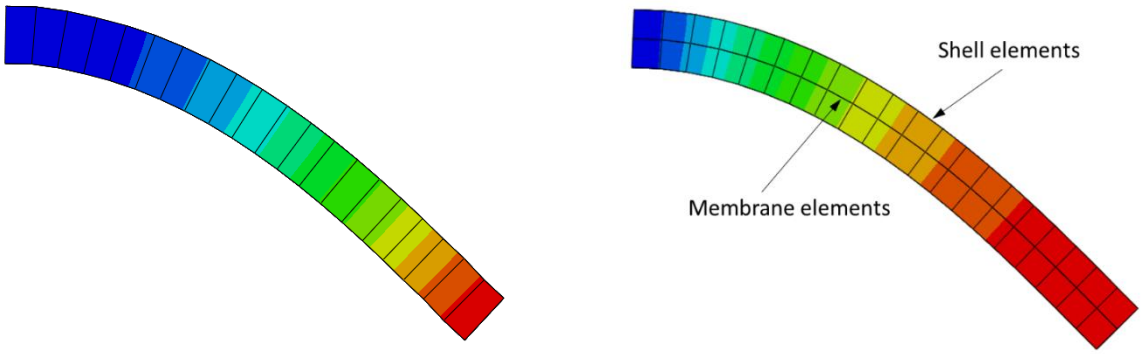

(a) (b)

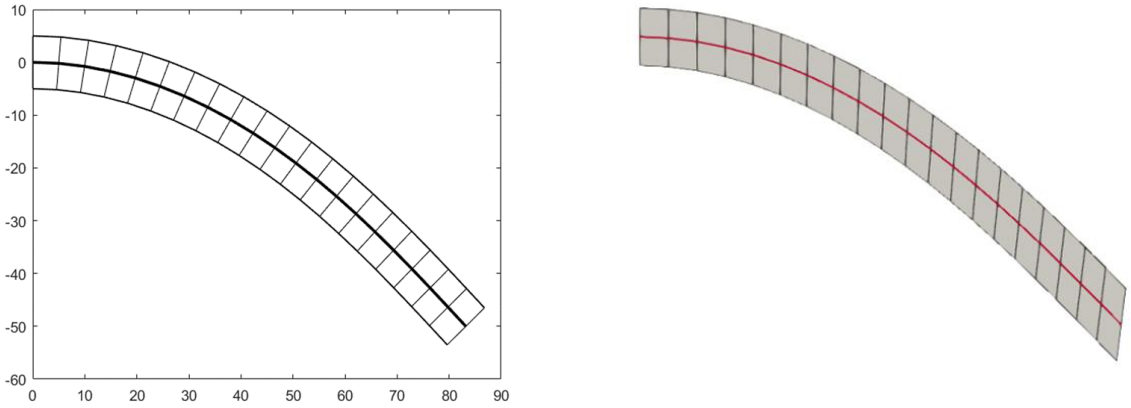

(c) (d)

Fig. 3.36. Cantilever simulation results using different approaches. (a) Laminated shell approach. (b) Superimposed element approach. (c) Stress resultant shell approach. (d) Fibrous shell approach.

b) Hemisphere forming test

The hemisphere forming tests are also conducted to investigate the normal rotation of different approaches. The geometry setting of the hemisphere forming is given in Fig. 3.13. The contour of the in-plane deformation is given in Fig. 3.37, and they share the same results.

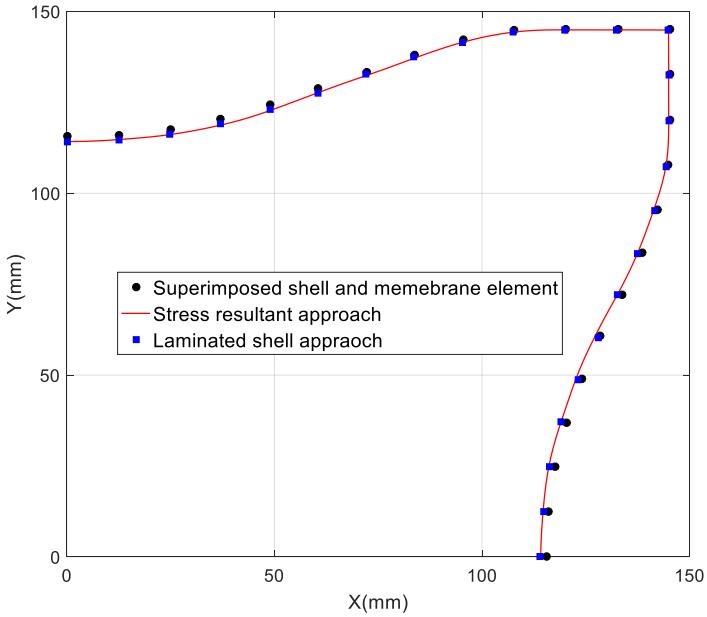

Fig. 3.37. Contour comparison of different approaches

Then the normal directors are plotted on the symmetry plane as shown in Fig. 3.38. The fibers are unfixed in this symmetry plane. It can been observed that the normal directors are still perpendicular to the mid-surface in the three previous approaches while the normal rotations occurs in the fibrous shell approach.

Through the above tests, we can know that the considered methods, except for the fiber shell approach specially developed for the deformation of thick materials, cannot simulate the normal rotation in the thickness direction. However, the fibrous shell approach is implemented in an in-house software that cannot be used for all users and based on the bending behavior of the thick material, the kinematic approach (introduced in section 1.3.1) can be adopted in the simulating of the normal rotation for the thick material with the same orientation. In the next section, the post-possessing method for predicting the normal rotation will be introduced.

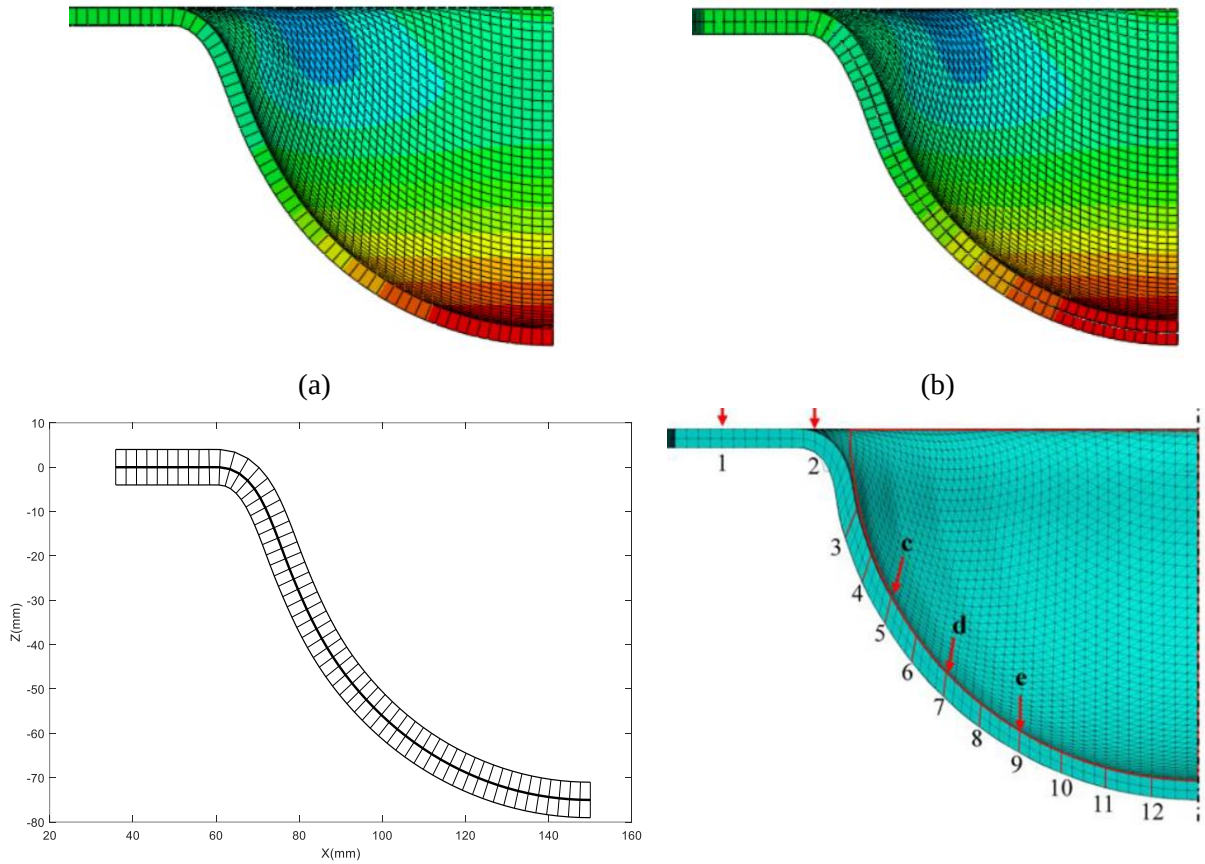

Fig. 3.38. Simulation results of hemisphere forming using different approaches. (a) Laminated shell approach (b) Superimposed element approach. (c) Stress result shell approach. (d) Fibrous shell approach

3.5.5 The post-processing method

Through the analysis of the bending deformation of thick fibrous material in section 3.5.3, the following assumptions can be made:

(1). The shell thickness doesn't change
(2). The fibers in the material are inextensibility
(3). The normal directors keep as a straight line

Based on the three assumption, the kinematic method will be presented in this chapter to obtain the normal rotation in the thickness directions for those approaches that only focus on the deformation at the mid-surface. And a post-processing code is programmed in the Matlab to conduct the calculation. The post-processing method is given in Fig. 3.39.

The position of the nodes on the mid-surface and the normal rotation in the global coordinate system will be the output of the simulation results using the simulation approaches like the laminated shells, superimposed elements, or stress resultant shell approach. These information will be input for the post-processing method. As shown in Fig. 3.39(a), the position of nodes on the bottom surface and top surface will be firstly determined according to the input information and the shell thickness using the equation as follows:

$$\begin{bmatrix} X_n \\ Y_n \\ Z_n \end{bmatrix} = \begin{bmatrix} X \\ Y \\ Z \end{bmatrix} + (-1)^n f \begin{bmatrix} R_2 \\ -R_1 \\ 1 \end{bmatrix} \tag{3.4}$$

Here, X, Y, Z are the position of the nodes on the mid-surface, and n belong to the set (1, 2). X_n, Y_n, Z_n are the position of the nodes on the top and bottom surface (n=1 represent the bottom and n=2 represent the top surface). R_1 and R_2 are the tangent values of the angle of the shell normal rotating around the x and y axes respectively. f is the thickness factor and it can be determined by:

$$f = \frac{h}{2\sqrt{1 + R_1^{\,2} + R_2^{\,2}}} \tag{3.5}$$

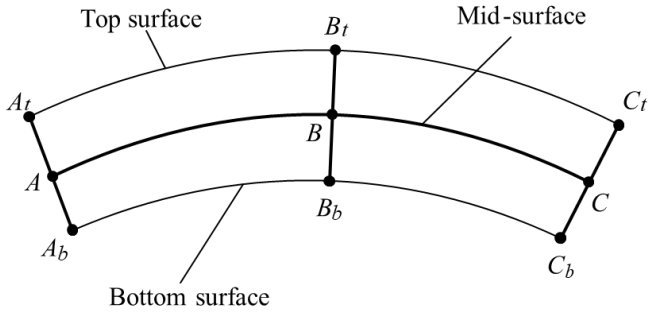

(a)

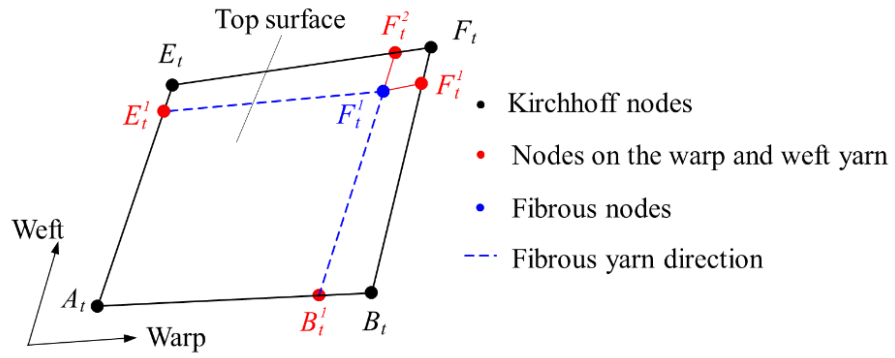

(b)

Fig. 3.39. Schematic diagram of the post-processing approach

As shown in Fig. 3.39, the nodes position calculated by the Eq (3.4) are marked as Kirchhoff nodes due to the fact that they are determined by the thickness lines that are perpendicular to the mid-surface. The warp and weft yarn direction will be initially determined by connecting these points. Base on the assumption that the fibers keep inextensibility ($A_tB_t^1 = AB$), the position of the fibrous nodes can be calculated in turn. At last, the normal direction will be obtained by connecting the corresponding fibrous point on the bottom surface and top surface.

3.5.6 Verification of the post processing

In order to verify the correctness of the post-processing method in calculating the normal rotation, the cantilever bending experiment test under gravity using the 130 layers with 13 mm thick papers is conducted. The geometry setting is shown in Fig. 3.40(a). The properties of a single-layer paper are listed in Table 3.6. The experimental result is given in Fig. 3.40 (b).

Table 3.6. The properties of a single-layer of papers

Properties	Values
Tensile stiffness	230 N·mm^{-1}
Bending stiffness	0.4 N·mm
Density	0.00081 g·mm^{-3}
thickness	0.1 mm

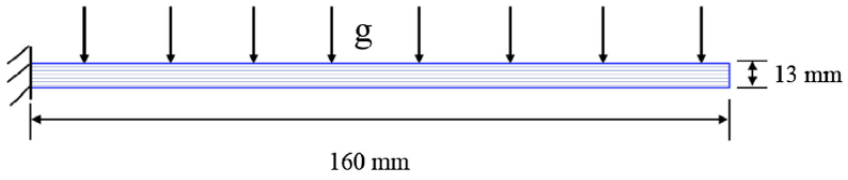

(a)

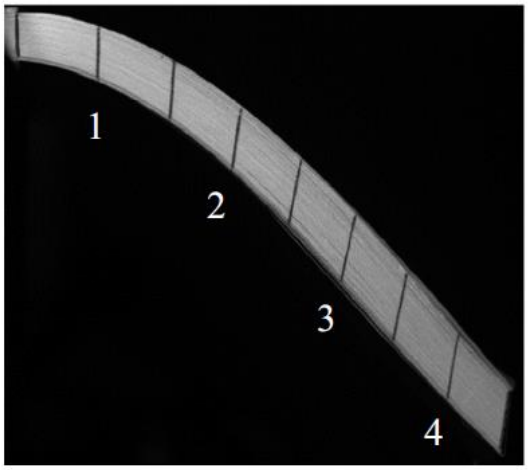

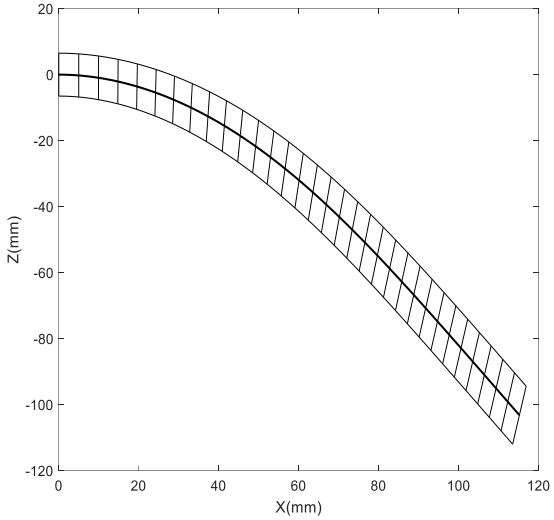

(b) (c)

Fig. 3.40. Cantilever bending test of 130 layers paper. (a) The geometry setting. (b) Experimental results [Liang et al., 2017] (c) Post-processing results.

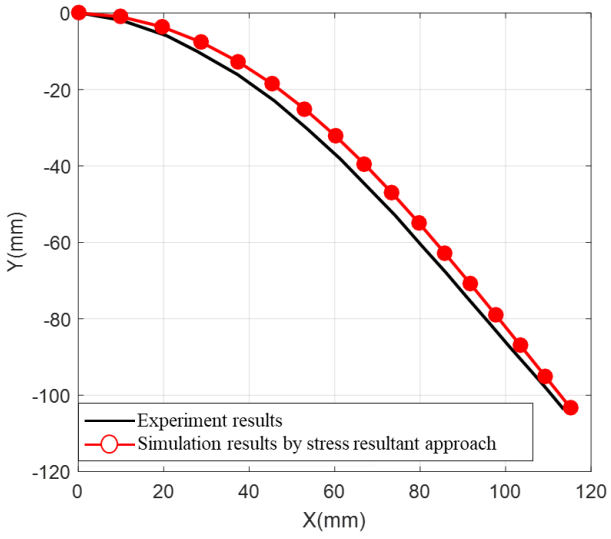

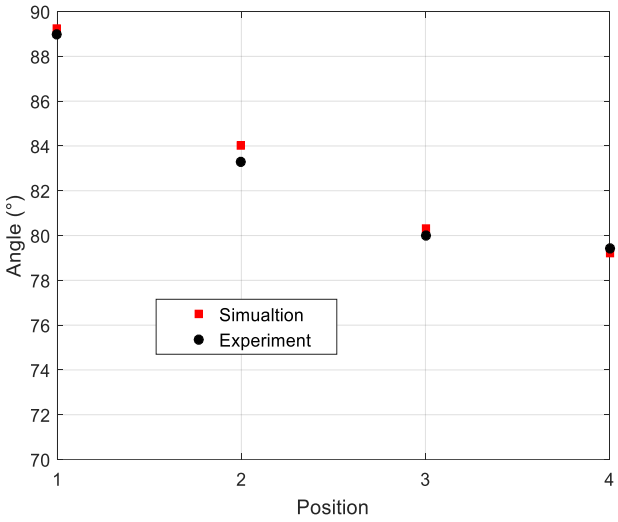

(a) (b)

Fig. 3.41. Comparison between experiment results and post-processing results (a) The Middle line comparison. (b) The normal rotation comparison.

The corresponding simulation is conducted in the Abaqus using the stress resultant approach to obtain the mid-surface deformation. The comparison of the mid-surface between the simulation

and the experiment is presented in Fig. 3.41 (a), they are quite close. And next the simulation results are input for the post-processing. The post-processing result is given in Fig. 3.40(c), it can be seen that the normal directors are not perpendicular to the mid-surface which is consistent with the experiment. The rotation of the normal directors is compared in Fig. 3.41(b). Through the comparison, it can be known that this fishnet-like post-processing method can correctly obtain the normal rotation in this case. For the more complicated boundary conditions, it may need to be future investigated.

3.6 Summary of Chapter 3

Due to the possible slippage between the fibers, the textile composite exhibit specificity of the bending deformation different from continuous material. To simulate the textile composite forming using the shell model, a hypoelastic stress resultant approach is proposed in Chapter 2. Through two benchmark shape forming: hemisphere and tetrahedron, this chapter is to validate the effectiveness of the proposed approach.

The experiment device to perform the forming experiment and to obtain the experimental result is firstly introduced, and the procedure to make the simulation of textile composite forming in Abaqus using the presented approach is also introduced. Then the hemisphere and tetrahedron forming with three layup configuration are conducted, the comparison between simulation and experiment are made from different aspects including the in-plane shear angle, fabric contour, punch force, and wrinkles. Through the comparison, it can be concluded that the presented approach can correctly predict the textile composite in-plane deformation.

Through several bending tests, it is found that the normal rotation of the shell element in the proposed approach follows the Kirchhoff assumption, and so did the other simulation approach that achieve the decoupling of bending behavior with membrane behavior. To overcome this drawback, a post-processing method is proposed based on the material kinematics. This fishnet-like post-processing method is validated effective by the simple cantilever case. For the more complicated boundary conditions, it may need to be future investigated.

In the forming experiment, it is also found that the wrinkles will appear when the material properties change even under the same boundary conditions. This phenomenon is due to the different material drapability and this will be discussed in Chapter 4.

Chapter 4 Experimental analysis of the textile composite drapability

Wrinkles is one of the main defects in the forming of textile composite reinforcement at the macro scale. The drapability is the ability of a textile material to be draped without wrinkling. This chapter aims to quantify the drapability. The relationship between wrinkles and material properties is studied, through a sets of square box and cylinder forming experiments, it is found that the in-plane shear stiffness decrease the tendency to wrinkle while the bending stiffness increases it. Based on this experimental phenomenon, a drapability ratio considering the material in-plane shear and bending properties is proposed to characterize the forming properties of the textile composite reinforcement.

Contribution: the research work of this chapter is directed by Philippe Boisse and Julien Colmars. The experiment in this chapter was completed in cooperation with Renzi Bai.

Content of Chapter 4

Chapter 4 Experimental analysis of the textile composite drapability 111

4.1 Drapability analysis of the textile composite 112

4.2 Introduction to the prepared textile composite reinforcement 114

4.3 Experimental determination of shear and bending behavior 115

4.3.1 In-plane shear stiffness 116

4.3.2 Bending stiffness 121

4.4 The definition of drapability ratio 123

4.5 Forming experiment 125

4.5.1 Experiment setup 126

4.5.2 Square box forming 126

4.5.3 Cylinder forming 131

4.6 Summary of Chapter 4 134

4.1 Drapability analysis of the textile composite

The onset of wrinkles will highly decrease the properties of the final composite part. It is necessary to avoid the wrinkles forming or transfer the wrinkle to the unimportant place. There are several factors that will induce the occurrence of the wrinkles including the process parameters (blank holder force, position, forming speed, etc.) and the used material. The process parameters can be optimized by numerical analysis. Besides that, the material properties play an important role in the forming of undesired wrinkles.

The draping behavior of textile composite reinforcement can be measured by the drape meter [Chu et al., 1950; Cusick, 1968]. As illustrated in Fig. 4.1(a), the drape meter consists of two circular supporting disk, and the circular fabric sample will be sandwiched between them. The fabric may drape under its gravity. The drape area will be projected on the Perspex with the light placed under the sample. The paper ring was placed on the Perspex. The radius of the paper ring is equal to the initial fabric sample. In the draping process, some obvious folds will be generated. The material drapability can be directly described by the number of the folds. A Drape coefficient is also defined to quantitate the material drapability. As shown in Fig. 4.1(b), the drape coefficient is the ratio of the projected area of the draped fabric sample to its undraped area[Chu et al., 1950].

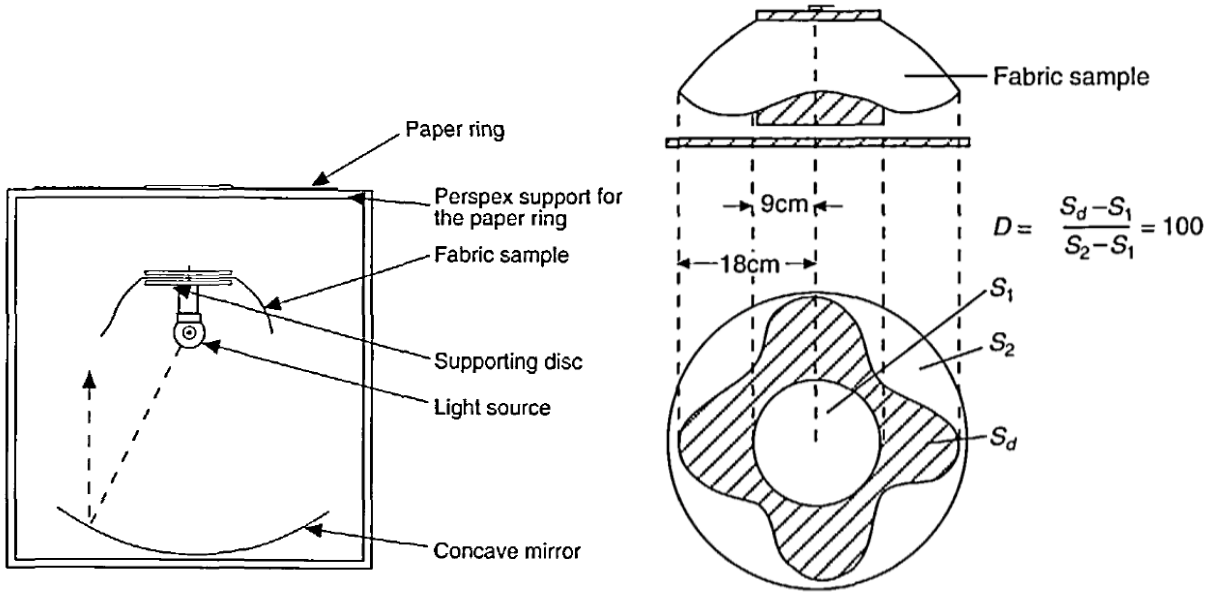

(a) (b)

Fig. 4.1 (a) Schematic diagram of the drape meter. (b) Calculation of the Drape coefficient. [Vangheluwe & Kiekens, 1993]

According to the principle of the drape meter, the tested number of folds or the drape coefficient is only linked with the bending behavior of the fabric. This is not sufficient to characterize the material's ability to resist wrinkling. At the macroscale scope, there are three main

material behavior that will influence the material deformation which are tensile, in-plane shear and bending stiffness. As shown in Fig. 4.2, the role of these three material behavior on the wrinkles forming have been studied by the numerical analysis, it is found that the in-plane shear behavior plays a main role on the onset of wrinkles while the bending stiffness will influence the shape of the wrinkles.

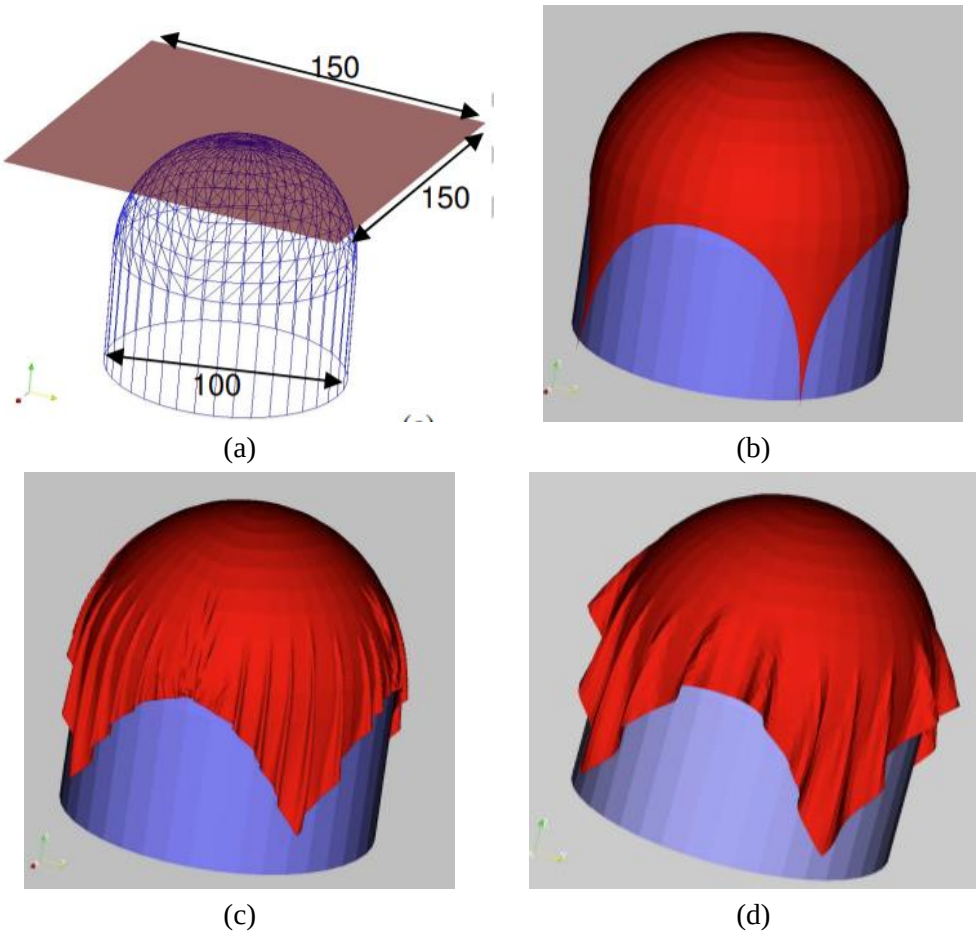

Fig. 4.2. The role of the material behavior on the wrinkles forming through simulation [Boisse et al., 2011] (a) geometry setting (b) Tensile stiffness only. (c) Tensile stiffness and in-plane shear stiffness. (d) Tensile stiffness, in-plane shear stiffness and bending stiffness.

There are also some researches from the experiment view on the onset of the wrinkles. Firstly, as discussed in Chapter 3, for the four-layer hemisphere forming experiment, it has been found that the status of wrinkles are different when using different material (the wrinkles appear in Fig. 3.17(a) using plain weave while no wrinkles are observed in Fig. 3.14(c) using G1151). In the work of Huang [J. Huang et al., 2021], it is found that the wrinkles will be also different for the single-layer square box forming for the two types of material with different weave pattern (shown in Fig. 4.3). In the work of Viisainen [Viisainen & Sutcliffe, 2021], two types of NCF with different

architecture are used to conduct the hemisphere forming, and it is observed that the wrinkles differ when used different material and also the different layer-up.

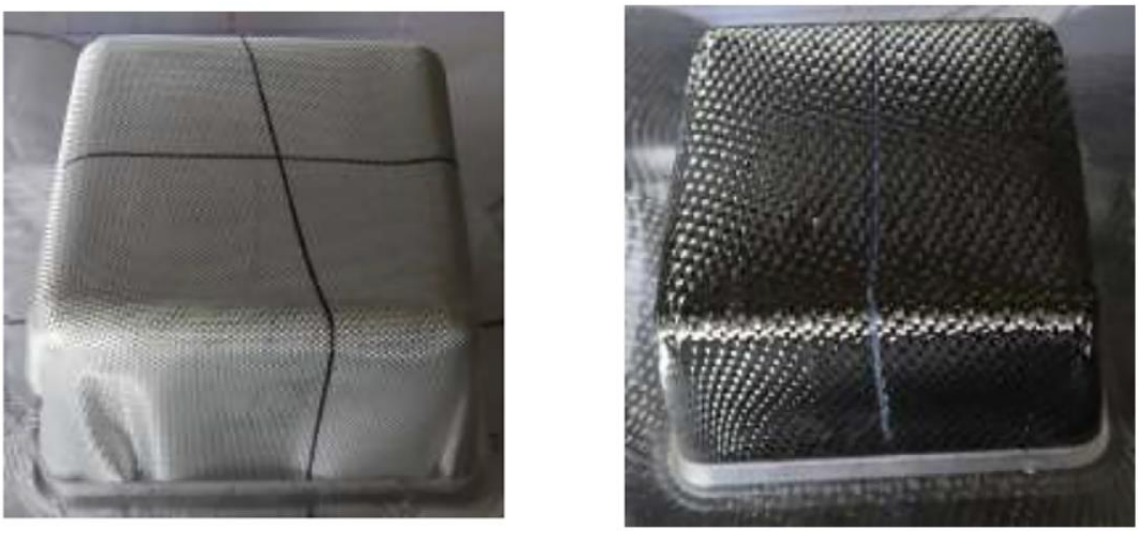

(a) (b)

Fig. 4.3. Square box forming of a single layer oriented at 0°/90°. (a) Glass plain weave. (b) Carbon plain weave [J. Huang et al., 2021].

In this chapter, the material drapability will be researched through the forming experiment using a variety of different textile composites. The drapability of the material is the ability to drape without wrinkles, and the material with good drapability means that the material tends to form a complex shape without wrinkles. The work of this chapter aims to quantify material drapability considering material behaviors.

4.2 Introduction to the prepared textile composite reinforcement

In order to study the drapability of the textile composite reinforcement, the forming experiments are conducted to observe the wrinkles, and several woven materials with different material properties are selected for the forming experiments. For comparison, an isotropic material is also used in the forming experiments. The selected materials are listed in Table 4.1.

Table 4.1 The selected materials for forming experiments

Plain	Glass 1 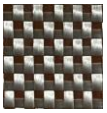	Glass 2 
	Glass 3 	Carbon 4 

Twill	Twill 1		Twill 2		Twill 3	
Satin	Satin					
Interlock	G1151		G1100			
NCF	NCF carbon		NCF triaxial			
Isotropic material	Plastic Film					

4.3 Experimental determination of shear and bending behavior

At the macro scale, three types of material properties plays the main role in the material forming process, shown in Fig. 4.4. Due to the possible relative slippage between warp and weft yarns, the in-plane shear stiffness and out-of-plane bending stiffness is much lower compared with the tensile stiffness. The rigidity in the fiber directions can be normally seen as quasi-inextensible, thus only the in-plane shear behavior and out-of-plane bending behavior are researched in this chapter. The in-plane shear stiffness and out-of-plane bending stiffness for different woven material will be tested below:

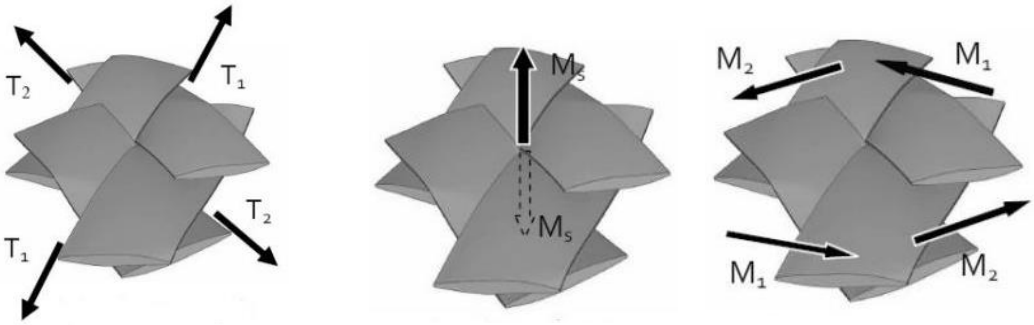

(a) (b) (c)

Fig. 4.4 The three material deformation modes of woven material at the macro scale. (a)Tensile (b) In-plane shear (c) Out-of-plane bending

4.3.1 In-plane shear stiffness

For the material shear behavior considered here, a shear moment on a unit cell $M_s(\gamma)$ (Unit: N·mm·mm^{-2}) is introduced to describe the shear response, and the shear deformation is described by the shear angle γ which is the angle change between the warp and weft yarns. The relationship between the shear moment $M_s(\gamma)$ and the shear angle γ is normally nonlinear, and the expression of the shear moment $M_s(\gamma)$ can be obtained by an odd degree polynomial fitting:

$$M_s(\gamma) = k_0\gamma + k_1\gamma^3 + k_2\gamma^5 \tag{4.1}$$

Then the material shear stiffness k_c can be calculated by taking derivative of Eq.(4.1). At here, in order to quantify the drapability concerning the material shear stiffness and bending stiffness, the in-plane shear stiffness is considered linear for simplicity. As shown in Fig. 4.5, selecting the shear moment data when the shear angle equals to 40° for linear fitting to obtain the material linear shear stiffness, and the material shear behavior expression will be simplified as below:

$$M_s(\gamma) = k_c\gamma \tag{4.2}$$

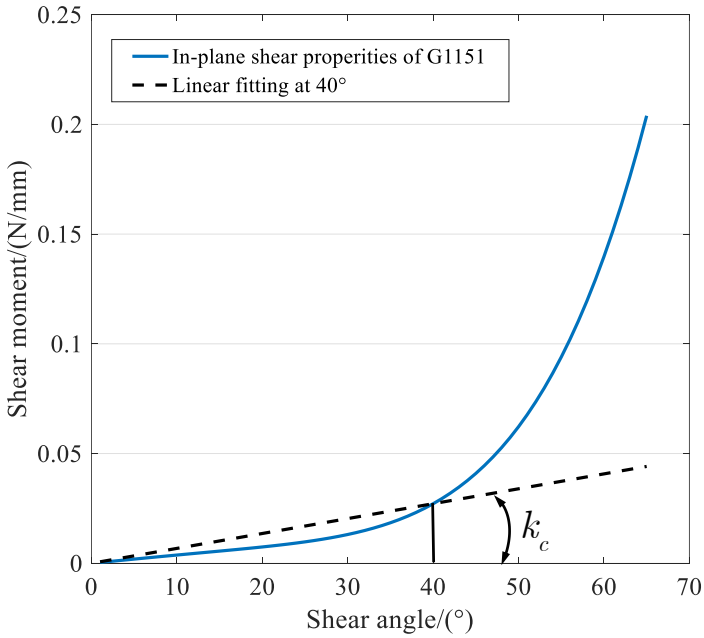

Fig. 4.5 The linear fitting of in-plane shear properties

For the textile composites, the in-plane shear stiffness can be tested by the bias extension test and picture frame test [Lebrun et al., 2003; Harrison et al., 2004; Launay et al., 2008; Cao et al., 2008]. For isotropic materials, the shear stiffness will be calculated according to the Young's modulus and Poisson's ratio.

a) Textile composites

The in-plane shear behavior of the textile composites can be determined by the bias extension test and the picture frame test which have been introduced in the section 2.4.2. The tested in-plane shear stiffness of the selected materials will be presented here.

(1). Bias extension test

In the experimental process, the external clamping force F is recorded through the load sensor used in the experiment. Based on the energy conservation, the relationship between the shear moment M_s and the clamping force can be expressed as [Launay et al., 2008; Cao et al., 2008]:

$$M_s(\gamma) = \frac{1}{2H - 3W}\left(\left(\frac{H}{W} - 1\right) \cdot F \cdot \left(\cos\frac{\gamma}{2} - \sin\frac{\gamma}{2}\right) - W \cdot M_s\left(\frac{\gamma}{2}\right)\right) \tag{4.3}$$

The recorded clamping force F as a function of the shear angle gives the expression of the shear moment $M_s(\gamma)$, which will be approximated by an odd degree polynomial fitting (Eq.(4.1)). Then the in-plane shear stiffness k_c can be obtained by calculating the slope of the linear fitting when the shear angle is 40° (0.698rad):

$$k_c = \frac{M_s(\gamma = 0.698)}{0.698} \tag{4.4}$$

Table 4.2 Experiment parameters of the bias extension test

Specimen length L (mm)	Specimen width W (mm)	Maximum stretch length d (mm)	Test range of the force sensor (N)
210	70	50	0-100

In the bias extension test to determine the in-plane shear stiffness, the experimental parameters adopted are listed in Table 4.2. Each set of the experiments was repeated twice to check the repeatability of the experimental results. Fig. 4.6 is the G1151 experimental curve of the clamping force F at a different stretch distance in the different tests, it showed that the repeatability of this experiment was good. Then the calculation of the in-plane shear stiffness took the average of the experimental data.

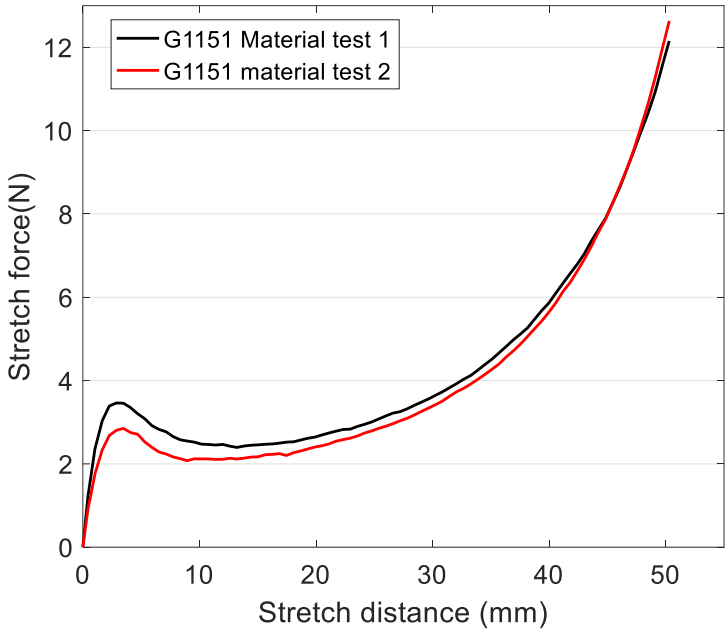

Fig. 4.6 G1151 experimental curve of the clamping force at different stretch distance

All the selected textile composites except the triaxial NCF adopt this method to get the shear stiffness. The tested in-plane shear stiffness is shown in Table 4.3.

Table 4.3 The in-plane shear stiffness k_c of the selected textile materials

In-plane shear behavior : $M_s(\gamma) = k_c\gamma$			
Material	k_c(N/mm)	Material	k_c(N/mm)
Glass 1	0.007	Twill 3	0.04
Glass 2	0.07	Satin	0.05
Glass 3	0.02	G1151	0.03
Carbon 4	0.2	G1100	0.02
Twill 1	0.02	NCF Carbon	0.008
Twill 2	0.03		

(2). Picture frame test

For the picture frame test, the introduced shear moment $M_s(\gamma)$ is related to the machine load *F* using the equation:

$$M_s(\gamma) = \frac{F_{sh}\cos\gamma}{L_{fabric}} = \frac{F\cos\gamma}{2L_{fabric}\cos\alpha} = \frac{F\cos\gamma}{2L_{fabric}\cos(\frac{\pi}{4}-\frac{\gamma}{2})} \tag{4.5}$$

Here, F_{sh} is the shear force on the side of the specimen, and L_{fabric} is the side length of the specimen. Then in the same way as the bias extension test, the expression of the shear moment $M_s(\gamma)$ will be approximated by a linear fitting, the shear stiffness k_c is calculated as $k_c = M_s(\gamma=0.698)/0.698$ (Eq.(4.4))

Table 4.4 Experiment parameters of the picture frame test

Frame length L_{frame} (mm)	Specimen length L_{fabric} (mm)	Maximum stretch length d (mm)	Test range of the force sensor (N)
135	90	60	0-1000

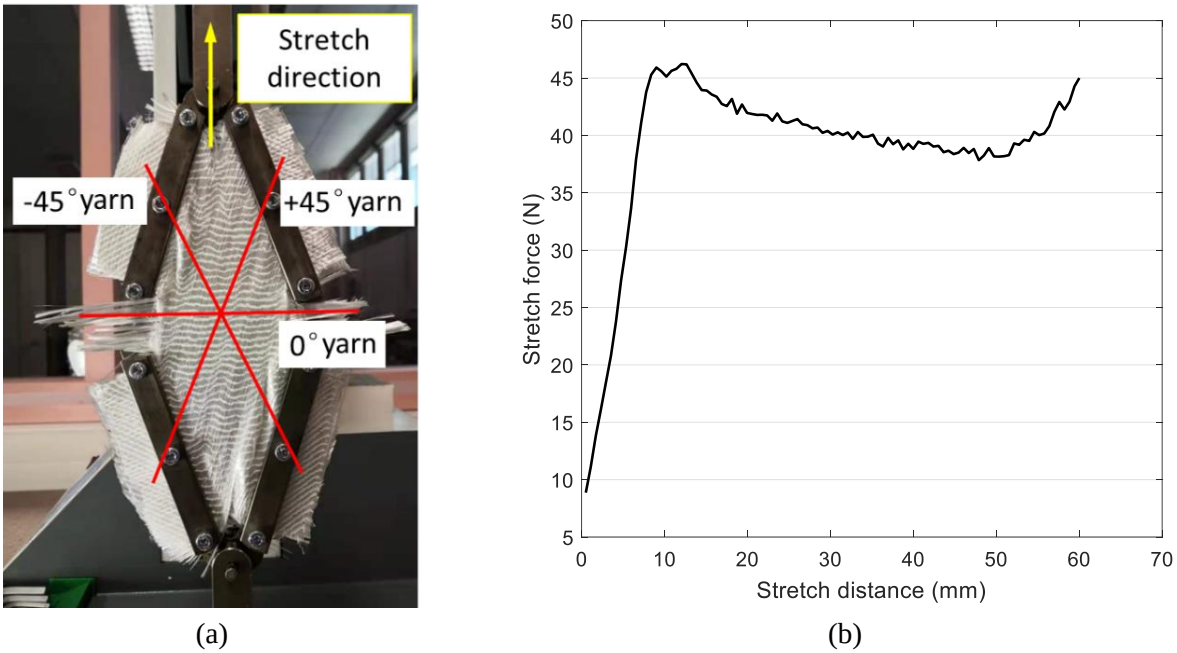

(a) (b)

Fig. 4.7 The picture frame test of triaxle NCF (a) Experimental setting (b) Experimental curve of stretch force versus stretch distance.

In the case of triaxial NCF, there are three yarns direction. The kinematics of triaxial NCF in the bias extension test is different with the case of bidirectional reinforcement. Nevertheless, the picture frame test can be performed to test its in-plane shear behavior. As shown in Fig. 4.7(a), the ±45° yarns are clamped by the picture frame, and third yarn direction is perpendicular to the stretching direction. The experimental parameters used in the test are listed in Table 4.4.

The experimental result of stretch force versus stretch distance is shown in Fig. 4.7(b). It can be seen that the stretch force increases linearly at the first 10 mm stretch distance. This is because that yarns in the different directions in NCF are connected together by stich, the shear resistance in the initial shear deformation mainly comes from the interaction between yarns and stich. Once the braided structure of the stich is destroyed due to the shear deformation, the shear resistance will come from the friction between yarns, then the stretch will remain stable in the following stretch displacement.

According to the Fig. 4.7, using Eq.(4.4) and (4.5), the shear stiffness of the triaxle NCF can be obtained as k_c = 0.48 N·mm^{-1}.

b) Isotropic material

For the isotropic material, the in-plane shear stiffness can be calculated directly based on Young's modulus E and Poisson's ratio υ. The shear modulus G is calculated as:

$$G = \frac{E}{2(1+\nu)} \tag{4.6}$$

The resultant shear force N_{12} is the integral of the in-plane shear stress along the thickness direction. Then the resultant shear force can be calculated:

$$N_{12} = \int_{-\frac{h}{2}}^{\frac{h}{2}} \frac{G\gamma}{2} dz \tag{4.7}$$

Here, h is the sample thickness. The resultant shear force N_{12} is related to the shear moment M_s:

$$M_s = N_{12} \cos\gamma \tag{4.8}$$

Combining Eqs. (4.6)-(4.8), the relationship between shear moment M_s and the shear angel γ of the isotropic material can be obtained:

$$M_s = \frac{Eh\gamma \cos\gamma}{4(1+\nu)} \tag{4.9}$$

Table 4.5 Experiment parameters of the tensile test

Specimen length L (mm)	Specimen width W (mm)	Specimen thickness h (mm)	Maximum stretch force F (N)	Test range of the force sensor (N)
100 mm	25 mm	0.5 mm	85 N	0 – 100 N

Then the tensile experiment is performed on the traction machine. The experimental parameters of the tensile test is given in the Table 4.5. Fig. 4.8 shows the experimental curve of the traction force and traction displacement.

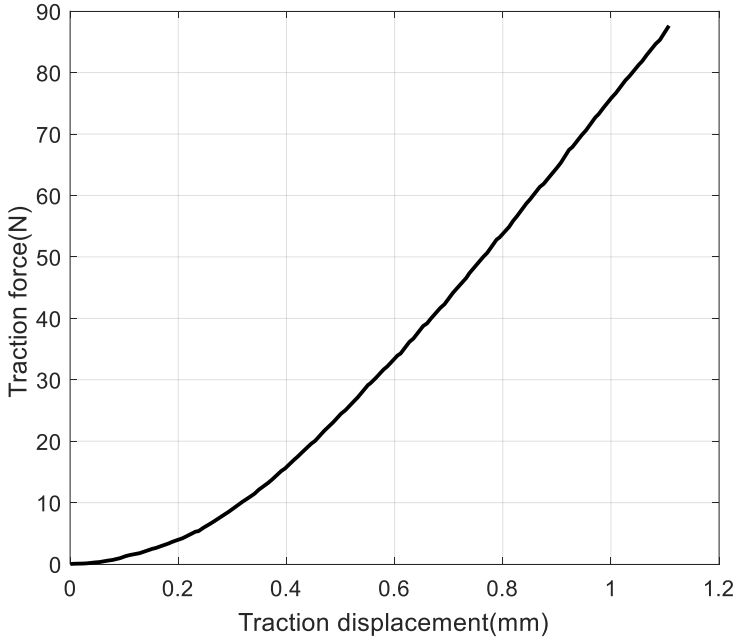

Fig. 4.8 Experimental curve of force versus displacement of the isotropic material.

Through the linear fitting of Fig. 4.8, the calculated Young's modulus E of the tested isotropic material is 822 Mpa. The isotropic material used in the experiment is composed of rubber, and it can be seen as incompressible material. Thus the Poisson's ratio υ is set as 0.5. The isotropic is selected as reference in the forming experiment. In order to compare with the textile material, the calculation of the shear stiffness still choose when the shear angle is 40°. According to Eq.(4.9), the in-plane shear stiffness of this isotropic material can be calculated as k_c = 52.5 N·mm^{-1}.

4.3.2 Bending stiffness

The bending stiffness can be assumed to be linear and it can be measured simply by the Peirce cantilever test [Peirce, 1930]. As shown in Fig. 4.9, in the Peirce cantilever test, the specimen is bent under its gravity, and the cantilever length will slowly increase until the material touch the plane with an inclination angle of 41.5°. Through measuring the cantilever length l, the material bending behavior can be calculated by [Peirce, 1930; Boisse et al., 2018]:

$$M_b(\chi) = D_b\chi \qquad \mathrm{D}_b = \frac{l^3}{8}w \tag{4.10}$$

Here, $M_b(\chi)$ is the bending moment, χ is the bending curvature, D_b is the bending stiffness, and ω is the material areal density.

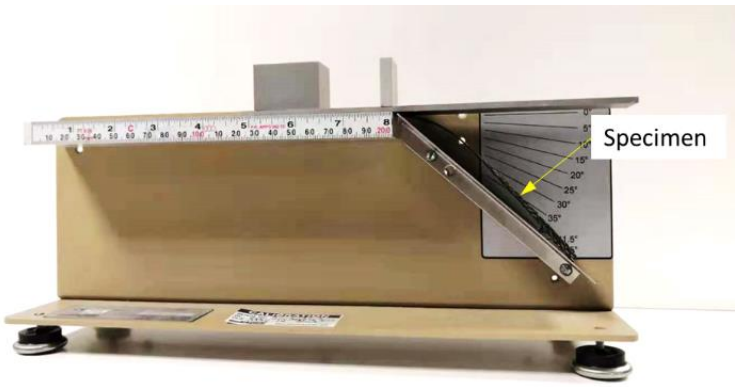

Fig. 4.9 The Peirce cantilever test

Table 4.6 The areal density of the selected materials

Material	Areal density w (g/m^2)	Material	Areal density w (g/m^2)
Glass 1	347	Satin	290
Glass 2	745	G1151	630
Glass 3	160	G1100	607
Carbon 4	675	NCF Carbon	312
Twill 1	418	NCF Triaxle	1133
Twill 2	235	Plastic Film	595
Twill 3	330		

According to the expression of the bending stiffness in Eq.(4.10), to obtain the bending stiffness, it is needed to get the material areal density *w* and the cantilever length *l*. The material areal density is tested by the electronic balance using Eq.(4.11) . The measured material areal density is given in the Table 4.6.

$$w = \frac{m}{A} \tag{4.11}$$

Where *m* is the tested mass of the sample, and *A* is the sample area.

Then the Pierce cantilever tests are conducted on all materials described in Table 4.1. For a material, the difference in bending stiffness in different yarn directions is ignored and an average value of the bending length along different yarn directions is used to calculate the bending stiffness.

Based on the Eq.(4.10), the calculated bending stiffness D_b of all the materials are listed in Table 4.7.

Table 4.7 The out of plane bending stiffness D_b of the selected materials

Out of plane bending behavior : $D_b = \frac{l^3}{8} w$			
Material	D_b(N·mm)	Material	D_b(N·mm)
Glass 1	0.2	Satin	3.4
Glass 2	2.7	G1151	4.5
Glass 3	0.1	G1100	3.4
Carbon 4	1.4	NCF Carbon	0.9
Twill 1	0.5	NCF Triaxle	1.5
Twill 2	3.1	Plastic Film	0.7
Twill 3	2.6		

4.4 The definition of drapability ratio

The textile composite materials can be seen as composed of a set of woven unit cell (Seen in Fig. 4.4). Considering the three material behaviors (tensile stiffness, in-plane shear stiffness and out of plane bending stiffness) at macro scale, the principle of virtual work of the textile material can be written in the following form:

$$\delta W_{\text{int}} = \delta W_t + \delta W_s + \delta W_b \tag{4.12}$$

Here, δW_t, δW_s, and δW_b are the increment of virtual works of tensile, in-plane shear and out of plane bending respectively. In a woven unit cell, they can be written as:

$$\delta W_t = \delta \varepsilon_{11} T^{11} + \delta \varepsilon_{22} T^{22} \tag{4.13}$$

$$\delta W_s = \delta \gamma M_s \tag{4.14}$$

$$\delta W_b = \delta \chi_{11} M^{11} + \delta \chi_{22} M^{22} \tag{4.15}$$

Here, $\delta\varepsilon_{11}$, $\delta\varepsilon_{22}$ are the tensile strain increment in the warp and weft yarn direction, $\delta\gamma$ is the shear strain increment, and $\delta\chi_{11}$, $\delta\chi_{22}$ are the bending curvature increment in the warp and weft direction. T^{11}, T^{22}, M_s, M^{11}, M^{22} are the corresponding stress and moment resultants.

When the material is subjected to deformation, it will cause the above three kinds of energy changes. Minimization of the total internal energy W_{int} lead to a competition between these three energy.

Due to the possible slippage between fibers, the material shear and bending stiffness are much smaller than the tensile stiffness, thus the internal energy will tend to be transferred to the part of shearing and bending energy causing the material to shear and bend. When the unexpected bending deformation occurs, wrinkles appear on the reinforcement. In the forming process, two main factors may cause the wrinkling:

(1) Yarn compression (Concerning tensile and bending behavior)
(2) In-plane shear deformation (Concerning in-plane shear and bending behavior)

For the yarn compression, the material is very prone to wrinkles. The energy involved in this type of deformation has tensile energy and bending energy, the material will tend to the out of plane bending deformation, because the bending energy caused by the bending deformation is much smaller than the tensile energy caused by the yarn compression. For this type of wrinkle, it can be avoided by the boundary condition, such as applying a blank holder. The blank holder will prevent energy transfer to the bending through adding the pressure on the blank holder.

For in-plane shear deformation, the shear energy will accumulate along with the shear deformation increase. When the shear angle increases to a certain extent, the energy will be also transferred to the bending, resulting in wrinkles. In some previous research [Prodromou & Chen, 1997], this shear angle is called the shear locking angle of the material (up to 40°-45° for textile composite). At the recent studies, it has been experimental found that the textile material can have wrinkles free when the shear angle is up to 60°, thus it's not sufficient to predict the wrinkles using the shear locking angle.

In order to better describe the influence of the shear and bending behavior on the wrinkles formation, a drapability ratio r is defined as below:

$$r = \frac{k_c}{D_b} \tag{4.16}$$

Here, k_c is the material in-plane shear stiffness, and D_b is the material bending stiffness. The in-plane shear stiffness and bending stiffness is determined in the Section 4.3, thus then all the material drapability ratio can be obtained using Eq.(4.16), list in Table 4.8. The drapability ratio is also given in Fig. 4.10 after sorting by value. The relationship between the defined ratio r and the material drapability will be investigated in the Section 4.5 through the forming test.

Table 4.8. The drapability ratio of the selected materials

Drapability ratio: $r = k_c / D_b$			
Material	*r*	Material	*r*
Glass 1	0.035	Satin	0.015
Glass 2	0.026	G1151	0.007
Glass 3	0.2	G1100	0.006
Carbon 4	0.14	NCF Carbon	0.009
Twill 1	0.04	NCF Triaxle	0.32
Twill 2	0.01	Isotropic	75
Twill 3	0.015		

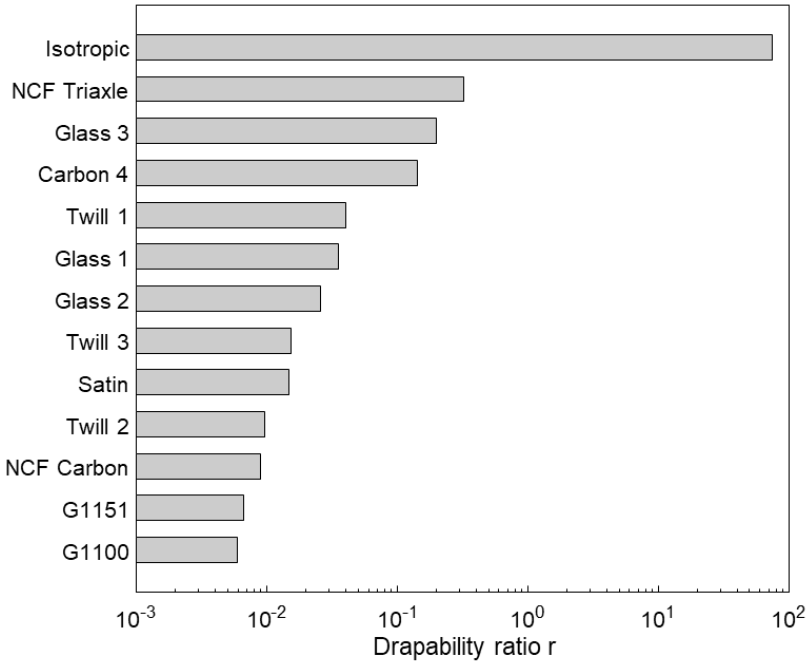

Fig. 4.10. The sorted drapability ratio of the selected materials

4.5 Forming experiment

To examine the relationship between the drapability ratio defined in this chapter and the material drapability (forming without wrinkles). A set of forming experiments are conducted including the square box and the cylinder. The forming experiments are done on a single ply which the thickness is small and more tendency to wrinkles.

4.5.1 Experiment setup

The experimental platform as shown in Fig. 4.11 is set up. The die module is constrained, the blank holder is loaded with a stable pressure, and the samples of various material are put between the blank holder and the die module. The platform is placed on the traction machine (ZwichRoell 100KN), the punch motion speed and displacement will be controlled by the traction machine. In the experimental process, the punch moves downwards, and the material will deform into the desired shapes under the control of the blank and the die module.

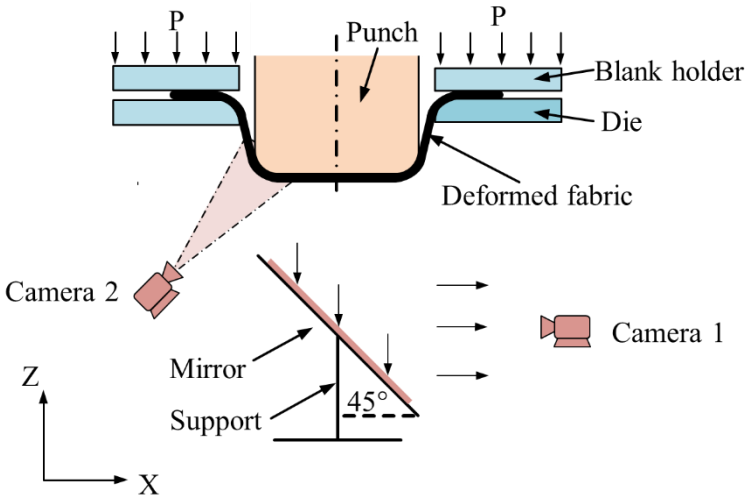

Fig. 4.11. Forming experiment setting

To record the experiment results and observe the wrinkles formed during the draping process, the blank holder and the die module are made transparent, and two cameras are used in the experiment. As shown in Fig. 4.11, through the reflection of the mirror, camera 1 is used to observe the deformation in the punch bottom and the material in the flat zone (between the blank holder and die). Camera is used to observe the deformation at the corner of the punch where wrinkles are most likely to occur. All the experiments are performed at room temperature.

4.5.2 Square box forming

The square box forming geometry parameters is shown in Fig. 4.12. The material used for the forming experiment will be firstly cut into a square, and the dimension is 300 mm × 300 mm. For the textile material, the material yarn configuration is 0°/90° with respect to the boundary of the square specimen.

When the ratio of the stamping depth to the square box length is large, the square box forming with wrinkle free using textile composites is sometimes considered impossible and some square box forming experiments introduced in the article [P. Wang, Legrand, et al., 2015] have shown the severe wrinkles. In addition to testing the relationship of the defined drapability with

the material drape ability, another purpose of this chapter is to prove that the square box can be formed wrinkle free using textile composite under certain conditions. In order to compare with the previous research about the square box forming[P. Wang, Legrand, et al., 2015; J. Huang et al., 2021] and also create a harsh forming condition, a large depth/width ratio 0.75 is selected. Thus the final punch displacement is set as 75 mm.

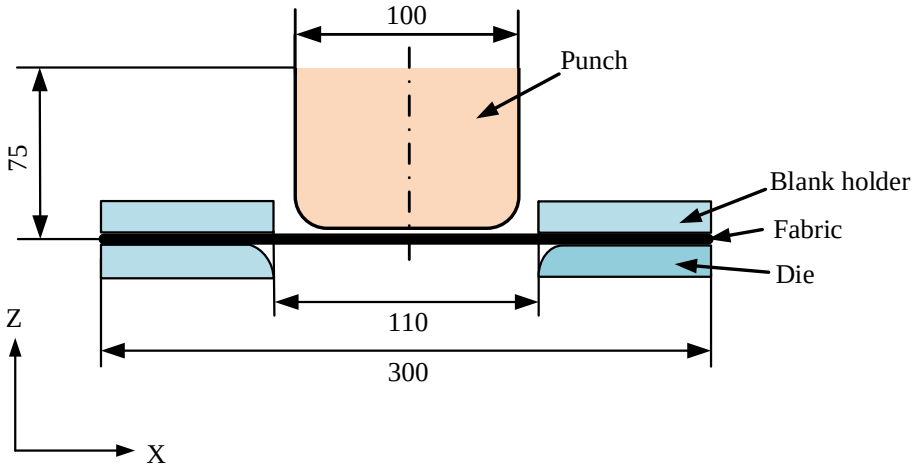

Fig. 4.12. Square box forming geometry parameters

The total thirteen materials are used for the square box forming, they were introduced in the Table 4.1. It's found in the square box forming experiment that some materials will appear wrinkles, and some materials will not appear wrinkles. The materials forming with wrinkles are shown in the Fig. 4.13, and the material forming with wrinkles free is presented in the Fig. 4.14.

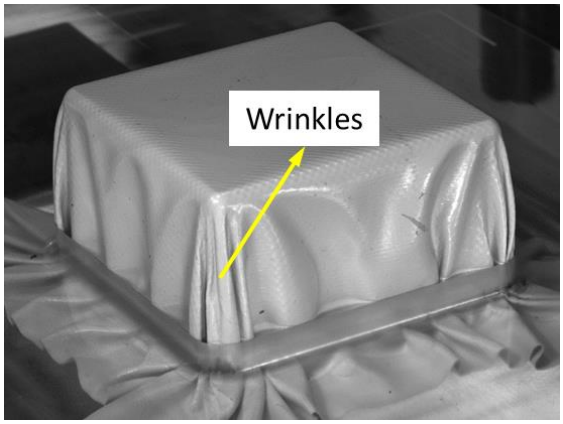

(a)

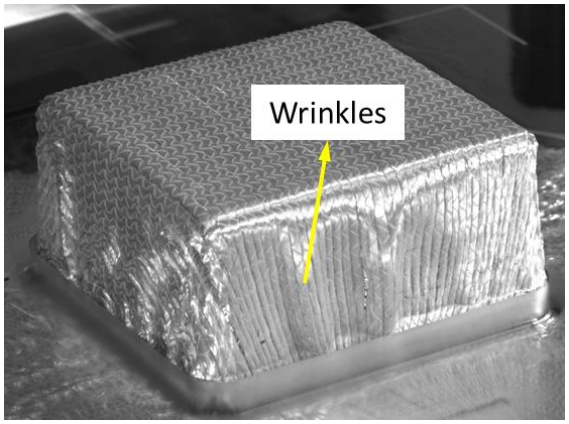

(b)

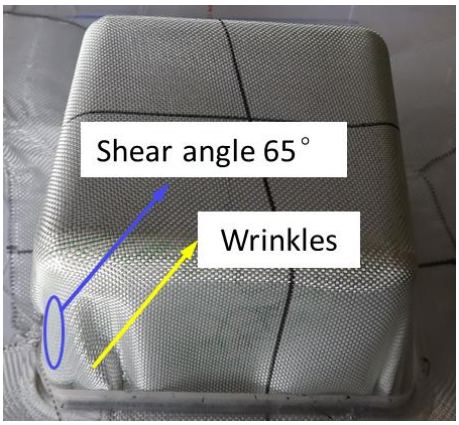

(c)

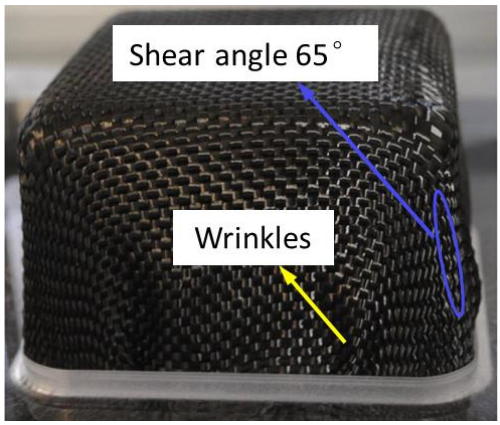

(d)

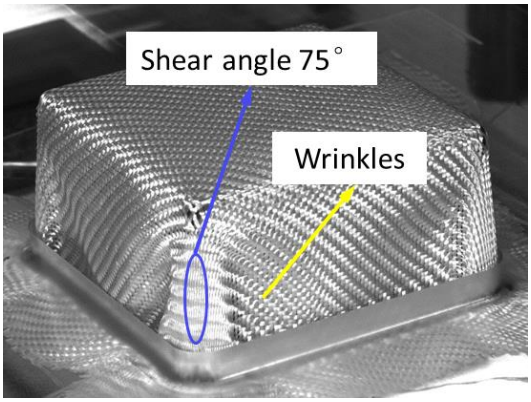

(e)

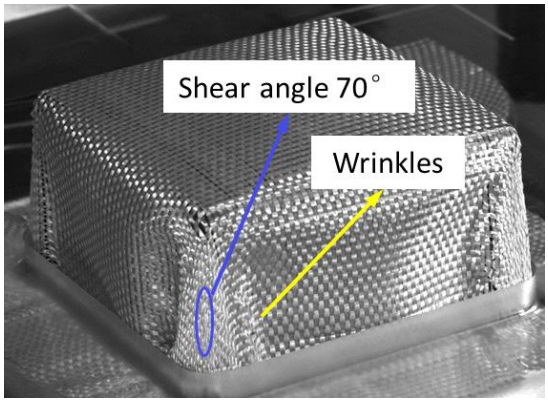

(f)

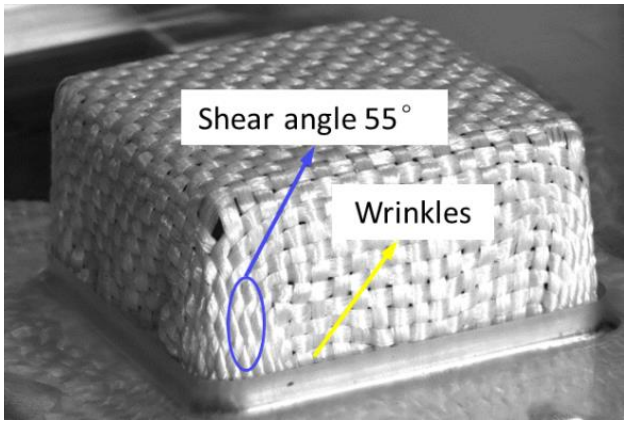

(g)

Fig. 4.13. Square box forming with wrinkles. (a) Isotropic material (b) NCF triaxle (c) Glass 3 (d) Carbon 4 (e) Twill 1 (f) Glass 1 (g) Glass 2

In Fig. 4.13, seven materials are shown with wrinkles during the forming process. Fig. 4.13(a) is the square box forming using isotropic material. For the isotropic material, this material is hard to shear due to the in-plane shear stiffness is very large while the bending stiffness is relative small, thus severe wrinkles occurs in the experiment. This condition also applied to the NCF triaxle material shown in Fig. 4.13(b). Because there are fibers in three directions 0°/45°/90°, the shear

deformation of the triaxle NCF is limited by the yarn stretching, which lead to the shear stiffness of the triaxle NCF to be much larger than that of the biaxial NCF. Triaxle NCF cannot be used to drape complex shapes like square box. Fig. 4.13(c) – (g) show the other 5 materials with wrinkles during forming, and the shear angle in the corner ranges from 55°to 75°. From Fig. 4.13(a) to Fig. 4.13(g), the drapability ratio of the material is getting smaller and smaller, the values are given in Fig. 4.10.

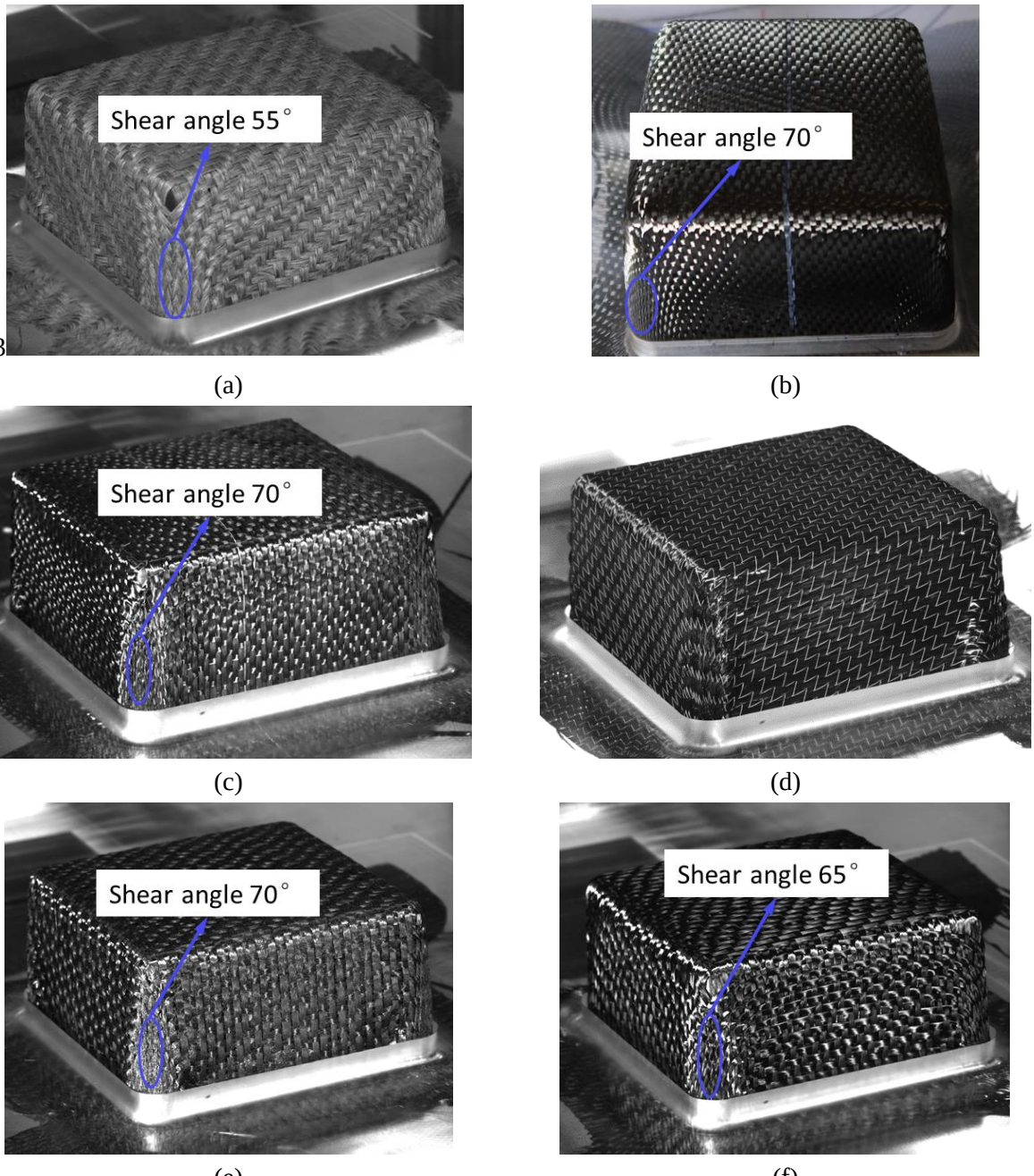

3

(a) (b)

(c) (d)

(e) (f)

Fig. 4.14. Square box forming without wrinkles (a) Twill 3 (b) Satin (c) Twill 2 (d)NCF Carbon (e) G1151 (f) G1100

Six other materials forming without wrinkles are presented in Fig. 4.14, the shear angle in the corner ranges from 55° to 70° (the shear angle for the biaxial NCF carbon in Fig. 4.14(d) is not given because only one direction yarn can be viewed from the picture). The drapability ratio of these six materials is smaller than that of the seven materials forming with wrinkles shown in Fig. 4.13. And from Fig. 4.14(a) to Fig. 4.14(f), the material drapability ratio is getting smaller and smaller.

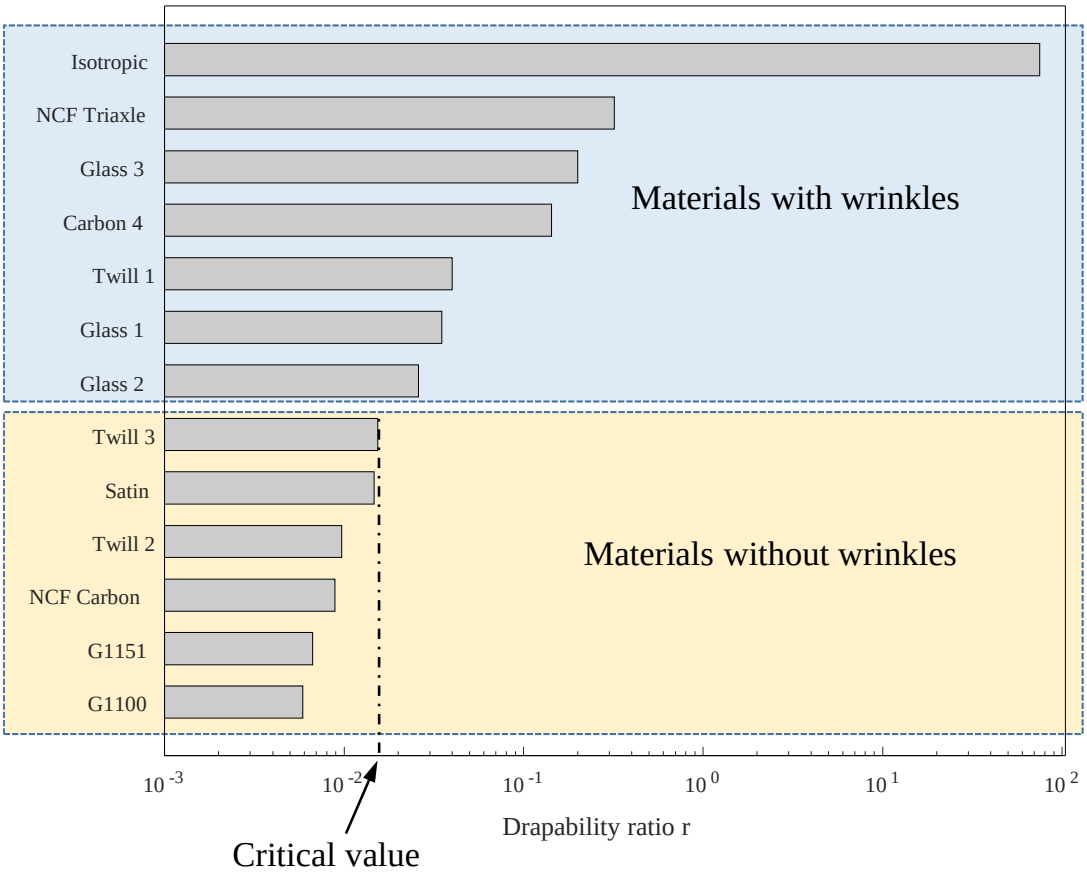

Fig. 4.15. The relationship between drapability ratio and the material deformation in square box forming

According to the experimental result of the total 13 materials and the calculated the corresponding drapability ratio, the materials can be divided into two parts according the value shown in the Fig. 4.15 , and it can be concluded that:

(1). The square box can be formed without wrinkles using the textile composite materials, even the shear angle can go up to 70° .

(2). Based on whether their ability to drape the square box without wrinkles, the defined drapability ratio can divide materials into two categories. The material with a lower drapability ratio has better forming performance.

(3). There is a critical value ($r_c = 0.015$) for the here considered square box forming. When the material drapability ratio is larger than the critical value, the forming wrinkles will appear, and otherwise, no wrinkles will appear.

4.5.3 Cylinder forming

The forming and development of wrinkles is a globe phenomenon which depends on the material behavior, the forming geometry and boundary condition. To verify the applicability of the defined drapability ratio in different forming shapes, the cylinder forming experiments using the introduced material in Table 4.1 are also performed. The cylinder geometry parameters are presented in Fig. 4.16. Same with the square box, the specimen are prepared as the square shape and the initial dimension is also 300 mm × 300 mm, the yarn configuration is 0°/90° with respect to the specimen boundary. The material is formed into the desired shape under the motion of the punch, and the punch final displacement is set as 70 mm (the final displacement of cylinder forming is different from the square box forming shown in section 4.5.2 due to the different punch geometry).

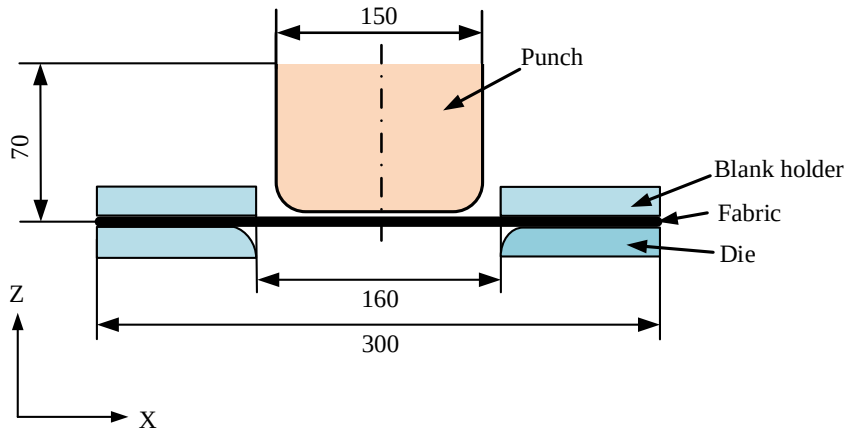

Fig. 4.16. Cylinder forming geometry parameters

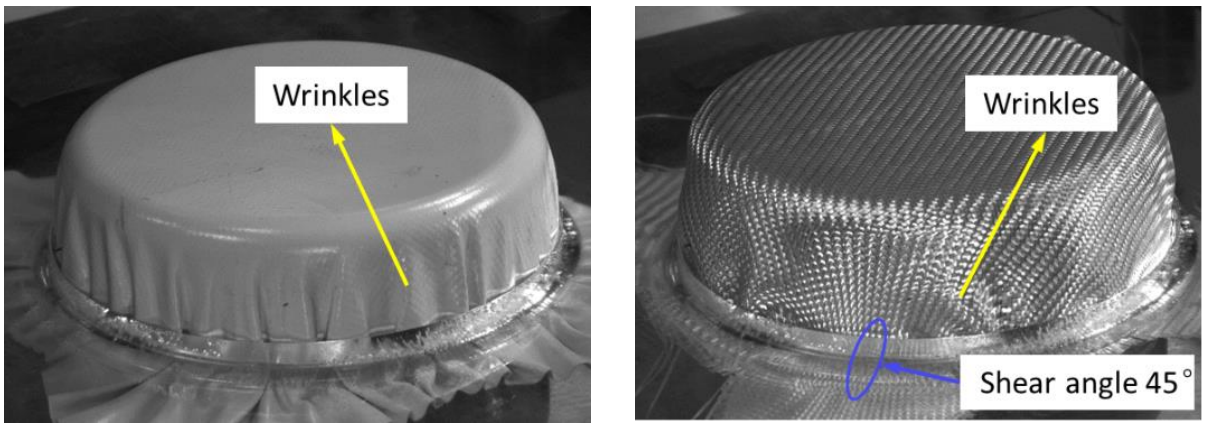

(a) (b)

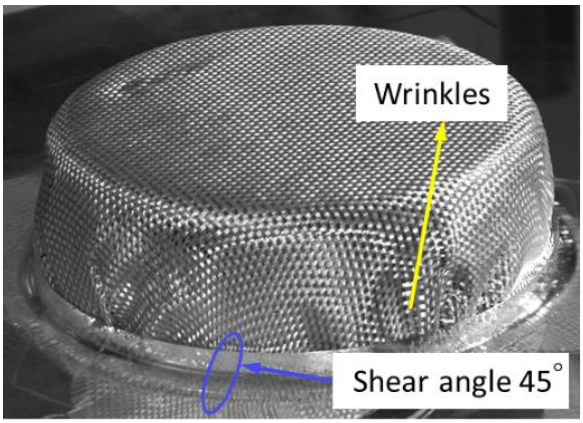

(c)

Fig. 4.17. Cylinder forming with wrinkles. (a) Isotropic material (b) Twill 1 (c) Glass 1

In the prepared thirteen materials, nine materials are selected for the cylinder forming, they are given in Fig. 4.19, the used material name is marked as red, and the bar of the drapability ratio is pained as green. In the cylinder forming process, experimental results are also different when using different materials. The final deformed shape with wrinkles are presented in Fig. 4.17 and the final deformed shape without wrinkles are given in Fig. 4.18.

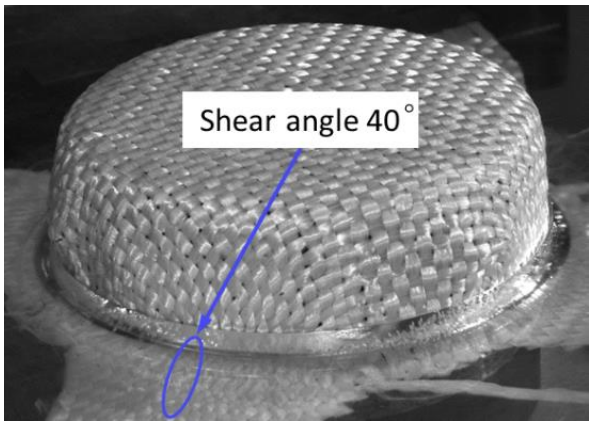

(a)

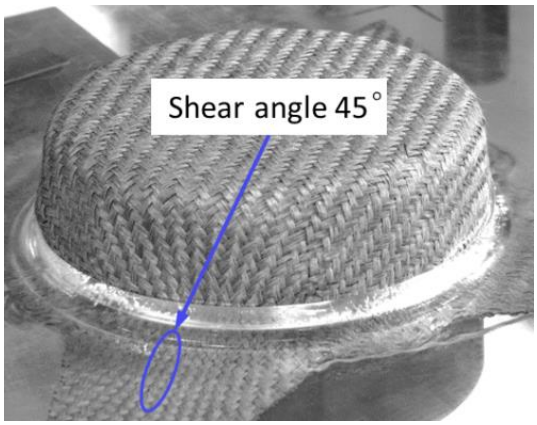

(b)

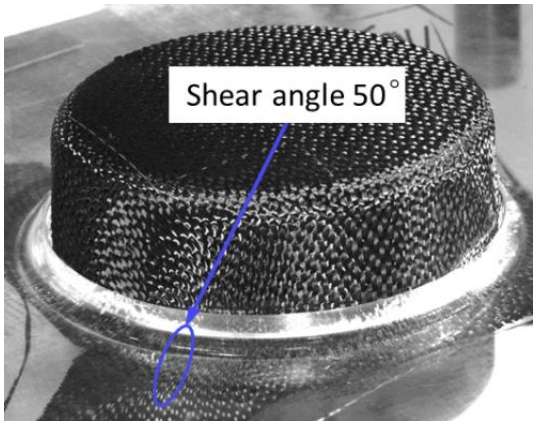

(c)

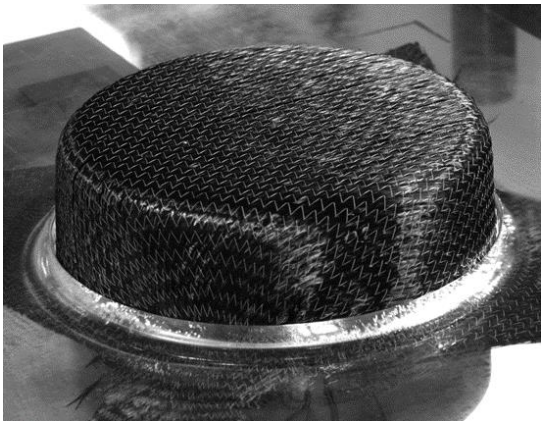

(d)

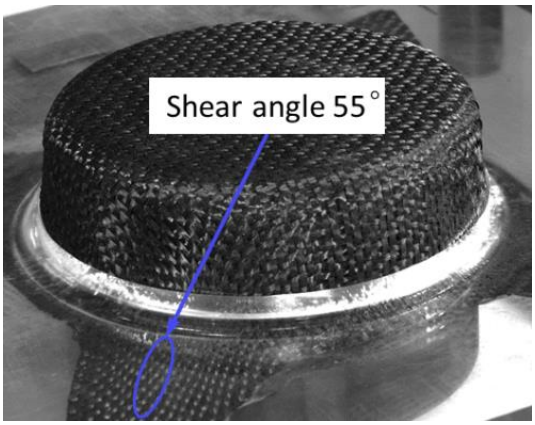

(e)

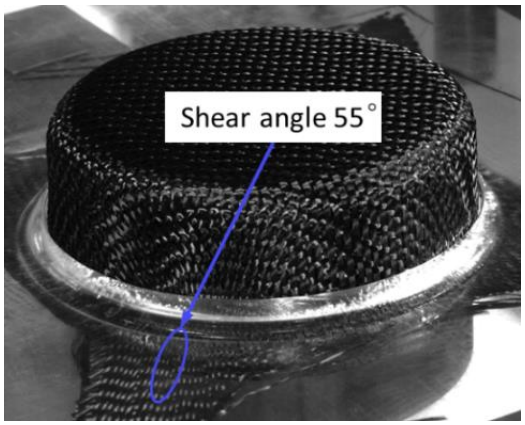

(f)

Fig. 4.18. Cylinder forming without wrinkles (a) Glass 2 (b) Twill 3 (c) Twill 2 (d) NCF Carbon (e) G1151 (f) G1100

In Fig. 4.17, there are three materials which appear wrinkles. For the isotropic material, the severe wrinkles appear during the forming process due to its material behavior (Shown in Fig. 4.17(a)). The textile material named Twill 1 and Glass 1 also form wrinkles in the cylinder forming, and the largest shear angle in the material is about 45°. The drapability ratio of these three materials is also relative large.

The other six materials that didn't generate wrinkle is given in Fig. 4.18, the material shear angle ranges from 40° to 55°. The shear angle of the material with wrinkles and the material without wrinkles both reached to more than 40°. Therefore, it can be known from this point that it's not comprehensive to determine whether the wrinkle will generate based on the shear locking angle. The drapability ratio of these six materials is also smaller than that of the three materials forming with wrinkles, and from Fig. 4.18(a) to Fig. 4.18(f), the drapability ratio of the material is smaller and smaller in order.

Thus, according to the cylinder experimental results, the used nine materials can also be divided into two parts shown in Fig. 4.19. Compare the Fig. 4.19 with Fig. 4.15, the material Glass 2 generate wrinkles in the square box forming, but no winkles in the cylinder forming, and thus the material critical drapability ratio changed (for the cylinder: $r_c = 0.026$, for the square box: $r_c = 0.015$). This is due to the different forming boundary condition. Furthermore, it can be seen that the drapability ratio of the material with forming wrinkles is larger than that of the materials without wrinkles, which is the same as what was found through the square box forming.

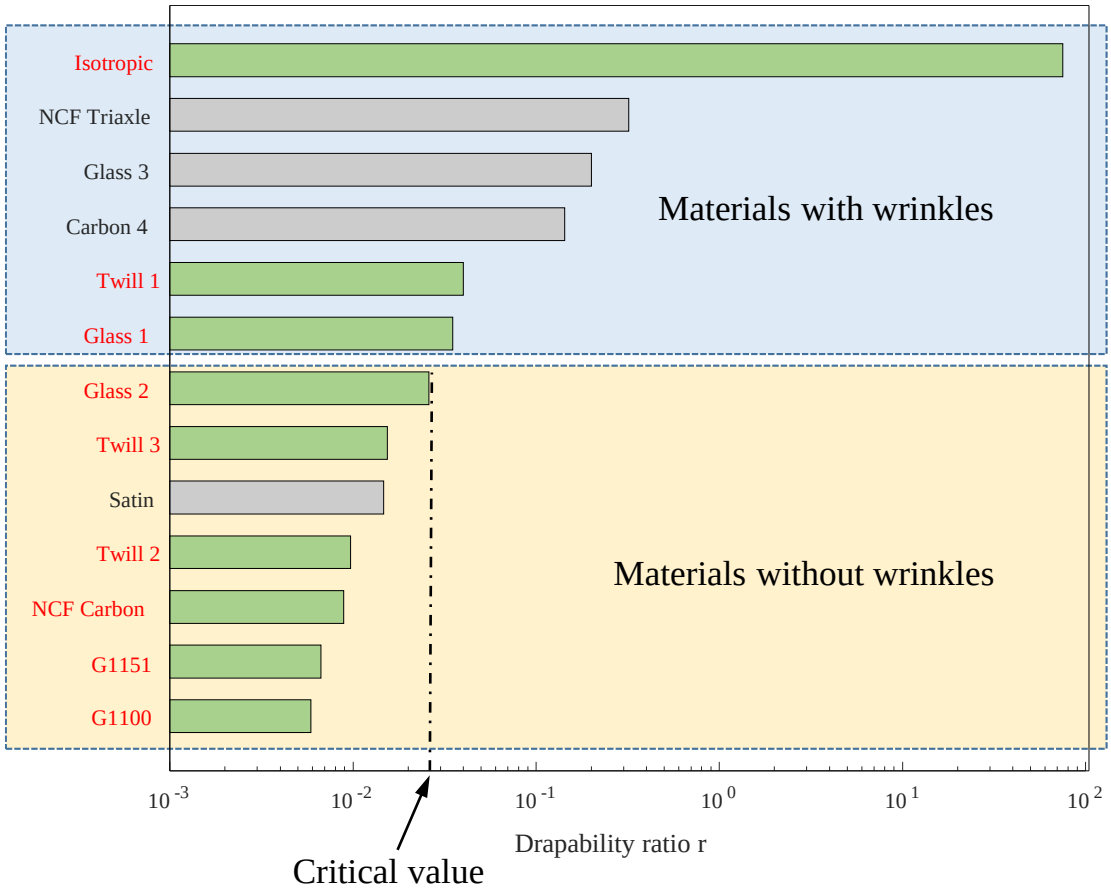

Fig. 4.19. The relationship between drapability ratio and the material deformation in cylinder forming (legends of green are material used on the cylinder forming)

4.6 Summary of Chapter 4

This chapter provides a complete experimental analysis of the textile composite drapability which is the ability to deform without wrinkles. Considering the material in-plane shear behavior and out of plane bending behavior, a drapability ratio is defined to quantify the material deformation ability. The characterization experiments of the material behavior are conducted firstly to determine material shear stiffness and bending stiffness, then the drapability ratio of all the materials is calculated and sorted from smallest to largest. Last, both square box and cylinder forming experiments are made to validate the relationship between the defined drapability ratio and the material deformation ability.

In the forming experiments, first of all, it is found that the material shear angle can be very large with wrinkles free (For square box, the shear angle is larger than 55° and for cylinder, the value is more than 40°), thus it can be known that the shear locking angle is not comprehensive to predict whether wrinkles will occur during forming process. When the forming shape changes, the critical value of the drapability ratio will also change, which is because of the formation and

development of wrinkles is also related to the geometry and the boundary conditions. However, regardless of whether it is a square box or a cylinder, the drapability ratio of the material with wrinkles is greater than that of the material without wrinkles.

To conclude, the forming and development of wrinkles is a global phenomenon which depends on the material behavior, forming geometry and boundary conditions. When all the other things are in same, the drapability ratio that was defined in this chapter can be an indicator of the textile deformation ability. The material with a lower drapability ratio are easier to form complex shapes without wrinkles.

Conclusion and prospective

Conclusion:

At the macroscopic, the textile composite reinforcement can be considered as a continuous medium which makes it possible to conduct the numerical simulation using shell elements. However, the specific woven architecture and the possible slippage between fibers give it a very specific behavior. The material bending stiffness is rather smaller than the membrane stiffness. Thus the classic shell elements like the Kirchhoff and Mindlin shell elements where the bending stiffness is determined by the membrane stiffness and shell thickness cannot be directly adopted. In order to accurately predict the material deformation, the bending behavior needs to be correctly described in the simulation process.

The thesis research work proposed a stress resultant approach for the simulation of the textile composite forming. Within the stress resultant shells, the membrane response and bending response are described by the stress resultant and the stress moments respectively. The stress resultants and the stress moments are related to membrane strains and curvatures by hypoelastic equations. Thus this approach can naturally decouple the bending behavior with membrane behavior which satisfies the material deformation mechanism. A series of comparison between experiment and simulation validated the effectiveness and correctness of the proposed approach.

The proposed simulation approach only focuses on the in-plane deformation, like the shear angle which determines the fiber direction, and the rotation of normal directors is neglected. It can be accepted for the case that the formed part is thin. When the material thickness goes larger, especially for the 3D fabrics, the position of normal directors will determine the fiber in the thickness. It is necessary to simulate the rotation of the normal directors. In this thesis research work, a post-processing method is proposed based on the material deformation mechanism. This method is simple, effective, and time-saving but only suitable for the multilayer fiber in the same orientation.

The wrinkles formation and development is a globe phenomenon that depends on the forming geometry, boundary condition, and the material behavior. For the first two factors, they can be optimized by the numerical simulation. For the factor of the material behavior, a series of the square box and cylinder forming experiments are conducted, it’s firstly found that the material shear locking angle is not sufficient to predict whether wrinkles will occur during forming process. Increasing the material shear stiffness will increase the tendency of wrinkles formation while the bending stiffness decreases it. A ratio of shear stiffness and bending stiffness is defined to characterize the drapability of different textile materials. Experiment indicated that the material with a smaller drapability ratio is easier to form complex shapes without wrinkles.

Prospective:

Based on the research conclusions obtained in the thesis work, further research work can be done in the following items:

1. In the present simulation approach, only the bending stiffness in the two yarn directions is considered. The influence of the cross bending stiffness D_{12} can be further investigated and perfect the bending constitutive equations.
2. The stress resultant shell simulation approach is validated by a series of forming experiments. Sensitivity analysis of the proposed simulation approach can be performed to further validate its response to the input material parameters.
3. To obtain the rotation of the normal directors, the post-processing method can only be used for the multilayer fiber with the same orientation. And this method cannot take the material properties into consideration. A further method within the stress resultant shell simulation approach needs to be researched.
4. The influence of material behavior on wrinkle formation has been studied by a series of forming experiments. This is only suitable for the case of single-layer. It is needed to be researched the influence of material behavior on the wrinkles in the multi-layer forming case.
5. Develop simpler and more accurate wrinkle measurement methods. Research the influence of the boundary conditions (like the blank holder shape, pressure, and the forming speed) on the wrinkles formation. Research and build a wrinkle elimination system with the help of simulation tools.

Bibliography

Adumitroaie, A., & Barbero, E. (2011). Beyond plain weave fabrics – II. Mechanical properties. *Composite Structures - COMPOS STRUCT*, *93*, 1449–1462. https://doi.org/10.1016/j.compstruct.2010.11.016

Ageyeva, T., Sibikin, I., & Kovacs, J. (2019). A Review of Thermoplastic Resin Transfer Molding: Process Modeling and Simulation. *Polymers*, *11*, 1555. https://doi.org/10.3390/polym11101555

Ahmad, S., Irons, B. M., & Zienkiewicz, O. C. (1970). Analysis of thick and thin shell structures by curved finite elements. *International Journal for Numerical Methods in Engineering*, *2*, 419–451. https://doi.org/10.1002/nme.1620020310

Allaoui, S., Boisse, P., Chatel, S., Hamila, N., Hivet, G., Soulat, D., & Vidal-Salle, E. (2011). Experimental and numerical analyses of textile reinforcement forming of a tetrahedral shape. *Composites Part A: Applied Science and Manufacturing*, *42*(6), 612–622. https://doi.org/10.1016/j.compositesa.2011.02.001

Allaoui, S., Hivet, G., Soulat, D., Wendling, A., Ouagne, P., & Chatel, S. (2014). Experimental preforming of highly double curved shapes with a case corner using an interlock reinforcement. *International Journal of Material Forming*, *7*(2), 155–165. https://doi.org/10.1007/s12289-012-1116-5

Alshahrani, H., & Hojjati, M. (2017). A new test method for the characterization of the bending behavior of textile prepregs. *Composites Part A: Applied Science and Manufacturing*, *97*, 128–140. https://doi.org/10.1016/j.compositesa.2017.02.027

Aono, M., Breen, D. E., & Wozny, M. J. (1994). Fitting a woven-cloth model to a curved surface: mapping algorithms. *Comput. Aided Des.*, *26*, 278–292.

Arif, M., Asif, M., & Ahmed, I. (2017). Advanced composite material for aerospace application—A review. *Int. J. Eng. Manuf. Sci*, *7*(2), 393–409.

Arnold, S. E., Sutcliffe, M. P. F., & Oram, W. L. A. (2016). Experimental measurement of wrinkle formation during draping of non-crimp fabric. *Composites Part A: Applied Science and Manufacturing*, *82*, 159–169. https://doi.org/https://doi.org/10.1016/j.compositesa.2015.12.011

ASTM. (2002). *Standard test method for stiffness of fabrics*. https://doi.org/10.1520/D1388-96R02

Badel, P., Vidal-Sallé, E., & Boisse, P. (2007). Computational determination of in-plane shear mechanical behaviour of textile composite reinforcements. *Computational Materials Science*, *40*(4), 439–448. https://doi.org/https://doi.org/10.1016/j.commatsci.2007.01.022

Badel, P., Vidal-Sallé, E., & Boisse, P. (2008). Large deformation analysis of fibrous materials using rate constitutive equations. *Computers and Structures*, *86*(11–12), 1164–1175. https://doi.org/10.1016/j.compstruc.2008.01.009

Badel, P., Vidal-Sallé, E., Maire, E., & Boisse, P. (2008). Simulation and tomography analysis of textile composite reinforcement deformation at the mesoscopic scale. *Composites Science and Technology*, *68*(12), 2433–2440. https://doi.org/10.1016/j.compscitech.2008.04.038

Bai, R., Colmars, J., Naouar, N., & Boisse, P. (2020). A specific 3D shell approach for textile composite reinforcements under large deformation. *Composites Part A: Applied Science and Manufacturing*, *139*, 106135. https://doi.org/https://doi.org/10.1016/j.compositesa.2020.106135

Bardl, G., Nocke, A., Cherif, C., Pooch, M., Schulze, M., Heuer, H., Schiller, M., Kupke, R., & Klein, M. (2016). Automated detection of yarn orientation in 3D-draped carbon fiber fabrics and preforms from eddy current data. *Composites Part B: Engineering*, *96*, 312–324. https://doi.org/https://doi.org/10.1016/j.compositesb.2016.04.040

Bel, S., Hamila, N., Boisse, P., & Dumont, F. (2012). Finite element model for NCF composite reinforcement preforming: Importance of inter-ply sliding. *Composites Part A: Applied Science and Manufacturing*, *43*(12), 2269–2277. https://doi.org/https://doi.org/10.1016/j.compositesa.2012.08.005

Belytschko, T., Liu, W. K., & Moran, B. (2000). *Nonlinear Finite Elements for Continua and Structures* . John Wiley & Sons, Ltd .

Bodaghi, M., Lomov, S. V, Simacek, P., Correia, N. C., & Advani, S. G. (2019). On the variability of permeability induced by reinforcement distortions and dual scale flow in liquid composite moulding: A review. *Composites Part A: Applied Science and Manufacturing*, *120*, 188–210. https://doi.org/https://doi.org/10.1016/j.compositesa.2019.03.004

Boeing Company. (2013). *787 Aircraft Rescue & Fire fighting Composite Structure*. https://doi.org/https://www.boeing.com/assets/pdf/commercial/airports/faqs/787_composite_arff_data.pdf

Boisse, P. (2004). *Mise en forme des renforts fibreux de composites*. Techniques de l'Ingénieur.

Boisse, P. (2015). *Advances in Composites Manufacturing and Process Design*. Woodhead Publishing.

Boisse, P., Cherouat, A., Gelin, J. C., & Sabhi, H. (1995). Experimental study and finite element simulation of a glass fiber fabric shaping process. *Polymer Composites*, *16*(1), 83–95. https://doi.org/https://doi.org/10.1002/pc.750160111

Boisse, P., Colmars, J., Hamila, N., Naouar, N., & Steer, Q. (2018). Bending and wrinkling of composite fiber preforms and prepregs. A review and new developments in the draping simulations. In *Composites Part B: Engineering* (Vol. 141, pp. 234–249). Elsevier Ltd. https://doi.org/10.1016/j.compositesb.2017.12.061

Boisse, P., Gasser, A., Hagege, B., & Billoet, J.-L. (2005). Analysis of the mechanical behavior of woven fibrous material using virtual tests at the unit cell level. *Journal of Materials Science*, *40*(22), 5955–5962. https://doi.org/10.1007/s10853-005-5069-7

Boisse, P., Hamila, N., Guzman-Maldonado, E., Madeo, A., Hivet, G., & dell'Isola, F. (2017). The bias-extension test for the analysis of in-plane shear properties of textile composite reinforcements and prepregs: a review. *International Journal of Material Forming*, *10*(4), 473–492. https://doi.org/10.1007/s12289-016-1294-7

Boisse, P., Hamila, N., Vidal-Sallé, E., & Dumont, F. (2011). Simulation of wrinkling during textile composite reinforcement forming. Influence of tensile, in-plane shear and bending stiffnesses. *Composites Science and Technology*, *71*(5), 683–692.

https://doi.org/10.1016/J.COMPSCITECH.2011.01.011

Boussu, F., Cristian, I., & Nauman, S. (2015). General definition of 3D warp interlock fabric architecture. *Composites Part B: Engineering*, *81*, 171–188. https://doi.org/https://doi.org/10.1016/j.compositesb.2015.07.013

Breuer, U., Neitzel, M., Ketzer, V., & Reinicke, R. (1996). Deep drawing of fabric-reinforced thermoplastics: Wrinkle formation and their reduction. *Polymer Composites*, *17*(4), 643–647. https://doi.org/https://doi.org/10.1002/pc.10655

Buet-Gautier, K., & Boisse, P. (2001). Experimental analysis and modeling of biaxial mechanical behavior of woven composite reinforcements. *Experimental Mechanics*, *41*(3), 260–269. https://doi.org/10.1007/BF02323143

Buet Gautier, K. (1998). *Analyse et simulation du comportement mecanique des renforts composites tisses*. http://www.theses.fr/1998ORLE2030

Bussetta, P., & Correia, N. (2018). Numerical forming of continuous fibre reinforced composite material: A review. In *Composites Part A: Applied Science and Manufacturing* (Vol. 113, pp. 12–31). Elsevier Ltd. https://doi.org/10.1016/j.compositesa.2018.07.010

C D Rudd, A C Long, K N Kendall, C. G. E. M. (1999). *Liquid Moulding Technologies* (1st ed.). Woodhead.

Cai, Z., & Gutowski, T. (1992). The 3-D Deformation Behavior of a Lubricated Fiber Bundle. *Journal of Composite Materials*, *26*(8), 1207–1237. https://doi.org/10.1177/002199839202600808

Campbell, F. C. (2004). *Manufacturing Processes for Advanced Composites* (F. C. B. T.-M. P. for A. C. Campbell (ed.)). Elsevier Science. https://doi.org/https://doi.org/10.1016/B978-185617415-2/50002-2

Cao, J., Akkerman, R., Boisse, P., Chen, J., Cheng, H. S., de Graaf, E. F., Gorczyca, J. L., Harrison, P., Hivet, G., Launay, J., Lee, W., Liu, L., Lomov, S. V., Long, A., de Luycker, E., Morestin, F., Padvoiskis, J., Peng, X. Q., Sherwood, J., … Zhu, B. (2008). Characterization of mechanical behavior of woven fabrics: Experimental methods and benchmark results. *Composites Part A: Applied Science and Manufacturing*, *39*(6), 1037–1053. https://doi.org/10.1016/j.compositesa.2008.02.016

Carvelli, V., Corazza, C., & Poggi, C. (2008). Mechanical modelling of monofilament technical textiles. *Computational Materials Science*, *42*(4), 679–691. https://doi.org/10.1016/j.commatsci.2007.10.003

Charmetant, A., Vidal-Sallé, E., & Boisse, P. (2011). Hyperelastic modelling for mesoscopic analyses of composite reinforcements. *Composites Science and Technology*, *71*(14), 1623–1631. https://doi.org/https://doi.org/10.1016/j.compscitech.2011.07.004

Chen, B., & Chou, T.-W. (2000). Compaction of woven-fabric preforms: nesting and multi-layer deformation. *Composites Science and Technology*, *60*(12), 2223–2231. https://doi.org/https://doi.org/10.1016/S0266-3538(00)00017-8

Chen, B., Colmars, J., Naouar, N., & Boisse, P. (2021). A hypoelastic stress resultant shell approach for simulations of textile composite reinforcement forming. *Composites Part A: Applied Science and Manufacturing*, *149*, 106558.

https://doi.org/10.1016/J.COMPOSITESA.2021.106558

Christ, S., Schnabel, M., Vorndran, E., Groll, J., & Gbureck, U. (2015). Fiber reinforcement during 3D printing. *Materials Letters*, *139*, 165–168. https://doi.org/https://doi.org/10.1016/j.matlet.2014.10.065

Chu, C. C., Cummings, C. L., & Teixeira, N. A. (1950). Mechanics of Elastic Performance of Textile Materials: Part V: A Study of the Factors Affecting the Drape of Fabrics—The Development of a Drape Meter. *Textile Research Journal*, *20*(8), 539–548. https://doi.org/10.1177/004051755002000802

Cusick, G. E. (1968). 21—THE MEASUREMENT OF FABRIC DRAPE. *The Journal of The Textile Institute*, *59*(6), 253–260. https://doi.org/10.1080/00405006808659985

Dafalias, Y. F. (1983). Corotational Rates for Kinematic Hardening at Large Plastic Deformations. *Journal of Applied Mechanics*, *50*(3), 561–565. https://doi.org/10.1115/1.3167091

Dangora, L. M., Mitchell, C. J., & Sherwood, J. A. (2015). Predictive model for the detection of out-of-plane defects formed during textile-composite manufacture. *Composites Part A: Applied Science and Manufacturing*, *78*, 102–112. https://doi.org/10.1016/j.compositesa.2015.07.011

Dasgupta, A., & Agarwal, R. K. (1992). Orthotropic Thermal Conductivity of Plain-Weave Fabric Composites Using a Homogenization Technique. *Journal of Composite Materials*, *26*(18), 2736–2758. https://doi.org/10.1177/002199839202601806

Dasgupta, A., Agarwal, R. K., & Bhandarkar, S. M. (1996). Three-dimensional modeling of woven-fabric composites for effective thermo-mechanical and thermal properties. *Composites Science and Technology*, *56*(3), 209–223. https://doi.org/https://doi.org/10.1016/0266-3538(95)00111-5

David, B., Goyheneche, J.-M., & Patrice, H. (2001). A global-local non-linear modeling of effective thermal conductivity tensor of textile-reinforced composites. *Composites Part A: Applied Science and Manufacturing*, *32*, 1443–1453. https://doi.org/10.1016/S1359-835X(01)00043-4

de Bilbao, E., Soulat, D., Hivet, G., & Gasser, A. (2010). Experimental Study of Bending Behaviour of Reinforcements. *Experimental Mechanics*, *50*(3), 333–351. https://doi.org/10.1007/s11340-009-9234-9

Deléglise, M., Le Grognec, P., Binetruy, C., Krawczak, P., & Claude, B. (2011). Modeling of high speed RTM injection with highly reactive resin with on-line mixing. *Composites Part A: Applied Science and Manufacturing*, *42*(10), 1390–1397. https://doi.org/10.1016/j.compositesa.2011.06.002

Desplentere, F., Lomov, S. V, Woerdeman, D. L., Verpoest, I., Wevers, M., & Bogdanovich, A. (2005). Micro-CT characterization of variability in 3D textile architecture. *Composites Science and Technology*, *65*(13), 1920–1930. https://doi.org/https://doi.org/10.1016/j.compscitech.2005.04.008

Dienes, J. K. (1979). On the analysis of rotation and stress rate in deforming bodies. *Acta Mechanica*, *32*(4), 217–232. https://doi.org/10.1007/BF01379008

Döbrich, O., Gereke, T., Diestel, O., Krzywinski, S., & Cherif, C. (2013). Decoupling the bending

behavior and the membrane properties of finite shell elements for a correct description of the mechanical behavior of textiles with a laminate formulation. *Journal of Industrial Textiles*, *44*(1), 70–84. https://doi.org/10.1177/1528083713477442

Dörr, D., Henning, F., & Kärger, L. (2018). Nonlinear hyperviscoelastic modelling of intra-ply deformation behaviour in finite element forming simulation of continuously fibre-reinforced thermoplastics. *Composites Part A: Applied Science and Manufacturing*, *109*, 585–596. https://doi.org/10.1016/j.compositesa.2018.03.037

Dörr, D., Schirmaier, F. J., Henning, F., & Kärger, L. (2017). A viscoelastic approach for modeling bending behavior in finite element forming simulation of continuously fiber reinforced composites. *Composites Part A: Applied Science and Manufacturing*, *94*, 113–123. https://doi.org/10.1016/j.compositesa.2016.11.027

Dransfield, K., Baillie, C., & Mai, Y.-W. (1994). Improving the delamination resistance of CFRP by stitching—a review. *Composites Science and Technology*, *50*(3), 305–317. https://doi.org/https://doi.org/10.1016/0266-3538(94)90019-1

Dufour, C., Wang, P., Boussu, F., & Soulat, D. (2013). Experimental Investigation About Stamping Behaviour of 3D Warp Interlock Composite Preforms. *Applied Composite Materials*, *21*, 725–738.

Durville, D. (2010). Simulation of the mechanical behaviour of woven fabrics at the scale of fibers. *International Journal of Material Forming*, *3*(2), 1241–1251. https://doi.org/10.1007/s12289-009-0674-7

Dvorkin, E. N., & Bathe, K. (1984). A continuum mechanics based four-node shell element for general non-linear analysis. *Engineering Computations*, *1*(1), 77–88. https://doi.org/10.1108/eb023562

Erol, O., Powers, B. M., & Keefe, M. (2017). Effects of weave architecture and mesoscale material properties on the macroscale mechanical response of advanced woven fabrics. *Composites Part A: Applied Science and Manufacturing*, *101*, 554–566. https://doi.org/https://doi.org/10.1016/j.compositesa.2017.07.016

Florimond, C. (2013). *Contributions à la modélisation mécanique du comportement de mèches de renforts tissés à l'aide d'un schéma éléments finis implicite*. https://tel.archives-ouvertes.fr/tel-01149065

Fu, S.-Y., Lauke, B., Mäder, E., Yue, C.-Y., & Hu, X. (2000). Tensile properties of short-glass-fiber- and short-carbon-fiber-reinforced polypropylene composites. *Composites Part A: Applied Science and Manufacturing*, *31*(10), 1117–1125. https://doi.org/https://doi.org/10.1016/S1359-835X(00)00068-3

Gasser, A., Boisse, P., & Hanklar, S. (2000). Mechanical behaviour of dry fabric reinforcements. 3D simulations versus biaxial tests. *Computational Materials Science*, *17*(1), 7–20. https://doi.org/https://doi.org/10.1016/S0927-0256(99)00086-5

Giorgio, I., Harrison, P., dell'Isola, F., Alsayednoor, J., & Turco, E. (2018). Wrinkling in engineering fabrics: a comparison between two different comprehensive modelling approaches. *Proceedings. Mathematical, Physical, and Engineering Sciences*, *474*(2216), 20180063. https://doi.org/10.1098/rspa.2018.0063

Gnaba, I., Legrand, X., Wang, P., & Soulat, D. (2018). Through-the-thickness reinforcement for composite structures: A review. *Journal of Industrial Textiles*, *49*(1), 71–96. https://doi.org/10.1177/1528083718772299

Gnaba, I., Soulat, D., Legrand, X., & Wang, P. (2021). Investigation of the formability behaviour during stamping of tufted and un-tufted carbon preforms: towards localized reinforcement technologies. *International Journal of Material Forming*, *14*(6), 1337–1354. https://doi.org/10.1007/s12289-020-01606-4

Grieser, T., & Mitschang, P. (2017). Investigation of the compaction behavior of carbon fiber NCF for continuous preforming processes. *Polymer Composites*, *38*(11), 2609–2625. https://doi.org/https://doi.org/10.1002/pc.23854

Gu, H., & Zhili, Z. (2002). Tensile behavior of 3D woven composites by using different fabric structures. *Materials & Design*, *23*(7), 671–674. https://doi.org/https://doi.org/10.1016/S0261-3069(02)00053-5

Guzman-Maldonado, E., Hamila, N., Naouar, N., Moulin, G., & Boisse, P. (2016). Simulation of thermoplastic prepreg thermoforming based on a visco-hyperelastic model and a thermal homogenization. *Materials & Design*, *93*, 431–442. https://doi.org/https://doi.org/10.1016/j.matdes.2015.12.166

Guzman-Maldonado, E., Wang, P., Hamila, N., & Boisse, P. (2019). Experimental and numerical analysis of wrinkling during forming of multi-layered textile composites. *Composite Structures*, *208*, 213–223. https://doi.org/10.1016/j.compstruct.2018.10.018

Haanappel, S. P., Ten Thije, R. H. W., Sachs, U., Rietman, B., & Akkerman, R. (2014). Formability analyses of uni-directional and textile reinforced thermoplastics. *Composites Part A: Applied Science and Manufacturing*, *56*, 80–92. https://doi.org/10.1016/j.compositesa.2013.09.009

Halimi, F., Golzar, M., Asadi, P., & Beheshty, M. (2012). Core modifications of sandwich panels fabricated by vacuum-assisted resin transfer molding. *Journal of Composite Materials*, *47*. https://doi.org/10.1177/0021998312451763

Hamila, N., & Boisse, P. (2013a). Locking in simulation of composite reinforcement deformations. Analysis and treatment. *Composites Part A: Applied Science and Manufacturing*, *53*, 109–117. https://doi.org/https://doi.org/10.1016/j.compositesa.2013.06.001

Hamila, N., & Boisse, P. (2013b). Tension locking in finite-element analyses of textile composite reinforcement deformation. *Comptes Rendus Mécanique*, *341*, 508–519. https://doi.org/10.1016/j.crme.2013.03.001

Hamila, N., Boisse, P., & Chatel, S. (2009). Semi-discrete shell finite elements for textile composite forming simulation. *International Journal of Material Forming*, *2*(1), 169–172. https://doi.org/10.1007/s12289-009-0518-5

Han, Z., Sun, S., Fu, H., & Fu, Y. (2017). Multi-Scale Low-Entropy Method for Optimizing the Processing Parameters during Automated Fiber Placement. *Materials (Basel, Switzerland)*, *10*. https://doi.org/10.3390/ma10091024

Hancock, S. G., & Potter, K. D. (2005). Inverse drape modelling—an investigation of the set of shapes that can be formed from continuous aligned woven fibre reinforcements. *Composites*

Part A: Applied Science and Manufacturing, *36*(7), 947–953. https://doi.org/https://doi.org/10.1016/j.compositesa.2004.12.001

Harrison, P., Clifford, M. J., & Long, A. C. (2004). Shear characterisation of viscous woven textile composites: A comparison between picture frame and bias extension experiments. *Composites Science and Technology*, *64*(10–11), 1453–1465. https://doi.org/10.1016/j.compscitech.2003.10.015

Harrison, P., Gomes, R., & Curado-Correia, N. (2013). Press forming a 0/90 cross-ply advanced thermoplastic composite using the double-dome benchmark geometry. *Composites Part A: Applied Science and Manufacturing*, *54*, 56–69. https://doi.org/10.1016/j.compositesa.2013.06.014

Hearle, J. W. S. (2015). *11 - Mechanical properties of textile reinforcements for composites* (P. B. T.-A. in C. M. and P. D. Boisse (ed.); pp. 231–251). Woodhead Publishing. https://doi.org/https://doi.org/10.1016/B978-1-78242-307-2.00011-7

Heisey, F. L., & Haller, K. D. (1988). Fitting Woven Fabric to Surfaces in Three Dimensions. *The Journal of The Textile Institute*, *79*(2), 250–263. https://doi.org/10.1080/00405008808659140

Henning, F., Kärger, L., Dörr, D., Schirmaier, F. J., Seuffert, J., & Bernath, A. (2019). Fast processing and continuous simulation of automotive structural composite components. In *Composites Science and Technology* (Vol. 171, pp. 261–279). Elsevier Ltd. https://doi.org/10.1016/j.compscitech.2018.12.007

Hosseini, A., Kashani, M. H., Sassani, F., Milani, A. S., & Ko, F. K. (2018). Identifying the distinct shear wrinkling behavior of woven composite preforms under bias extension and picture frame tests. *Composite Structures*, *185*, 764–773. https://doi.org/10.1016/j.compstruct.2017.11.033

Hsiao, S. W., & Kikuchi, N. (1999). Numerical analysis and optimal design of composite thermoforming process. *Computer Methods in Applied Mechanics and Engineering*, *177*, 1–34.

Hsieh, J. (2003). *Computed tomography: principles, design, artifacts, and recent advances* (Vol. 114). SPIE press.

Huang, J., Boisse, P., Hamila, N., Gnaba, I., Soulat, D., & Wang, P. (2021). Experimental and numerical analysis of textile composite draping on a square box. Influence of the weave pattern. *Composite Structures*, *267*, 113844. https://doi.org/10.1016/J.COMPSTRUCT.2021.113844

Huang, Y., King, D. R., Sun, T. L., Nonoyama, T., Kurokawa, T., Nakajima, T., & Gong, J. P. (2017). Energy-Dissipative Matrices Enable Synergistic Toughening in Fiber Reinforced Soft Composites. *Advanced Functional Materials*, *27*(9), 1605350. https://doi.org/https://doi.org/10.1002/adfm.201605350

Hughes, T. J. R., & Winget, J. (1980). Finite rotation effects in numerical integration of rate constitutive equations arising in large-deformation analysis. *International Journal for Numerical Methods in Engineering*, *15*(12), 1862–1867. https://doi.org/https://doi.org/10.1002/nme.1620151210

Ibrahimbegović, A. (1994). Stress resultant geometrically nonlinear shell theory with drilling rotations-Part I. A consistent formulation. *Computer Methods in Applied Mechanics and Engineering*, *118*(3–4), 265–284. https://doi.org/10.1016/0045-7825(94)90003-5

Jahan, I. (2017). Effect of Fabric Structure on the Mechanical Properties of Woven Fabrics. *Advance Research in Textile Engineering*, *2*. https://doi.org/10.26420/advrestexteng.2017.1018

Jauffrès, D., Sherwood, J. A., Morris, C. D., & Chen, J. (2010). Discrete mesoscopic modeling for the simulation of woven-fabric reinforcement forming. *International Journal of Material Forming*, *3*(2), 1205–1216. https://doi.org/10.1007/s12289-009-0646-y

Kärger, L., Bernath, A., Fritz, F., Galkin, S., Magagnato, D., Oeckerath, A., Schön, A., & Henning, F. (2015). Development and validation of a CAE chain for unidirectional fibre reinforced composite components. *Composite Structures*, *132*, 350–358. https://doi.org/https://doi.org/10.1016/j.compstruct.2015.05.047

Kärger, L., Galkin, S., Zimmerling, C., Dörr, D., Linden, J., Oeckerath, A., & Wolf, K. (2018). Forming optimisation embedded in a CAE chain to assess and enhance the structural performance of composite components. *Composite Structures*, *192*, 143–152. https://doi.org/https://doi.org/10.1016/j.compstruct.2018.02.041

Kaw, A. K. (2005). *Mechanics of Composite Materials*. https://doi.org/https://doi.org/10.1201/9781420058291

Kawabata, S., Niwa, M., & Kawai, H. (1973). The finite deformation theory of plain weave fabrics. Part I: the biaxial deformation theory. *The Journal of The Textile Institute*, *64*(1), 21–46. https://doi.org/10.1080/00405007308630416

Khan, A. H., & Chaudhuri, R. A. (2014). Fan-beam geometry based inversion algorithm in computed tomography (CT) for imaging of composite materials. *Composite Structures*, *110*, 297–304.

Khan, M. A., Mabrouki, T., Vidal-Sallé, E., & Boisse, P. (2010). Numerical and experimental analyses of woven composite reinforcement forming using a hypoelastic behaviour. Application to the double dome benchmark. *Journal of Materials Processing Technology*, *210*(2), 378–388. https://doi.org/10.1016/j.jmatprotec.2009.09.027

Khan, M. A., Reynolds, N., Williams, G., & Kendall, K. N. (2015). Processing of thermoset prepregs for high-volume applications and their numerical analysis using superimposed finite elements. *Composite Structures*, *131*, 917–926. https://doi.org/https://doi.org/10.1016/j.compstruct.2015.06.056

Khan, M. A., Saleem, W., Asad, M., & Ijaz, H. (2015). A parametric sensitivity study on preforming simulations of woven composites using a hypoelastic computational model. *Journal of Reinforced Plastics and Composites*, *35*(3), 243–257. https://doi.org/10.1177/0731684415613567

Komeili, M., & Milani, A. S. (2016). On effect of shear-tension coupling in forming simulation of woven fabric reinforcements. *Composites Part B: Engineering*, *99*, 17–29. https://doi.org/10.1016/j.compositesb.2016.05.004

Lammens, N., Kersemans, M., Luyckx, G., Van Paepegem, W., & Degrieck, J. (2014). Improved

accuracy in the determination of flexural rigidity of textile fabrics by the Peirce cantilever test (ASTM D1388). *Textile Research Journal*, *84*(12), 1307–1314. https://doi.org/10.1177/0040517514523182

Latil, P., Orgéas, L., Geindreau, C., Dumont, P. J. J., & Rolland du Roscoat, S. (2011). Towards the 3D in situ characterisation of deformation micro-mechanisms within a compressed bundle of fibres. *Composites Science and Technology*, *71*(4), 480–488. https://doi.org/10.1016/j.compscitech.2010.12.023

Launay, J., Hivet, G., Duong, A. V., & Boisse, P. (2008). Experimental analysis of the influence of tensions on in plane shear behaviour of woven composite reinforcements. *Composites Science and Technology*, *68*(2), 506–515. https://doi.org/10.1016/j.compscitech.2007.06.021

Le Corre, S., Orgéas, L., Favier, D., Tourabi, A., Maazouz, A., & Venet, C. (2002). Shear and compression behaviour of sheet moulding compounds. *Composites Science and Technology*, *62*(4), 571–577.

Lebrun, G., Bureau, M. N., & Denault, J. (2003). Evaluation of bias-extension and picture-frame test methods for the measurement of intraply shear properties of PP/glass commingled fabrics. *Composite Structures*, *61*(4), 341–352. https://doi.org/10.1016/S0263-8223(03)00057-6

Lee, J. S., Hong, S. J., Yu, W.-R., & Kang, T. J. (2007). The effect of blank holder force on the stamp forming behavior of non-crimp fabric with a chain stitch. *Composites Science and Technology*, *67*(3), 357–366. https://doi.org/https://doi.org/10.1016/j.compscitech.2006.09.009

Lekakou, C., Johari, M. A. K. B., & Bader, M. G. (1996). Compressibility and flow permeability of two-dimensional woven reinforcements in the processing of composites. *Polymer Composites*, *17*(5), 666–672. https://doi.org/https://doi.org/10.1002/pc.10658

Liang, B., Colmars, J., & Boisse, P. (2017). A shell formulation for fibrous reinforcement forming simulations. *Composites Part A: Applied Science and Manufacturing*, *100*, 81–96. https://doi.org/10.1016/j.compositesa.2017.04.024

Liang, B., Hamila, N., Peillon, M., & Boisse, P. (2014). Analysis of thermoplastic prepreg bending stiffness during manufacturing and of its influence on wrinkling simulations. *Composites Part A: Applied Science and Manufacturing*, *67*, 111–122. https://doi.org/10.1016/j.compositesa.2014.08.020

Lim, T.-C., & Ramakrishna, S. (2002). Modelling of composite sheet forming: a review. *Composites Part A: Applied Science and Manufacturing*, *33*(4), 515–537. https://doi.org/https://doi.org/10.1016/S1359-835X(01)00138-5

Lin, H., Wang, J., Long, A. C., Clifford, M. J., & Harrison, P. (2007). Predictive modelling for optimization of textile composite forming. *Composites Science and Technology*, *67*(15–16), 3242–3252. https://doi.org/10.1016/j.compscitech.2007.03.040

Liu, L., Wang, P., Legrand, X., & Soulat, D. (2017). Investigation of mechanical properties of tufted composites: Influence of tuft length through the thickness reinforcement. *Composite Structures*, *172*, 221–228. https://doi.org/https://doi.org/10.1016/j.compstruct.2017.03.099

Loix, F., Badel, P., Orgéas, L., Geindreau, C., & Boisse, P. (2008). Woven fabric permeability: From textile deformation to fluid flow mesoscale simulations. *Composites Science and*

Technology, *68*(7), 1624–1630. https://doi.org/https://doi.org/10.1016/j.compscitech.2008.02.027

Lomov, S. (2011). Non-Crimp Fabric Composites Manufacturing, Properties and Applications. In S. V. B. T.-N.-C. F. C. Lomov (Ed.), *Woodhead Publishing Series in Composites Science and Engineering*. Woodhead Publishing. https://doi.org/https://doi.org/10.1016/B978-1-84569-762-4.50026-6

Lomov, S., & Verpoest, I. (2006). Model of shear of woven fabric and parametric description of shear resistance of glass woven reinforcements. *Composites Science and Technology*, *66*, 919–933. https://doi.org/10.1016/j.compscitech.2005.08.010

Lomov, S. V, Belov, E. B., Bischoff, T., Ghosh, S. B., Truong Chi, T., & Verpoest, I. (2002). Carbon composites based on multiaxial multiply stitched preforms. Part 1. Geometry of the preform. *Composites Part A: Applied Science and Manufacturing*, *33*(9), 1171–1183. https://doi.org/https://doi.org/10.1016/S1359-835X(02)00090-8

Lomov, S. V, Gusakov, A. V, Huysmans, G., Prodromou, A., & Verpoest, I. (2000). Textile geometry preprocessor for meso-mechanical models of woven composites. *Composites Science and Technology*, *60*(11), 2083–2095. https://doi.org/https://doi.org/10.1016/S0266-3538(00)00121-4

Lomov, S. V, Ivanov, D. S., Verpoest, I., Zako, M., Kurashiki, T., Nakai, H., & Hirosawa, S. (2007). Meso-FE modelling of textile composites: Road map, data flow and algorithms. *Composites Science and Technology*, *67*(9), 1870–1891. https://doi.org/https://doi.org/10.1016/j.compscitech.2006.10.017

Lomov, S. V, Willems, A., Verpoest, I., Zhu, Y., Barburski, M., & Stoilova, T. (2006). Picture Frame Test of Woven Composite Reinforcements with a Full-Field Strain Registration. *Textile Research Journal*, *76*(3), 243–252. https://doi.org/10.1177/0040517506061032

Lukaszewicz, D. H. J. A., & Potter, K. D. (2011). The internal structure and conformation of prepreg with respect to reliable automated processing. *Composites Part A: Applied Science and Manufacturing*, *42*(3), 283–292. https://doi.org/10.1016/j.compositesa.2010.11.014

Mack, C., & Taylor, H. M. (1956). 39—The Fitting of Woven Cloth to Surfaces. *Journal of the Textile Institute Transactions*, *47*(9), T477–T488. https://doi.org/10.1080/19447027.1956.10750433

Matveev, M. Y., Endruweit, A., De Focatiis, D. S. A., Long, A. C., & Warrior, N. A. (2019). A novel criterion for the prediction of meso-scale defects in textile preforming. *Composite Structures*, *226*, 111263. https://doi.org/https://doi.org/10.1016/j.compstruct.2019.111263

Miao, Y., Zhou, E., Wang, Y., & Cheeseman, B. A. (2008). Mechanics of textile composites: Micro-geometry. *Composites Science and Technology*, *68*(7), 1671–1678. https://doi.org/https://doi.org/10.1016/j.compscitech.2008.02.018

Mitchell, C. J., Dangora, L. M., & Sherwood, J. A. (2016). Investigation into a robust finite element model for composite materials. *Finite Elements in Analysis and Design*, *115*, 1–8. https://doi.org/10.1016/j.finel.2016.02.003

Mouritz, A. P., Bannister, M. K., Falzon, P. J., & Leong, K. H. (1999). Review of applications for advanced three-dimensional fibre textile composites. *Composites Part A: Applied Science*

and Manufacturing, *30*(12), 1445–1461. https://doi.org/https://doi.org/10.1016/S1359-835X(99)00034-2

Naouar, N., Vidal-Salle, E., Schneider, J., Maire, E., & Boisse, P. (2015). 3D composite reinforcement meso F.E. analyses based on X-ray computed tomography. *Composite Structures*, *132*, 1094–1104. https://doi.org/https://doi.org/10.1016/j.compstruct.2015.07.005

Naouar, N., Vidal-Sallé, E., Schneider, J., Maire, E., & Boisse, P. (2014). Meso-scale FE analyses of textile composite reinforcement deformation based on X-ray computed tomography. *Composite Structures*, *116*, 165–176.

Nguyen, Q. T., Vidal-Sallé, E., Boisse, P., Park, C. H., Saouab, A., Bréard, J., & Hivet, G. (2013). Mesoscopic scale analyses of textile composite reinforcement compaction. *Composites Part B: Engineering*, *44*(1), 231–241. https://doi.org/https://doi.org/10.1016/j.compositesb.2012.05.028

Nosrat Nezami, F., Gereke, T., & Cherif, C. (2017). Active forming manipulation of composite reinforcements for the suppression of forming defects. *Composites Part A: Applied Science and Manufacturing*, *99*, 94–101. https://doi.org/https://doi.org/10.1016/j.compositesa.2017.04.011

Obermeyer, E. J., & Majlessi, S. A. (1998). A review of recent advances in the application of blank-holder force towards improving the forming limits of sheet metal parts. *Journal of Materials Processing Technology*, *75*(1), 222–234. https://doi.org/https://doi.org/10.1016/S0924-0136(97)00368-3

Orliac, J.-G. (2012). *Analyse et simulation du comportement anisotrope lors de la mise en forme de renforts tissés interlock*.

Parisch, H. (1995). A continuum-based shell theory for non-linear applications. *International Journal for Numerical Methods in Engineering*, *38*(11), 1855–1883. https://doi.org/https://doi.org/10.1002/nme.1620381105

Peirce, F. T. (1930). 26—THE "HANDLE" OF CLOTH AS A MEASURABLE QUANTITY. *Journal of the Textile Institute Transactions*, *21*(9), T377–T416. https://doi.org/10.1080/19447023008661529

Peng, X. Q., & Cao, J. (2005). A continuum mechanics-based non-orthogonal constitutive model for woven composite fabrics. *Composites Part A: Applied Science and Manufacturing*, *36*(6), 859–874. https://doi.org/10.1016/j.compositesa.2004.08.008

Pfrommer, J., Zimmerling, C., Liu, J., Kärger, L., Henning, F., & Beyerer, J. (2018). Optimisation of manufacturing process parameters using deep neural networks as surrogate models. *Procedia CIRP*, *72*, 426–431. https://doi.org/https://doi.org/10.1016/j.procir.2018.03.046

Pickett, A. K., Creech, G., & de Luca, P. (2005). Simplified and advanced simulation methods for prediction of fabric draping. *Revue Européenne Des Éléments Finis*, *14*(6–7), 677–691. https://doi.org/10.3166/reef.14.677-691

Pickett, A. K., Queckbörner, T., de Luca, P., & Haug, E. (1995). An explicit finite element solution for the forming prediction of continuous fibre-reinforced thermoplastic sheets. *Composites Manufacturing*, *6*, 237–243.

Poppe, C., Dörr, D., Henning, F., & Kärger, L. (2018). Experimental and numerical investigation of the shear behaviour of infiltrated woven fabrics. *Composites Part A: Applied Science and Manufacturing*, *114*, 327–337. https://doi.org/https://doi.org/10.1016/j.compositesa.2018.08.018

Potluri, P., Perez Ciurezu, D. A., & Ramgulam, R. B. (2006). Measurement of meso-scale shear deformations for modelling textile composites. *Composites Part A: Applied Science and Manufacturing*, *37*(2), 303–314. https://doi.org/https://doi.org/10.1016/j.compositesa.2005.03.032

Prodromou, A. G., & Chen, J. (1997). On the relationship between shear angle and wrinkling of textile composite preforms. *Composites Part A: Applied Science and Manufacturing*, *28*(5), 491–503. https://doi.org/10.1016/S1359-835X(96)00150-9

Sachs, U., & Akkerman, R. (2017). Viscoelastic bending model for continuous fiber-reinforced thermoplastic composites in melt. *Composites Part A: Applied Science and Manufacturing*, *100*, 333–341. https://doi.org/10.1016/j.compositesa.2017.05.032

Schirmaier, F. J., Dörr, D., Henning, F., & Kärger, L. (2017). A macroscopic approach to simulate the forming behaviour of stitched unidirectional non-crimp fabrics (UD-NCF). *Composites Part A: Applied Science and Manufacturing*, *102*, 322–335. https://doi.org/https://doi.org/10.1016/j.compositesa.2017.08.009

Schirmaier, F. J., Weidenmann, K. A., Kärger, L., & Henning, F. (2016). Characterisation of the draping behaviour of unidirectional non-crimp fabrics (UD-NCF). *Composites Part A: Applied Science and Manufacturing*, *80*, 28–38. https://doi.org/https://doi.org/10.1016/j.compositesa.2015.10.004

Seuffert, J., Rosenberg, P., Kärger, L., Henning, F., Kothmann, M. H., & Deinzer, G. (2020). Experimental and numerical investigations of pressure-controlled resin transfer molding (PC-RTM). *Advanced Manufacturing: Polymer & Composites Science*, *6*(3), 154–163. https://doi.org/10.1080/20550340.2020.1805689

Shanwan, A., & Allaoui, S. (2019). Different experimental ways to minimize the preforming defects of multi-layered interlock dry fabric. *International Journal of Material Forming*, *12*(1), 69–78. https://doi.org/10.1007/s12289-018-1407-6

Shen, H., Wang, P., & Legrand, X. (2021). In-plane shear characteristics during the forming of tufted carbon woven fabrics. *Composites Part A: Applied Science and Manufacturing*, *141*, 106196. https://doi.org/https://doi.org/10.1016/j.compositesa.2020.106196

Shen, H., Wang, P., Legrand, X., & Liu, L. (2019). Characterisation and optimisation of wrinkling during the forming of tufted three-dimensional composite preforms. *Composites Part A: Applied Science and Manufacturing*, *127*, 105651. https://doi.org/https://doi.org/10.1016/j.compositesa.2019.105651

Shen, H., Wang, P., Legrand, X., Liu, L., & Soulat, D. (2019). Influence of the tufting pattern on the formability of tufted multi-layered preforms. *Composite Structures*, *228*, 111356. https://doi.org/https://doi.org/10.1016/j.compstruct.2019.111356

Sherburn, M. (2007). *Geometric and mechanical modelling of textiles*. University of Nottingham Nottingham, UK.

Simo, J. C., & Fox, D. D. (1989). On a stress resultant geometrically exact shell model. Part I: Formulation and optimal parametrization. *Computer Methods in Applied Mechanics and Engineering*, *72*(3), 267–304. https://doi.org/10.1016/0045-7825(89)90002-9

SIMULIA. (2019). *Abaqus documentation*.

Sozer, E. M., Simacek, P., & Advani, S. G. (2012). Resin transfer molding (RTM) in polymer matrix composites. In *Manufacturing Techniques for Polymer Matrix Composites (PMCs)* (pp. 245–309). Elsevier. https://doi.org/10.1533/9780857096258.3.243

Sutton, M. A., Orteu, J.-J., & Schreier, H. W. (2009). *Image Correlation for Shape, Motion and Deformation Measurements: Basic Concepts,Theory and Applications*.

Syerko, E., Comas-Cardona, S., & Binetruy, C. (2012). Models of mechanical properties/behavior of dry fibrous materials at various scales in bending and tension: A review. In *Composites Part A: Applied Science and Manufacturing* (Vol. 43, Issue 8, pp. 1365–1388). Elsevier. https://doi.org/10.1016/j.compositesa.2012.03.012

Sze, K. Y., & Liu, X. H. (2005). A new skeletal model for fabric drapes. *International Journal of Mechanics and Materials in Design*, *2*(3), 225–243. https://doi.org/10.1007/s10999-006-9004-0

Thompson, A. J., Belnoue, J. P.-H., & Hallett, S. R. (2020). Modelling defect formation in textiles during the double diaphragm forming process. *Composites Part B: Engineering*, *202*, 108357. https://doi.org/10.1016/j.compositesb.2020.108357

Trabelsi, W., Michel, L., & Othomene, R. (2010). Effects of Stitching on Delamination of Satin Weave Carbon-Epoxy Laminates Under Mode I, Mode II and Mixed-Mode I/II Loadings. *Applied Composite Materials*, *17*. https://doi.org/10.1007/s10443-010-9128-0

Vallons, K., Adolphs, G., Lucas, P., Lomov, S. V, & Verpoest, I. (2014). The influence of the stitching pattern on the internal geometry, quasi-static and fatigue mechanical properties of glass fibre non-crimp fabric composites. *Composites Part A: Applied Science and Manufacturing*, *56*, 272–279. https://doi.org/https://doi.org/10.1016/j.compositesa.2013.10.015

Van Der Weeën, F. (1991). Algorithms for draping fabrics on doubly-curved surfaces. *International Journal for Numerical Methods in Engineering*, *31*(7), 1415–1426. https://doi.org/https://doi.org/10.1002/nme.1620310712

Vangheluwe, L., & Kiekens, P. (1993). Time Dependence of the Drape Coefficient of Fabrics. *International Journal of Clothing Science and Technology*, *5*(5), 5–8. https://doi.org/10.1108/eb003022

Verpoest, I., & Lomov, S. V. (2005). Virtual textile composites software WiseTex: Integration with micro-mechanical, permeability and structural analysis. *Composites Science and Technology*, *65*(15), 2563–2574. https://doi.org/https://doi.org/10.1016/j.compscitech.2005.05.031

Verrey, J., Wakeman, M. D., Michaud, V., & Månson, J. A. E. (2006). Manufacturing cost comparison of thermoplastic and thermoset RTM for an automotive floor pan. *Composites Part A: Applied Science and Manufacturing*, *37*(1), 9–22. https://doi.org/10.1016/j.compositesa.2005.05.048

Viisainen, J. V, Hosseini, A., & Sutcliffe, M. P. F. (2021). Experimental investigation, using 3D digital image correlation, into the effect of component geometry on the wrinkling behaviour and the wrinkling mechanisms of a biaxial NCF during preforming. *Composites Part A: Applied Science and Manufacturing*, *142*, 106248. https://doi.org/https://doi.org/10.1016/j.compositesa.2020.106248

Viisainen, J. V, & Sutcliffe, M. P. F. (2021). Characterising the variability in wrinkling during the preforming of non-crimp fabrics. *Composites Part A: Applied Science and Manufacturing*, *149*, 106536. https://doi.org/https://doi.org/10.1016/j.compositesa.2021.106536

Wang, J., Wang, P., Hamila, N., & Boisse, P. (2020). Mesoscopic analyses of the draping of 3D woven composite reinforcements based on macroscopic simulations. *Composite Structures*, *250*, 112602. https://doi.org/https://doi.org/10.1016/j.compstruct.2020.112602

Wang, J., Wang, P., Hamila, N., & Boisse, P. (2022). Meso-Macro Simulations of the Forming of 3D Non-Crimp Woven Fabrics. In *Textiles* (Vol. 2, Issue 1). https://doi.org/10.3390/textiles2010006

Wang, P., Hamila, N., & Boisse, P. (2013). Thermoforming simulation of multilayer composites with continuous fibres and thermoplastic matrix. *Composites Part B: Engineering*, *52*, 127–136. https://doi.org/https://doi.org/10.1016/j.compositesb.2013.03.045

Wang, P., Hamila, N., Boisse, P., Chaudet, P., & Lesueur, D. (2015). Thermo-mechanical behavior of stretch-broken carbon fiber and thermoplastic resin composites during manufacturing. *Polymer Composites*, *36*(4), 694–703. https://doi.org/https://doi.org/10.1002/pc.22988

Wang, P., Hamila, N., Pineau, P., & Boisse, P. (2012). Thermomechanical analysis of thermoplastic composite prepregs using bias-extension test. *Journal of Thermoplastic Composite Materials*, *27*(5), 679–698. https://doi.org/10.1177/0892705712454289

Wang, P., Legrand, X., Boisse, P., Hamila, N., & Soulat, D. (2015). Experimental and numerical analyses of manufacturing process of a composite square box part: Comparison between textile reinforcement forming and surface 3D weaving. *Composites Part B: Engineering*, *78*, 26–34. https://doi.org/10.1016/J.COMPOSITESB.2015.03.072

Wang, Y., & Sun, X. (2001). Digital-element simulation of textile processes. *Composites Science and Technology*, *61*(2), 311–319. https://doi.org/https://doi.org/10.1016/S0266-3538(00)00223-2

West, B. Van, & Luby, S. C. (1997a). Fabric draping simulation in composites manufacturing. Part I: Description and applications. *Journal of Advanced Materials*, *28*, 29–35.

West, B. Van, & Luby, S. C. (1997b). Fabric draping simulation in composites manufacturing. Part II: Analytical methods. *Journal of Advanced Materials*, *28*, 36–41.

Willems, A., Lomov, S. V., Verpoest, I., & Vandepitte, D. (2008). Optical strain fields in shear and tensile testing of textile reinforcements. *Composites Science and Technology*, *68*(3–4), 807–819. https://doi.org/10.1016/j.compscitech.2007.08.018

Xiang, Z., Jakkpat, K.-I., Ducharne, B., Capsal, J.-F., Mogniotte, J.-F., Lermusiaux, P., Cottinet, P.-J., Della Schiava, N., & Le, M. Q. (2020). Enhancing the Low-Frequency Induction Heating Effect of Magnetic Composites for Medical Applications. *Polymers*, *12*(2). https://doi.org/10.3390/polym12020386

Xiao, H., Bruhns, O. T., & Meyers, A. (1997). Hypo-Elasticity Model Based upon the Logarithmic Stress Rate. *Journal of Elasticity*, *47*(1), 51–68. https://doi.org/10.1023/A:1007356925912

Xue, P., Cao, J., & Chen, J. (2005). Integrated micro/macro-mechanical model of woven fabric composites under large deformation. *Composite Structures*, *70*, 69–80. https://doi.org/10.1016/j.compstruct.2004.08.013

Yang, H. T. Y., Saigal, S., Masud, A., & Kapania, R. K. (2000). A survey of recent shell finite elements. *International Journal for Numerical Methods in Engineering*, *47*(1-3), 101–127. https://doi.org/https://doi.org/10.1002/(SICI)1097-0207(20000110/30)47:1/3<101::AID-NME763>3.0.CO;2-C

Yu, W.-R., Harrison, P., & Long, A. (2005). Finite element forming simulation for non-crimp fabrics using a non-orthogonal constitutive equation. *Composites Part A: Applied Science and Manufacturing*, *36*(8), 1079–1093. https://doi.org/https://doi.org/10.1016/j.compositesa.2005.01.007

Yu, W. R., Pourboghrat, F., Chung, K., Zampaloni, M., & Kang, T. J. (2002). Non-orthogonal constitutive equation for woven fabric reinforced thermoplastic composites. *Composites Part A: Applied Science and Manufacturing*, *33*(8), 1095–1105. https://doi.org/https://doi.org/10.1016/S1359-835X(02)00053-2

Yudhanto, A., Watanabe, N., Iwahori, Y., & Hoshi, H. (2013). Effect of stitch density on tensile properties and damage mechanisms of stitched carbon/epoxy composites. *Composites Part B: Engineering*, *46*, 151–165. https://doi.org/https://doi.org/10.1016/j.compositesb.2012.10.003

Zhang, W., Ren, H., Liang, B., Zeng, D., Su, X., Dahl, J., Mirdamadi, M., Zhao, Q., & Cao, J. (2017). A non-orthogonal material model of woven composites in the preforming process. *CIRP Annals*, *66*(1), 257–260. https://doi.org/https://doi.org/10.1016/j.cirp.2017.04.112

Zhou, G., Sun, X., & Wang, Y. (2004). Multi-chain digital element analysis in textile mechanics. *Composites Science and Technology*, *64*(2), 239–244. https://doi.org/https://doi.org/10.1016/S0266-3538(03)00258-6

Zimmerling, C., Poppe, C., Stein, O., & Kärger, L. (2022). Optimisation of manufacturing process parameters for variable component geometries using reinforcement learning. *Materials & Design*, *214*, 110423. https://doi.org/https://doi.org/10.1016/j.matdes.2022.110423

Zouari, B., Daniel, J.-L., & Boisse, P. (2006). A woven reinforcement forming simulation method. Influence of the shear stiffness. *Computers & Structures*, *84*(5), 351–363. https://doi.org/https://doi.org/10.1016/j.compstruc.2005.09.031

Thesis publications

Articles publications:

1. **Chen, B**, Boisse, P., Colmars, J., Naouar, N., Bai, R., & Chaudet, P. (2021). Analysis of the Forming of Interlock Textile Composites Using a Hypoelastic Approach. Applied Composite Materials. https://doi.org/10.1007/s10443-021-09966-z
2. **Chen, B**, Colmars, J., Naouar, N., & Boisse, P. (2021). A hypoelastic stress resultant shell approach for simulations of textile composite reinforcement forming. Composites Part A: Applied Science and Manufacturing, 149, 106558. https://doi.org/10.1016/J.COMPOSITESA.2021.106558
3. Bai, R., Colmars, J., **Chen, B**., Naouar, N., & Boisse, P. (2022). The fibrous shell approach for the simulation of composite draping with a relevant orientation of the normals. Composite Structures, 285, 115202. https://doi.org/https://doi.org/10.1016/j.compstruct.2022.115202

Conferences participation:

1. International conference. The 9th world conference on 3D fabric and their applications, April 2021.
2. National conference. JNC22 - Journées Nationales sur les Composites, Juin 2021.
3. International conference. The25th International Conference on Material Forming, April 2022, article accepted, Braga, Portugal.

FOLIO ADMINISTRATIF

THESE DE L'UNIVERSITE DE LYON OPEREE AU SEIN DE L'INSA LYON

NOM : Chen DATE de SOUTENANCE :

(avec précision du nom de jeune fille, le cas échéant)

Prénoms : Bo

TITRE : Approches de coques en efforts résultants pour la simulation de la mise en forme des renforts textiles de composites

NATURE : Doctorat Numéro d'ordre : 2022LYSEI034

Ecole doctorale : Ecole Doctorale N° 162 Mécanique, Energétique, Génie civil, Acoustique

Spécialité : Génie Mécanique

RESUME : La simulation numérique du renfort composite textile joue un rôle essentiel dans l'amélioration de la qualité de fabrication, la réduction du cycle de fabrication et le coût de fabrication. L'épaisseur du renfort composite textile est nettement inférieure aux deux autres dimensions, ce qui permet de faire la simulation à l'aide d'élément de coque. Cependant, le glissement possible entre les fibres confère au matériau un comportement bien particulier : le comportement en flexion est indépendant du comportement de la membrane. La théorie classique de la coque ne peut pas être directement adoptée. Une approche coque résultante de contrainte est proposée pour la simulation du renfort composite textile. Cette approche introduit une rigidité en flexion indépendante pour découpler le comportement en flexion avec le comportement de la membrane. Les résultantes de contrainte et les moments de contrainte sont liés aux déformations et aux courbures de la membrane par des équations constitutives de vitesse (lois hypoélastiques). Différents types d'expériences de formage sous différentes conditions aux limites sont menées pour faire la comparaison entre la simulation et l'expérience. La comparaison montre l'efficacité et la justesse de l'approche proposée pour prédire la formation du composite textile. Cette approche est implémentée dans le logiciel commercial ABAQUS et peut être utilisée par tous les utilisateurs de ce logiciel.

Spécifique aux approches de simulation existantes qui ne peuvent se concentrer que sur la déformation dans le plan du matériau, une méthode de post-traitement est proposée pour prédire la rotation des directeurs normaux. Basée sur le mécanisme de déformation du matériau, cette méthode suppose que la fibre est quasi-inextensible et que l'épaisseur restera constante. Ensuite, la rotation des directeurs normaux peut être obtenue sur la base de la déformation dans le plan. Un programme Matlab est codé pour effectuer le calcul. Le test de flexion en porte-à-faux multicouche est effectué pour valider l'efficacité de la méthode de post-traitement.

Le froissement est l'un des principaux défauts lors de la mise en forme du renfort composite textile. Un ratio est défini pour caractériser la drapabilité du matériau textile qui est la capacité à se déformer sans plis. Une série d'expériences de formation de boîtes carrées et de cylindres est menée en utilisant différents types de renforts composites textiles. Il est démontré que le rapport défini peut représenter la drapabilité du matériau. Et le matériau avec un rapport de drapabilité plus petit est plus facile à former des formes complexes sans plis.

MOTS-CLÉS : Composite textile; Analyse par éléments finis; Coques résultant de contraintes; Rotation normale; Drapabilité.

Laboratoire (s) de recherche : Laboratoire de Mécanique des Contacts et des Structures (LAMCOS), INSA-Lyon

Directeur de thèse: Philippe BOISSE, Julien Colmars

Président de jury :Christophe Binetruy

Composition du jury: Christophe Binetruy, Luise kärger, Peng Wang, Naim Naouar, Philippe boisse, Julien Colmars